Design and synthesis of novel fluorescent chemosensors for selective detection of different metal ions with applications in live cell imaging

Thesis Submitted for the Degree of
Doctor of Philosophy (Science)
2024

Submitted By

MOHAFUZA KHATUN

Index No. 21/19/Chem./26 of 2019
Registration No. SCHEM1402119
Department of Chemistry
Jadavpur University

Under the Supervision of

Prof. Amrita Saha
Professor
Department of Chemistry
(Inorganic Section)
Jadavpur University
Kolkata-700032

যাদবপুর বিশ্ববিদ্যালয়
কলকাতা-৭০০০৩২, ভারত

*JADAVPUR UNIVERSITY
KOLKATA-700 032, INDIA

FACULTY OF SCIENCE: DEPARTMENT OF CHEMISTRY : INORGANIC CHEMISTRY SECTION

CERTIFICATE FROM THE SUPERVISOR

This is to certify that the thesis entitled "**Design and synthesis of novel fluorescent chemosensors for selective detection of different metal ions with applications in live cell imaging**" submitted by Ms. **Mohafuza Khatun**, who got her name registered on 14/08/2019 (Index no. 21/19/chem./26/Registration no. SCHEM1402119) for the award of Ph. D. (Science) Degree of Jadavpur University, is absolutely based upon his own work under the supervision of Prof. Amrita Saha (Professor, Department of Chemistry, Jadavpur University, Kolkata-700032) and that neither this thesis nor any part of it has been submitted for either any degree / diploma or any other academic award anywhere before.

Amrita Saha

(Prof. Amrita Saha)
Professor
Department of Chemistry
(Inorganic section)
Jadavpur University
Kolkata-700040

Date: 13.08.2024.

Dr. Amrita Saha
Professor
Department of Chemistry
Jadavpur University
Kolkata-700032

Dedicated
to
My parents and
my husband

Acknowledgements

With great pleasure and honor, I am ready to submit my Ph.D. thesis entitled **"Design and synthesis of novel fluorescent chemosensors for selective detection of different metal ions with applications in live cell imaging"** which is based entirely on research I conducted at Jadavpur University, Department of Chemistry. In this regard, I want to express my profound gratitude to everyone who helped me throughout this journey and enhanced my experience.

First and foremost, I would also like to sincerely thank Prof. Amrita Saha, Professor, Department of Chemistry, Inorganic section Jadavpur University, who has been my mentor, philosopher, and guide. My work has been completed because of her unwavering commitment, intense curiosity, and, most importantly, her enormous desire to support her pupils. Her prompt guidance, careful examination, academic counsel and scientific methodology have all been very helpful to me in my job. She not only taught me a lot about science, but also how to focus and have patience in the future. This work would not have been feasible without her creative oversight and her constant, unwavering support.

I would like to express my sincere gratitude to Prof. K. K. Rajak, (Head of the Department) and Prof. P. Roy (Section-In-Charge) of Jadavpur University for their kind help, co-operation and suggestion. I am also grateful to Prof. S. Bhattachary, Prof. C. Sinha, Prof. S. Das, Prof. S. Koner, Prof. S. Baitalik, Dr. B. B. Show, Dr. P. Mahata, Prof. S. Chattopadhyay, Prof. M. Ali, (Inorganic Chemistry Section), Prof. T. Bhaumik (Organic Chemistry Section) and Prof. P. P. Parui (Physical Chemistry Section) for their spontaneous help and co-operation.

I heartily acknowledge Dr. S. Blasco, Prof. E. García-España, Prof. P. Karmakar and Dr. A. Panja, Dr. A. Barui for their kind collaboration.

I would like to express thankfulness to my lab mates, especially Dr. Pravat Ghorai, Dr. Jayanta Mandal, and Mr. Suvomoy Malik (Research Scholar), Department of Chemistry, Jadavpur University, for their invaluable support, endless help and suggestions in every aspect during my research work. I convey my gratefulness to Dr. Narayan Ch. Jana (NISER, Bhubaneswar), Mr. S. G. Chowdhury (Department of Life Science and Biotechnology, Jadavpur University), Mr. Rajdeep Ganguly (IIEST, Howrah), Dr. Anirban Ghosh (IACS, Kolkata) and many others for their suggestions and scientific support. Also I would like to thank Vanessa W. Tamang, Rahul K. Prasad, Arindam Sanphui for their valuable support.

With great pleasure, I express my gratitude to my parents, my husband and my entire family for their unwavering understanding, moral support and encouragement over the years.

Finally, I give thanks to the Almighty God for giving me the bravery and strength to complete this journey.

Mohafuza Khatun

(MOHAFUZA KHATUN)
Department of Chemistry
Jadavpur University
Kolkata-700032

Date:. 13·08·2024

Contents

PREFACE

The thesis entitled, **"Design and synthesis of novel fluorescent chemosensors for selective detection of different metal ions with applications in live cell imaging,"** provides a summary of my whole research work on design and synthesis of fluorescence chemosensors and their applications. These days, research on chemosensors is very interdisciplinary due to its significance and applications in a variety of sectors, including chemistry, biology, medicine, and environmental studies. In my Ph.D work I have prepared novel chemosensors which are characterized using mass analysis, and a number of spectroscopic methods, including ^{1}H, ^{13}C-NMR, UV-Vis and FT-IR. Single crystal X-ray diffraction is used to confirm the representative probes' structural integrity. The sensing mechanisms of the probes are supported by theoretical calculations based on Density Functional Theory (DFT). The research work was successfully completed entirety at Jadavpur University, Department of Chemistry, under the supervision and direction of Prof. Amrita Saha, Professor, Department of Chemistry of this university. There are six chapters in this thesis, which are outlined below:

Chapter 1 represents a brief discussion regarding the significance of various metal ions, spectroscopic techniques: analytical approaches. Different fluorescence sensing mechanisms have been made. Furthermore, a concise review has been provided on previously reported fluorescent chemosensors based on DFP, Pyridoxal and Rhodamine (fluorophoric units) to recognize different metal ions

In **Chapter 2**, two aza-phenol based macrocyclic probes have been designed for "CHEF-on" multi analytes sensing and study its application in biological cell imaging. The chemical structures as well as the photophysical properties of the probes are thoroughly studied in 1X PBS buffer medium.

Chapter 3 contains design and synthesis of a hydrazinopthalazine derived chemosensor, which detect Zn^{2+}, Al^{3+} metal ions via CHEF effect. The mechanism is further established by theoretical calculation. The chemosensors are thoroughly characterized by different spectroscopic techniques. Biological study has been performed using cervical cancer cell line HeLa.

Chapter 4 represents a pyridoxal based bio-compatible fluorometric chemosensor for recognition of Zn^{2+} ion. All spectroscopic analysis has been done in HEPES buffer at pH = 7.4 (MeOH:H_2O, 9:1, (v/v)). Theoretical calculations also carried out and its result supports its experimental data. Biological studies are performed in PC3 (prostate cancer cell) cell line.

Chapter 5 describes derivative of clove oil which used as chemosensor for colorimetric and fluorometric detection of Al^{3+}. Its crystal structure description and live cell imaging using ***MC3T3*** cell line are also included here. All spectroscopic experiments have been performed in HEPES buffer at pH = 7.4 (MeOH:H_2O, 9:1, (v/v)).

Chapter 6 covers the development and synthesis of an euganol-sulfonyl based fluorescent probe for recognition of Al^{3+}. Biological cell imaging is also discussed here.

In keeping with the general practice of reporting scientific observation, due acknowledgement has been made whenever the work described as based on the findings of other investigators. I must take the responsibility of any unintentional oversights and errors which might have crept in spite of due precautions.

(MOHAFUZA KHATUN)

List of Abbreviations and symbols

τ	: Fluorescence Lifetime
Φ	: Quantum yield
π	: Pi
σ	: Sigma
Δr	: Charge transfer index
σ_S	: Hole-electron overlapping indices
a	: Crystallographic distance along 'x' axis of a unit cell (in angstrom)
b	: Crystallographic distance along 'y' axis of unit cell (in angstrom)
c	: Crystallographic distance along 'z' axis of unit cell (in angstrom)
α	: Crystallographic angle in a unit cell between *b* and *c* (in degree)
β	: Crystallographic angle in a unit cell between *c* and *a* (in degree)
γ	: Crystallographic angle in a unit cell between *a* and *b* (in degree)
ρ	: Density (in g cm^{-3})
Mo-Kα	: Molybdenum Kα radiation
F(000)	: Crystallographic (000) plane
Å	: Angstrom
BH	: Benesi Hildebrand
DFT	: Density functional theory
TDDFT	: Time dependent functional theory
DMSO-d_6	: Deuterated dimethyl sulfoxide
F	: Fluorescence intensity
ex	: Excitation
em	: Emission
UV	: Ultraviolet
vis	: Visible
λ	: Wavelength
%T	: Percentage of transmittance
h	: Hour(s)
KBr	: Potassium bromide
$CHCl_3$	: Chloroform
ACN	: Acetonitrile
MeOH	: Methanol
DCM	: Dichloromethane
DMF/dmf	: *N*,*N*-Dimethylformamide

DMSO/dmso : Dimethyl sulfoxide
DMSO-d_6 : Deuterated dimethyl sulfoxide
mL : Milliliter
μM : Micromolar
nM : Nanomolar
eV : Electron-volt
ESI MS : Electron Spray Ionization Mass spectrometry
FTIR : Furrier Transform Infrared Spectroscopy
EPR : Electron Paramagnetic Resonance
NMR : Nuclear Magnetic Resonance
PXRD/XRPD : Powder X-ray Diffraction/X-ray Powder Diffraction
CT : Charge Transfer
PET : Photo-Induced Electron Transfer
PCT : Photo-Induced Charge Transfer
ICT : Internal Charge Transfer
ET : Energy Transfer
FRET : Fluorescence Resonance Energy Transfer
ESIPT : Excited-State Intramolecular Proton Transfer
HOMO : Highest Occupied Molecular Orbital
LUMO : Lowest Unoccupied Molecular Orbital
CHEF : Chelation Enhanced Fluorescence
CHQF : Chelation-quenched fluorescence
K_f / K_a : Association constant
K_d : Dissociation constant
HeLa : Human epithelial carcinoma cell
MC3T3 : Mus musculus (mouse) calvaria cell
PC3 : Prostate cancer cell
PBS : Phosphate-buffered saline
Tris : Tris(hydroxymethyl)aminomethane
LOD : Limit of Detection
EDTA : Ethylenediaminetetraacetic acid
HEPES : 4-(2-Hydroxyethyl)piperazine-1-ethanesulfonic acid
eV : Electron volt
ORTEP : Oak Ridge Thermal Ellipsoid Plot

Chapter 1

General introduction & literature survey

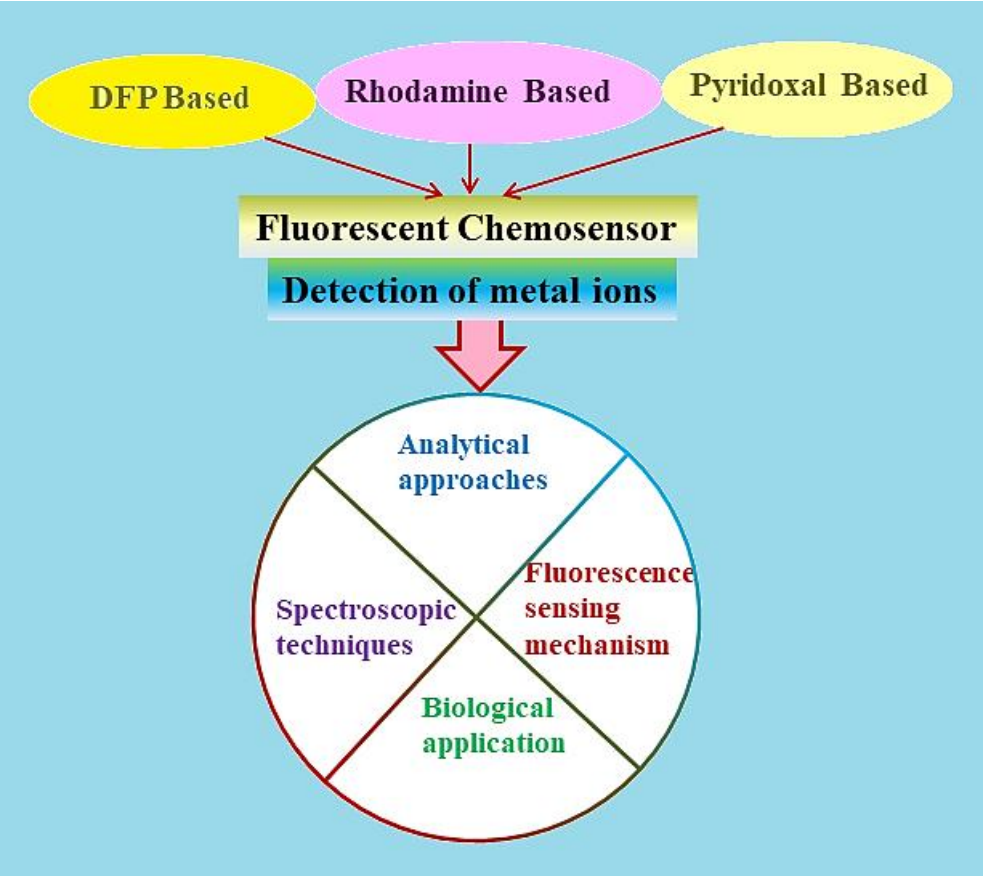

Chapter 1	*General introduction & literature survey*

Abstract

Here, a brief discussion regarding the significance of various metal ions, spectroscopic techniques: analytical approaches, fluorescence sensing mechanisms have been made. Furthermore a concise review has been provided on previously reported fluorescent chemosensors based on DFP, Pyridoxal and Rhodamine (fluorophoric units) to recognize different metal ions.

Chapter 1	*General introduction & literature survey*

1.1. Introduction

Metal ions, anions and biomolecules detection are very important as they play significance role in human body as well as other living system. The main group of elements like: potassium (K), sodium (Na), magnesium (Mg), and calcium (Ca) as well as the transition metal group's copper (Cu), iron (Fe), nickel (Ni), molybdenum (Mo), and cobalt (Co), also other element as zinc (Zn), aluminium (Al) are the necessary metals for humans' normal biological functions [1.1,1.2]. But a number of heavy metal ions, such as mercury (Hg^{2+}), cadmium (Cd^{2+}) and lead (Pb^{2+}) are hazardous and seriously harm human health as well as the environment. Development and synthesis of these metal ions detector at trace level is most demanding work, especially for environmental and health science [1.3-1.10]. There are so many methods for detection of metal ions, for example: inductively coupled plasmaeoptical emission spectrometry (ICP-OES) [1.11], liquid-cathode glow discharge-atomic emission spectrometry [1.12], high performance liquid chromatography (HPLC) [1.13-1.15], neutron activation analysis [1.16], electrophoresis [1.17], atomic absorption and emission spectroscopy [1.18-1.20], anodic stripping voltammetry [1.21,1.22], and stripping voltammetry [1.23-1.25]. These techniques have quick measurement speeds, high selectivity, and high sensitivity; nevertheless, they have certain drawbacks, including being costly, difficult to use, and requiring a lot of sample preparation [1.26, 1.27]. Therefore, sensitive techniques that are both technically straightforward and effective are still needed for the identification of these contaminants. For analyzing various substances, the most practical analytical method is colorimetric and fluorometric detection. Both methods provide rapid, easy, cost-effective, simple, efficient, and highly sensitive detection capabilities [1.27–1.30]. The term "fluorescence" was initially used in 1852 by English mathematician and physicist Sir George G. Stokes. A substance that retains the inherent capacity to release fluorescent photons upon appropriate wavelength excitation is known as a fluorescent chemosensor.

Fluorescent probes find extensive uses in the fields of cell biology, immunology, molecular biology, neurobiology, and biophysics, including pharmaceutical research, clinical diagnostics, and high-throughput screening for the identification of nucleic acids, enzymes, lipids, proteins, antibodies, etc. The use of diverse chemosensors, especially fluorescence sensors, to distinguish between distinct metal ions or anions has enhanced molecular recognition technology in recent years. The development of sensors based on proteins, peptides, quinolines, fluorescein, and coumarin has been utilized to measure intracellular ion concentrations. F. Goppelsro¨der described the first fluorescent chemosensor in 1867. It used a method of producing a strongly fluorescent morin chelate to determine the aluminium ion (Al^{3+}) [1.31]. Fluorescent chemosensors typically use one or more of the widely used photophysical mechanisms to detect analytes, such as chelation-induced enhanced fluorescence (CHEF) [1.31], intramolecular charge transfer (ICT) [1.32], photoinduced electron transfer (PET) [1.33], aggregation-induced emission (AIE) [1.34], and more.

1.2. Discussion regarding the significance of various metal ions and their fluorescent chemosensors

1.2.1. Alkali and alkali earth metal ions

Potassium ions (K^+) are the most significant cations found in living systems due to their vital functions in numerous biological processes. Mammals have a K^+ content inside their cells of approximately 150 mM, which is nearly thirty times higher than the external environment. Numerous illnesses, including diabetes, heart disease, anorexia, and Alzheimer's disease are intimately linked to potassium imbalances. Several K^+ fluorescent chemosensors have been produced. The greatest K^+-selective chelator, 2-triazacryptand [2,2,3]-1-(2-methoxyethoxy)benzene (TAC) group is available right now, which shows highest selectivity to detect K^+ over other physiologically relevant metal ions. J. K. Tusa *et al*. published the first report on the TAC group in 2003 [1.35a]. Using an ethylene group, they

integrated the TAC group into a 4-aminonaphthalimide-based polymer to create chemosensor **1.1**, which measures potassium levels in extracellular fluid (serum or whole blood) using a PET mechanism (**Scheme 1.1**). Again, Y. Tian and his coauthors synthesized and investigated a new mitochondria-targeted fluorescent potassium ion sensor **1.2** (**Scheme 1.1**), offering potential broad applications. **1.2** showed good response towards K^+, with a broad detection range, short response time, high sensitivity, and minimal responses to physiological pH and other metal ions. It allowed high-throughput in-situ monitoring of mitochondrial K^+ fluxes, making it beneficial for ion channel relative drug screening and mitochondrial potassium channel investigation [1.35b].

Again, Sodium is the sixth most common element (2.83%) in the Earth′s crust. In mammals, sodium ions can be utilized against potassium ions to facilitate the transfer of electrostatic charges across cell membranes, so enabling nerve impulse transmission. Humans require sodium for proper muscle and nerve function as well as for the maintenance of the bodily fluid balance. Sodium is therefore categorized as one of the "dietary inorganic macro-minerals for animals". However, a diet heavy in sodium can harm the kidneys and raise blood pressure [1.36]. A. Tamilselvi and his group reported a ratiometric highly fluorescent small molecular probe (**1.3**) (**Scheme 1.1**) for detection of Na^+ ions in DMF:water (1:9,v/v) media. Through single crystal XRD, the chemical structure of the Na^+-complex of the probe was verified. Studies on fluorescence decay revealed that Na-**1.3** had a shorter lifespan than chemosensor **1.3**. Quantum chemistry investigations explore electronic transitions and ESIPT mechanism, using impedance spectra and cyclic voltammetry. Additionally, it had been demonstrated that the probe can be used for paper-based Na^+ ion imaging and sensing in U87 cell lines [1.137a]. A novel dipodal fluorescent sensor **1.4** (**Scheme 1.1**) was developed for detection of Na^+ ion by B. K. Kanungo *et al.* The sensor used PET mechanism and showed excellent selectivity for Na^+ among other metal ions with a remarkable enhancement in the

fluorescence intensity from 345.5 to 705.5 a.u. at λ_{max} = 532.9 nm. The sensor's 1:2 binding stoichiometry confirmed its high association constant ($7.7 \times 10^6\ M^{-2}$) with the sodium metal ion. The study explored potential applications for Na^+ ion detection in environmental and industrial settings [1.137b].

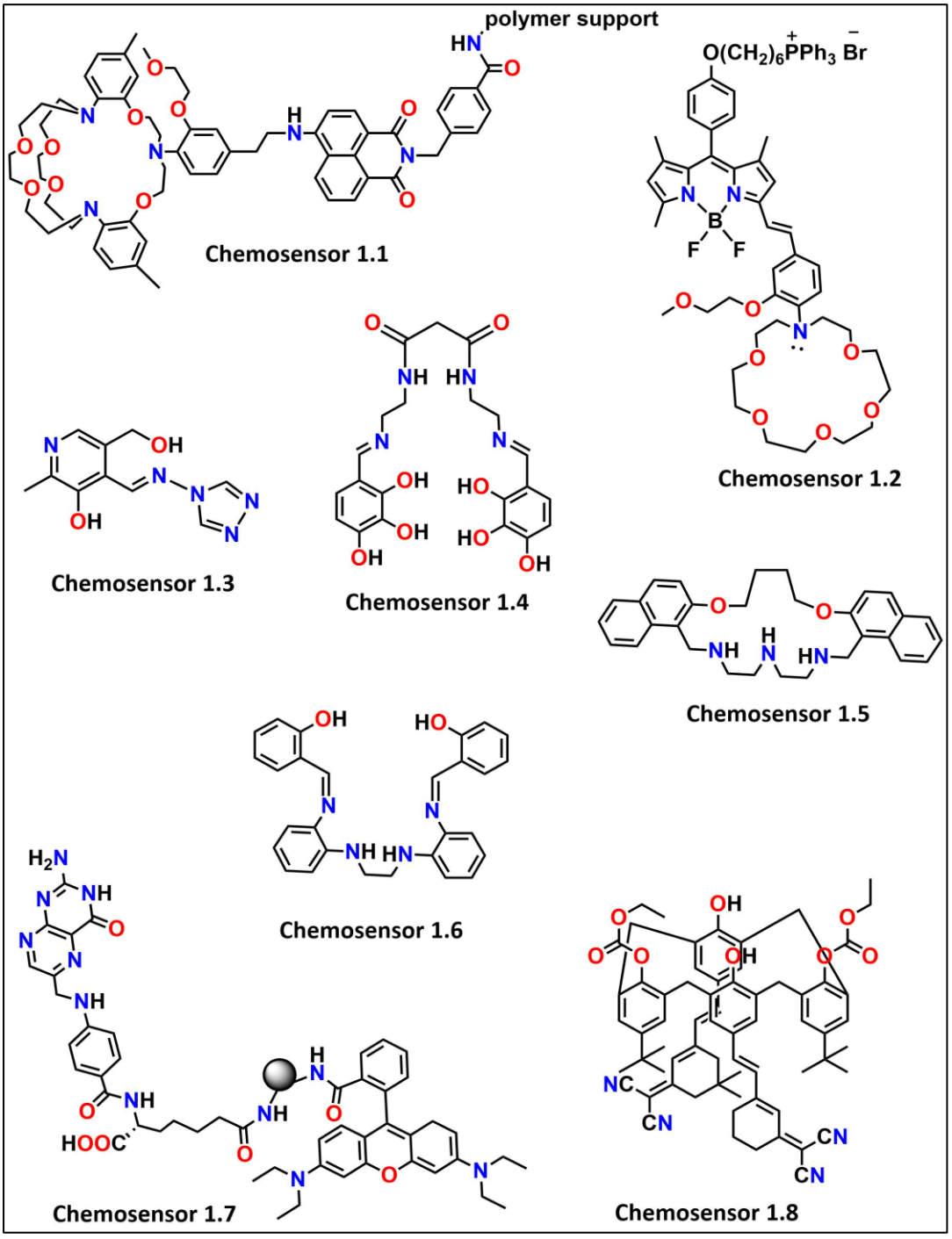

Scheme 1.1. Structure of chemosensors **1.1-1.8**.

The most prevalent divalent cation in cells is the magnesium ion (Mg^{2+}), which performs several vital functions like enzyme cofactor, DNA conformation stabilizer, and trans-membrane ion transport facilitator in animal [1.38a-c]. Importantly, Mg^{2+} is the primary component of chlorophyll, controls photosynthesis in plants. Numerous illnesses, including Parkinson's disease, diabetes, migraines, and hypertension, are linked to abnormal Mg^{2+} ion exposures. A new N_3O_2 aza-crown macrocyclic ligand (chemosensor **1.5**) (**Scheme 1.1**) with fluorophore naphthalene moieties was synthesized by M. Koolivand and his team. Comparative studies showed that **1.5** was a sensitive and selective fluorescent chemosensor for Mg^{2+}, with a binding constant of 1.36×10^5 M^{-1} and a detection limit of 2.51×10^{-8} M [1.38d]. Another new fluorescent Schiff base chemosensor **1.6** (**Scheme 1.1**) was developed by S. Menatic *et al.* for the selective detection of Mg^{2+} ions. The **1.6** was a weak fluorescent compound that enhances fluorescence upon addition of Mg^{2+}, but had no significant effect on fluorescence in the presence of other metal ions. The detection limit of the ligand had a quick response time of 3.04×10^{-9} M towards Mg^{2+} ions [1.138e].

Other significant alkaline earth metal ion is calcium (Ca^{2+}). The most prevalent element in the human body, Ca^{2+} is essential to numerous biological functions. Since abnormalities in intracellular free Ca^{2+} are linked to a variety of illnesses, including heart disease, skeletal muscle problems, and neurodegeneration, it is crucial to monitor this level. R. Safaralizadeh and his group prepared a sensor **1.7** (**Scheme 1.1**) for measuring ionized calcium in water samples and cancer cells. This **1.7** nanoparticle was used for bioimaging of folate receptor-overexpressed cancer cells, showing a low-interference and excellent biocompatibility [1.39a]. Again, a novel chemosensor **1.8** (**Scheme 1.1**) was designed by S. Malkonduto *et al.* to recognize calcium ions in various environmental sample, including human body. The isophorone unit and calix[4]arene derivative combine to create a unique chromogenic and fluorogenic response towards Ca^{2+} ions in EtOH/H_2O (v/v, 9/1, Tris-HCl

buffer, pH 8.5). **1.8** can monitor selectively Ca^{2+} ions, with potential applications in smartphone, cotton swab, yeast cells, and water samples [1.39b].

1.2.2. Heavy and poisonous metal ions

One of the most common and fatal toxins on the planet is mercury (Hg), which is produced from a variety of sources including coal plants, thermometers, barometers, mercury lamps, and the mining of gold. These metals are known to induce a number of maladies, including neurological, cardiac, and developmental conditions. Numerous fluorescent chemosensors have been developed in recent decades to detect Hg^{2+}. Ajavakom *et al.* reported a unique fluorescent chemosensor, **1.9** based on thiourea-dihydropyridine which showed selective "turn on" fluorescence for Hg^{2+} in pure aqueous solutions, with a LOD of 69 nM (**Scheme 1.2**). Additionally, the probe **1.9** demonstrated nontoxic characteristics towards the RAW264.7 murine macrophage cell line in living cells [1.40a]. A chromone-based fluorescent chemosensor **1.10** (**Scheme 1.2**) was developed by P. Sakthivel and his coauthors for the selective detection of Hg^{2+} in a semiaqueous solution. It fluoresced significantly in its aggregated state and exhibited a 1:1 stoichiometry complex with Hg^{2+} with a binding constant of 9.10×10^3 M^{-1}. The probe **1.10** was successfully applied for bio-capability analysis in nematode worm [140b].

Lead ion (Pb^{2+}) poses a major risk to human health and the environment because of its extreme toxicity, [1.41a,b]. The primary sources of anthropogenic Pb^{2+} pollution are metal plating, waste incineration, battery production, petrol, and coal burning [1.41c]. Lead poisoning, ingestion, and skin adsorption can cause serious damage to a number of human organs, including the kidney, reproductive, and cardiovascular systems [1.41d,e]. Therefore, it is very desirable to have efficient techniques for tracking and identifying Pb^{2+} ions in the environment or polluted water. A chemosensor **1.11** based on naphthalene derivative was created by R. Azadbakht and his team (**Scheme 1.2**). It demonstrated high selectivity over

other competitive metal cations in CH_3CN/H_2O (9:1, v/v) mixture and strong fluorescence intensityt in the presence of trace amounts of Pb^{2+}, which can be ascribed due to restriction of the photo induced electron transfer (PET) effect [1.41f]. Another new chemosensor **1.12** (**Scheme 1.2**), derivative of 1H-pyrazolo[3,4-b]quinoline was synthesized and studied by T. Uchacz *et al.* using fluorescence and UV–vis absorption spectroscopy. The probe **1.12** exhibited good selectivity towards Pb^{2+} and Zn^{2+}. Its low fluorescence quantum yield and short fluorescence lifetime, making it efficient for optical detection of Pb^{2+} and Zn^{2+} and the detection limits were 1.07×10^{-6} M and 1.06×10^{-6} M, respectively. **1.12** can mimic an OR-type optical logic gate in cooperation with Pb^{2+} and Zn^{2+} [1.41f].

On the other hand rapid cadmium detection is widely wanted because cadmium is a crucial transition element that is employed in many different areas such as electroplating, industry and agriculture. Also it causes a variety of health issues like liver and kidney failure, 'itai-itai disease', osteoporosis, respiratory and immune system diseases, reproductive disorders, and even cancers [1.42a,b]. Chemosensor **1.13** (**Scheme 1.2**) was a new fluorescent chemosensor with pyridine rings was synthesized by J. Chen and his coworkers. With a very low detection limit, the chemosensor **1.13** was used as the sensitive and specific detection of Cd^{2+} ions. The chemosensor was able to identify Cd^{2+} ions in living cells at a trace level, as demonstrated by the cell imaging experiment [1.42c]. Again, N. B. Hamedani *et al.* developed a new fluorescent sensor **1.14** (**Scheme 1.2**) for cadmium detection using dialdehyde and diethylenetriamine. The chemosensor **1.14** showed a 3-fold enhancement in emission intensity towards Cd^{2+} ions at 430 nm (LOD = 2.7×10^{-9} M). Charge transfer was responsible for this enhancement. The sensor and its complexes showed antioxidant potency and antibacterial activity against bacteria [1.42d].

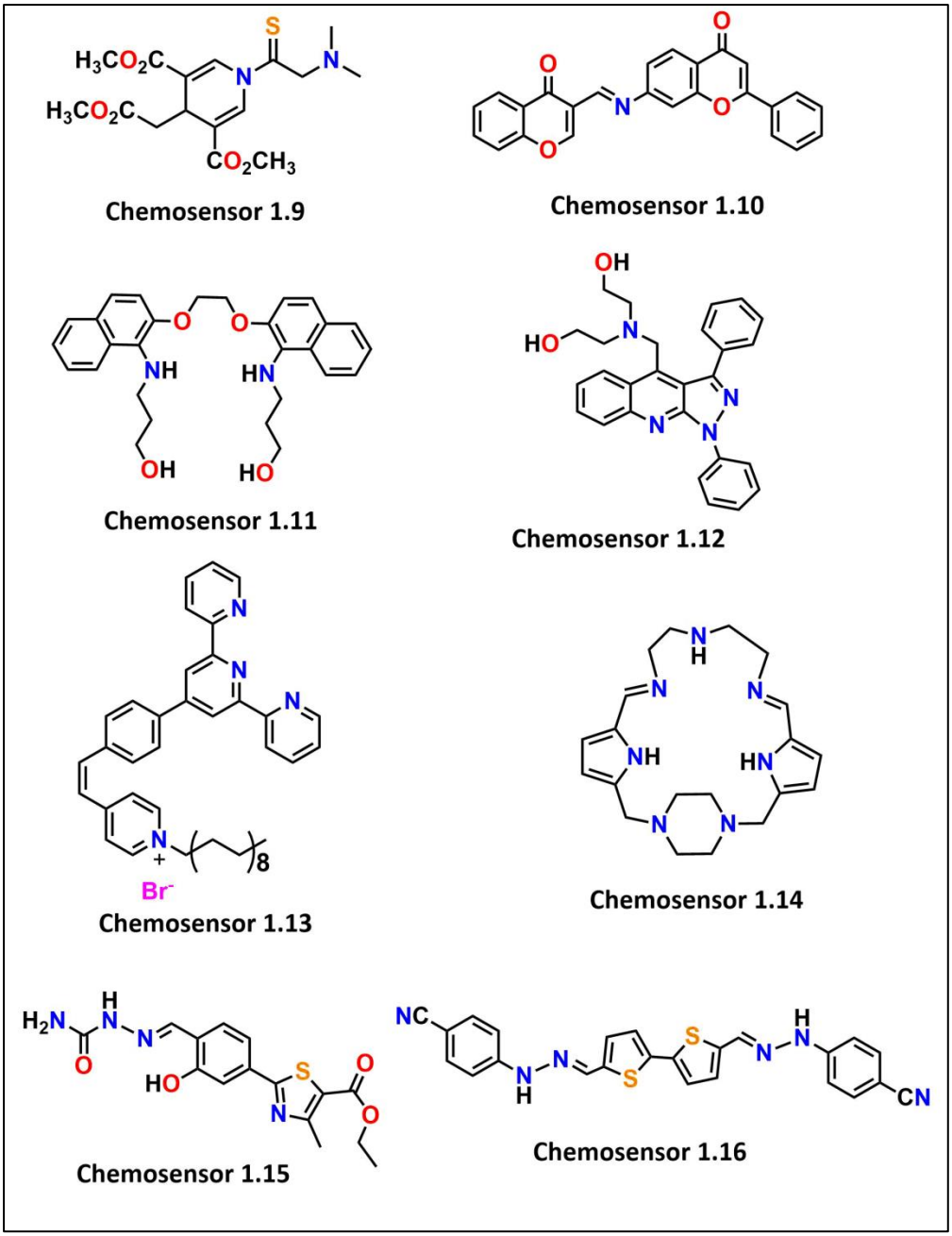

Scheme 1.2. Structure of chemosensors **1.9-1.16**.

One of the most hazardous and common heavy metals in the environment and ecosystem is arsenic (As^{3+}). It is extensively dispersed throughout the environment, including the air, rocks, soils, creatures, and marine species. Liquid wastewater and industrial waste are the main causes of heavy metal pollution in natural waterways, including rivers and groundwater [1.43a,b]. As^{3+} poisoning brought on by prolonged exposure to high

concentrations of trivalent arsenic is called ascenicosis in this context. Its symptoms include skin lesions and hard patches on the palms of the hands and soles of the feet, diseases of the blood vessels in the legs, malignancies of the skin and internal organs, diabetes, hypertension, and abnormalities of the reproductive system [1.43c,d]. Prolonged contact with inorganic As^{3+} has been related to a number of grave health issues, including esophageal and stomach pain, malignancies of the lung, liver, kidney, skin, and bladder, hyperkeratosis, diarrhoea, weakness in the muscles, lack of appetite, nausea, changes in pigmentation, and vomiting [1.43e]. Thiazole based dual chemosensor **1.15** was reported by A. A. Napoleon and his team to selectively detect arsenic (As^{3+}) ions in a DMSO:H_2O (7:3, v/v) solvent system (**Scheme 1.2**). The addition of As^{3+} ions caused the absorption spectrum alterations of **1.15**, resulting in a colour change from colourless to yellow that was visible to the naked eye. The photoluminescence and UV-visible titration methods yielded a limit of detection (LOD) of 7.19×10^{-9} M and 16.5×10^{-9} M for As^{3+} ions, respectively. The practical applications of As^{3+} ions in biological systems were established by fluorescence imaging experiments conducted on the MCF-7 breast cancer cell line [1.43f]. Again, D. R. Trivedi *et al.* synthesized chemosensor **1.16** (**Scheme 1.2**) with two acidic binding sites and demonstrated the ability to differentiate arsenite and arsenate in organo-aqueous mediums. **1.16** distinguished arsenite with a peacock blue color and arsenate with a pale green color, with specific selectivity for arsenite. The sensor demonstrated stability over a pH range of 5 to 12, and successfully detected arsenite in water, honey, and milk samples [1.43g].

1.2.3. Transition and other metal ions

Vanadium, the second most common transition metal in oceans, is found in seawater in concentrations of 30 to 35 nM in the form of $Na^{+}H_2VO_4^{-}$. The saliva, stomach and intestinal system all experience speciation following the oral absorption of vanadium compounds. Vanadium ions are present in considerable quantities as toxins in a few numbers

of species. Moderate toxicity is also present in certain other vanadium salts in addition to its oxide [1.44a]. P. M. Selvakumar *et al.* presented an efficient fluorescent chemosensor **1.17** for the first time that can recognize vanadyl ions (VO^{2+}) through fluorescent turn-on pathway (**Scheme 1.3**) [1.44b]. It was discovered that the combination **1.17**–VO^{2+} has an association constant of 4.19×10^4 M^{-1}. In addition, **1.17** functions as a NOT molecular logic gate in the presence of inputs H^+ and VO^{2+}. Using DFT calculations, the suggested binding mechanism between **1.17** and vanadyl ions was described. On the other hand, Z. X. Nie and his groups described the optical characteristics of a newly developed rhodamine based chemosensor **1.18** in a methanol:HEPES solution (**Scheme 1.3**) [1.44c]. The new sensor showed selectivity for Cu^{2+}, as evidenced by a colourless to dark red colour changes, which was examined with UV-visible spectroscopy. Conversely, the determination of selectivity towards VO^{2+} was based on variations in the emission spectra within the nanomolar range. This is the first rhodamine-based sensor that has been documented to be able to detect VO^{2+} and Cu^{2+} in two separate modes.

A vast range of industrial operations, including metal electroplating, corrosion protection, and leather tanning, rely on chromium because of its special qualities. Chromium, one of the most harmful contaminants in soil, groundwater and surface water, also, widely used in industry. In the environment, chromium is mostly found as Cr(VI) and Cr(III). The most common oxidation state found in soil and water is +3 [1.45a]. The human body uses Cr^{3+} to stabilize proteins and nucleic acids, activate specific enzymes and control the action of insulin through glucose tolerance factors (GTFs) [1.45b]. Intracellular reducing agents decrease Cr^{6+} to Cr^{3+}, which binds DNA through the phosphate backbone and guanine N7 [1.45c]. Chromium deficiency can heighten the risks of diabetes, neurological system disorders, cardiovascular diseases and other disorders, while elevated Cr^{3+} levels have the potential to induce cancer [1.45d]. D. Divya *et.al* obtained a chemosensor **1.19** (**Scheme 1.3**)

for detection of Cr^{3+} ions showing significant hypsochromic shift (335 nm → 285 nm) in the absorption spectra. The Benesi-Hildebrand plot results the binding constant (K_a) of 0.21×10^5 M^{-1}, whereas the limit of detection (LOD) and limit of quantification (LOQ) of the chemosensor **1.19** towards Cr^{3+} ions were 4.70×10^{-7} M and 1.56×10^{-7} M, respectively. Also they have done the theoretical calculation and real sample analysis for this chemosensor and its metal bound complex [1.45e]. A new chalcone-based chemosensor **1.20** (**Scheme 1.3**) combined from 6-chlorothiochroman-4-one and cinnamaldehyde by the team of M. Umadevi [1.45f]. Chemosensor **1.20** showed the maximum fluorescence intensity enhancement in presence of Cr^{3+} over other metal ions, and the binding or association constant and detection limit were 1.684×10^5 M^{-1} and 0.2245×10^{-9} M, respectively.

Another metal ion, Manganese (Mn) which is a crucial trace nutrient in all life forms, also essential for photosynthesis. Manganese has structural and catalytic roles in a variety of proteins, including superoxide dismutase and the photosynthetic machinery [1.46a]. Through Mn-binding transcription factors, it has significant effects on gene expression, and metalloregulatory proteins contribute to the homeostasis specific to particular metals [1.46b]. Its functions in oxidative virulence [1.46c] and stress [1.46d] have been established. Mn^{2+} is frequently employed as a flexible instrument for biological research at the cellular and organ levels. Exposure to high levels of manganese dusts and fumes can lead to impaired motor skills, cognitive disorders, and increased intellectual impairment in children. Overexposure can cause oxidative stress, mitochondrial dysfunction, glutamate-mediated excitoxicity and protein aggregates [1.46e]. Recently, a novel method for Mn^{2+} ion sensing via fluorescence "off-on" mode based on supramolecular metal displacement mechanism was reported [1.46f]. T. S. Singh and his group has developed an novel fluorescent chemosensor **1.21** (**Scheme 1.3**) by condensation of 6-3(thienyl)pyridine-2-carboxaldehyde and 1, 2-phenylenediamine in the ethanolic medium. It is a fluorescent turn-on detector for Mn^{2+} over other metal ions

[1.46g]. A. Umit investigated the selectivity and sensitivity of as a fluorescent chemosensor **1.22** (**Scheme 1.3**) against Mn^{2+} ions, determining a 1:1 binding stoichiometry by the Benesi-Hildebrand method [1.46h].

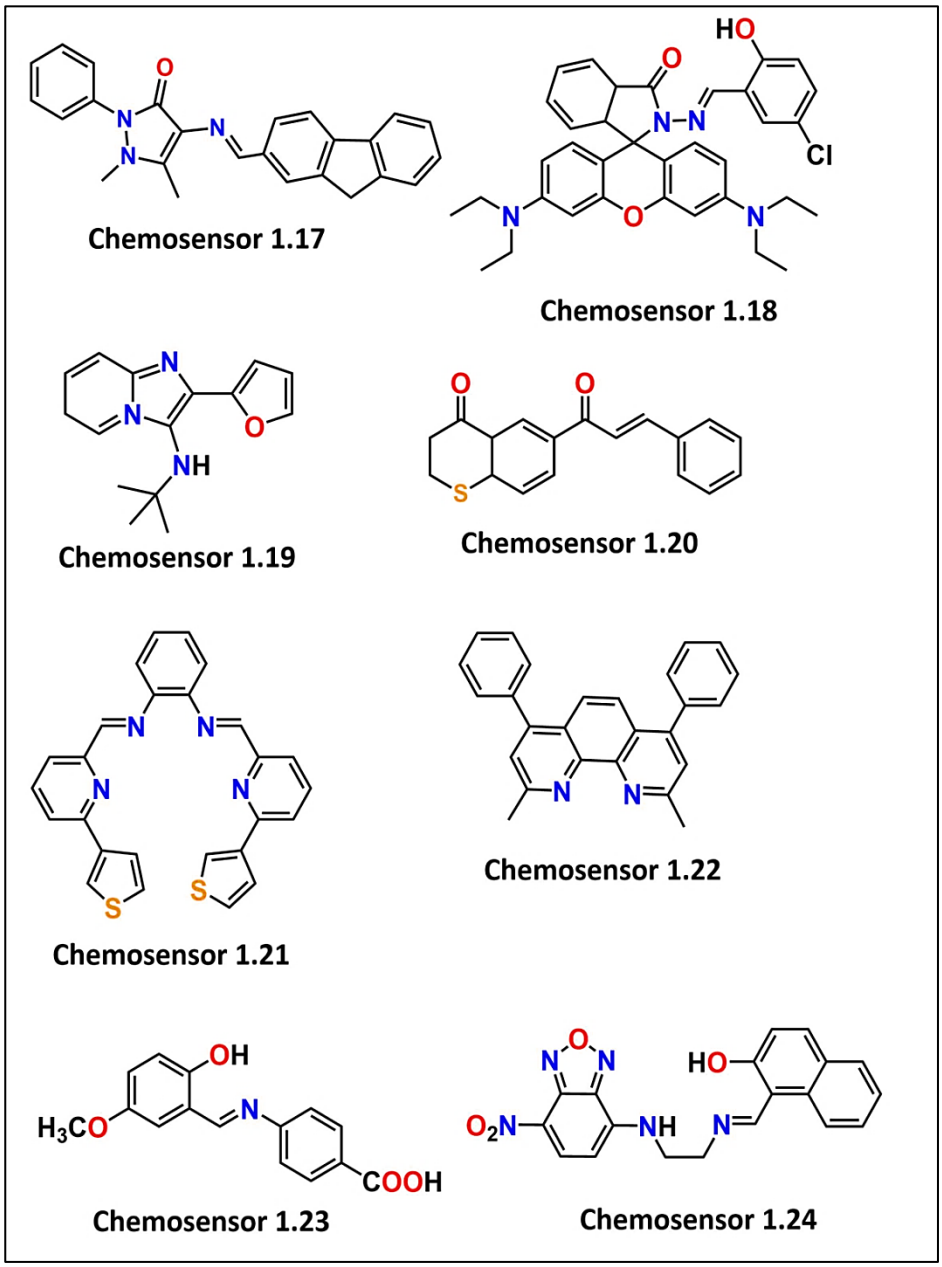

Scheme 1.3. Structure of chemosensors **1.17-1.24**.

The most common metal ion at the moment and one that is essential to all living things is iron (Fe^{3+}/Fe^{2+}), another transition metal. A substantial amount of iron is required for both photosynthesis and respiration. Furthermore, ingesting a lot of iron can damage cells

in a variety of ways, which can ultimately lead to human and other forms of life death. However, a substantial amount of iron is required for both oxygen uptake and metabolism [1.47a]. Only 6% of the iron present in some proteins and enzymes is available for the creation of ferritin in the blood and cells, while 70% of the iron in human blood is located in haemoglobin [1.47b]. Therefore, it is imperative that fluorescent chemosensors be developed immediately in order to detect Fe^{3+} in an easy, economical, and highly selective and sensitive manner. Z. Li and his coworkers derived a chemosensor **1.23** (**Scheme 1.3**) which exhibited typical aggregation-induced emission behaviour in an aqueous solution and was utilized as a highly sensitive and selective turn-off fluorescence sensor for Fe^{3+} detection in a THF-H_2O system (3:7, v/v). With a LOD value (0.079 μM) of the fluorescent probe demonstrated a very wide dynamic response range (0.5–500 μM) for the selective recognition of Fe^{3+} showing real-world application [1.47c]. A Schiff-base fluorescent chemosensor **1.24** (**Scheme 1.3**) synthesized by S. Shuang *et al.* for spectral sensing of Fe^{3+} ions at neutral pH [1.47d]. **1.24** showed good selectivity and sensitivity, with detection limit as low as 4.51 nM. It was successfully applied in fluorescence imaging of exogenous and endogenous Fe^{3+} in live cells.

Cobalt, one of the most significant heavy metals and the majority of cobalt ions can be found in rocks, minerals, and soils. The concentration range of Co^{2+} in environment is up to 100 μg L^{-1} in wastewater and 0.5–12 μg L^{-1} in sea water [1.48a]. Because of its hardness and resistance to oxidation, cobalt is used in the production of electric cables, magnets, batteries, mining, pigments, automotive industries, stainless steel alloys, coloring, catalysts, and other products and processes [1.48b,c]. The human body has between 1.1 and 1.5 mg of Co^{2+} overall, with 14% of it found in bone and 43% in muscles and soft tissues. Once more, as a component of vitamin B12, cobalt is advantageous to human health. Because of this, life requires Co(II) in trace amounts, but larger concentrations can be injurious to human health

[1.48a]. Using 9-anthracene carboxaldehyde and 2-amino 5-nitro benzophenone, a unique and highly selective fluorescent optical sensor **1.25** (**Scheme 1.4**) was produced by J. Shakina *et al.* for Co^{2+} detection in ethanol medium via charge transfer and the CHEF mechanism [1.48d]. The detection limit was determined to be 0.00091 µM, significantly lower than the WHO-recommended acceptable limit. Biological application and real sample analysis were done for **1.25**. Another chemosensor **1.26** (**Scheme 1.4**) was reported by K. W. Tan and his team using rhodamine B hydrazide and 2,3,4-trihydroxybenzaldehyde for detection of Co^{2+} ions by 'naked-eye'[1.48e]. It can detect a wide range of metal ions and had a low detection limit. The sensor's reversibility as a Co^{2+} ion detector was confirmed, and low-cost test strips were fabricated for easy detection. The MTT assay was conducted to determine its cytotoxicity against human cell lines.

Nickel is a moderately hazardous element with widespread applications across multiple industries when compared to other heavy metals. Due to its extensive use in electroplating for superior alloying metal, it is extensively utilized in the steel sector [1.49a,b]. Moreover, nickel, is a component of the urease enzyme's structure [1.49c]. Even though nickel is essential to human life, exposure to nickel compounds at greater quantities can lead to severe health complications such as nickel eczema and cancer of the respiratory system [1.49d]. R. M. Al-As'ad and his coworkers synthesized a Schiff-base **1.27** (**Scheme 1.4**) which was used as an optical chemical sensor for Ni^{2+} because it showed a consistent variation in absorption intensity with Ni^{2+} concentration at wavelength 385 nm in the range of 0–50 µM [1.49e]. The Schiff-base's biological activity demonstrates strong antibacterial properties, making it a potential treatment for several common Staphylococcus aureus-related illnesses. The chemosensor **1.28** (**Scheme 1.4**), a colorimetric chemosensor, was developed by S. Moon *et al.* for the consecutive detection of Ni^{2+} and CN^{-} in water samples [1.49f]. It detected Ni^{2+} exclusively, with a detection limit of 0.209 µM. The **1.28**-Ni^{2+} complex showed

selective color variation for CN^-, with a detection limit of 20.8 μM. The binding ratios were determined as 1:1, and binding mechanisms were demonstrated through various methods.

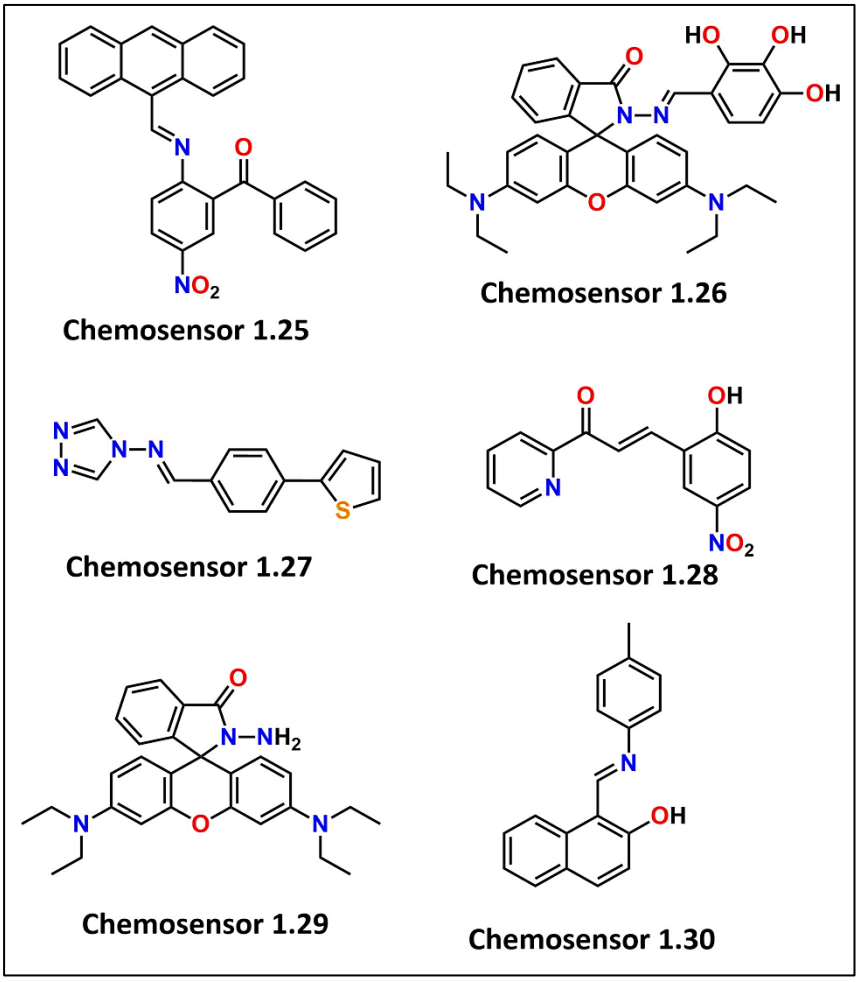

Scheme 1.4. Structure of chemosensors **1.25-1.30**.

The third most prevalent transition metal in the human body, copper (Cu) is vital to all living things as it plays a number of physiological and pathogenic procedures. Diseases including Menkes (copper shortage), Wilson's (copper excess), Alzheimer's, prion disorders, neurodegeneration, and cancer are all associated with a loss of copper homeostasis. Czarnik et al. (1997) published groundbreaking work on a derivative of rhodamine-B and its ring-opening process for the detection of copper ions (Cu^{2+}) [1.50a]. Fluorescent rhodamine B is the result of a selective hydrolysis reaction between Cu^{2+} and the fluorescent chemosensor

1.29, as illustrated in **Scheme 1.4**. This work attracted a lot of attention to the rhodamine ring-opening mechanisms. A fluorescent chemosensor **1.30 (Scheme 1.4)** was developed by J. S. Algethami and his coworkers [150b]. **1.30** showed excellent selectivity and sensitivity towards Cu^{2+} in both solution and solid mediums and the detection limit was low (0.0025 ppm).

Similar to iron, zinc is an abundant metal with endless biological significance in our bodies even its relatively modest concentration (about 2-3 gm overall). Serious illnesses including Parkinson's and Alzheimer's disease have been connected to human populations with high zinc metal ion concentrations [1.51a-e]. Zn^{2+} has been identified as one of the most important metal cations by zinc-containing enzymes and DNA-binding proteins due to its function as a structural cofactor and in catalytic centres. Zn^{2+} metal ions (d^{10} configuration) are frequently very challenging to recognize in biological organisms due to its low activity in electron paramagnetic resonance, UV-Vis spectroscopy [1.51f]. It is an exciting project to develop Zn^{2+} chemosensors based on fluorescence spectroscopic analysis and utilizing supramolecular chemistry principles. Recently, A. Tamilselvi *et al.* developed a simple pyridoxal based chemosensor **1.31** (**Scheme 1.5**) which selectively detects Zn^{2+} ion among other competitive metal ions, solid and solution medium. Crystallographic analysis confirms the structure of this recently synthesized sensor. They have reported a quick and precise "turn-on" in fluorescence towards Zn^{2+} ion in an aqueous ethanolic (9:1, v/v) HEPES buffer (pH = 7.0). The limit of detection (LOD) of chemosensor **1.31** is 9.5850 ± 0.3835 nM for Zn^{2+} ion which makes it suitable for biological study. The suggested tetrahedral shape of the Zn^{2+} complex was supported by density functional theory (DFT) and time-dependent density functional theory (TD-DFT) computations [1.52a]. V. Manivannan and his coworkers reported a polydentate chelating ligand (**1.32**) (**Scheme 1.5**) which was synthesized from 4-tertbutyl-2,6-diformylphenol and 3-hydrazineylquinoxalin-2(1H)-one and characterized using

single crystal XRD, mass spectrometry, IR, and NMR spectroscopy. **1.32** was weakly fluorescent in EtOH–HEPES buffer (5 mM, pH = 7.4, 8:2, v/v) but selective for Zn^{2+} ion due to restriction of ESIPT, PET, and C = N isomerization processes. The LOD value of **1.32** for Zn^{2+} ion is 95 nM. Also DFT/TDDFT calculation supported the experimental electronic absorption spectrum [1.52b].

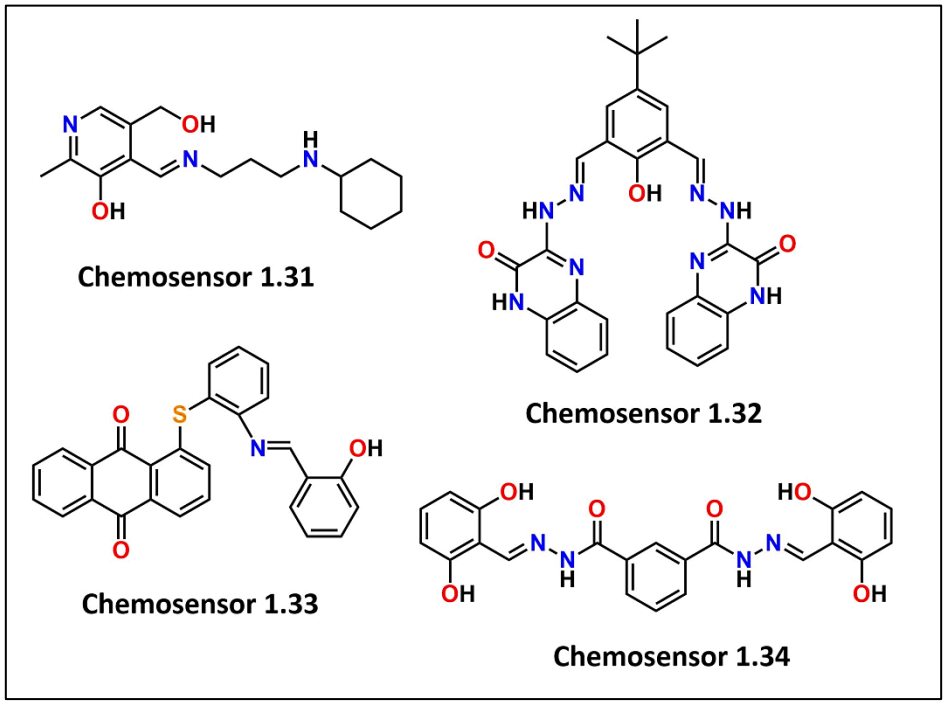

Scheme 1.5. Structure of chemosensors **1.31-1.34**.

Historically, nature has been rich with aluminium, the most prevalent metallic element in the Earth's crust [1.53a]. It is extensively utilized in a variety of industries, including food packaging, water purification, medicine, cosmetics, dye production, and kitchenware. Although aluminium ions (Al^{3+}) have no physiological or biological function and are not essential to the human body, their presence in the body can limit cellular metabolism. Furthermore, Al^{3+} has been identified by the World Health Organisation (WHO) as a source of food contamination, with a maximum allowable level of 7.41 μM in drinking

water. Chronic illnesses like osteoporosis, Parkinson's disease, and Alzheimer's disease may be brought on by the aberrant fluctuations in the Al^{3+} level [1.53b,c].

C. Dong and his co-workers synthesized a chemosensor **1.33** (**Scheme 1.5**) based on anthraquinone. The cleavage of –C=N bonds occurs during Al^{3+}-induced hydrolysis and the probe can be utilized to specifically detect Al^{3+}. By extracting Al^{3+}, the Al^{3+}-bound complex ensembles were able to reversibly detect PPi. Both theoretically and empirically, the feasible binding mechanism was identified. Biological cell imaging study with Al^{3+} and PPi ion were done using zebrafish as well as Hela cells [1.53d]. Another new chemosensor **1.34** (**Scheme 1.5**) was reported by R. Rana *et al.* [1.53e] This Schiff base-based chemosensor **1.34**, was synthesized using isophthalohydrazide and 2,6-dihydroxybenzaldehyde in an ethanol solvent. The compound was characterized using NMR spectroscopy and HRMS. **1.34** exhibited fluorescence sensing characteristics, specifically towards Al^{3+} in acetonitrile. The sensor had a low detection limit of 0.44 μM, suitable for Al^{3+} detection in various systems. The sensor's reversibility was demonstrated through the introduction of pyrophosphate, allowing it to be utilized for Al^{3+} identification.

1.3. Different spectroscopic techniques: Analytical approaches

For detection of metal ions, several approaches can be used based on a range of variables and characteristics, including cost, sample throughput, detection limit, degree of sensitivity, ranges of concentrations, regulatory criteria, the makeup of the environmental matrix, and other components that interfere [1.54]. There are present so many types of spectroscopic techniques as well as volumetric, electrochemical and gravimetric methods for analytical analysis of chemosensor and metal bound complexes. Each of these approaches has benefits and drawbacks.

1.3.1. Atomic absorption spectroscopy (AAS)

The most well-known and established elemental analysis method is atomic absorption spectroscopy or AAS. First invented in 1952, flame atomic absorption spectroscopy (also known as Flame AAS) which was mostly commercialized in the 1960s. The method's exceptional dependability and simplicity have led to its widespread acceptance. It is employed to ascertain an element's concentration in a particular sample. It operates on the premise that light rays with certain and distinguishable wavelengths can be absorbed by atoms or ions [1.55]. According to the Beer-Lambert rule, the concentration and the amount of light absorbed are exactly proportionate. AAS method is mainly based on Beer-Lambert law. Initial calibration for AAS measurement necessitates the use of a solution containing the target metals. This is referred to as the blank and is utilized to calculate the baseline absorption [1.56]. The measurements are made of the absorptions of a range of prepared solutions with different known concentrations of metal ions. The data that shows how concentration and absorbance are related are used to create the calibration curve. It is a tried-and-true analytical method for element quantification at trace concentrations as high as micrograms per litre, and it allows the use of very little sample—typically less than 100 μL. Using this method, a predetermined amount of the sample's solution is injected into a tube made of pyrolytic graphite, which is then heated to cause the analyte to evaporate and atomize. The next step is the atoms' absorption of UV or visible light, which causes an electronic transition [1.57]. Graphite furnace atomic absorption spectroscopy (GFAAS) is now often used to quantify heavy metals in biological matrices, water, and soil.

1.3.2. Cold vapour atomic absorption spectrometry (CVAAS)

This is one of the most popular analytical techniques used for mercury quantification, is a special kind of metal ions whose physicochemical characteristics make quantification extremely difficult. Compared to other ions, it has a higher vapour pressure and is found in

many forms. Hatch originally presented cold vapour atomic absorption spectrometry (CVAAS) in 1968. When Hatch and his colleague Ott added a component to AAS that improved the conversion of Hg (II) into Hg (0), CVAAS was discovered [1.58].

1.3.3. UV-Vis spectroscopy

UV-Vis spectroscopy is an analytical method based on the absorption of light by an unidentified material. Beer's law is used to assess the analyte's content spectrophotometrically, and the absorbance of the resultant coloured complex is directly proportionate to its content. It entails illuminating the sample with various wavelengths of electromagnetic radiation falling into the near-infrared and UV-visible regions of the electromagnetic spectrum. Part of the light is absorbed, depending on the chemical under analysis. The remaining light component is subsequently transmitted, and this is used to record the wavelength using an appropriate detector, resulting in the UV spectrum of the sample. The measurement of absorbance at a specific wavelength yields the concentrations of a given analyte in an aqueous medium; the concentration is computed from the absorbance. The UV-Vis device's linearity is influenced by a number of factors, including the signal-to-noise ratio, the instrument's resolution and interactions between molecules and ions at high concentrations. The metal ions react with a chemical agent in UV-Vis spectroscopy, forming a coloured intermediate or products as a result [1.59]. A common use for UV-Vis is the measurement of highly conjugated molecules and transition metal ions in solution. It is employed to calculate the molar absorptivity of different metal types. The concentrations of the metals are determined using molar absorptivity in accordance with the defined calibration curve. It is thought that there is a linear relationship between the metal ion concentrations and the absorptivity intensity. This is an instrumental analytical method for figuring out of an element's contents in a specific sample.

1.3.4. Inductively coupled plasma atomic emission spectroscopy (ICP-AES)

An alternative name for it is inductively coupled plasma atomic emission spectroscopy (ICP-AES). A source of ionized argon gas at high temperatures is referred to as the plasma. Through inductive coupling from extremely cooled electrical coils, typically at megahertz frequencies, the plasma is created and sustained [1.60]. This method operates under the premise that atoms and ions have the ability to absorb energy, which excites their electrons. The 10,000 K argon plasma is used as the energy source for the inductively coupled plasma atomic emission spectroscopy (ICP-OES). As the excited atoms return to their ground state, light is released. The quantity of ions or atoms undergoing the transition directly correlates with the amount of light produced at each wavelength. Beer-Lambert law applies to the relationship. The calibration graph is used to determine the metal's concentration. This method is incredibly reliable for soil, solid waste, groundwater, and wastewater analysis. It is used to measure contaminants for the purpose of evaluating the quality of the environment and metals with higher regulatory limits [1.61].

1.3.5. Inductively coupled plasma mass spectrometry (ICP-MS)

Inductively coupled plasma mass spectrometry (ICP-MS) is a distinct type of mass spectrometry that ionizes the material using ICP. Upon ionizing the material, it produces atomic and polyatomic ions, which are subsequently measured. This method is well renowned for its exceptional ability to detect many nonmetals in addition to metal ions. It is also highly helpful in the field of isotopic labeling since it can identify different isotopic forms of these metals. The ions in this multi-elemental study come from inductively coupled plasma [1.62]. Metal detection at incredibly tiny concentrations as low as one part per quadrillion may be possible with it. The process of ionizing the sample involves the utilization of ICP, which is produced by heating argon gas. Currently, this instrumental technique can be used to determine over seventy distinct components [1.63].

1.3.6. Fluorescence spectroscopy

A photon source is used to excite sample molecules in fluorescence spectroscopy, a sensitive optical emission technique. By measuring the intensity of such emission, it is possible to identify the molecules that relax through radiant emission. When a colorimetric method is insufficiently sensitive or selective to identify the drug, fluorimetry is typically employed. The chemistry of bioluminescence and immunoassays, the two crucial applications for the identification of organic and inorganic compounds are reviewed. When using single-molecule fluorescence spectroscopy, intensity variations in light emitted from single fluorophores or pairs of fluorophores are detected. When UV or visible light is absorbed, electrons move from their singlet ground state to their singlet excited state. Since this state is unstable, it releases energy in the form of visible or ultraviolet light before returning to the solitary ground state. Fluorescence emission occurs as the fluorophore decays from the singlet electronic excited states to a vibrational level that is allowed in the electronic ground state. The fluorescence excitation and emission spectra, respectively, reflect the excited electronic states and the vibrational level structures in the ground. This phenomenon was described by Jablonski diagram (**Fig. 1.1**) [1.64].

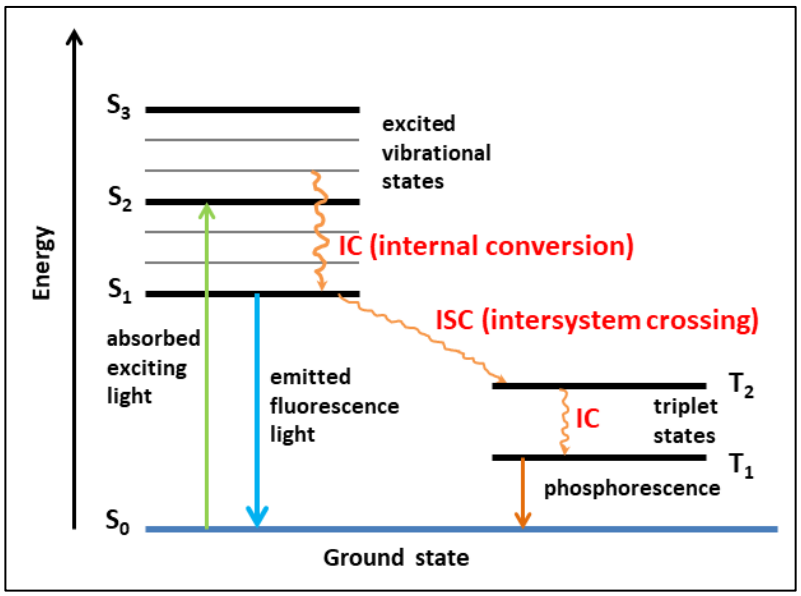

Fig. 1.1. Jablonski diagram.

1.3.7. Electrochemical method-Cyclic voltammetry (CV)

Cyclic voltammetry (CV) is a very flexible electroanalytical method for identifying and measuring various metallic species. It is used to measure the reduction and oxidation processes that involve various molecules. In this process, the electrical reversibility is related to the rates of electron transport between the electrode and the target analyte [1.65].

Among all of these techniques, the most popular and effective for identifying physiologically and environmentally significant analytes are fluorescence and UV-visible spectroscopy methods. Because of their appropriate and valuable features—such as their non-invasive nature, appreciable detection selectivity, quick response, high intrinsic sensitivity, cost-effectiveness, operational simplicity, easy signal detection, and high temporal resolution—fluorescence-based techniques are valuable tools in chemical and biochemical research. Also their low limit of detection (LOD) may also contribute to their applicability for live cell imaging in biological media.

1.4. Classification of fluorescent chemosensors

Now a days there is a lot of interest in fluorescent systems since they can sense different chemically, ecologically, and physiologically significant species [1.66]. Most of these fluorescence sensors are made up of three parts: a guest binding unit, a signalling unit, and a linker that joins the two components. Light is absorbed and emitted by the signalling unit, known as the fluorophore; the complexation and decomplexation of the guest are facilitated by the guest binding unit, known as the receptor; and the electronic communication between the fluorophore and receptor is frequently established by the linking unit, known as the spacer. There are relatively few fluorescent sensor systems for transition metal ions reported in the literature, in contrast to the numerous fluorophore-spacer-receptor systems available for sensing alkali and alkaline earth metal ions [1.67,1.68] **(Fig. 1.2)**. These

fluorescence sensors show either enhancement of fluorescence or quenching of fluorescence in presence of metal ions [1.69–1.73].

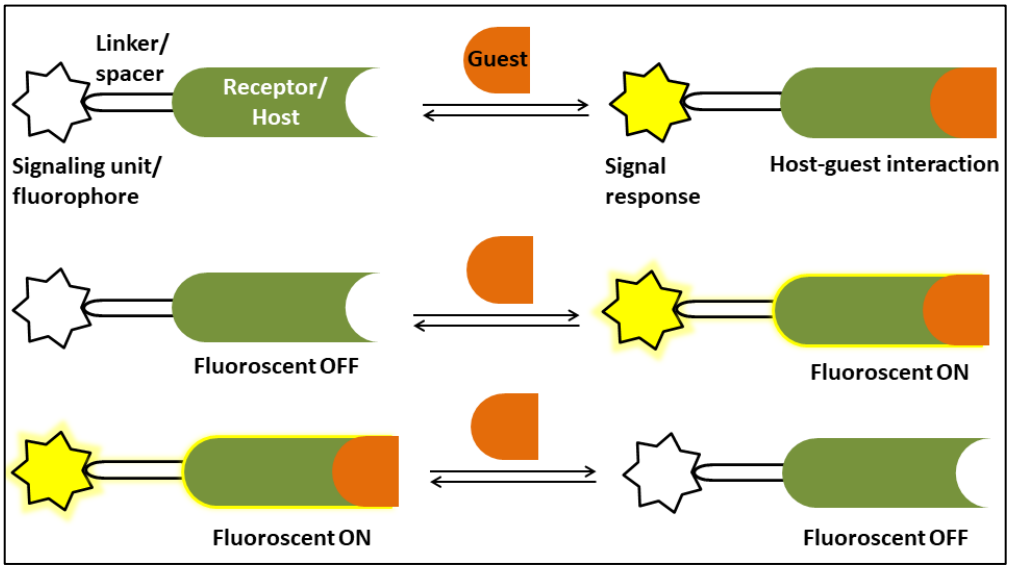

Fig. 1.2. Schematic representation of Host-Guest interaction.

The study of the mechanisms involved the photophysics of fluorogenic chemosensors has been covered in some outstanding reviews, and it is not our goal to a thorough explanation of those mechanisms [1.74,1.75]. The mechanism of the photo-induced processes that cause the photophysical alterations following metal ion coordination is an interesting subject to study. Particularly, these effects are associated with the application of the displacement technique and the binding site-signaling subunit strategy. Based on this mechanism of binding of fluorescent chemosensors can be divided into 4 distinct categories: (a) turn-off fluorescent chemosensor, (b) turn-on fluorescent chemosensor, (c) ratiometric and (d) chemodosimeters.

(a) Turn-on fluorescent chemosensor: When these type of chemosensors bind to the target analytes, the fluorescence emission is amplified. It may be mildly fluorescent or non-fluorescent, but after chelating with the analytes, it becomes a highly emissive molecules. The analytes binding mechanism is reversible in this instance [1.76] (**Fig. 1.3**).

(b) Turn-off fluorescent chemosensor: Chemosensors of this kind are often quite emissive. When the chemosensor binds to the target analytes, the fluorescent intensity is quenched. Furthermore this procedure is reversible in nature [1.77,1.78] (**Fig. 13**).

(c) Ratiometric fluorescent chemosensor: Ratiometric fluorescent probes measure the ratio of two fluorescence intensities at two different wavelengths, which allows them to take environmental variability into account. This ratiometric measurement offers a useful internal referencing that significantly enhancements the probe's sensitivity and enhances quantification. The consideration of changes in the intensity of two or more emission bands caused by the analytes justifies this. Because of this, the signal obtained from measuring the ratio of the fluorescence at these two bands will only be connected to the analytes and will not be influenced by the surroundings [1.79] (**Fig. 1.3**).

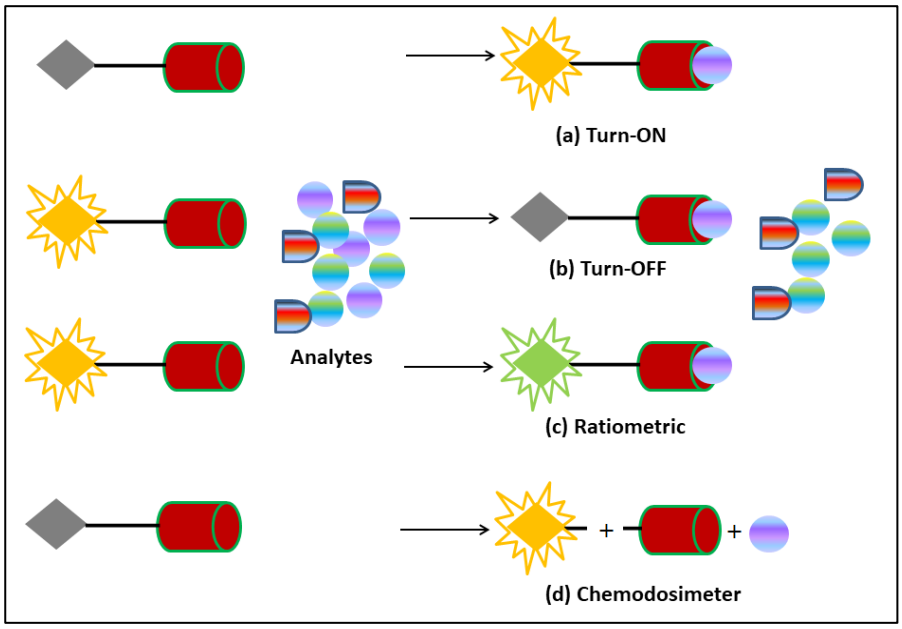

Fig. 1.3. Pictorial representation of different (a-c) fluorescent chemosensors and (d) chemodosimeter, respectively.

(d) Chemodosimeter: It works by detecting an analyte by a chemical reaction between the target analyte and the dosimeter molecule that is very selective and typically irreversible. As

a result, there is a recognizable signal that builds up and is thus closely correlated with the analyte concentration. A specific reaction involving the formation and disruption of covalent bonds can be induced by the target analyte, which can be an anion, cation, or neutral molecule (**Fig. 1.3**). As a result, chemodosimeters are frequently useful due to their excellent selectivity. The chemodosimeter devised and the products generated during this procedure have different optical characteristics [1.80].

1.5. Fluorescence sensing mechanisms

The design of new fluorescence chemosensors continues to be interested in the investigation of novel processes of interaction between signal reporting units and recognition. Chemists have taken a realistic strategy for creating novel, well-organized chemosensors, utilising supramolecular chemistry concepts and basic photophysical mechanisms at the molecular level. In fact, a variety of established signalling systems has been created for the visual detection of various species. These include photo induced electron transfer (PET) [1.81], chelation enhanced quenching (CHEQ) and fluorescence (CHEF) effect [1.82], intramolecular charge transfer (ICT) [1.83], metal–ligand charge transfer (MLCT) [1.84], fluorescence resonance energy transfer (FRET) [1.85], aggregation-induced emission (AIE) [1.86,1.87], -C=N isomerization [1.88] and excited-state intramolecular proton transfer (ESIPT) [1.89].

1.5.1. Photo-induced electron transfer (PET)

A spacer connects a fluorophore to a receptor that has a non-bonding electron pair in photoinduced electron transfer, or PET mechanism. The fluorescence is quenched when an electron moves from the receptor's (donor) highest occupied molecular orbital (HOMO) to the fluorophore's (acceptor) half-occupied HOMO during the excitation process. On the other hand, when the donor's non-bonding electron pair is attached to a guest molecule (analyte), the donor's redox potentials increase and the donor's HOMO energy drops below the

fluorophore. As a result, the fluorescence is turned back to its "on" state and the PET process is restricted (**Fig. 1.4**) [1.90, 1.91].

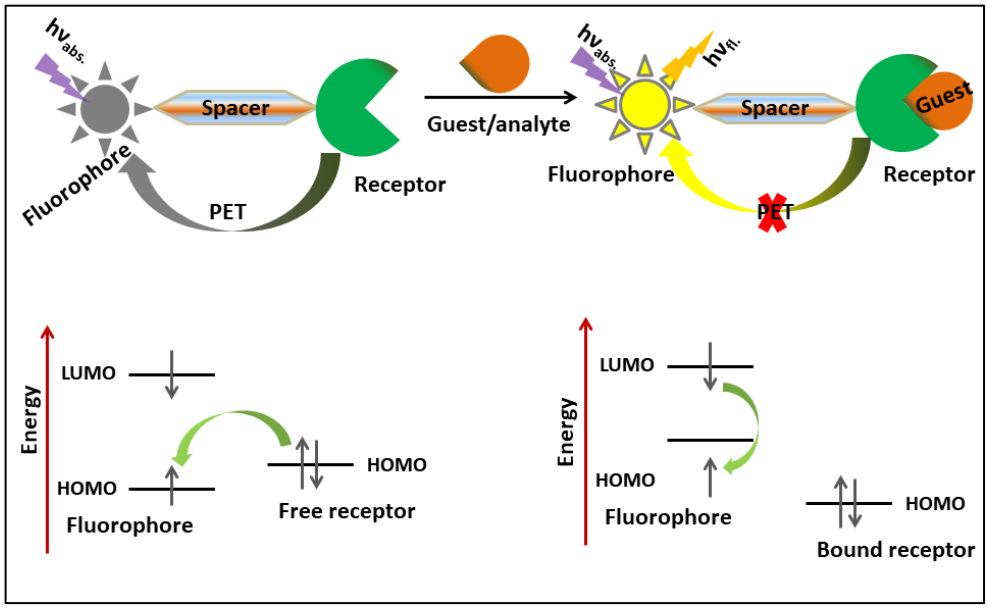

Fig.1.4. Schematic diagram for PET mechanism.

1.5.2. Chelation enhanced fluorescence (CHEF) and Chelation enhanced quenching (CHEQ)

The binding of a metal ion to a receptor in a fluorescent probe can either enhance or quench emission intensity. This phenomenon is referred to as chelation enhanced fluorescence (CHEF) or chelation enhanced quenching (CHEQ), and it results a red or blue shift in the emission band (**Fig. 1.5**) [1.82]. In CHEF, the molecule becomes more rigid when the analyte and receptor coordinate and energy are then transmitted via the radiative pathway. In CHEQ, the spin-forbidden intersystem crossover (ISC) accelerates during the quenching process because a paramagnetic metal ion is near the fluorophore. Excitation of metal complexes causes them to ISC from the S1 to T1 state of the fluorophore, after which they are deactivated by non-radiative mechanisms.

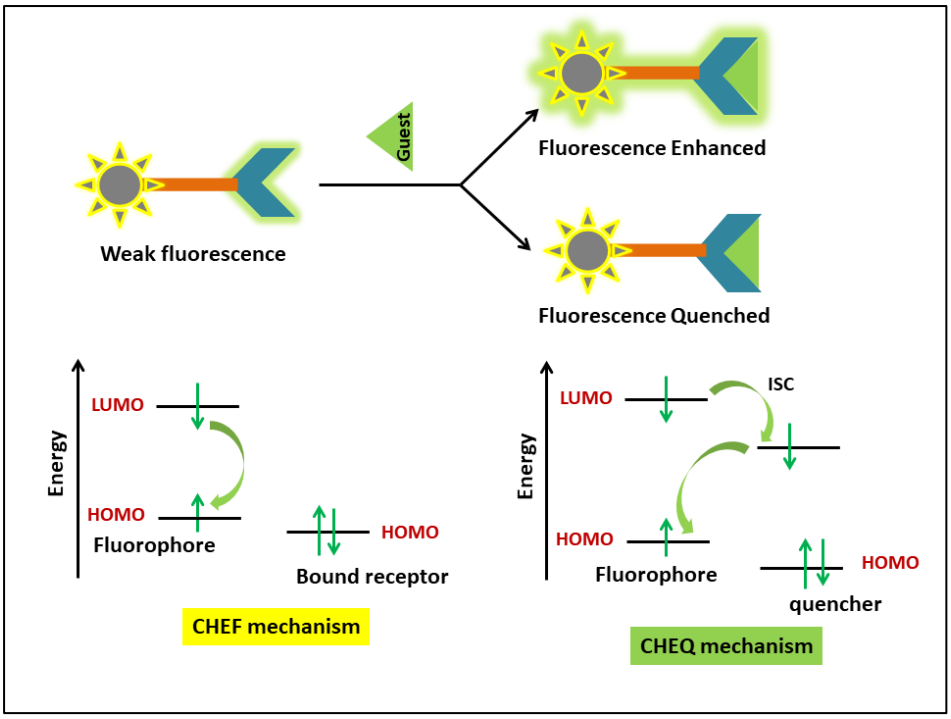

Fig.1.5. Schematic representation of CHEF and CHEQ mechanism.

1.5.3. Intra and intermolecular charge transfer (ICT)

Within the framework, intramolecular charge transfer (ICT) based fluorescence mechanism is observed where an electron donor or acceptor can be readily switched between by directly connecting a fluorophore and a receptor, creating a single entity with two functions. Upon activation, a strong dipole with ICT forms from the donor to the acceptor, even though the electron density of the sensor's HOMO is close to the electron-donating end and its LUMO is close to the acceptor. Analytes have the ability to bind to donor or acceptor areas, which can affect the donor-acceptor species' dipole strength and as a result, induce intensity variations and spectrum shifts. The acceptor group's increased electron-withdrawing property results from analyte interaction and this causes a redshift in the emission spectrum. On the other hand, a blue-shift in the emission spectrum will be seen as a result of the analyte's interaction with the donor moiety, which lowers the donor's electron-donating character (**Fig. 1.6**) [1.83,1.90,1.91].

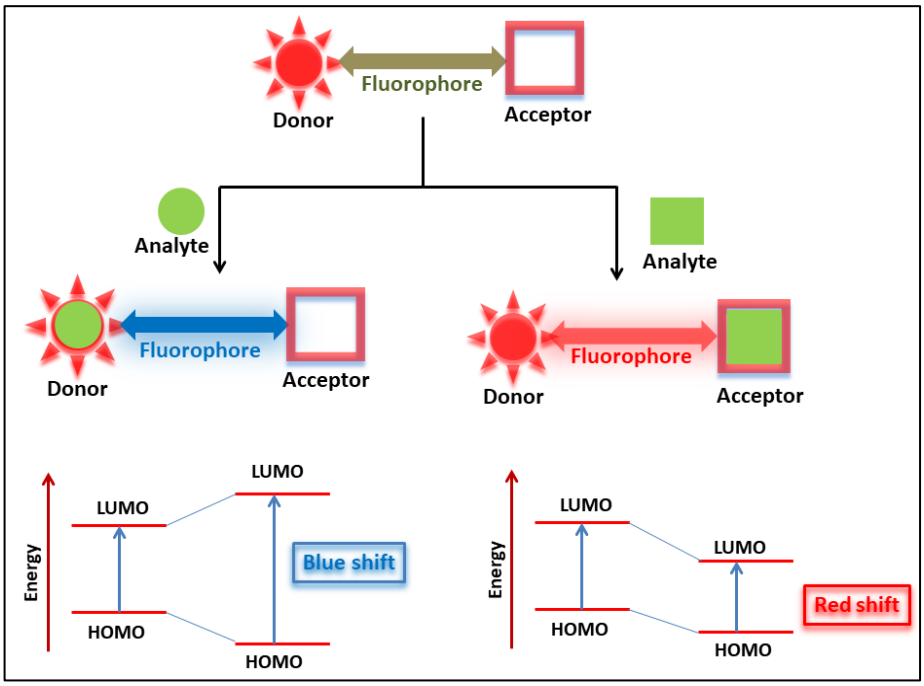

Fig.1.6. Schematic representation of ICT mechanism.

1.5.4. Fluorescence resonance energy transfer (FRET)

Fluorescence sensing probes have made extensive use of fluorescence resonance energy transfer (FRET), a significant photo-physical process that occurs between donor-acceptor pairs. According to this mechanism, the excited donor molecule gives the acceptor molecule its excitation energy so that, in the right circumstances, the acceptor molecule can produce light. The FRET process is controlled by two critical parameters: the spectral overlap between the acceptor's absorption band and the donor's emission band, and the distance between the two that permits non-radiative dipole dipole coupling. When both the donor and the acceptor in an energy transfer system are fluorescent, we will see the acceptor's emission profile rather than the excited donor's. This process is a useful method for creating ratiometric fluorescent probes (**Fig. 1.7**) [1.86, 1.91,1.92].

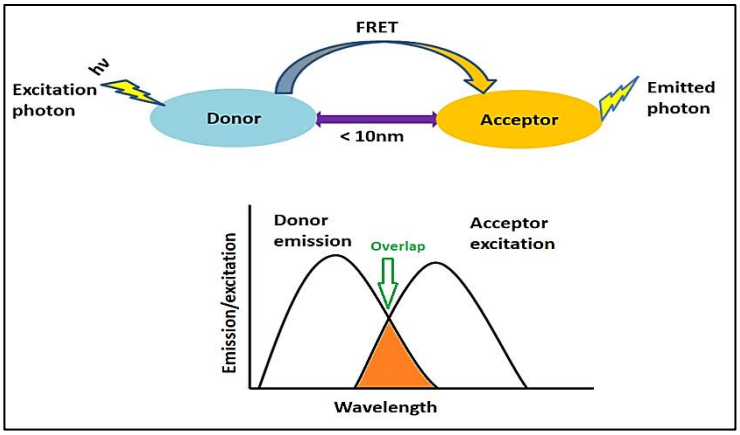

Fig.1.7. Schematic representation of FRET mechanism.

1.5.5. Aggregation-induced emission (AIE)

AIE phenomenon was primarily caused by intramolecular rotation being restricted in the aggregates. When AIE molecules are allowed to rotate freely, the corresponding excited states efficiently decay non-radiatively, rendering the molecules non-emissive. When molecules come together in an appropriate setting, intramolecular rotation is constrained, which significantly increases emission [1.87,1.93].

1.5.6. -C=N isomerization

It was discovered in 2007 that C=N isomerization functions as a signalling process. The research of conformationally constrained compounds' photophysical characteristics served as the inspiration for this concept. It was discovered that compounds with an unbridged C=N structure frequently lack fluorescence because C=N isomerization is the main route of excited state decay. Conversely, the suppression of C=N isomerization in the excited states causes a sharp rise in the fluorescence of their analogues with a covalently bridged C=N structure (**Fig. 1.8**) [1.88, 1.94].

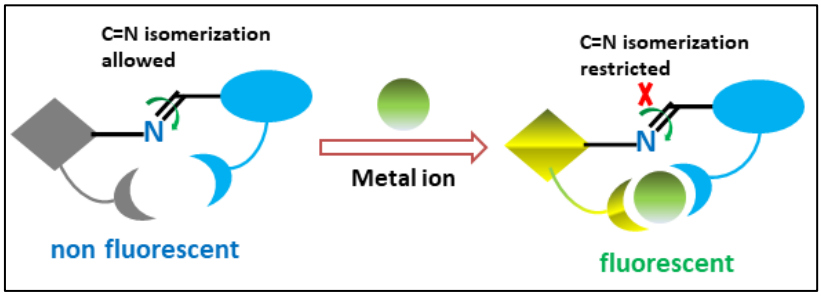

Fig.1.8. Schematic representation of –C=N isomerization.

1.5.7. Excited-state intramolecular proton transfer (ESIPT)

Protons leave or join molecules in ESIPT systems at various rates depending on whether they are excited or in the ground state. In general, ESIPT is a quicker process than electron transfer; reported times for this process range from tens to fractions of picoseconds [1.89]. ESIPT is a distinct four-level photochemical process in which enol (E) is the usual electronic ground state of ESIPT fluorophores as 2-(2′-hydroxyphenyl)benzimidazole (HBI), 2-(2′-hydroxyphenyl)benzoxazole (HBO) and 2-(2′-hydroxyphenyl)benzothiazole (HBT), quinoline, benzophenones, flavones, anthraquinones, benzotriazoles, N-salicylideneaniline, and quinoxalines etc. These molecules can transfer their electrical charge during photoexcitation. The excited state enol form (E*) quickly converts to its excited keto form (K*), resulting in an incredibly fast enol to keto phototautomerization ($k_{ESIPT} > 10^{12}$ s^{-1}) event. A reverse proton transfer creates the original E form once it has radiatively decayed back to its electronic ground state [1.95,1.96]. The environment affects the step of proton transfer, which slows down significantly and takes nanoseconds to happen. With steady-state spectra, the ESIPT process is easily identified because the fluorescence differs greatly from the absorbance, which is often similar to that of the parent chromophore. Since ESIPT dyes often have a large Stokes shift, they make excellent choices for fluorescence labels because they prevent interference from other fluorescent components in the sample. The nearly total lack of spectrum overlap between absorption and emission is a benefit of the substantial Stokes shift, which makes ESIPT dyes interesting for application in fluorescence sensors (**Fig. 1.9**). A hydroxyl (or amino) proton is often transferred through an already-existing six- or five-membered ring hydrogen bonding configuration to a carbonyl oxygen (or imine nitrogen) less than 2A˚ distant during the ESIPT process.

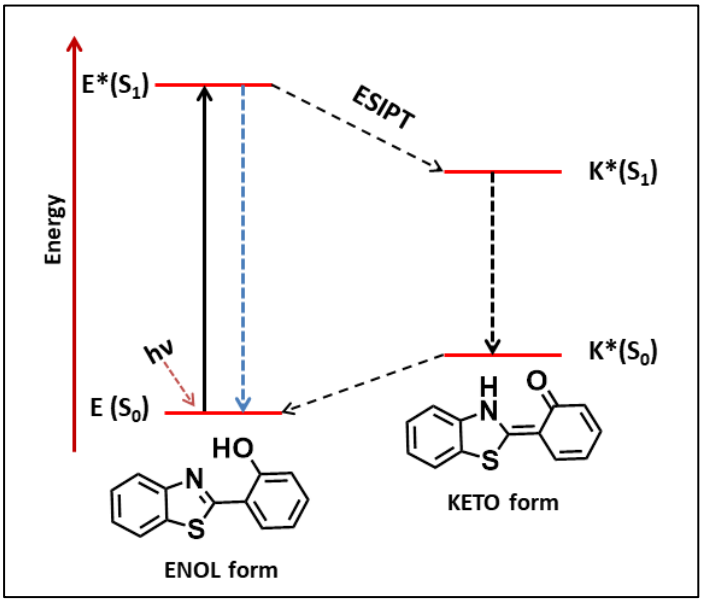

Fig.1.9. Schematic representation of ESIPT mechanism.

1.6. A brief review of the literature on new fluorescent chemosensors

Over the years, multiple types of chemosensors have been reported for detection of different metal ions, such as Al^{3+}, Zn^{2+}, Fe^{3+}, Cr^{3+}, etc. Numerous fluorophoric units have been exemplified in these, including DFP (4-Methyl-2,6-diformylphenol), pyridoxal, rhodamine, quinoline, anthracene, BODIPY (boron-dipyrromethene), coumarin, pyrine [1.97-1.101], etc. A literature on the many chemosensors for detection cations that have been published recently is summarised below in brief and arranged by the fluorophore used. Nevertheless, under harsh circumstances, a large number of them exhibit difficult synthesis, limited solubility, and low recognition sensitivity [1.102]. Therefore, there is always space for improvement in the way that probes are designed to get around these limitations. Because of their ease of synthesis and structural modification, schiff bases, also known as imines, are one class of substance that has received attention in a number of chemistry-related domains [1.103–1.105]. Additionally, Schiff bases with coordination sites like N and O can firmly attach to a variety of transition metal ions, causing a fluorescence turn-on reaction [1.106–1.109]. Schiff bases are therefore used in cellular imaging and operate as intriguing turn-on

probes with a selective affinity for metal cations when combined with other suitable fluorophores in synergistic systems [1.110–1.112].

1.6.1. Chemosensors based on 4-Methyl-2,6-diformylphenol (DFP)

4-Methyl-2,6-diformylphenol (DFP), also known as 2-hydroxy-5-methylisophthalaldehyde or 2-hydroxy-5-methylbenzene-1, 3-dialdehyde. It has been widely utilized to synthesis macrocyclic and acyclic ligands for the production of transition metal complexes [1.113, 1.114]. Conversely, several reports exist of DFP-based compounds that function as chemosensors for different types of analytes. Also different sections have been arranged as DFP based chemosensors for metal ion, pH sensors, multiple analytes, anion sensors and neutral molecules.

Another DFP based chemosensor **1.35** (**Scheme 1.6**) functions as a highly selective fluorescence sensor for Cu^{2+} and Zn^{2+} ions in aqueous conditions which was synthesized by A. J. L. Pombeiro *et.al* [1.115]. X-ray single crystal techniques used to characterize complexes. Even in the presence of other frequently coexisting ions, electronic absorption and fluorescence titration experiments of **1.35** with various metal cations in a CH_3CN/0.02 M HEPES buffer media (pH = 7.3) reveal a highly selective binding affinity only towards Cu^{2+} and Zn^{2+} ions. The fluorescence titration analysis quantification demonstrates that the chemosensor **1.35** can detect Cu^{2+} and Zn^{2+} even at extremely low concentrations of 17.3 and 16.5 ppb, respectively. They also check the cytotoxicity and sensitivity of **1.35** on cancer cells.

C. Sinha *et al.* [1.116] reported chemosensor **1.36** (**Scheme 1.6**) which acts as a turn-on fluorescence chemosensor towards Zn^{2+} and exhibits green emission (λ_{em} = 492 nm) with an amazing limit of detection (LOD), 0.59 nM. Data from HR-MS, ^1H NMR, Job's plot, supported the sensing mechanism (CHEF) of chemosensor **1.36** towards Zn^{2+} and complexation between **1.36** and Zn^{2+}. Zn^{2+} and $H_2PO_4^-$ sequential turn-on-off detection has

also been successfully applied to the INHIBIT molecular logic gate engineering process. The non-toxic sensor was utilized to detect Zn^{2+} within the intracellular space of kidney cells from African green monkeys (Vero cells).

Again, a simple Schiff base chemosensor **1.37** was developed by our group [1.117] that may be used to detect Zn^{2+} and Cu^{2+} ions in HEPES buffer at a pH of 7.4 fluorimetrically and colorimetrically (**Scheme 1.6**). DFT, Job's Plot confirmed 1:1, ligand: metal binding stoichiometry. We have isolated the structure of Zn^{2+}-complex by X-ray diffraction investigation. In the presence of Na_2EDTA solution, the chemosensor's reversibility in interacting with Zn^{2+} and Cu^{2+} ions independently was also investigated. For both ions, the limits of detection (LOD) values were in the range of 10^{-9} M. The data indicated that chemosensor **1.37** was a potentially useful chemosensor for precisely and accurately monitoring Zn^{2+} and Cu^{2+} ions in biological and environmental studies.

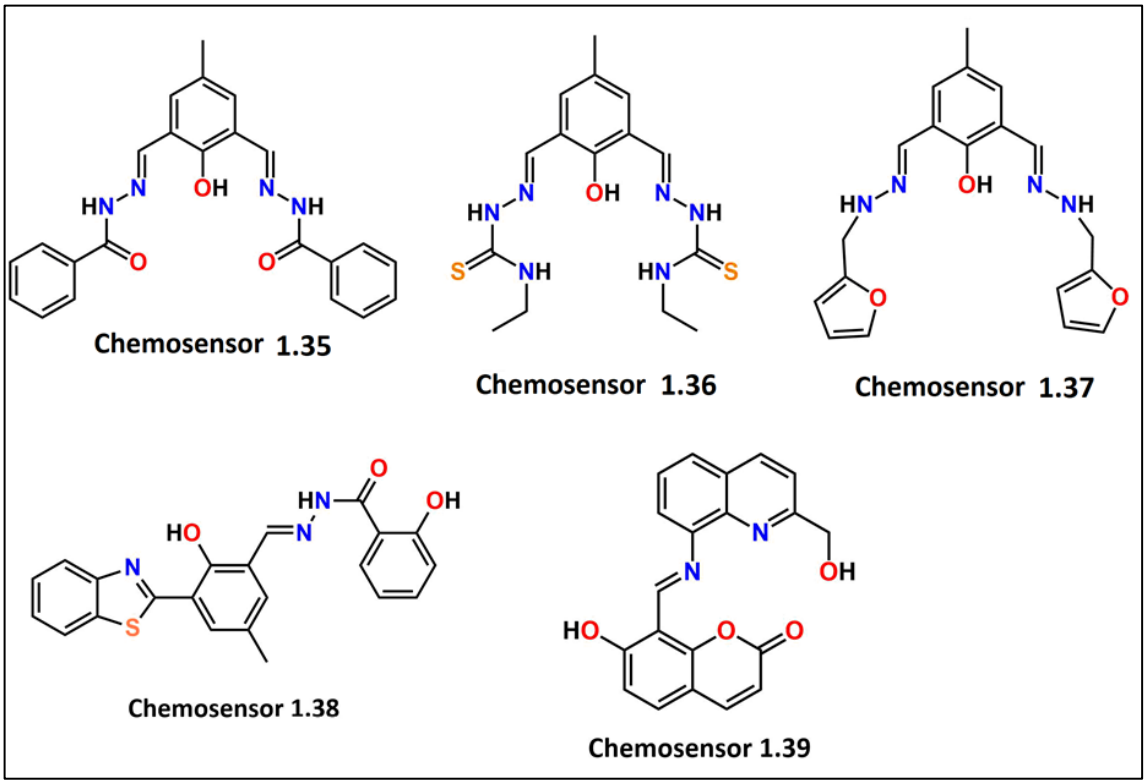

Scheme 1.6. Structure of DFP based chemosensors **1.35-1.39**.

J. L. Li *et al.* [1.118] (**Scheme 1.6**) had synthesized and characterized a dual-function chemosensor **1.38** with benzothiazole moiety as signal unit for the simultaneous detection of Zn^{2+} and Al^{3+} in DMF/H_2O (1/1, v/v, 0.01 M HEPES, pH = 6.0). Probe **1.38** recognized Zn^{2+} and Al^{3+} both through fluorescence turn-on and absorbance ratiometric response. The LOD according to the fluorescence titration for Zn^{2+} and Al^{3+} were ~10^{-7} M range. Furthermore, the significant color changes could be detected by naked eye under uv-lamp or daylight. According to Job plot, the binding ratio of **1.38** with Zn^{2+} and Al^{3+} were determined as 1:1 and 2:1, respectively. The binging mode was further confirmed by ^{1}H NMR titration and ESI-MS analysis as well. Moreover, probe **1.38** was successfully applied in the detection Zn^{2+} and Al^{3+} in real sample and test strip.

A novel Schiff base fluorescent chemosensor **1.39** (**Scheme 1.6**) consist of formylcoumarin and aminoquinoline moieties was synthesized for dual detection of Zn^{2+} and Al^{3+} ions by the group of K. Xu [1.119]. Probe **1.39** exhibited high selective and sensitive response towards Zn^{2+} (270 fold) and Al^{3+} (230 fold) ions through different color changes and significant fluorescence turn-on response in MeOH-H_2O (4/1, v/v) over other cations, with lower detection limits (~10^{-8} M). The binding mechanism of intramolecular charge transfer (ICT) were proposed from fluorescence and UV–vis titrations, Job's plot, ^{1}H NMR titration, HRMS and DFT calculations. Both the complexes exhibited dramatic fluorescent "turn-off" properties for PPi and PPi/F^- respectively through snatching metal ions and released free probe. Moreover, probe **1.39** showed low biotoxicity and fluorescent bio-imaging of Zn^{2+}/Al^{3+} and PPi/F^- in PC12 cells.

Here, chemosensor **1.40** (**Scheme 1.7**) was synthesized and characterized by P. Roy and his co-workers [1.120]. It was created using a condensation process in acetonitrile between DFP and 2-aminopyrimidine (1:2 ratio). Chemosensor **1.40** detects Al^{3+} colourimetrically as well as fluorimetrically. When 1 eqv. Al^{3+} was added to 10 mM HEPES

buffer in water:DMSO (1:9, v/v) (pH 7.4), the fluorescence intensity of **1.40** increased 12 times among other cations and its quantum yield and fluorescence life time both increased. 1:1 (chemosensor **1.40:** Al^{3+}) binding stoichiometry proved by Job′s plot. The detection limit of this chemosensor towards Al^{3+} was also calculated and the value was 1.27 μM. Al^{3+} has been found in a "real sample" using the probe.

Our group also prepared azacrown-based macrocyclic chemosensor **1.41** (**Scheme 1.7**) [1.121] for the selective detection of Zn^{2+} and Cu^{2+} with fluorescent response in HEPES buffer media (pH 7.4). The chemosensor's reversibility in binding Zn^{2+} and Cu^{2+} ions was also investigated using a Na_2EDTA solution. When Zn^{2+} ions were present, chemosensor **1.41** showed a chelation-enhanced fluorescence (CHEF) effect; when paramagnetic Cu^{2+} ions were present, it showed a quenching effect (CHEQ). Furthermore, DFT and TDDFT calculations have been used to examine the geometry and spectral characteristics of the chemosensor and Zn^{2+} bound complex. For Cu^{2+} and Zn^{2+}, the corresponding LOD values were in the order ~10^{-9} M. Through fluorescence cell imaging, the ability of chemosensor **1.41** to identify intracellular Cu^{2+} and Zn^{2+} ions in human breast cancer cell line has been established.

A. Misra *et al.* [1.122] reported 2,6-diformyl-p-cresol (DFC)-4-amino antipyrine (AP) based chemosensor **1.42** (**Scheme 1.7**) which act as fluorescence “turn-on” dual sensor for Zn^{2+} and Al^{3+} and its selective fluorescence “turn-off” sensing towards 2,4,6-trinitrophenol (TNP). High fluorescence enhancements were noticed for Zn^{2+} (168 fold at 508 nm) and Al^{3+} (195 fold at 480 nm) in methanol with binding constants, $K = 3.42 \times 10^4\ M^{-1}$ and $7.63 \times 10^4\ M^{-1}$, respectively. 1:1 complexation of chemosensor **1.42** with both Al^{3+} and Zn^{2+} proved by Job’s method. **1.42** showed high sensitivity towards the detection of Zn^{2+} and Al^{3+} ions with very low detection limit values of ca. ~21 nM and 30 nM, respectively. Chemosensor **1.42** with high sensitivity for a selected explosive TNP through ground state complexation with a

LOD value of ca. ~1.74 μM and especially a high Stern–Volmer quenching constant of ca. ~4.14 × 10^5 M^{-1}. They have also showed the naked eye detection of TNP by this probe using paper strips test.

S. Goswami′s team synthesized two unsymmetrical and dipodal Schiff–Mannich combo ligands, **1.43** and **1.44** (Scheme 1.7) in semi-aqueous media [1.123]. Both the probes selectively showed a turn-on response to Zn^{2+} as a result of the combined effect of chelation induced enhanced fluorescence (CHEF) and restriction of photo-induced electron transfer (PET). Detailed experimental studies revealed that **1.43** and **1.44** can detect Zn^{2+} in solutions with limit of detections of 27 nM and 46 nM, respectively. The structures of probe-Zn^{2+} ensembles were studied by ESI-MS, FT-IR spectroscopy, ^{1}H NMR titration and DFT/TD-DFT methods. Moreover, both the chemosensors were successfully employed in the detection of Zn^{2+} in HuH-7 cells, seedlings of chickpea and mung beans, and paper strips.

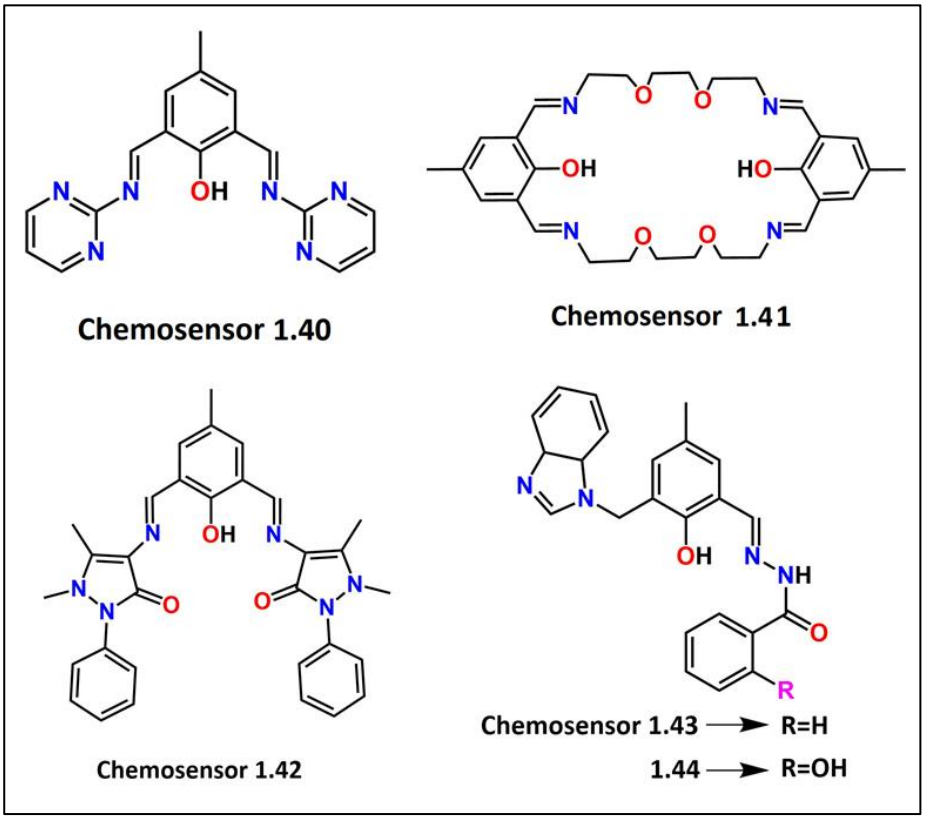

Scheme 1.7. Structure of DFP based chemosensors **1.40-1.44**.

1.6.2. Chemosensors based on pyridoxal

Among all pyridoxal derivatives pyridoxal 5'-phosphate (PLP) is the most active vitamer, participating actively in decarboxylation, transamination, and racemization through over 140 enzymatic activities in our body [1.124a]. It forms a Schiff base with the enzyme's lysine side chain, forming pyridoxamine-5′-phosphate (PMP) and keto acid substrate. Apart from their function in enzymatic processes, PLP has anticancer, antioxidant, and antimicrobial properties. Their bioactive nature, water-solubility, strong chelating capacity and photophysical properties have led to research in sensing and biosensing. The aldehyde group of the cofactors pyridoxal and PLP can be easily condensed with an amine to form a Schiff base. Schiff bases are well-known metal chelators and are applied extensively for the chromo-fluorogenic sensing of metal ions [1.124b,c].

F. Chengca *et al.* [1.125] described a pyridoxal-based fluorescein derivative namely chemosensor **1.45** (**Scheme 1.8**) which was synthesized by reacting fluorescein hydrazide and pyridoxalhydrochloride in ethanol and characterized by NMR, ESI-MS and X-ray. The probe displayed selectivity toward Zn^{2+} and Cu^{2+}, which was characterized using UV–visible, fluorescence spectroscopy in methanol: HEPES solution. Also **1.45** showed visual detection of Zn^{2+} as well as Cu^{2+} by colour changes from colorless to green and colorless to yellow, respectively. In contrast, selectivity was determined in the emission spectra showing OFF–ON type fluorescence with the association constant value ~10^5 M^{-1}. Furthermore, it can be used to bioimaging.

Another pyridoxal based sensor molecule **1.46** (**Scheme 1.8**) was developed by S. Goswami and his co-workers [1.126] which exhibited selective turn-on type response towards Zn^{2+} in ethanol-water mixture at physiological pH. Noticeable fluorescence enhancement occured upon addition of Zn^{2+} to the chemosensor **1.46** as a result of inhibited C=N isomerisation and excited state intramolecular proton transfer (ESIPT) leading to efficient

chelation enhanced fluorescence (CHEF). The relevant properties, including reversibility, life time measurements and detection limit have been determined for the sensor system. The experimental and theoretical supports in terms of ^{1}H and ^{13}C NMR spectroscopy and DFT/TDDFT study are provided to establish the binding mode of **1.46** to Zn^{2+}. This probe was employed as a sensor for detection of Zn^{2+} in Human gastric adenocarcinoma (AGS) cells.

S. K. Sahoo *et.al* [1.127] (**Scheme 1.8**) reported a new fluorescent receptor (chemosensor **1.47**) by using pyridoxal, a cofactor of vitamin B6 and 1-pyrenemethylamine to facilitate Schiff base condensation. The excimer production that results in the fluorescence colour change from blue to bluish-green caused the chemosensor **1.47** to exhibit noticeable fluorescence amplification at 485 nm upon contact with Zn^{2+}. As a result of the demetalation of Zn^{2+} from the metal complex, the addition of $H_2PO_4^-$ and cysteine restored the fluorescence of the **1.47** when the in-situ produced zinc complex interacted with different anions and amino acids. In light of this, chemosensor **1.47** was created to detect three significant bioactive analytes Zn^{2+}, $H_2PO_4^-$, and cysteine with a detection limit of 2.3×10^{-6} M, 2.18×10^{-7} M, and 1.59×10^{-7} M, respectively. Furthermore, in living HeLa cells, the chemosensor **1.47** was utilised to detect intracellular Zn^{2+} ions.

Another new vitamin B_6 cofactor derivative (chemosensor **1.48**) that was simple to make in a one-pot condensation process between pyridoxal and 3-hydroxy-2-naphthoic hydrozide, was synthesized by S. K. Sahoo and his group [1.128] (**Scheme 1.8**). It was then used for the optical detection of Zn^{2+} and cysteine in the aqueous DMSO medium. A blue-shift (from 530 nm to 475 nm) in the fluorescence spectra of chemosensor **1.48** was observed after addition of Zn^{2+} ions. This resulted in the ability to detect Zn^{2+} ions with a detection limit 8.73×10^{-7} M without interference of other metal ions. The detection of intracellular Zn^{2+} ions in living HeLa cells was also accomplished. Furthermore, the addition of cysteine

caused the in situ produced Zn^{2+} complex to react with different amino acids, changing its colour instantly from bright yellow to colourless and quenching the complex's absorbance at 435 nm. Moreover, LOD of Zn^{2+} complex towards cysteine was 6.63×10^{-7} M after the chemosensor **1.48**-Zn^{2+} complex′s the fluorescence was quenched.

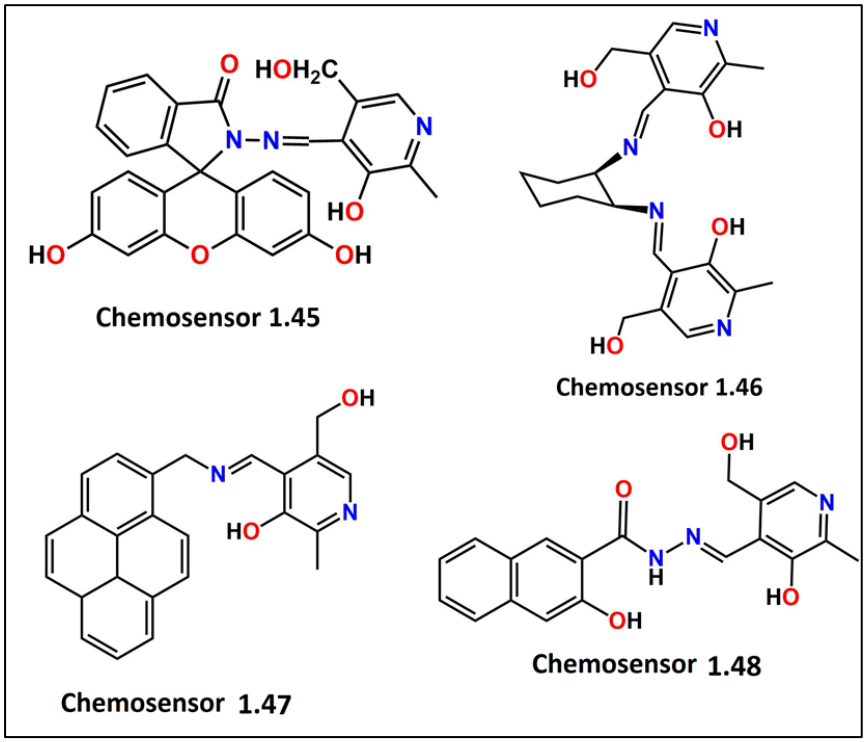

Scheme 1.8. Structure of pyridoxal based chemosensors **1.45-1.48**.

A. G. Sykes and his colleagues [1.129] created a novel chemosensor **1.49** (**Scheme 1.9**) that is based on pyridoxal. Through a fluorescence turn-on response, the optical characteristics of the synthesized ligand were examined in an aqueous buffer solution and it was discovered to be extremely selective and sensitive towards Zn^{2+} ion. Competition experiments showed that Cu^{2+} ion suppressed the response for zinc ion, which was unaffected by all alkali and alkaline earth metals. The zinc ion detection limit was 2.77×10^{-8} M, far less than the WHO recommendation of 76.5 mM. A 2:1, Zn^{2+} compound with a binding constant of 1.2×10^{9} M^{-2} was found by stoichiometric investigations. Zn^{2+} ion binding in a hydrated

zinc complex was shown by the crystal structure. Zinc ions were detected in HEK293 cell lines using the ligand, which exhibited high luminescence, as a sensor. Additionally, they had synthesised the **1.49**-Cu^{2+} complex, and the crystal structure revealed the development of a 1:1 adduct, exposing 1-dimensional polymeric networks with coordinated Cu^{2+} that is octahedral.

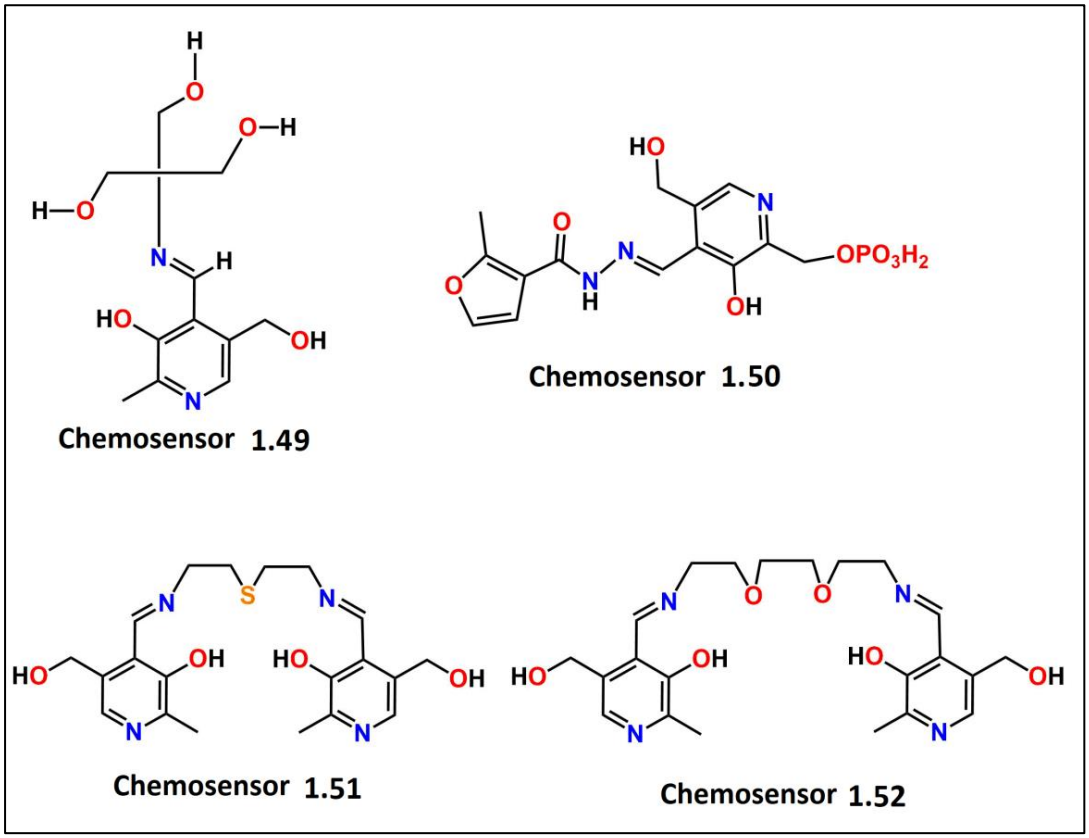

Scheme 1.9. Structure of pyridoxal based chemosensors **1.49-1.52**.

The synthesis and characterisation of a novel chemosensor **1.50** for Zn^{2+} ions, a hydrazone generated from 3-methyl-2-furoylhydrazide and pyridoxal 5′-phosphate, was presented by Y .S. Marfin *et.al* [1.130] (**Scheme 1.9**). The ligand can identify Zn^{2+} in the aqueous solution with selectivity. The mechanism of detection relies on the production of the Zn^{2+}-complex, which exhibited higher fluorescence intensity than free hydrazone. A thorough characterization of the complex was also performed, yielding information on its structure

characteristics, quantum yield, and stability constant. The optimized structures of free ligand along with Zn^{2+}bound complex were studied by quantum chemistry methods at the B3LYP/ECP10MWB (Zn)/cc-pVTZ (H, C, N, O, P) level of density functional theory. Possible real-world uses for the created chemosensor include drug and water analysis, as well as bio-imaging.

Again, two pyridoxal-based chemosensors (**1.51** and **1.52**) were prepared by our group, [1.131] using 2,2′-thiobis(ethylamine) or 1,2-bis(2-aminoethoxy)ethane and pyridoxal hydrochloride. These chemosensors were highly selective towards Zn^{2+} ions in aqueous solution (10 mM, HEPES buffer at pH = 7.4) and exhibited strong fluorescence enhancement (~20 times) in the presence of Zn^{2+} (**Scheme 1.9**). The chemosensors have low LOD values for Zn^{2+} (~10^{-8} M range), making them ideal for real-life and biological applications. The crystal structure of both the metal bound chemosensors has been solved. It's interesting to see that it matches the theoretical result well. Both chemosensors are used in cell imaging studies to detect Zn^{2+} ions in human cervical cancer cells.

1.6.3. Chemosensors based on rhodamine

Within the field of fluorescence chemosensors, rhodamine is one of the dyes that is used the most. The structural derivative of xanthene, rhodamine was originally produced in 1905 by Noelting and Dziewonsky [1.132]. Czarnik et al. employed rhodamine in 1997 as the first report for Cu^{2+} detection[1.50a]. Since then, numerous studies have been published that demonstrate the good application of chemosensors based on rhodamine. Rhodamine-based chemosensors for cations are designed by modifying the rhodamine scaffold with metal-binding groups, allowing the metal ion to be selectively binded and a fluorescence signal is produced. Several spectroscopic methods, including fluorescence and time-resolved fluorescence spectroscopy, as well as intracellular fluorescence spectroscopy, can be used to identify and quantify this fluorescence signal. This xanthene derivative is non-fluorescent in

its free form due to the presence of a closed spirolactam ring in its fundamental structure. However, when the dye is coupled to a cation, the closed spirolactum ring opens, producing a powerful emission that usually appears as an emission band at a wavelength greater than 550 nm. Rhodamine-based chemosensors showed ability in chemical sensing, environmental monitoring, biomedical research, and diagnosis due to their unique optical properties, including high photostability, large Stokes shift, and tunable fluorescence, making them ideal candidates for highly sensitive and selective chemosensors. Usually, Rhodamine-B and Rhodamine-6G, two prototypes of rhodamine dyes, are used for this purpose.

A. Jana and his group [1.133] synthesized a rhodamine and azobenzene conjugated chemosensor **1.53** (**Scheme 1.10**) which showed turn-on fluorescence for Al^{3+} in aqueous ethanol through the processes of blocked photo-induced electron transfer (PET) and chelation enhanced fluorescence (CHEF) followed by the transition from non-fluorescent spirolactam to fluorescent ring-opened amide. The high binding constant (K_a = 7.033 × 10^3 M^{-1}) of the opened spirolactam ring indicates that it forms a 1:1 binding complex with the metal in the presence of Al^{3+}. It was discovered that the limits of quantification (LOQ) and detection (LOD) were 10^{-7} M range. In the presence of Na_2EDTA, the reversible identification of Al^{3+} was also demonstrated using fluorometric titration and UV-Vis. DFT/TDDFT computations confirmed the chemosensor's sensing behaviour towards Al^{3+}.

V. P. Singh *et al.* [1.134] developed a new rhodamine-functionalized probe **1.54** (**Scheme 1.10**) that acts as a colorimetric and fluorometric chemosensor towards Al^{3+}, Fe^{3+}, and Cr^{3+} metal ions. The spectral changes were visible to the unaided eye and were clearly noticeable in the absorption spectrum. For the metal ions Al^{3+}, Fe^{3+}, and Cr^{3+}, the fluorescence quantum yield, stoichiometric ratio, binding constant, and detection limit of **1.54** have all been determined. Moreover, **1.54**–M^{3+} complexes behaved like a molecular logic gate since they were reversible and sensitive to EDTA. Metal ions Al^{3+}, Fe^{3+}, and Cr^{3+} were

used intracellularly in human model cells. Another rhodamine-based chemosensor **1.55** (**Scheme 1.10**) was designed by R. Kumar and his group for the selective recognition of trivalent metal ion Cr^{3+} [1.135]. Fluorescence and UV-visible spectroscopy studies showed fluorescence and colorimetric changes for Cr^{3+} over other metal ions. **1.55** exhibited 1:1 complex formation with Cr^{3+}, with a limit of detection of 0.21 mM. It also demonstrated practical utility through detection of Cr^{3+} in the solid state logic gate.

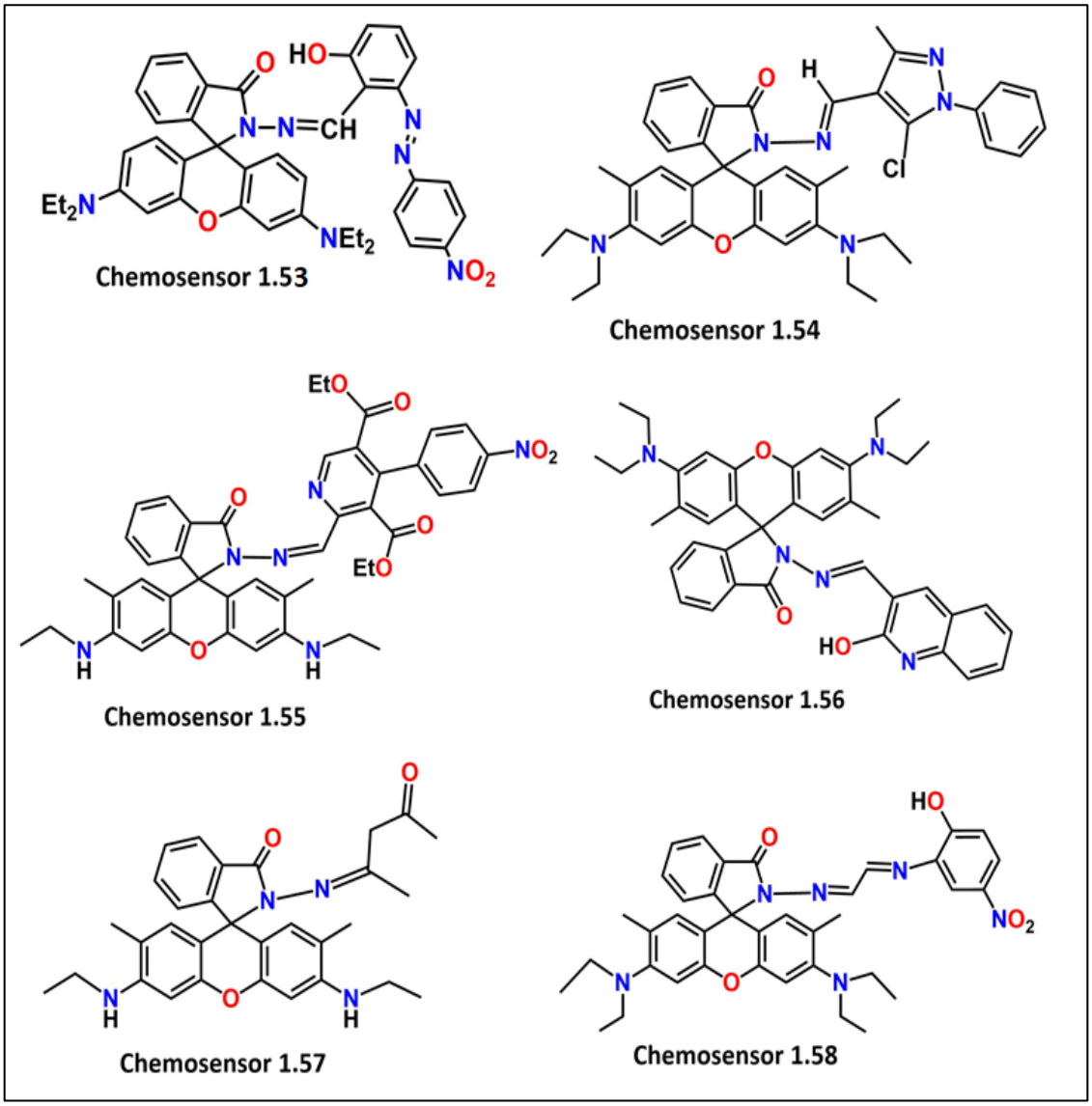

Scheme 1.10. Structure of rhodamine based chemosensors **1.53-1.58**.

One rhodamine-B-quinoline-based chemosensor **1.56** (**Scheme 1.10**) was synthesized and characterized by A. Misra and his co-workers [1.136]. It showed fluorescence emission and colorimetric sensitivity and selectivity towards trivalent metal ions (Al^{3+} and Cr^{3+}) and anion (HSO_4^-) in aqueous medium. A notable enhancement in emission intensity for **1.56**-Al^{3+} (~341 fold), **1.56**-Cr^{3+} (~292 fold), and **1.56**- HSO_4^- (~136 fold) complexes compare to chemosensor **1.56** were observed. The sensitivity mechanism was confirmed through various techniques. The limit of detection for Al^{3+}, Cr^{3+}, and HSO_4^- were 2.2 × 10^{-8} M, 2.12 × 10^{-8} M and 8.63 × 10^{-7} M, respectively. An advanced level 3 input OR-INHIBIT logic gate was constructed using chelating ligand EDTA. They have also performed the cell imaging and cytotoxicity test for this chemosensor.

Another rhodamine-based receptor molecule (**1.57**) (**Scheme 1.10**) was synthesized using rhodamine hydrozide and acetylacetone. This work was done by A. Sivaiah *et al.* [1.137] Spectroscopic methods like FTIR, ^{1}H NMR, ^{13}C NMR, and ESI-MS were used to characterize **1.57**. Chemosensor **1.57** showed a turn-on response towards Cu^{2+} ions, with a detection limit of 3.58 × 10^{-8} M. The receptor molecule was found to be biologically applicable for in vitro detection of Cu^{2+} ions in living cells.

H. Xu and his team developed a rhodamine-based multi-ion fluorescent sensor, **1.58** (**Scheme 1.10**), for the selective detection of (Hg^{2+}) in ethanol and water medium whereas trivalent cations (Fe^{3+}, Al^{3+} and Cr^{3+}) in ethanol system [1.138]. The sensor achieved detection through fluorescence turn-on, with low detection limits (nM) for Fe^{3+}, Al^{3+}, Cr^{3+} and Hg^{2+}. Density functional theory (DFT) calculation showed decreased HOMO-LUMO energy gaps and increased dipole moments, indicating the effective coordination of the sensor with the corresponding metal ions to form more stable complexes. Its potential applications include environmental water samples, L929 cells, and zebrafish, with potential biomedical applications in heavy metal ion-induced diseases were also investigated.

M. Ali and his co-workers [1.139] designed and prepared a novel supramolecular fluorescent probe, chemosensor **1.59** (**Scheme 1.11**), based on rhodamine 6G, which recognises trivalent metal ions, Fe^{3+}, Al^{3+} and Cr^{3+} among other competitive metal ions. Noticeable absorption and fluorescence intensity increased (Fe^{3+} (669-fold), Al^{3+} (653-fold), and Cr^{3+} (667-fold)) when 2.6 equivalents of these metal ions were added to the probe in H_2O/CH_3CN (7:3, v/v, pH 7.2). K_d values (~10^{-5} M) were determined for the probe towards respective metal ions. Using rhodamine-6G as the standard, the quantum yields of the chemosensor **1.59** with Fe^{3+}, Al^{3+} and Cr^{3+} were 0.0005, 0.335, 0.327 and 0.333, respectively. The LODs were ascertained using 3σ techniques and the values were μM order. Advanced level molecular logic circuits were built using a memory device and two distinct inputs (two and four).

Another work, a novel fluorescence resonance energy transfer (FRET) ratiometric fluorescent chemosensor **1.60** (**Scheme 1.11**) for the selective detection of Al^{3+} over other significant metal ions in mixed aqueous solution was developed by M. Bhattacharyya *et.al* [1.140] using triphenylamine and rhodamine-B. They have suggested that the **1.60** is non-toxic and can effectively identify the Al^{3+} ion in human peripheral blood mononuclear cells (PBMCs) through an intracellular "FRET-ON" process. The limit of detection (LOD) was around 10^{-8} M. In the presence of EDTA, the ligand–Al^{3+} complex exhibited reversible binding with demetallation. The fluorescence output at 576 nm from two active chemical inputs, EDTA and Al^{3+}, followed an INHIBIT logic gate truth table in accordance with this reversibility.

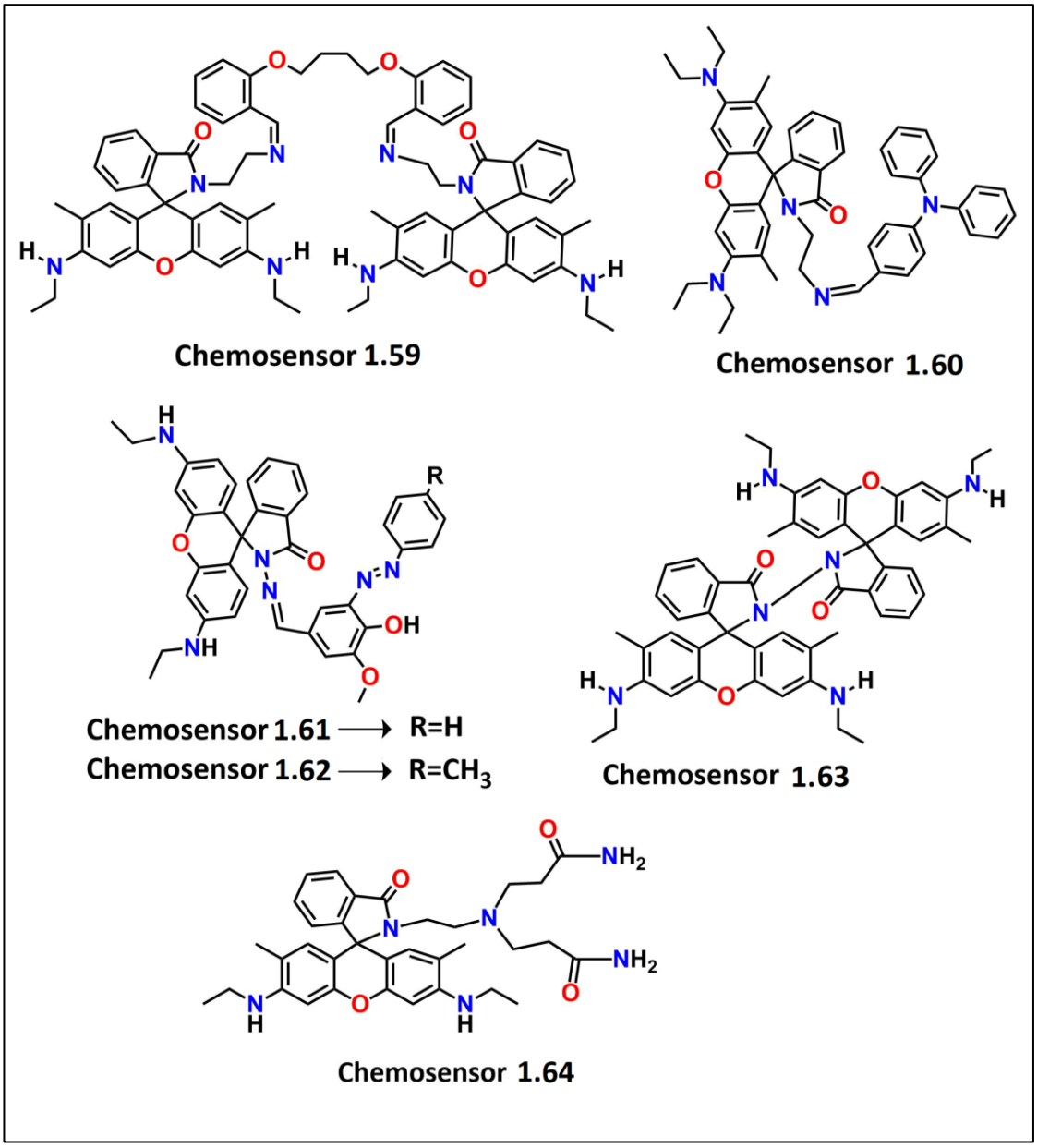

Scheme 1.11. Structure of rhodamine based chemosensors **1.59-1.64**.

Three trivalent metal ions Al^{3+}, Cr^{3+}, and Fe^{3+} can be detected colorimetrically and fluorometrically using two rhodamine and azo-based chemosensors **1.61** and **1.62** (Scheme 1.11) were derived by our group [1.141]. The spirolactam ring opens at 490 nm in absorption spectra in the Britton-Robinson buffer solution (H_2O/MeOH 1:9 v/v; pH 7.4) due to the presence of trivalent metal ions. A strong fluorescent pinkish-yellow coloration resulting from complexation caused by the probe's spirolactam ring opening and increased

fluorescence intensity when Al^{3+}, Cr^{3+} (~400-fold) and Fe^{3+} (~100-fold) ions were present. 2:1 binding stoichiometry of the probes with the respective ions has been confirmed by Job's plot analysis. Elucidation of the crystal structures of the Al^{3+} bound chemosensors also justified their binding mode. Both chemosensors have limit of detection (LOD) values in the range of around ~10^{-9} M for the respective metal ions, which validates their use in the biological study. The MTT assay has been used to investigate the ligands' biocompatibility.

A new simple rhodamine based fluorescent probe (chemosensor **1.63**) (**Scheme 1.11**) was developed by G. Jin *et al.* [1.142]. This chemosensor showed high selectivity and sensitivity towards Al^{3+} and Fe^{3+} over other metal ions. They have found single crystal of compounds from slow evaporation of solvent. Compounds were characterized by NMR, ESI-MS and other methods. The relative limits of detection were 0.49 nM and 0.76 nM. When Al^{3+} and Fe^{3+} were present, the solution turned pink from colourless. The fluorescence emission spectra and the UV–vis spectrum both exhibited a notable shift at the same time. Furthermore, studies on biological systems indicate that the probe possesses a high degree of membrane permeability and may be used to identify Al^{3+} and Fe^{3+} in Hela cells.

Using the Michael addition procedure, a novel rhodamine-6G based biocompatible chromo- and fluorogenic "OFF-ON" sensor **1.64** (**Scheme 1.11**) towards Fe^{3+} was created by M. Ali and his group [1.143]. They have used IR, NMR, and HRMS spectroscopic analyses to characterize the sensor. The addition of 11.5 equivalent Fe^{3+} ions to the chemosensor in H_2O (pH 7.2, 10 mM HEPES buffer) resulted in a 14-fold increase in fluorescence intensity and a colour shift from colourless to reddish yellow, which was visible to the naked eye. With a 1:1 stoichiometry, the appropriate binding constant was calculated to be $(1.16 \pm 0.04) \times 10^4$ M^{-1}. Quantum yields were determined for both ligand as well as complex (0.013 and 0.523, respectively). LOD value was 4.184 μM for Fe^{3+}-bound complex. The probe's non-fluorescent spirolactam ring shape was re-attained when the cyanide ion removed Fe^{3+} from

complex and quenching the fluorescence was observed. The reversible nature of the sensing phenomenon aids in the framing of memory devices and INHIBIT logic gates.

1.7. Aim of my research work

The previously mentioned discussion highlights the significance of fluorescence probes in the identification of physiologically significant analytes. Our group is devoting intellectual energy to the development of sensors for ions and small molecule studies, given the significance of techniques in selective sensing. Because of their biological activity, Schiff bases have been extensively studied for a variety of industrial applications, although more research is still needed in this class of chemicals. The study of Schiff bases and their metal complexes is an extremely fascinating field that continuously yields fresh insights into recently synthesised molecules. Many analytical devices are available to detect metal ions at very low concentrations (M to nM); however, these instruments are expensive and have limitations when it comes to real-time detection during field monitoring. This thesis synthesises a variety of Schiff base ligands (**Scheme 1.12**) with various moieties, including amide (O=C-NH) and imine (-C=N-) of 4-Methyl-2,6-diformylphenol, pyridoxal, rhodamine and eugenol derivatives. Simple, inexpensive, and environmentally friendly methods are used to synthesise the probes and occasionally their coordination complexes. Complete spectrum characterisation and X-ray analysis are then performed to corroborate certain structural details. Zn^{2+}, Al^{3+}, Fe^{3+}, and Cr^{3+} are among the various physiologically and environmentally significant ions that can be detected using Schiff base molecules as chemosensors. They have been characterised using a variety of spectroscopic techniques, including FT-IR, NMR, ESI-mass, and micro analysis data. Whenever possible, X-ray diffractometric measurements are used to confirm the structures. A preliminary computational study employing density functional theory (DFT) was also included in several of the studies in order to obtain a broad understanding of the molecular level interactions between the probe and analytes. Bio-cell

imaging uses human lung fibroblast cell line (WI-38), HeLa cells, prostate cancer cell (PC3), MC3T3 and Human lung cancer cell line (A549), etc.

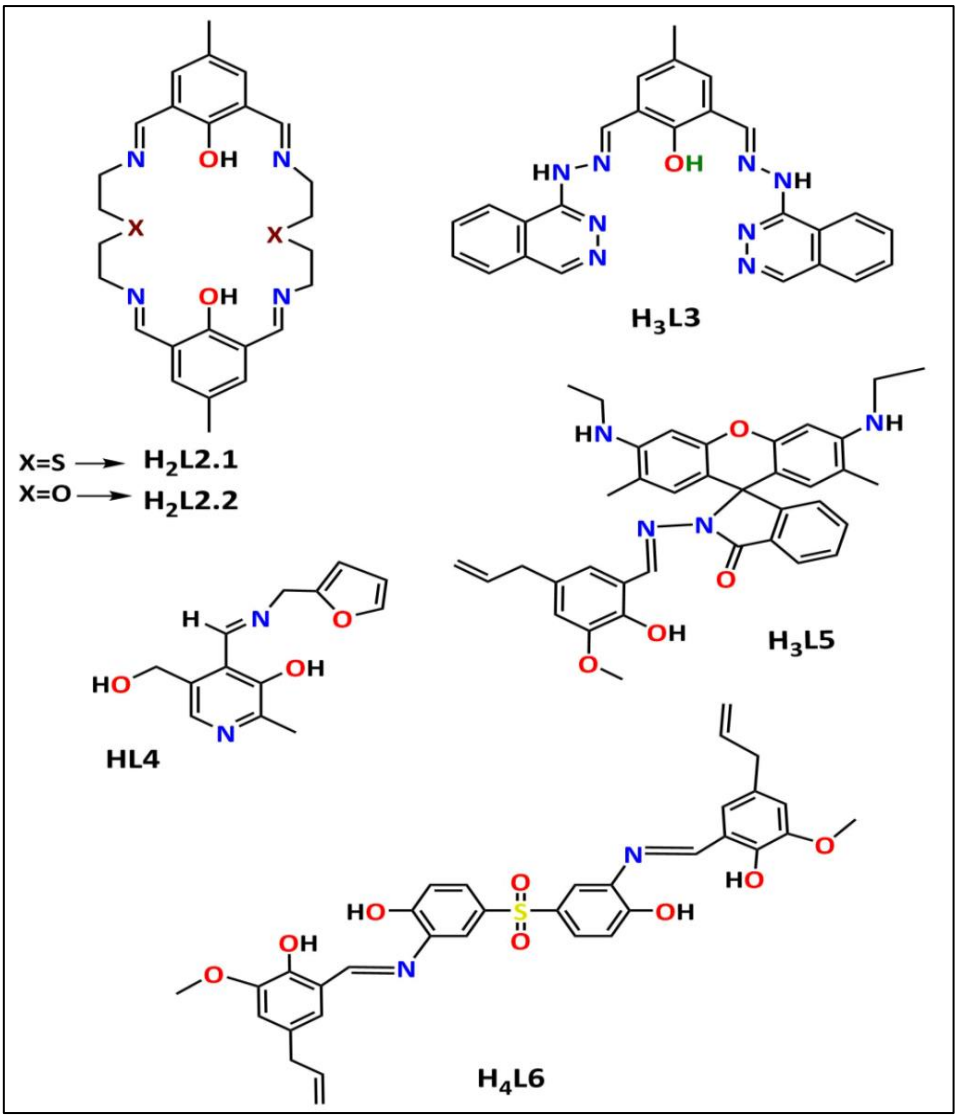

Scheme 1.12. Design of target Schiff base probes.

1.8 Instrumentations

(i) C, H, N analysis: Elemental analysis (C, H, N) data were collected on Perkin Elmer 2400 Series-II CHN analyzer, USA elemental analyzer using the pure solid sample.

(ii) FT-IR spectra: FT-IR spectral data (KBr disk, 4000–400 cm^{-1}) were collected by Perkin Elmer LX-1 FTIR spectrophotometer with samples prepared as KBr pellets.

(iii) Mass Spectroscopy: ESI mass spectra were recorded by a MICROMASS Q-TOF mass spectrometer.

(iv) NMR spectra: ^{1}H and ^{13}C NMR spectra were obtained from Bruker 400 MHz spectrometer or Bruker 300 MHz spectrometer using DMSO-d_6, CD_3OD and $CDCl_3$ as solvent using tetramethylsilane as internal standard.

(v) Single crystal X-ray diffraction study:

Single crystals of the ligands and their complexes will be attempted to be obtained either by diffusion of another solvent into the solution or by slow evaporation of the solvent from the solution. Data will be collected on a Bruker SMART Apex CCD area detector by graphite monochromated Mo K_α radiation with wavelength of 0.71073 Å. Using Bruker SAINT plus [1.144], all reflections within the $2\theta_{max}$ range were collected and adjusted for polarisation and Lorentz factors. Afterwards, SADABS [1.145] was used to adjust the reflections for absorption, inter-frame scaling, and other systematic flaws. Using the ORTEP-32 [1.146], SHELX-2018/3 [1.147], and WinGX [1.148] software package the structures were solved directly and then refined using the full matrix least-square technique based on F^2. All non-hydrogen atoms underwent anisotropic thermal parameter refinement. At geometrical places where $U_{iso} = 1/2U_{eq}$ to those to which they are coupled, C-H hydrogen atoms were inserted.

(vi) UV-Vis spectra: Absorption spectra of solution of samples at the necessary concentration were recorded using an Agilent Cary 60 spectrophotometer and Shimadzu UV

1800 spectrophotometer. The solution was stored in a quartz cell with a 1 cm path length and measured the spectra from the visible to the ultraviolet region.

(vii) Fluorescence spectra: Fluorescence spectra were measured with HORIBA Fluoromax-4 spectrofluorometer and Duetta-fluorescence and absorbance spectrometer, HORIBA.

(viii) Quantum yield calculation:

The area under the fluorescence curves was integrated using the following formula to determine the fluorescence quantum yields (Φ),

$$\Phi_{sample} = \{(OD_{standard} \times A_{sample} \times \eta^2_{sample})/(OD_{sample} \times A_{standard} \times \eta^2_{standard})\} \times \Phi_{standard}$$

The compound's optical density at the excitation wavelength is represented by OD in the equation above, the solvent's refractive index by η, and the area under the emission spectral curve by A. The standard value for Φ is 0.52 in the case of quinine sulphate.

(ix) LOD and binding constant calculations:

IUPAC approved equation for calculating limit of detection (LOD) was:

LOD=3σ/slope , where σ represents standard deviation of the curve Using the equation (1) LOD was calculated from fluorescence titration data..

Again from the fluorescence titration data the apparent binding constant (K) of chemosensors towards metal ions was calculated using the Benesi− Hildebrand equation: [1.149]

$$(F_{max} - F_0)/(F_x - F_0) = 1 + \{(1/K)\ (1/[M^{n+}])\ \}$$

Where, F_{max}, F_0, and F_x are fluorescence intensities in the presence of maximum concentration of metal ions added ($[M^{n+}]$) (no. of equivalents), free ligand (no. of equivalents) and any intermediate $[M^{n+}]$ concentration, respectively. On the other hand using web support: https://supramolecular.org [1.150] binding constant (K) of chemosensors towards metal ions was also calculated from the absorbance titration data.

(x) Life time measurement:

The steady-state fluorescence lifetime measurements of the samples were performed by a TCSPSC (time-correlated single photon counting) set up from Horiba Jobin-Yvon. The

luminescence decay data were collected on a Hamamatsu MCP photomultiplier (R3809) and were analyzed using the IBH DAS6 software.

(xi) Theoretical and Computational study:

Using the Gaussian 09 software, the DFT (density functional theory) method was performed by selecting B3LYP or CAM-B3LYP basis function to optimize the ground-state structures and calculate the energies of all the chemosensing probes and their respective metal bound complexes [1.151]. The LanL2DZ [1.152] basis set with effective core potential was used for different metals whereas the 6-31G [1.153–1.159] basis set was consigned to C, H, N, O, and S. The optimized geometries are confirmed to represent the local minima by vibrational frequency computations, which only produced positive eigenvalues. Theoretical UV-Vis spectral transitions are detected from the conductor-like polarizable continuum model (CPCM) [1.160–1.162], which was also used to develop Time Dependent Density Functional Theory (TD-DFT). By using GAUSSSUM [1.163], the percentage of contributions from different groups in each molecular orbital was also determined.

(xii) Biological study: Cell images were taken using Leica fluorescence microscope. To check the cytotoxicity of probe towards cell MTT assay protocol has used [1.164,1.165].

1.9. References

[1.1] D. R. Willams, The metals of life, Van Nostrand, London (1971).

[1.2] I. Bertini, H. B. Gray, S. J. Lippard, J. S. Valentine, Bioinorganic Chemistry, University Science Books, Mill Valley, California (1994).

[1.3] Y. Guo, H. Zhao, Y. Han, X. Liu, S. Guan, Q. Zhang, X. Bian, Spectrochim Acta A Mol. Biomol. Spectroscopy 173 (2017) 532–536.

[1.4] V. S. A. Piriya, P. Joseph, S. C. G. K. Daniel, S. Lakshmanan, T. Kinoshita, S. Muthusamy, Mater. Sci. Eng. C 78 (2017) 1231–1245.

[1.5] U. Jeong, Y. Kim, J. Ind. Eng. Chem. 31 (2015) 393–396.

[1.6] B. F. Ye, Y. J. Zhao, Y. Cheng, T. T. Li, Z. Y. Xie, X. W. Zhao, Z. Z. Gu, Nanoscale 4 (2012) 5998–6003.

[1.7] Y. Zhang, W. Wang, R. Li, E. Zhang, Z. Li, L. Tang, B. Han, X. Hou, J. J. Wang, Spectrochim. Acta A Mol. Biomol. Spectrosc. 230 (2020) 118050.

[1.8] A. Liu, L. Yang, Z. Zhang, Z. Zhang, D. Xu, Dye. Pigment. 99 (2013) 472–479.

[1.9] M. Formica, V. Fusi, L. Giorgi, M. Micheloni, Coord. Chem. Rev 256 (2012) 170–192.

[1.10] G. Ambrosi, S. Ciattini, M. Formica, V. Fusi, L. Giorgi, E. Macedi, M. Micheloni, P. Paoli, P. Rossi, G. Zappia, Chem. Commun. (2009) 7039–7041.

[1.11] J. Otero-Romaní, A. Moreda-Pi~neiro, P. Bermejo-Barrera, A. Martin-Esteban, Talanta 79 (2009) 723–729.

[1.12] Q. Lu, S. Yang, D. Sun, J. Zheng, Y. Li, J. Yu, M. Su, Spectrochim. Acta Part B At. Spectrosc. 125 (2016) 136–139.

[1.13] Y. Shijo, H. Sato, N. Uehara, S. Aratake, Analyst 121 (1996) 325–328.

[1.14] S. H. Chen, Z. Y. Yang, H. L. Wu, H. S. Kou, S. J. Lin, J. Anal. Toxicol. 20 (1) (1996) 38–42.

[1.15] V. V. Mihaylova, B. R. Todorov, V. V. Lyubomirova, R. G. Djingova, Bulg. Chem. Commun. 53 (1) (2021).

[1.16] R. O. Allen, W. Brookhart, Anal. Chem. 46 (9) (2002) 1297–1299.

[1.17] O. V. Popova, V. V. Sursyakova, G. V. Burmakina, A. I. Rubaylo, J. Anal. Chem. 70 (2) (2015) 198–202.

[1.18] M. Ghaedi, F. Ahmadi, A. Shokrollahi, J. Hazard Mater. 142 (1-2) (2007) 272–278.

[1.19] E. Young, T. Tarawou, Int. J. Biol. Chem. Sci. 8 (6) (2015) 2891.

[1.20] M. Arienzo, R. Capasso, J. Agric. Food Chem. 48 (4) (2000) 1405–1410.

[1.21] S. Wang, E. S. Forzani, N. Tao, Anal. Chem. 79 (12) (2007) 4427–4432.

[1.22] F. Menzinger, P. Schmitt-Kopplin, D. Freitag, A. Kettrup, J. Chromatogr. A 891 (2000) 45-67.

[1.23] Y. Gao, B. Feng, L. Miao, Y. Chen, J. Di, Microchem. J. 157 (2020) 104995.

[1.24] S. A. Tukur, N. A. Yusof, R. Hajian, J. Chem. Sci. 127 (6) (2015) 1075–1081.

[1.25] Z. Stojanovi_c, Z. Koudelkova, E. Sedlackova, D. Hynek, L. Richtera, V. Adam, Anal. Methods 10 (24) (2018) 2917–2923.

[1.26] S. Khan, X. Chen, A. Almahri, E. S. Allehyani, F. A. Alhumaydhi, M. M. Ibrahim, S. Ali, J. Environ. Chem. Eng. 9 (6) (2021) 106381.

[1.27] G. M. Abu-Taweel, M. M. Ibrahim, S. Khan, H. M. Al-Saidi, M. Alshamrani, F. A. Alhumaydhi, S. S. Alharthi, Crit. Rev. Anal. Chem. 54 (2024) 599–616.

[1.28] S. Khan, M. Muhammad, J. S. Algethami, H. M. Al-Saidi, A. Almahri, A. A. Hassanian, J. Fluoresc. 32 (2022) 1889–1898.

[1.29] S. Khan, M. Muhammad, H. M. Al-Saidi, A. A. Hassanian, W. Alharbi, K. H. Alharbi, J. Saudi Chem. Soc. 26 (4) (2022) 101503.

[1.30] Y. Nural, E. Keleş, B. Aydıner, N. Seferoğlu, H. Atabey, Z. Seferoğlu, J. Mol. Liq. 327 (2021) 114855.

[1.31] A. W. Czarnik, American Chemical Society, Washington, DC (1993).

[1.32] A. P. de Silva, H. Q. N. Gunaratne, T. Gunnlaugsson, A. J. M. Huxley, C. P. McCoy, J. T. Rademacher, T. E. Rice, Chem. Rev. 97 (1997) 1515–1566.

[1.33] B. Daly, J. Ling, A. P. de Silva, Chem. Soc. Rev. 44 (2015) 4203–4211.

[1.34] R. T. K. Kwok, C. W. T. Leung, J. W. Y. Lam, B. Z. Tang, Chem. Soc. Rev. 44 (2015) 4228–4238.

[1.35] (a) H. He, M. A. Mortellaro, M. J. P. Leiner, R. J. Fraatz, J. K. Tusa, J. Am. Chem. Soc. 125 (2003) 1468-1469; (b) J. Ninga, Y. Tian, Sens. Actuators: B. Chemical 307 (2020) 127659.

[1.36] M. Constantin, I. Alexandru, Balneo-Research Journal, 2 (1) (2011).

[1.37] (a) K. A. Karthick, B. Shankar, M. K. Aravind, B. Ashokkumar, A. Tamilselvi, Chemistry Select 7 (2022) e202203235 (1 of 16); (b) V. Dangi, M. Baral, B. K. Kanungo, J. Appl. Spectroscopy 87 (2020).

[1.38] (a) H. Rubin, Arch. Biochem. Biophys. 458 (2007) 16–23; (b) F. I. Wolf, A. Torsello, A. Fasanella, A. Cittadini, Mol. Aspects Med., 2003, 24, 11–25; (c) J. R. Moll, A. Acharya, J. Gal, A. A. Mir, C. Vinson, Nucleic Acids Res. 30 (2002) 1240–1246; (d) F. Khanbabai, R.

Azadbakht, M. Koolivand, New J. Chem. 47 (2023) 2635; (e) R. Azadbakhta, M. Koolivandb, S. Menatic, Inorg. Chim. Acta 514 (2021) 120021.

[1.39] (a) M. Salek-Maghsoodi, Z. Golsanamlu, S. Sadeghi-Mohammadi, M. Gazizadeh, J. Soleymani, R. Safaralizadeh, RSC Adv. 12 (2022) 31535; (b) S. Erdemir, O. Kocyigit, S. Malkondu, J. Photochem. Photobiol. A: Chemistry 425 (2022) 113713.

[1.40] (a) I. Muttaqin, W. Paisuwan, T. Pattarakankul, T. Palaga, M. Sukwattanasinitt, A. Ajavakom, Talanta Open, 9 (2024) 100316; (b) K. Ramki, G. Thiruppathi, S. K. Ramasamy, P. Sundararaj, P. Sakthivel, Methods 221 (2024) 1–11.

[1.41] (a) D. P. Pompeani, M. B. Abbott, B. A. Steinman, D. J. Bain, Environ Sci Technol 47 (2013) 5545–5552; (b) D. C. Bellinger, N. Engl. J. Med. 374 (2016) 101–1103; (c) H. F. Cheng, Y. A. Hu, Environ Pollut 158 (2010) 1134–1146; (d) C. Kaewprom, P. Sricharoen, N. Limchoowong, P. Nuengmatcha, S. Chanthai, Spectrochim. Acta A: Mol. Biomol. Spectroscopy 207 (2019) 79–87; (e) E. A. Dil, M. Ghaedi, A. Asfaram, F. Mehrabi, Ultrason Sonochem 36 (2017) 409–419; (f) R. Azadbakht, H. Vaisi, H. Mohamadvand, J. Khanabadi, Spectrochim. Acta A: Mol. Biomol. Spectrosc. 145 (2015) 575–579; (g) A. Kolbus, A. Danel, P. Moskwa, K. Szary, T. Uchacz, Dye. Pigments 223 (2024) 111956.

[1.42] (a) G. F. Nordberg, R. F. M. Herber, L. Alessio (Eds.), Lyon, 1992; (b) D. M. Templeton, Y. Liu, Chem. Biol. Interact. 188 (2010) 267–275; (c) W. Lin, X. Xie, Y. Wang, J. Chen, Z Anorg. Allg. Chem. 645 (2019) 645–648; (d) H. Keypour, M. Abdollahi-Moghadam, H. Zeynali, R. Karamian, N. B. Hamedani, J. Mol. Struct. 1295 (2024) 136803.

[1.43] (a) M. Yang, T. J. Jiang, Y. Wang, J. H. Liu, L. N. Li, X. Chen, X. J. Huang, Sens. Actuators, B 245 (2017) 230–237; (b) S. Saha, P. Sarkar, Talanta 158 (2016) 235–245; (c) M. R. Awual, S. Urata, A. Jyo, M. Tamada, A. Katakai, Water Res. 42 (2008) 689–696; (d) M. R. Awual, M. A. Hossain, M. A. Shenashen, T. Yaita, S. Suzuki, A. Jyo, Environ. Sci. Pollut.

Res. 20 (2013) 421–430; (e) K. T. Kitchin, Toxicol. Appl. Pharmacol. 172 (2001) 249–261; (f) K. Dhanasekaran, R. Tamizhselvi, S. Mohandoss, M. Beena, A. Palaniappan, A. A. Napoleon, Spectrochim. Acta Part A: Mol. Biomol. Spectroscopy 316 (2024) 124325; (g) K. Nagaraj, A. N. Shettya, D. R. Trivedi, Anal. Methods (2024).

[1.44] (a) D. Rehder, Metallomics 7 (2015) 730–742; (b) C. Varadaraju, G. Tamilselvan, I. V. M. V. Enoch, V. Srinivasadesikan, S. -L. Lee, P. M. Selvakumar, N. J. Chem. 42 (2018) 3833; (c) F. J. Huo, J. Su, Y. Q. Sun, C. X. Yin, H. B. Tong, Z. X. Nie, Dye. Pigments 86 (2010) 50–55.

[1.45] (a) Y. Liu, S. –H. Wu, C. Hua, X. Han, Desalination and Water Treatment 52 (2014) 4183–4189; (b) A. K. Singh, V. K. Gupta, B. Gupta, Anal. Chim. Acta 585 (2007) 171–178; (c) H. Arakawa, R. Ahmad, M. Naoui, H. Ali, T. Riahi,. Biol. Chem. 275 (2000) 10150–10153; (d) J. B. Vincent, Nutr. Rev. 58 (2000) 67–72; (e) D. Divya, M. Ramanjaneyulu, M. Nandhagopal, V. Srinivasan, S. Thennarasu, Spectrochim. Acta Part A: Mol. Biomol. Spectroscopy 316 (2024) 124286; (f) A. Mumthaj, M. Umadevi, Spectrochim. Acta Part A: Mol. Biomol. Spectroscopy 308 (2024) 123741.

[1.46] (a) A. -F. Miller, FEBS Lett. 586 (2012) 585-595; (b) M. V. Golynskiy, W. A. Gunderson, M. P. Hendrich, S. M. Cohen, Biochemistry 45 (2006) 15359–15372; (c) S. Rivera-Mancia, C. Rios, S. Montes, Biometals 24 (2011) 811–825; (d) A. W. Dobson, M. Aschner, ed. Elsevier, Amsterdam (2007) p. 433; (e) M. F. Bouchard, S. Sauve, B. Barbeau, M. Legrand, M. Brodeur, T. Bouffard, E. Limoges, D. C. Bellinger, D. Mergler, Environ Heal Perspect 119 (2010) 138–143; (f) F. Gruppi, J. Liang, B. Bartelle, M. Royzen, D. H. Turnbull, J. W. Canary, Chem. Commun. 48 (2012) 10778–10780; (g) N. Roy, A. Dutta, P. Mondal, P. C. Paul, T. S. Singh, J. Luminescence 165 (2015) 167–173; (h) A. Umit, Adv. Biol. Chemistry 12 (2022) 161–170.

[1.47] (a) S. K. Sahoo, D. Sharma, R. K. Bera, G. Crisponi, J. F. Callan, Chem. Soc. Rev. 41 (2012) 7195–7227; (b) S. Chakraborty, M. Mandal, S. Rayalu, Inorg. Chem. Commun. 121 (2020) 108189; (c) Z. Li, K. Liu, Y. Wang, T. Han, H. Han, L. Zhang, Y. Li, Spectrochim. Acta Part A: Mol. Biomol. Spectroscopy 309 (2024) 123809; (d) Y. Che, J. Yang, Z. Dong, J. Wang, X. Yan, Y. Wang, S. Shuang, Spectrochim. Acta Part A: Mol. Biomol. Spectroscopy 308 (2024) 123799.

[1.48] (a) S. Nsanzamahoroa, W. Chenga, F. P. Mutuyimana, L. Lia, W. Wang, C. Ren, T. Yic, H. Chena, X. Chen, Talanta 210 (2020) 120636; (b) P. Rafighi, M. Yaftian, N. Noshiranzadeh, Sep. Purif. Technol. 75 (2010) 32–38; (c) A. Ahmadpour, M. Tahmasbi, T. R. Bastami, J. A. Besharati, J. Hazard. Mater. 166 (2009) 925–930; (d) J. J. Celestina, P. Tharmaraj, C. D. Sheela, J. Shakina, J. Luminescence 239 (2021) 118359; (e) W. C. Chan, H. M. Saad, K. S. Sim, V. S. Lee, C. W. Ang, K. Y. Yeong, K. W. Tan, Spectrochim. Acta Part A: Mol. Biomol. Spectroscopy 262 (2021) 120099.

[1.49] (a) Y. A. Iyaka, Nickel in soils: Sci. Res. Essays 6 (2011) 6774–6777; (b) A. W. Lothongkum, Y. Khemglad, N. Usomboon, U. Pancharoen, J. Alloys Comp. 476 (2009) 940–949; (c) K. Alizadeh, H. Nemati, S. Zohrevand, P. Hashemi, A. Kakanejadifard, M. Shamsipur, M. R. Ganjali, F. Faridbod, Mater. Sci. Eng. C 33 (2013) 916–922; (d) M. J. Zirwas, M. A. Molenda, J. Clin. Aesthet. Dermatol. 2 (2009) 39–43; (e) M. M. Alqasaimeh, A. -A. M. Abu-Yamin, S. A. Matar, I. A. Sarairah, M. M. Salman, R. M. Al-As'ad, J. Photochem. Photobiol. A: Chemistry 447 (2024) 115277; (f) S. Moon, J. J. Lee, C. Kim J. Mol. Struct. 1282 (2023) 135210.

[1.50] (a) V. Dujols, F. Ford, A. W. Czarnik, J. Am. Chem. Soc. 119 (1997) 7386–7387; (b) S. Khan, M. Muhammad, A. W. Kamran, H. M. Al-Saidi, S. S. Alharthi, J. S. Algethami, Environ. Monit. Assess 195 (2023) 633.

[1.51] (a) B. K. Rani, S. A. John, J. Photochem. Photobiol. A Chemistry 418 (2021) 113372; (b) X. -B. Yang, B. -X. Yang, J. -F. Ge, Y. -J. Xu, Q. -F. Xu, J. Liang, J. -M. Lu, Org. Lett. 13 (2011) 2710–2713; (c) A. Jana, P. K. Sukul, S. K. Mandal, S. Konar, S. Ray, K. Das, J. A. Golen, A. L. Rheingold, S. Mondal, T. K. Mondal, A. R. Khuda-Bukhsh, S. K. Kar, Analyst 139 (2013) 495–504; (d) J. -A. Zhou, X. -L. Tang, J. Cheng, Z. -H. Ju, L. -Z. Yang, W. -S. Liu, C. -Y. Chen, D. -C. Bai, Dalton Trans. 41 (2012) 10626–10632; (e) P. Jiang, Z. Guo, Coord. Chem. Rev. 248 (2004) 205–229; (f) E. Kimura, T. Koike, Chem. Soc. Rev. 27 (1998) 179–184.

[1.52] (a) K. A. Karthick, K. Kaleeswari, C. U. Maheswari, G. Sivaraman, B. Shankar, A. Tamilselvi, J. Photochem. Photobiol. A: Chemistry 428 (2022) 113861; (b) S. Kumar, S. Mahata, V. Manivannan, J. Photochem. Photobiol. A: Chemistry 450 (2024) 115436.

[1.53] (a) G. D. Torre, J. I. Mujika, E. Formoso, E. Matito, M. J. Ramos, X. Lopez, Dalton Trans. 47 (2018) 9592–9607; (b) D. P. Perl, D. C. Gajdusek, R. M. Garruto, R. T. Yanagihara, C. J. Gibbs, Science, 217 (1982) 1053–1055; (c) D. P. Perl, A. R. Brody, Science 208 (1980) 297–299; (d) C. Zhao, M. Asif, W. Lu, S. Shuang, Y. Tang, C. Dong, J. Mol. Liquids 400 (2024) 124507; (e) Heena, A. Silswal, D. Sharma, A. L. Koner, H. Om, R. Rana, Spectrochim. Acta Part A: Mol. Biomol. Spectroscopy 320 (2024) 124575.

[1.54] C. C. Kaonga, I. B. M. Kosamu, W. R. Utembe, Atmosphere 12 (2021) 891.

[1.55] J. Silva, A. Queiroz, A. Oliveira, V. Kartnaller, Frontiers in Bioenergy and Biofuels (2017).

[1.56] C. J. Rhodes, Science Progress, 102 (4) (2019) 304–350.

[1.57] B. Petovar, K. Xhanari, M. Finsgar, Anal. Chim. Acta 1004 (2018) 10–21.

[1.58] E. Mohammed, T. Mohammed, A. Mohammed, MethodsX 5 (2018) 824–833.

[1.59] A. Ahmed, A. Singh, B. Padha, A. Sundramoorth, A. Tomar, S. Arya, Chemosphere 303 (2022) 135208.

[1.60] S. C. Wilschefski, M. R. Baxter, Clin. Biochem. Reviews 40 (3) (2019) 115–133.

[1.61] I. Sharma, J. Environ. Biol. 5 (1) (2020) 027–033.

[1.62] D. Profrock, A. Prange, Applied Spectroscopy 66 (8) (2012) 843–868.

[1.63] S. Wilschefski, A. Baxter, Clinical Biochemist Reviews 40 (3) (2019) 115–133.

[1.64] A. Bose, I. Thomas, G. Kavitha, E. Abraham, Int. J. Advances in Pharmaceutical Analysis 8 (2018) 01–08.

[1.65] I. G. Munteanu, C. Apetrei, Int. J. Mol. Sci. 22 (2021) 3380.

[1.66] A. P. de Silva, P. Tecilla, J. Mater. Chem. 15 (2005) 2637–2639.

[1.67] L. Prodi, F. Bolletta, M. Montalti, N. Zaccheroni, Coord. Chem. Rev. 205 (1) (2000) 59–83.

[1.68] K. Rurack, Spectrochim. Acta, Part A 57 (2001) 2161–2195.

[1.69] P. Ghosh, P. K. Bharadwaj, S. Mandal, S. Ghosh, J. Am. Chem. Soc. 118 (1996) 1553–1554.

[1.70] B. Ramachandram, A. Samanta, Chem. Commun. (1997) 1037.

[1.71] K. Rurack, M. Kollmannsberger, U. Resch-Genger, J. Daub, J. Am. Chem. Soc. 122 (2000) 968.

[1.72] S. Banthia, A. Samanta, J. Phys. Chem. B 106 (2002) 5572.

[1.73] S. Banthia, A. Samanta, Org. Biomol. Chem. 3 (2005) 1428–1434.

[1.74] L. Fabbrizzi, A. Poggi, Chem. Soc. Rev. 24 (1995) 197–202.

[1.75] B. Valeur, I. Leray, Coord. Chem. Rev. 205 (2000) 3–40.

[1.76] J. Liu, Y. Q. Xie, Q. Lin, B. B. Shi, P. Zhang, Y. M. Zhang, T. B. Wei, Sens. Actuators B 186 (2013) 657–665.

[1.77] S. A. Ingale, F. Seela, J. Org. Chem. 77 (2012) 9352–9356.

[1.78] I. Ravikumar, P. Ghosh, Inorg. Chem. 50 (2011) 4229–4231.

[1.79] A. Bigdeli, F. Ghasemi, S. Abbasi-Moayed, M. Shahrajabian, N. Fahimi-Kashani, S. Jafarinejad, M. A. F. Nejad, M. R. Hormozi-Nezhad, Anal. Chim. Acta 1079 (2019) 30–58.

[1.80] D. T. Quang, J. S. Kim, Chem. Rev. 110 (10) (2010) 6280–6301.

[1.81] T. Gunnlaugsson, H. D. P. Ali, M. Glynn, P. E. Kruger, G. M. Hussey, F. M. Pfeffer, C. M. D. Santos, J. Tierney, J. Fluoresc. 15 (2005) 287–299.

[1.82] P. Li, X. Zhou, R. Huang, L. Yang, X. Tang, W. Dou, Q. Zhaoa, W. Liu, Dalton Trans. 43 (2014) 706–713.

[1.83] G. -Y. Li, K. -L. Han, WIREs Comput. Mol. Sci. 8 (2018).

[1.84] R. Martinez-Manez, F. Sancenon, Chem. Rev. 103 (2003) 4419–4476.

[1.85] K. E. Sapsford, L. Berti, I. L. Medintz, Angew. Chem. Int. Ed. 45 (2006) 4562–4589.

[1.86] Y. N. Hong, J. W. Y. Lam, B. Z. Tang, Chem. Commun. (2009) 4332–4353.

[1.87] M. Wang, G. X. Zhang, D. Q. Zhang, D. B. Zhu, B. Z. Tang, J. Mater. Chem. 20 (2010) 1858–1867.

[1.88] A. Tamrakar, M. A. Wani, G. Mishra, A. Srivastava, R. Pandey, M. D. Pandey, Anal. Methods 16 (2024) 2198–2228.

[1.89] P. Zhou, K. Han, Aggregate 3 (5) (2022) 160.

[1.90] (a) V. Balzani, Ed. Wiley-VCH: Weinheim, Germany, 2001; (b) M. Natali, S. Campagna, F. Scandola, Chem. Soc. Rev. 43 (2014) 4005–4018; (c) D. Escudero, Chem. Res. 49 (2016) 1816–1824.

[1.91] A. Gupta, N. Kumar, RSC Adv. 6 (2016) 106413–106434.

[1.92] N. Kumar, V. Bhalla, M. Kumar, Analyst 139 (2014) 543–558.

[1.93] Y. N. Hong, J. W. Y. Lam, B. Z. Tang, Chem. Commun. (2009) 4332–4353.

[1.94] J. S. Wu, W. M. Liu, X. Q. Zhuang, F. Wang, P. F. Wang, S. L. Tao, X. H. Zhang, S. K. Wu, S. T. Lee, Org. Lett. 9 (2007) 33–36.

[1.95] A. C. Sedgwick, L. Wu, H. H. Han, S. D. Bull, X. P. He, T. D. James, J. L. Sessler, B. Z. Tang, H. Tian, J. Yoon, Chem. Soc. Rev. 47 (2018) 8842–8880.

[1.96] C. C. Hsieh, Y. M. Cheng, C. J. Hsu, K. Y. Chen, P. T. Chou, J. Phys. Chem. A 112 (2008) 8323–8332.

[1.97] S. Lohar, S. Pal, M. Mukherjee, A. Maji, N. Demitri and P. Chattopadhyay, RSC Adv. 7 (2017) 25528–25534.

[1.98] D. Maity, A. Mukherjee, S. K. Mandal, P. Roy, J. Lumin. 210 (2019) 508–518.

[1.99] J. H. Kim, J. Y. Noh, I. H. Hwang, J. Kang, J. Kim, C. Kim, Tetrahedron Lett. 54 (2013) 2415–2418.

[1.100] C. Liu, S. Huang, H. Yao, S. He, Y. Lu, L. Zhao, X. Zeng, RSC Adv. 4 (2014) 16109–16114.

[1.101] H. N. Kim, M. H. Lee, H. J. Kim, J. S. Kim, J. Yoon, , Chem. Soc. Rev. 37 (2008) 1465–1472.

[1.102] K. T. A. Priyangga, Y. S. Kurniawan, K. Ohto, J. Jumina, J. Multidiscip. Appl. Nat. Sci. 2 (2022) 23–40.

[1.103] J. L. Segura, M. J. Mancheno, F. Zamora, Chem. Soc. Rev. 45 (2016) 5635–5671.

[1.104] J. Wang, Q. Meng, Y. Yang, S. Zhong, R. Zhang, Y. Fang, Y. Gao, X. Cui, ACS Sens. 7 (2022) 2521–2536.

[1.105] C. M. Da Silva, L. V. Modolo, R. B. Alves, M. A. de Resende, C. V. Martins, A. de Fátima, J. Adv. Res. 2 (2011) 1–8.

[1.106] J. Cheng, K. Wei, X. Ma, X. Zhou, H. Xiang, J. Phys. Chem. C 117 (2013) 16552–16563.

[1.107] P. G. Cozzi, Chem. Soc. Rev. 33 (2004) 410–421.

[1.108] S. Khan, X. Chen, A. Almahri, E. S. Allehyani, F. A. Alhumaydhi, M. M. Ibrahim, S. Ali, J. Environ. Chem. Eng. 9 (2021) 106381.

[1.109] V. K. Gupta, A. K. Singh, L. K. Kumawat, Sens. Actuators B: Chemical 195 (2014) 98–108.

[1.110] J. Berrones-Reyes, B. M. Munoz-Flores, A. Gomez-Trevino, M. A. Treto-Suarez, D. Paez-Hernandez, E. Schott, X. Zarate, V. M. Jimenez-Perez, Mater. Chem. Phys. 233 (2019) 89–101.

[1.111] Y. Wang, Z. Y. Ma, D. L. Zhang, J. L. Deng, X. Chen, C. Z. Xie, X. Qiao, Q. Z. Li, J. Y. Xu, Spectrochim. Acta, Part A: Mol. Biomol. Spectrosc. 195 (2018) 157–164.

[1.112] H. Tian, X. Qiao, Z. L. Zhang, C. Z. Xie, Q. Z. Li, J. Y. Xu, Spectrochim. Acta, Part A: Mol. Biomol. Spectrosc. 207 (2019) 31–38.

[1.113] A. Aguiari, N. Brianese, S. Tamburini, P. A. Vigato, Inorg. Chim. Acta 235 (1995) 233–244.

[1.114] P. A. Vigato, S. Tamburini, Coord. Chem. Rev. 248 (2004) 1717–2128.

[1.115] S. Anbu, R. Ravishankaran, M. F. C. G. da Silva, A. A. Karande, A. J. L. Pombeiro, Inorg. Chem. 53 (2014) 6655–6664.

[1.116] R. Purkait, A. D. Mahapatra, D. Chattopadhyay, C. Sinha, Spectrochim. Acta Part A: Mol. Biomol. Spectrosc. 207 (2019) 164–172.

[1.117] P. Ghorai, S. Banerjee, D. Nag, S. K. Mukhopadhyay, A. Saha, J. Luminescence 205 (2019) 197–209.

[1.118] T. T. Liu, J. Xu, C. Liua, S. Zeng, Z. Y. Xing, X. J. Sun, J. L. Li, J. Mol. Liquids 300 (2020) 112250.

[1.119] J. Fu, Y. Chang, B. Li, X. Wang, X. Xie, K. Xu, Spectrochim. Acta Part A: Mol. Biomol. Spectroscopy 225 (2020) 117493.

[1.120] A. Hazra, P. Roy, Inorg. Chem. Commun. 130 (2021) 108694.

[1.121] P. Ghorai, S. G. Chowdhury, K. Pal, J. Mandal, P. Karmakar, A. Franconetti, A. Frontera, S. Blasco, E. García-España, P. P. Parui, A. Saha, Inorg. Chem. 61 (2022) 1982–1996.

[1.122] S. Dey, A. Maity, M. Shyamal, D. Das, S. Maity, P. K. Giri, N. Mudi, S. S. Samanta, P. Hazra, A. Misra, Photochem. Photobiol. Sci. 18 (2019) 2717.

[1.123] R. Bag, Y. Sikdar, S. Sahu, M. M. Islam, S. Mandal, S. Goswami, New J. Chem. 46 (2022) 16161.

[1.124] (a) Suban K. Sahoo & Darshna Sharma & Rati Kanta Bera, J. Mol. Model 18 (2012) 1993–2001; (b) L. Fabbrizzi, J. Org. Chem. 85 (2020) 12212–12226; (c) S. K Sahoo, New J. Chem. 45 (2021) 8874-8897.

[1.125] L. Qua, C. Yina, F. Huob, J. Chaob, Y. Zhangb, F. Chengca, Sens. Actuators B 191 (2014) 158–164.

[1.126] S. Mandal, Y. Sikdar, D. K. Maiti, R. Sanyal, D. Das, A. Mukherjee, S. K. Mandal, J. K. Biswas, A. Bauzá, A. Frontera, S. Goswami, J. Photochem. Photobiol. A: Chemistry 334 (2017) 86–100.

[1.127] Y. Upadhyay, T. Anand, L. T. Babu, P. Paira, G. Crisponi, A. Kumar SK, R. Kumara, S. K Sahoo, Dalton Trans. 47 (2018) 742–749.

[1.128] T. Anand, A. S. K. Kumar, S. K. Sahoo, Photochem. Photobiol. Sci. 17 (2018) 414–422.

[1.129] D. C. Cork, L. D. Lewandowski, P. K. Shrestha, S. Giri, X. Wang, A. G. Sykes, A. Hussain, K. Mariappan, RSC Adv. 11 (2021) 34181–34192.

[1.130] M. N. Zavalishin, G. A. Gamov, O. A. Pimenov, A. E. Pogonin, V. V. Aleksandriiskii, S. D. Usoltsev, Y. S. Marfin, J. Photochem. Photobiol, A: Chemistry 432 (2022) 114112.

[1.131] J. Mandal, N. Ch. Jana, S. G. Chowdhury, P. Karmakar, A. Saha, Inorg. Chem. Commun. 156 (2023) 111217.

[1.132] E. Noelting, K. Dziewonsky, Ber. Dtsch. Chem. Ges. 38 (1905) 3516.

[1.133] S. Mabhai, M. Dolai, S. Dey, A. Dhara, B. Das, A. Jana, New J. Chem. 42 (2018) 10191–10201.

[1.134] S. Gond, P. Yadav, A. Singh, S. Garai, A. Shekher, S. C. Guptab, V. P. Singh, Org. Biomol. Chem. 21 (2023) 4482.

[1.135] S. Negi, P. Gahlyan, R. Bawa, B. Singh, M. Bhandari, R. Kakkar, B. Pani, R. Kumar, Anal. Methods 15 (2023) 4000.

[1.136] S. S. Samanta, U. Mandal, B. Das, S. Mandal, P. Upadhyay, T. D. Singh, A. Misra, J. Photochem. Photobiol. A: Chemistry 442 (2023) 114806.

[1.137] M. Prajapati, N. Pandey, S. Kalla, S. Bandaru, A. Sivaiah, Sens. Diagn. 3 (2024) 412.

[1.138] K. Zhang, X. Tian, P. Xu, Y. Zhu, S. Guang, H. Xu, Spectrochim. Acta Part A: Mol. Biomol. Spectroscopy 318 (2024) 124484.

[1.139] D. Das, R. Alam, M. Ali, Analyst 147 (2022) 471.

[1.140] S. Das, P. P. Das, J. W. Walton, K. Ghoshal, L. Patra, M. Bhattacharyya, New J. Chem. 45 (2021) 1853–1862.

[1.141] J. Mandal, K. Pal, S. G. Chowdhury, P. Karmakar, A. Panja, S. Banerjee, A. Saha, Dalton Trans. 51 (2022) 15555–15570.

[1.142] Y. Liu, M. Zhou, S. Wang, J. Feng, T. Chai, M. Zhang, X. Feng, L. Huang, C. Lu, G. Jin, J. Mol. Struct. 1312 (2024) 138552.

[1.143] D. Das, R. Alam, M. Sasmal, A. Katarkar, A. Dutta, M. Ali, Inorg. Chim. Acta 563 (2024) 121902.

[1.144] G. M. Sheldrick, SAINT, Version 6.02, SADABS, Version 2.03, Bruker AXS Inc., Madison, Wisconsin (2002).

[1.145] G. M. Sheldrick, SADABS: Institute fur Anorganische Chemieder Universitat, Gottingen, Germany (1999–2003).

[1.146] L. J. Farrugia, J. Appl. Cryst. 30 (1997) 565.

[1.147] G. M. Sheldrick, Acta Cryst. 71 (2015) 3–8.

[1.148] A. L. Spek, J. Appl. Cryst. 36 (2003) 7–13.

[1.149] H. A. Benesi, J. H. Hildebrand, J. Am. Chem. Soc. 71 (1949) 2703–2707.

[1.150] D. B. Hibbert, P. Thordarson, Chem. Commun. 52 (2016) 12792–12805.

[1.151] M. J. Frisch, G. W. Trucks, H. B. Schlegel, P. M. W. Gill, B. G. Johnson, M. A. Robb, J. R. Cheeseman, T. A. Keith, G. A. Petersson, J. A. Montgomery, K. Raghavachari, M. A. Al-Laham, V. G. Zakrzewski, J. V. Ortiz, J. B. Foresman, J. Cioslowski, B. B. Stefanov, A. Nanayakkara, M. Challacombe, C. Y. Peng, P. Y. Ayala, W. Chen, M. W. Wong, J. L. Andres, E. S. Replogle, R. Gomperts, R. L. Martin, D. J. Fox, J. S. Binkley, D. J. Defrees, J. Baker, J. P. Stewart, M. Head-Gordon, C. Gonzalez, J. A. Pople, Gaussian 98, Gaussian Inc. Pittsburgh, PA, (1998).

[1.152] P. J. Hay, W. R. Wadt, J. Chem. Phys. 82 (1985) 270–283.

[1.153] H. G. Korth, M. I. De Heer, P. Mulder, J. Phys. Chem. A 106 (2002) 8779–8789.

[1.154] B. G. Johnson, P. M. W. Gill, J. A. Pople, J. Chem. Phys. 98 (1993) 5612–5626.

[1.155] P. K. Chowdhury, J. Phys. Chem. A 107 (2003) 5692–5696.

[1.156] V. Chis, Chem. Phys. 300 (2004) 1–11.

[1.157] A. Asensio, N. Kobko, J. J. Dannenberg, J. Phys. Chem. A 107 (2003) 6441–6443.

[1.158] A. Müller, M. Losada, S. Leutwyler, J. Phys. Chem. A 108 (2004) 157–165.

[1.159] N. S. Goncalves, R. Cristiano, M. G. Pizzolatti, F. da S. Miranda, J. Mol. Struct. 733 (2005) 53–61.

[1.160] A. D. Becke, J. Chem. Phys. 96 (1992) 2155–2160.

[1.161] M. Cossi, V. Barone, J. Chem. Phys. 115 (2001) 4708–4717.

[1.162] M. Cossi, N. Rega, G. Scalmani, V. Barone, J. Comput. Chem. 24 (2003) 669–681.

[1.163] N. M. O'Boyle, A. L. Tenderholt, K. M. Langner, J. Comput. Chem. 29 (2008) 839–845.

[1.164] M. H. Wang, S. H. Jeong, H. Guo, J. B. Park, J. Oral Sci, 58 (2016) 125–131.

[1.165] A. KOC, A. Z. Karabay, T. Ozkan, Z. Buyukbingol, F. Aktan, J. Res Pharm. 26 (2022) 494–501.

Chapter 2

Aza-phenol based macrocyclic probes design for "CHEF-on" multi analytes sensor: Crystal structure elucidation and application in biological cell imaging

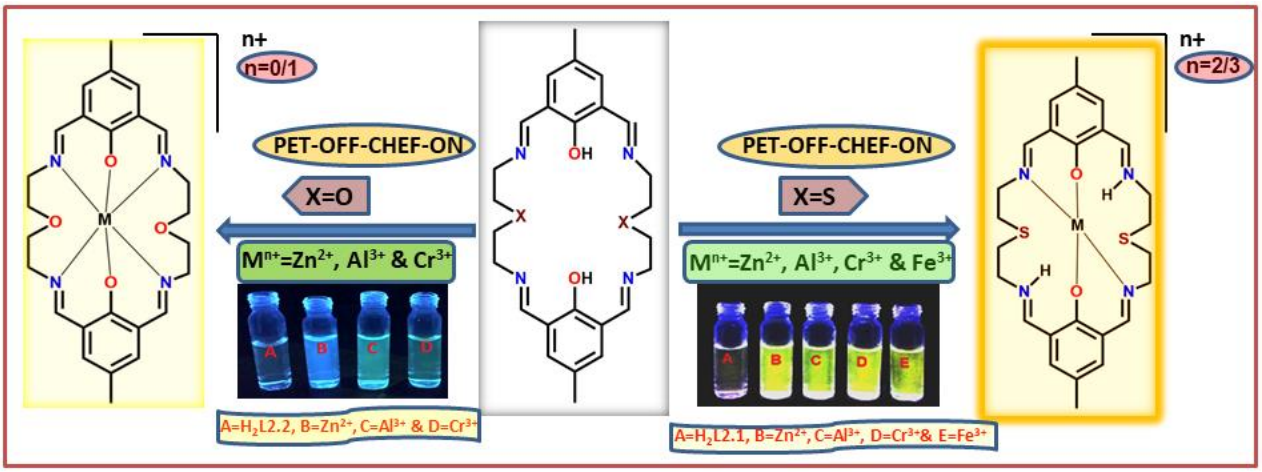

ACS Omega 8 (2023) 7479-7491

Abstract

Metal bound macrocyclic compounds found in biological systems inspired us to design and synthesize two Robson-type macrocyclic Schiff-base chemosensors, **H_2L2.1** (**H_2L2.1** =1,11-dimethyl-6,16-dithia-3,9,13,19-tetraaza-1,11(1,3)-di-benzenacycloicosaphane-2,9,12,19-tetraene-1,11-diol) and **H_2L2.2** (**H_2L2.2**=1,11-dimethyl-6,16-dioxa-3,9,13,19-tetraaza-1,11(1,3)-di- benzenacycloicosaphane-2,9,12,19-tetraene-1,11-diol). Both the chemosensors have been characterized with different spectroscopic techniques. They act as multianalyte sensor and exhibit "turn-on" fluorescence toward different metal ions in 1X PBS (Phosphate Buffered Saline) solution. In presence of Zn^{2+}, Al^{3+}, Cr^{3+} and Fe^{3+} ions, **H_2L2.1** exhibits ~6-fold enhancement of emission intensity, while **H_2L2.2** shows ~6-fold enhancement of emission intensity in the presence of Zn^{2+}, Al^{3+} and Cr^{3+} ions. The interactions between the different metal ion and chemosensors have been examined by absorption, emission, and ^{1}H NMR spectroscopy as well as by ESI-MS^+ analysis. We have successfully isolated and solved the crystal structure of the complex [Zn(**H_2L2.1**)(NO_3)]NO_3 (**2.1**) by X-ray crystallography. The crystal structure of **2.1** shows 1:1 metal:ligand stoichiometry and helps to understand the observed PET-Off-CHEF-On sensing mechanism. LOD values of **H_2L2.1** and **H_2L2.2** toward metal ions are found to be ~10^{-8} and ~10^{-7} M, respectively. Large Stokes shifts of the probes against analytes (~100 nm) make them a suitable candidate for biological cell imaging studies. Robson type phenol based macrocyclic fluorescence sensors are very scarce in the literature. Therefore, the tuning of structural parameters as the number and nature of donor atoms, their relative locations and presence of rigid aromatic groups can lead to the design of new chemosensors, which can accommodate different charged/neutral guest(s) inside its cavity. The study of the spectroscopic properties of this type of macrocyclic ligands and their complexes might open a new avenue of chemosensors.

2.1. Introduction

Metals are crucial for living systems as they are actively participating in many biological processes. Among them, alkali and alkaline earth metals like Na, K, Ca, and Mg play crucial roles in osmotic regulation, biomineralization, etc., whereas transition metals like Fe, Zn, Cu, Mn, Co, Ni, Mo, and V are important for catalysis, metabolism, and signaling processes [2.1,2.2]. Typically, transition metals are present at trace levels in biological systems,[1] and they act as cofactors in diverse enzymes like cytochrome oxidase, histidine ammonia-lyase, glutamate mutase, catalase, etc. [2.2,2.3], due to their electronic structures and redox properties. On the contrary, overdose or deficiency of transition metals are responsible for acute and long-term diseases, including heart disease, cancer and neurodegeneration. Therefore, the assessment and under- standing of the distribution of metal ions in living systems are fundamental for homeostasis and its related diseases [2.4]. Among different techniques, fluorescence spectroscopy is recognized as a useful tool to sense biologically important metal ions and, thus, widely used in biology, physiology, pharmacology, and in environmental science also. In this respect, tailored molecular chemosensors can be highly specific and sensitive toward analyte molecules with fast response time [2.5]. Chemosensors that can detect more than one analyte simultaneously have attracted great attention in recent years. This not only reduces production costs but also improves analysis time [2.6]. However, the development of fluorescence chemosensors that can both recognize multiple analytes and differentiate them still remains a great challenge [2.7]. In this context, we are mainly concentrating on chemosensor which can detect Zn^{2+}, Al^{3+}, Cr^{3+} and Fe^{3+} ions [2.8–2.16]. Iron and zinc are the first and second most abundant transition metals present in human body [2.17]. In many biochemical processes, both iron and zinc play essential role to complete the biocycle. Iron is indispensable for oxygen storage and transport at the cellular level [2.18].

Whereas, zinc-containing active sites are present in many metalloenzymes such as carbonic anhydrase, carboxy-peptidase A, alcohol dehydrogenase, RNA polymerase, etc [2.19]. However, the imbalance of both ions is responsible of different neurological disorders as Alzheimer's disease [2.20]. The presence of chromium decreases uptake of iron and thus reduces oxidative stress, heart disease, cancer, osteoporosis, and arthritis. The scarcity of chromium can raise the risk associated with diabetes and cardiovascular diseases [2.21,2.22]. Aluminum is one of the most used metals by our society. Its wide and multidimensional role in industry as well as in daily life provides some comfort, but excess accumulation in the human body causes several serious health issues as Alzheimer's disease, amyotrophic lateral sclerosis, encephalopathy, Parkinson's disease, [2.23−2.25] etc. Fluorometric detection of these metal ions (Al^{3+}, Zn^{2+}) has been reported by several physicochemical "Turn-On" processes like photo induced electron transfer (PET), chelation induced enhanced fluorescence (CHEF), fluorescence resonance energy transfer (FRET), intermolecular charge transfer (ICT) [2.26−2.30]. On the other hand, Cr^{3+} and Fe^{3+}, due to their paramagnetic nature of, can act as fluorescence quenchers rather than as activators [2.8−2.15].

Generally, rhodamine, anthraquinone, BODIPY, salicylalde-hyde, fluorescein and coumarin based chemosensors are used for trivalent cation sensing [2.31−2.37], while for Zn^{2+} sensing chemosensors are based typically on di-2-picolylamine (DPA) [2.38−2.41], quinoline [2.42−2.47], bipyridyl [2.43], etc. units. Therefore, simultaneous sensing of all these cations in a single platform is a challenging task. Several parameters such as avoiding multistep preparations of the probes, solubility in common solvents, high sensing ability, real sample analysis and biological applications (**Chart 2.1**) [2.48-2.58] need to be considered for the preparation of the chemosensors. Nature chooses macrocyclic ligands for stability of variety of biological systems which include chlorophyll, hemoglobin and vitamin B12 etc. Macrocyclic Schiff-

base ligands have wide applicability in the fields of analytical process, medicinal chemistry, supramolecular chemistry [2.59a,b], biochemistry [2.59c,d], organic synthesis, materials science,[2.59e] recognition [2.59f] catalysis,[2.59g] etc. Synthetic macrocyclic complexes are much more thermally stable, more resistance toward degradation, chemically unreactive to acids and alkali in comparison with their metal-containing open-chain analogues. Metal coordination gives structural rigidity to the macrocyclic ligand so that the system can emulate active site structure of a metalloprotein [2.59h]. In spite of this, it is important to mention that most of the reported chemosensors for metal ions are of acyclic nature and macrocyclic chemosensors are uncommon [2.60]. Cyclodextrin, pillar[n]arene, and metal−organic coordination macrocycles are some interesting macrocyclic compounds which exhibit interesting applications in the fields of molecular sensing, self-assembly, catalysis and molecular machines [2.61−2.64], etc. Important structural parameters of Robson-type macrocyclic Schiff-bases [2.65] like number and nature of donor atoms, their relative locations, presence of rigid aromatic groups can be tuned to accommodate different charged or neutral guest(s) inside the cavity. Ō kawa and co-workers have made many modifications in the basic structure of phenol based macro- cyclic ligands like using of different lateral chains, introduction of an additional donor atom on one lateral chain or made partial or full saturation of azomethine bond. Macrocycles with symmetrical lateral chains give hetero dinuclear Cu(II)M(II) or M(II)Cu(II) [M(II)=Mn, Co, Ni, Cu, Zn] compounds depending on the synthetic procedure and nature of donor sites [2.66,2.67]. A. E. Martell *et al*. have synthesized hydrogenated macrocyclic ligands to study their basicity and their coordination compounds are further studied for phosphate di ester catalytic process [2.68]. Some macrocyclic chemosensors are collected in **Chart 2.2**. Among them, most of the chemsonsors are selective

toward single metal ion. G. Ambrosi *et al*. have prepared a fluorescent oxadiazole derivative which selectivity detect Zn(II) in alkaline medium. The synthesis involved multistep procedure and presence of alkaline medium restrict cell imaging study of the chemosensor [2.69a]. B. Ghanbari

and his group have reported two naphthalene based aza-crown macrocyclic ligands for selective detection of Al(III) ions in ethanol. The LOD values for Al(III) cation by the chemo-sensors were found to be $\sim 10^{-9}$ M order [2.69b]. A piperazine linked diimine phenol has been reported by S. Goswami and his group which selectively detect Zn(II) in mixed aquous medium. The Zn-chemosensor complex has been utilized as a receptor for dihydrogen phosphate (DHP) sensing in aqueous medium by metal displacement approach resulting quenching of fluorescence intensity and generating the free chemosensor. The chemosensor further used for sensing of Zn^{2+} and DHP in living cells [2.69c]. Another aza-crown macrocyclic chemosensor, namely, 1-Hydroxy-diaza-15-Crown-4, was used by C. Sinha and co-workers for chromogenic sensing of Al^{3+} in DMSO- water medium. The probe also exhibits fluorescent turn on in the presence of Al^{3+} and Zn^{2+} ions. Furthermore, fluorescence cell imaging study of the probe had been performed in SCC084 (Human Oral carcinoma) cell lines [2.69d]. P. K. Panda and his group have designed a novel meso-expanded calix[4]pyrrolemacrocycle, where a rigid o-phenylene unit is incorporated as a spacer between the *α*,*α′*-positions of the tetrapyrrane moiety. It belongs to its smallest expanded analogue. Its selectivity detects fluoride ion via a turn-on response [2.69e]. R. Azadbakh *et al*. have developed a novel fluorescent nanochemosensor starting from a reduced macro- cyclic Schiff Base ligand. It acts as a highly selective and sensitive sensor toward Fe(III) and I^- through a fluorescence "'on−off'" process, with a limit of detection in nM range [2.69f]. D. Das *et al*. have found that an acyclic phenol-based Schiff base compartmental ligand, *N*,*N′*-propylene-bis(3-formyl-5-*tert*-bu- tylsalicylaldimine) upon reaction with Zn(II) produced a

dinuclear Zn(II)-cyclic compound. The acyclic compound containing C=N bonds undergone hydrolysis in the presence of Lewis acid $ZnCl_2$ in organic-aqua medium. Free ligand exhibits yellowish green fluorescence emission at 523 nm when excited at 437 nm in 1:1 water− acetonitrile. In the presence of Zn^{2+}, a new fluorescence emission band appears at 481 nm and the intensity enhanced gradually. Thus, the acyclic compound acts as a ratiometric fluorescence chemodosimeter for the selective detection of Zn(II) ions [2.69g]. V. Fusi *et al.* have synthesized a cyclophane macrocyclic probe containing 1,3- bis(benzo[d]oxazol-2-yl)phenyl fluorophore as sensing unit. It acts as a PET-mediated fluorescent chemosensor, at acidic medium. The macrocyclic probe signals the presence of Zn(II) and Cd(II) metal ions via fluorescence enhancement in a mixed acetonitrile−aqueous medium at physiological pH. Furthermore, experimental and theoretical studies suggested the formation of both mononuclear and dinuclear Zn^{2+}-probe complexes, while only the mononuclear complex was found in the case of Cd^{2+} [2.69h]. P. Paul and his group have designed a fluorescent compound involving a Re(I)-bipyridine moiety as a fluorogenic unit and amide-incorporated modified calix[4]- arene as recognition moiety. It behaves as a dual chemosensor which selectively enables turn-on fluorescence in the presence of Hg^{2+} and naked eye colorimetric detection of Cu^{2+} among different metal ions [2.69i].

Here, we report two aza-phenol based macrocyclic Schiff base ligands, **H_2L2.1** [**H_2L2.1**=1,11-dimethyl-6,16-dithia- 3,9,13,19-tetraaza-1,11(1,3)-dibenzenacycloicosaphane-2,9,12,19-tetraene-1,11-diol] and **H_2L2.2** [**H_2L2.2**=1,11-dimethyl-6,16-dioxa-3,9,13,19-tetraaza-1,11(1,3)-di- benzenacycloicosaphane-2,9,12,19-tetraene-1,11-diol)] as multi analyte chemosensors which fluorimetrically detects different cations (**H_2L2.1**: Zn^{2+}, Al^{3+}, Cr^{3+} and Fe^{3+} and **H_2L2.2**: Zn^{2+}, Al^{3+} and Cr^{3+}) in 1X PBS solution. The interaction of the metal ions with our chemosensors have been examined by absorption, emission and ^{1}H NMR spectroscopies as well as by elemental and ESI-MS^+ analysis. The binding mode of Zn^{2+} with **H_2L2.1** (complex **2.1**)

has been established by X-ray crystallography. Both the chemosensors exhibit ~6-fold enhancement of emission intensity in the presence of different metal ions. The LOD values of the probes, **H_2L2.1** and **H_2L2.2** toward these cations are found to be $\sim10^{-8}$ and $\sim10^{-7}$ M, respectively. Bioimaging studies of **H_2L2.1** and **H_2L2.2** using *HepG2* cells along with MTT assays were also performed. The use of aza-phenol based macrocyclic chemosensors for multiple-analyte detection is a unique attempt. The judicious choice of donor centres and ligand topologies results in selective coordination of selected metal ions with high binding constants. The study of the spectroscopic properties of such a type of macrocyclic ligands and of their metal complexes may open new avenues for obtaining multianalyte sensors.

Chart 2.1. Literature survey of DFP derivatives in multi analytes sensing.

Sl. No.	Probe	Method of detection	Sensing of metal ion(s)	Sensing media	Excitation / Emission (nm)	Limit of detection (LOD) (M)	Binding constant (M^{-1})	Crystal structure (metal complex)	Biological study	Ref.
1.	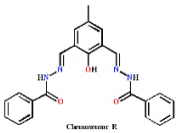	PET	Zn^{2+} Cu^{2+}	CH_3CN/ HEPES buffer (2:8, v/v, pH 7.3)	370/497 370/493	0.252×10^{-9} 0.272×10^{-9}	2.68×10^{5} 1.87×10^{6}	Yes	Cell imaging	**2.48**
2.	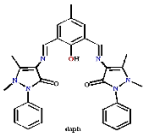	CHEF	Al^{3+} Zn^{2+}	HEPES buffer (EtOH: H_2O, 1/4, v/v, pH 7.4)	385/520 385/490	4.6×10^{-8} 5.7×10^{-7}	$(3 \pm 0.1) \times10^{5}$ $(4.9 \pm 0.2) \times10^{4}$	Yes	Cell imaging	**2.49**
3.	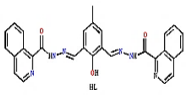	ICT	Zn^{2+} Mg^{2+}	DMF–water (v/v, 9: 1, PBS buffer, pH 7.4) CH_3CN	460/536 350/560	3.07×10^{-7} 2.97×10^{-8}	5.00×10^{4} 6.56×10^{4}	No	Cell imaging	**2.50**

4.	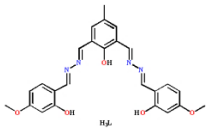	CHEF	Zn^{2+} Cd^{2+} I^-	DMSO/ water (9:1, v/v) THF (HEPES buffer, pH 7.2)	482/545 482/560 530/630	2.7×10^{-9} 6.6×10^{-9} 5×10^{-9}	2.7×10^{4} 9.6×10^{3} 5.2×10^{3}	No	No	**2.51**
5.	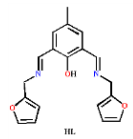	CHEF	Zn^{2+} Cu^{2+}	HEPES buffer, pH 7.4	450/475 450/500	3.67×10^{-9} 2.29×10^{-9}	6.72×10^{5} 1.43×10^{6}	Yes	Cell imaging	**2.52**
6.	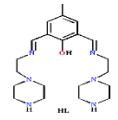	PET	Zn^{2+} Cu^{2+}	HEPES buffer, pH 7.4	440/480 440/510	3.53×10^{-9} 1.05×10^{-9}	7.14×10^{4} 2.18×10^{5}	No	Cell imaging	**2.53**
7.	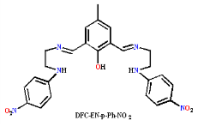	CHEF	Al^{3+} PPi	CH_3OH/ H_2O (8:2, v/v, HEPES, pH 7.2)	370/486 370/534	7.55×10^{-6} 3.34×10^{-6}	$(5.29\pm 1.11)\times10^{4}$ $(1.34 \pm0.81)\times 10^{3}$	No	Cell imaging	**2.54**
8.	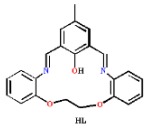	ESIPT	Zn^{2+} Al^{3+}	DMSO/H_2 O (v/v, 3/2, HEPES, pH 7.4)	372/505 372/580	2.1×10^{-9} 1.2×10^{-9}	3.0×10^{3} 2.5×10^{3}	No	Cell imaging	**2.55**
9.	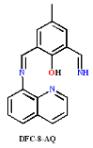	CHEF	Mg^{2+} Zn^{2+}	CH_3CN/H $_2$O (9:1, v/v, HEPES, pH 7.2)	430/526 430/539	2.04×10^{-9} 5.81×10^{-9}	$(1.52 \pm 0.21)\times10^{5}$ $(9.34 \pm 4.0) \times 10^{3}$	No	Cell imaging	**2.56**
10.	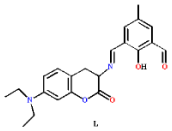	ESIPT	Mg^{2+} Zn^{2+}	CH_3OH containing 1% DMF	450/550 450/558	3.1×10^{-9} 0.92×10^{-9}	2.39×10^{4} 2.11×10^{4}	No	Cell imaging	**2.57**
11.	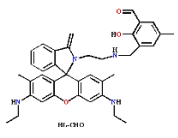	CHEF	Al^{3+} Cr^{3+} Fe^{3+}	HEPES buffer (H_2O/CH_3 OH, 1: 9, v/v, pH 7.4)	500/550	6.97×10^{-9} 15.8×10^{-9} 14.0×10^{-9}	1.47×10^{5} 6.24×10^{4} 8.74×10^{4}	No	Cell imaging	**2.58**

12	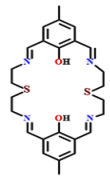 (H_2L 2.1)	CHEF	Zn^{2+} Al^{3+} Cr^{3+} Fe^{3+}	1X PBS buffer medium	435/530 435/530 435/530 435/530	7.99×10^{-8} 9.65×10^{-8} 8.86×10^{-8} 8.43×10^{-8}	1.67×10^{5} 1.82×10^{5} 1.66×10^{5} 1.26×10^{5}	Yes	Cell imaging	This work
13	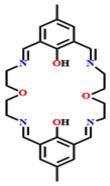 (H_2L2.2)	CHEF	Zn^{2+} Al^{3+} Cr^{3+}	1X PBS buffer medium	435/530 435/530 435/530	3.09×10^{-7} 2.31×10^{-7} 2.06×10^{-7}	1.27×10^{5} 1.59×10^{5} 1.53×10^{5}	No	Cell imaging	This work

Chart 2.2. Literature survey of macrocyclic chemosensors.

Sl. No.	Probe	Method of detection	Sensing of metal ion(s)	Sensing media	Excitation(nm)/ Emission(nm)	Limit of detection (LOD) (M)	Binding constant (M^{-1})	Crystal structure (metal complex)	Biological study	Refs.
1.	 H_2DTC	CHEF	Zn^{2+} and Cu^{2+}	HEPES buffer medium (pH 7.4)	415/475 and 410/-	0.11×10^{-9} 0.27×10^{-9}	logK1=6.032 logK1=6.085	Yes	Cell imaging	**2.60(b)**
2.	 L	PET	Zn^{2+}	water/ethanol (99/1 v/v)	280/365	-	-	No	No	**2.69(a)**
3.	 L	CHEF	Al^{3+}	Ethanol	280/363	3×10^{-9}	1.36×10^{5}	No	No	**2.69(b)**
4.	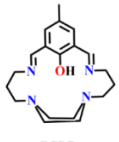 PCDP	CHEF	Zn^{2+} Al^{3+}	CH_3CN/ aqueous HEPES buffer (1 mM, pH 7.4; 1:1 v/v)	330/456	-	-	No	Cell imaging	**2.69(c)**

5.	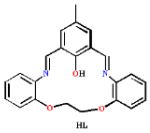	ESIPT	Zn^{2+} Al^{3+}	DMSO/ H_2O (v/v, 3/2, HEPES, pH 7.4)	372/505 372/580	2.1 nM 1.2 µM	3.0×10^3 2.5×10^3	No	Cell imaging	**2.69(d)**
6.	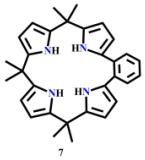	fluorescence ‘‘turn-on’’ process	F^-	HEPES buffer, pH 7.4	280/421	-	K_a =3.27 $\times 10^3$	Yes	No	**2.69(e)**
7.		fluorescence ‘‘on–off’’ process	Fe^{3+} I^-	HEPES buffer	280/360 280/360	6.85 $\times 10^{-8}$M	-	No	No	**2.69(f)**
8.	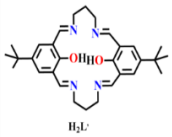	CHEF	Zn^{2+}	50 : 50 water–acetonitrile medium	365/523	-	-	Yes	No	**2.69(g)**
9.	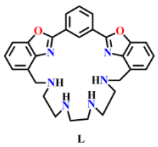	CHEF	Zn^{2+} Cd^{2+}	aqueous medium (acetonitrile–water, 4:1 v/v)	305/385 305/395	3.1×10^{-7} 2.9×10^{-7} mol dm^{-3}	-	No	No	**2.69(h)**
10.	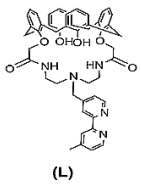	PET	Hg^{2+} Cu^{2+}	Acetonitrile	368/592 368/592	3.5-63.0µm 2.5-776µm	5.02±0.1 4×10^5 2.27±0.2 $\times 10^4$	No	No	**2.69(i)**

2.2. Experimental section

2.2.1. Materials and physical measurements

All reagent or analytical grade chemicals and solvents were purchased from commercial sources and used without further purification. Elemental C, H and N analysis was carried out using a Perkin–Elmer 240C elemental analyzer. Infrared spectra (400–4000 cm^{-1}) were recorded from KBr pellets on a Nicolet Magna IR 750 series-II FTIR spectrophotometer. Absorption spectra were measured with a sensitive UV-vis spectrophotometer (UV-2450 spectrophotometer (Shimadzu, Japan)) equipped with double beam light source with a 1-cm-path-length quartz cell. Electron spray ionization mass ($ESI\text{-}MS^{+}$) spectra were recorded on a MICROMASS Q-TOF spectrometer. Emission spectra were collected using a Fluromax-4 spectrofluorometer at room temperature (298 K) under degassed condition. Fluorescence lifetimes were measured using a time-resolved spectrofluorometer from IBH, UK. Measurements of ^{1}H and ^{13}C NMR spectra were conducted using a BRUKER 300 spectrometers, respectively.

2.2.2. Synthesis of 2,6-diformyl-4-methylphenol (DFP)

2,6-Diformyl-4-methylphenol (DFP) was prepared following a standard literature procedure [2.70].

2.2.3. Synthesis of chemosensor $H_2L2.1$ [$H_2L2.1$=1,11-dimethyl-6,16-dithia-3,9,13,19-tetraaza-1,11(1,3)-dibenzenacycloicosaphane-2,9,12,19-tetraene-1,11-diol]

A mixture of 2,6-diformyl-4-methylphenol (2.0 mmol, 0.3283 g) and 2,2-thiobis(ethylamine) (2.0 mmol, 0.2404 g) was stirred (~30 min.) and then heated to reflux for 4 h in a chloroform-methanol (1:9 v/v) mixture. An orange colored gummy mass was obtained after evaporation of the solvent.

Yield: 0.427g (86%). Anal. Calc. for $C_{26}H_{32}N_4O_2S_2$: C 60.40%; H 6.26%; N 9.99%. Found: C 60.19%; H 6.17%; N 10.02%. IR (cm^{-1}, KBr): υ(C=N) 1634s; ν(O-H) 3363s. ESI-MS^+ in MeOH: The base peak was detected at *m/z* = 497.18, corresponding to [**H_2L2.1**+H]$^+$. UV-Vis, λ_{max} (nm), (ε ($dm^3mol^{-1}cm^{-1}$)) in 1X PBS buffer medium: 435 (6450), 265(5850).

^{1}H NMR (DMSO-d_6, 300 MHz) δ ppm: 2.19 (Ar-CH_3) (s, 6H), 2.87 (-CH_2) (t, 8H, J_1= J_2 = 6 Hz), 3.74 (-CH_2) (t, 8H, J_1 = J_2 = 6 Hz), 7. 35 (Ar-H) (s, 4H), 8.48 (-CH=N) (s, 4H), 13.98(Ar-OH) (s, 2H).

^{13}C NMR (DMSO-d_6, 75 MHz) δ ppm: 20.06, 20.34, 32.38, 33.49, 52.89, 55.61, 119.42,121.08, 124.77, 125.49, 126.62, 132.83, 135.14, 139.93, 161.94,167.10.

2.2.4. Synthesis of chemosensor H_2L2.2 [**H_2L2.2**=1,11-dimethyl-6,16-dioxa-3,9,13,19-tetraaza-1,11(1,3)-dibenzenacycloicosaphane-2,9,12,19-tetraene-1,11-diol]

A mixture of hydrochloride salt of 2,2'-oxybis(ethan-1-amine) (2.0 mmol, 0.354 g) and sodium acetate (6.0 mmol, 0.492 g) was stirred for ~30 min in methanol solvent. A clear solution was found. After that 2,6-diformyl-4-methylphenol (2.0 mmol, 0.328 g) was added to this solution and heated to reflux for 4 h in a chloroform-methanol (1:9 v/v) mixture. Deep yellow colored solid mass was obtained after evaporation of the solvent.

Yield: 0.394g (85%). Anal. Calc. for $C_{26}H_{32}N_4O_4$: C 67.22%; H 6.94%; N 12.06%. Found: C 67.19%; H 6.91%; N 12.02%. IR (cm^{-1}, KBr): υ(C=N) 1637s; ν(O-H) 3392. ESI-MS^+ in MeOH: The base peak was detected at *m/z* = 465.23, corresponding to [**H_2L2.2**+H]$^+$. UV-Vis, λ_{max} (nm), (ε ($dm^3mol^{-1}cm^{-1}$)) in 1X PBS buffer medium: 440 (2975), 348(2350).

^{1}H NMR (DMSO-d_6, 300 MHz) δ ppm: 2.13 (Ar-CH_3) (s, 6H), 3.55(-CH_2) (s, 8H) 3.67 (-CH_2) (t, 8H, J_1 = J_2 = 3 Hz), 7. 21 (Ar-H) (s, 4H), 8.36 (-CH=N) (s, 4H), 13.82(Ar-OH) (s, 2H).

^{13}C NMR (DMSO-d_6, 75 MHz) δ ppm: 20.36, 20.44, 58.89, 59.35, 59.16, 69.89, 121.12, 126.20, 126.47, 132.10, 154.42, 159.48, 160.13, 162.40, 164.00, 170.50.

2.2.5. Synthesis of complex (2.1) {[Zn(H_2L2.1)(NO_3)]NO_3}

A 5 mL methanolic solution of zinc nitrate hexahydrate (1.0 mmol, 0.297 g) was added dropwise to a 20 mL methanolic solution of **H_2L2.1** (1.0 mmol, 0.497 g). The resultant reaction mixture was stirred for ~4 h. Yellow colored block shape crystals were obtained after few days.

Yield: 0.514g (75%). Anal. Calc. for $C_{26}H_{32}N_6O_8S_2Zn$: C 45.52%; H 4.70%; N 12.25%. Found: C 45.44%; H 4.62%; N 12.19%. IR (cm^{-1}, KBr): υ(C=N) 1638s; υ(NO_3^-)1363s; ν(C-H) 769 s. ESI-MS^+ in MeOH: The base peak was detected at *m/z* = 279.96, corresponding to [Zn (**H_2L2.1**)]$^{2+}$. UV-Vis, λ_{max} (nm), (ε ($dm^3mol^{-1}cm^{-1}$)) in 1X PBS buffer medium: 435(3900), 255(11500).

^{1}H NMR (DMSO-d_6, 300 MHz) δ ppm: 2.31 (-CH_3) (s, 6H), 3.01 (s, 2H), 3.07 (s, 2H), 3.71 (s, 2H), 3.93 (-CH_2) (s, 2H), 7.53 (Ar-H) (s, 2H), 7.78 (Ar-H) (s, 2H,), 8.40 (-CH=N) (s, 2H), 8.68 (-CH=N) (s, 2H,).

^{13}C NMR (DMSO-d_6, 300 MHz) δ ppm: 19.63, 19.84, 30.62, 34.50, 55.05, 60.50, 116.55, 121.20, 122.38, 123.78, 125.49, 141.18, 141.82, 147.62, 169.96, 170.94.

2.2.6. Synthesis of complex (2.2) {[Al(H_2L2.1)(NO_3)](NO_3)$_2$}

A 5 mL methanolic solution of aluminium nitrate nonahydrate (1.0 mmol, 0.375 g) was added drop wise to a 20 mL methanolic solution of **H_2L2.1** (1.0 mmol, 0.497 g). The resultant reaction mixture was stirred for ~4h. A greenish-yellow solid mass was obtained after evaporation of the solvent.

Yield: 0.517 g (73%). Anal. Calc. for $C_{26}H_{32}N_7O_{11}S_2Al$: C 44.00%; H 4.55%; N 13.82%. Found: C 43.98%; H 4.50%; N 13.76%. IR (cm^{-1}, KBr): υ(C=N) 1638s; υ(NO_3^-)1339s; ν(C-H) 772 s. ESI-MS^+ in MeOH: The base peak was detected at *m/z* = 174.85, corresponding to $[Al(\mathbf{H_2L2.1})]^{3+}$. UV-Vis, λ_{max} (nm), (ε ($dm^3mol^{-1}cm^{-1}$)) in 1X PBS buffer medium: 435 (5350), 255 (10300).

^{1}H NMR (DMSO-d_6, 300 MHz) δ ppm: 2.26 ppm (-CH_3) (s, 6H), 3.00 (s, 4H), 3.95 (-CH_2) (s, 4H), 7.70 (Ar-H) (d, 2H, *J* = 9 Hz), 7.86 (Ar-H) (s, 2H), 8.61 (-CH=N) (d, 2H, *J* = 12 Hz), 8.76 (-CH=N) (s, 2H).

^{13}C NMR (DMSO-d_6, 300 MHz) δ ppm: 20.00, 20.07, 28.14, 28.64, 30.35, 30.94, 31.72, 32.12, 50.75, 52.00, 117.30, 117.38, 119.44, 123.06, 123.74, 124.73, 125.73, 129.76, 132.87, 137.84,139.89, 146.40, 167.12, 167.17, 168.81, 168.98.

2.2.7. Synthesis of complex (2.3) {$[Cr(H_2L2.1)(NO_3)](NO_3)_2$}

A 5 mL methanolic solution of chromium nitrate nonahydrate (1.0 mmol, 0.400 g) was added drop wise to a 20 mL methanolic solution of **H_2L2.1** (1.0 mmol, 0.497 g).The resultant reaction mixture was stirred for ~4 h. A wine red colored solid mass was obtained after evaporation of the solvent.

Yield: 0.543g (74%). Anal. Calc. for $C_{26}H_{32}N_7O_{11}S_2Cr$: C 42.51%; H 4.39 %; N 13.35%. Found: C 42.49%; H 4.35%; N 13.30%. IR (cm^{-1}, KBr): υ(C=N) 1634s; υ(NO_3^-)1305s; ν(C-H) 818s.UV-Vis, λ_{max} (nm), (ε ($dm^3mol^{-1}cm^{-1}$)) in 1X PBS buffer medium: 435 (5495), 255 (10000).

2.2.8. Synthesis of complex (2.4) {$[Fe(H_2L2.1)(NO_3)](NO_3)_2$}

A 5 mL methanolic solution of iron nitrate nonahydrate (1.0 mmol, 0.404 g) was added drop wise to a 20 mL methanolic solution of **H_2L2.1** (1.0 mmol, 0.497 g). The resultant reaction

mixture was stirred for ~4 h. A dark brown colored solid mass was obtained after evaporation of the solvent.

Yield: 0.568g (77%). Anal. Calc. for $C_{26}H_{32}N_7O_{11}S_2Fe$: C 42.28%; H 4.37 %; N 13.28%. Found: C 42.24%; H 4.32%; N 13.19%. IR (cm^{-1}, KBr): υ(C=N) 1632s; υ(NO_3^-)1332s; ν(C-H) 762s.UV-Vis, λ_{max} (nm), (ε ($dm^3mol^{-1}cm^{-1}$)) in 1X PBS buffer medium: 435 (7000), 260 (12450).

2.2.9. Synthesis of complex (2.5) [Zn(L2.2)]

A 5 mL methanolic solution of zinc nitrate hexahydrate (1.0 mmol, 0.297 g) was added drop wise to a 20 mL methanolic solution of **H_2L2.2** (1.0 mmol, 0.464 g). The resultant reaction mixture was stirred for ~4 h. Yellow colored solid mass was obtained after evaporation of the solvent.

Yield: 0.410g (78%). Anal. Calc. for $C_{26}H_{30}N_4O_4Zn$: C 59.15%; H 5.73%; N 10.61%. Found: C 59.10%; H 5.69%; N 10.58%. IR (cm^{-1}, KBr): υ(C=N) 1661s. ESI-MS^+ in MeOH: The base peak was detected at *m/z* = 527.13, corresponding to $[Zn(\mathbf{L2.2})+H]^+$. UV-Vis, λ_{max} (nm), (ε ($dm^3mol^{-1}cm^{-1}$)) in 1X PBS buffer medium: 435(6850), 348(3900).

^{1}H NMR (DMSO-d_6, 300 MHz) δ ppm: 2.12 (-CH_3) (s, 6H), 3.77 (-CH_2) (t, 8H, J_1 = 6 Hz & J_2 = 3 Hz), 3.84 (s, 8H), 7.42 (Ar-H) (s, 4H), 8.54 (-CH=N) (s, 4H).

^{13}C NMR (DMSO-d_6, 300 MHz) δ ppm: 19.81, 20.10, 46.23, 48.10, 73.10, 73.69, 121.38, 124.09, 126.31, 136.52, 141.09, 141.37, 148.89, 155.79, 165.52, 172.80.

2.2.10. Synthesis of complex (2.6) {[Al(L2.2)](NO$_3$)}

A 5 mL methanolic solution of aluminium nitrate nonahydrate (1.0 mmol, 0.375 g) was added drop wise to a 20 mL methanolic solution of **H_2L2.2** (1.0 mmol, 0.464 g). The resultant

reaction mixture was stirred for ~4h. An orange colored solid mass was obtained after evaporation of the solvent.

Yield: 0.372 g (76%). Anal. Calc. for $C_{26}H_{30}N_5O_7Al$: C 56.62%; H 5.48%; N 12.70%. Found: C 56.58%; H 5.46%; N 12.65%. IR (cm^{-1}, KBr): υ(C=N) 1637s; υ(NO_3^-)1328s. ESI-MS^+ in MeOH: The base peak was detected at *m/z* = 539.50, corresponding to [Al(**L2.2**)(H_2O)(CH_3OH)]$^+$. UV-Vis, λ_{max} (nm), (ε ($dm^3mol^{-1}cm^{-1}$)) in 1X PBS buffer medium: 435 (6900), 348 (3400).

^{1}H NMR (DMSO-d_6, 300 MHz) δ ppm: 2.12 (-CH_3) (s, 6H), 3.60 (t, 8H, $J_1 = J_2$ = 3 Hz), 3.77 (-CH_2) (t, 4H, $J_1 = J_2$ = 3 Hz), 3.88(-CH_2) (s, 4H), 7.37 (Ar-H) (s, 2H), 7.77 (Ar-H) (s, 2H), 8.48 (-CH=N) (d, 4H, J = 9 Hz).

^{13}C NMR (DMSO-d_6, 300 MHz) δ ppm: 19.97, 21.55, 51.50, 55.68, 66.75, 67.07, 116.74, 119.26, 122.09, 125.25, 129.76, 137.90, 146.03, 154.54, 168.71, 172.55.

2.2.11. Synthesis of complex (2.7) {[Cr(L2.2)](NO$_3$)}

A 5 mL methanolic solution of chromium nitrate nonahydrate (1.0 mmol, 0.400 g) was added drop wise to a 20 mL methanolic solution of **H_2L2.2** (1.0 mmol, 0.464 g). The resultant reaction mixture was stirred for ~4 h. A dark green colored solid mass was obtained after evaporation of the solvent.

Yield: 0.416g (81%). Anal. Calc. for $C_{26}H_{30}N_5O_7Cr$: C 54.16%; H 5.24 %; N 12.15%. Found: C 54.13%; H 5.22%; N 12.11%. IR (cm^{-1}, KBr): υ(C=N) 1639s; υ(NO_3^-)1330s. UV-Vis, λ_{max} (nm), (ε ($dm^3mol^{-1}cm^{-1}$)) in 1X PBS buffer medium: 435 (7150), 348 (3400).

2.2.12. UV-visible and fluorescence spectroscopic studies

Stock solutions of the various ions (1×10^{-3}M) were prepared in deionized water. A stock solution of **H_2L2.1** and **H_2L2.2** (1×10^{-3}M) were prepared in MeOH medium. All the spectroscopic experiments including competitive assays of various cations and anions were performed in 1X PBS buffer medium. In titration experiments, a 60 µL solution of (1×10^{-3}M) **H_2L2.1** and **H_2L2.2** were taken for 3000 µL in a quartz optical cell of 1.0 cm optical path length and the corresponding metal stock solutions of the metal ions were gradually added to it, respectively.

2.2.13. X-ray crystallography

Single crystal X-ray data of **2.1** was collected on a Bruker SMART APEX-II CCD diffractometer using graphite monochromated MoKα radiation (λ = 0.71073 Å) at room temperature. Data processing, structure solution, and refinement were performed using the Bruker Apex-II suite program. All available reflections in $2\theta_{max}$ range were harvested and corrected for Lorentz and polarization factors with Bruker SAINT plus [2.71]. Reflections were then corrected for absorption, inter-frame scaling, and other systematic errors with SADABS [2.72]. The structures were solved by direct methods and refined by means of full matrix least-square technique based on F^2 with SHELX-2018/3 software package [2.73]. All the non hydrogen atoms were refined with anisotropic thermal parameters. C-H hydrogen atoms were inserted at geometrical positions with $U_{iso} = 1/2U_{eq}$ to those, they are attached. Crystal data and details of data collection and refinement for complex **2.1** are summarized in **Table 2.1**.

2.2.14. Cell culture

The HepG2 cells and WI38 were obtained from the National Center for Cell Science (NCCS) Pune, India. The cells were grown in DMEM with 10% FBS (Fetal Bovine Serum), penicillin/streptomycin (100 units/ml) at 37 ºC and 5% CO_2. All the treatments were conducted at 37 ºC and at a cell density allowing exponential growth.

2.2.15. Cell imaging

The *HepG2* cells were grown in coverslips for 24 h. Then the cells were either mock-treated or treated with 10µM of ligand **H_2L2.1** and **H_2L2.2**, Zn^{2+} salt (10µM), Al^{3+} salt (10µM**),** Cr^{3+} salt (10µM**)** and Fe^{3+} salt (10µM) for 24 hrs at 37ºC. The cells were washed with 1X PBS. Then they were mounted on a glass slide and observed under fluorescence microscope (Leica) with a filter having excitation of 450-500 nm (blue) and an emission of 500-570 nm (green).

2.2.16. Cell survivability assay

Cell survivability of **H_2L2.1** and **H_2L2.2** were studied for WI-38 (non-cancerous cells), following reported procedure [2.74]. In brief, viability of these cells after exposure to various concentrations of ligand was assessed by MTT assay. The cells were seeded in 96-well plates at 1×10^4 cells per well and exposed to ligand at concentrations of 0 µM, 20 µM, 40 µM, 60 µM, 80 µM, 100 µM for 24 h. The resulting formazan crystals were dissolved in an MTT solubilization buffer and the absorbance was measured at 570 nm by using a spectrophotometer (BioTek) and the value was compared with control cells. The cell cytotoxicity of the complexes towards the WI-38 cell was envisaged following the above mentioned MTT assay protocol.

2.3. Results and discussion

2.3.1. Synthesis and characterization

2,6-Diformyl-4-methylphenol (DFP) has been prepared following a standard procedure [2.59]. 2,2′-Thiobisethylamine or hydrochloride salt of 2,2'-oxybis(ethan-1-amine) was mixed with DFP in 1:1 molar ratio in a chloroform-methanolic (1:9, v/v) solution under reflux (**Scheme 2.1**) to generate the Schiff base ligands **H_2L2.1** and **H_2L2.2** without further purification. **H_2L2.1** and **H_2L2.2** were thoroughly characterized using different spectroscopic methods (UV-Vis, FT-IR, ^{1}H and ^{13}C NMR) and by elemental analysis. In the ESI-MS$^+$ analysis, the base peak was found at *m/z* = 497.18 and 465.23, corresponding to [**H_2L2.1**+H]$^+$ and [**H_2L2.2**+H]$^+$, respectively (**Figs. 2.1** and **2.2**). In the FT-IR spectra of the chemosensors a broad band at around ~3300 cm^{-1} indicates the presence of the phenolic–OH groups and the band at ~1640 cm^{-1} is attributed to the C=N (for azomethine) stretching frequency (**Fig. 2.3**).

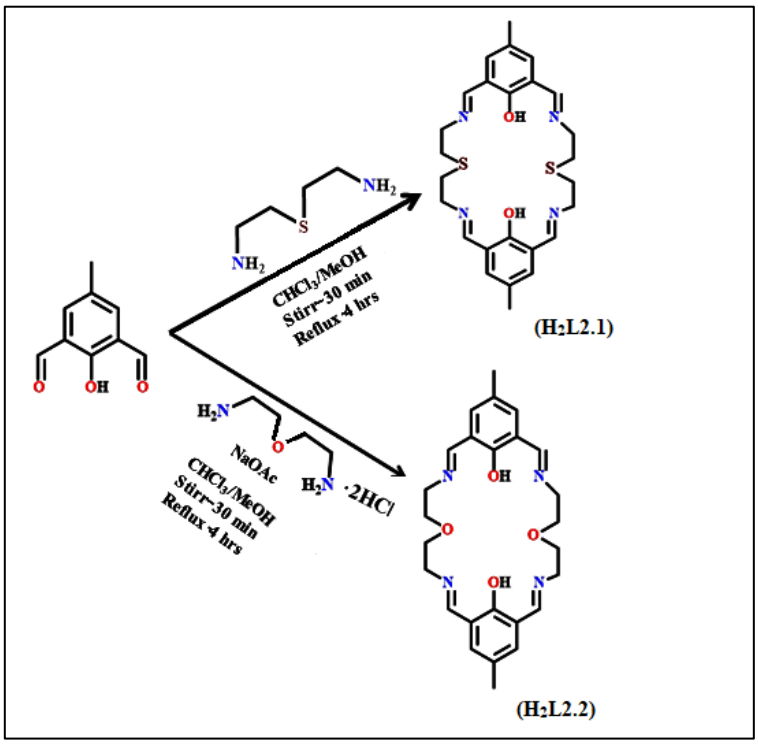

Scheme 2.1. Route to the synthesis of chemosensors **H_2L2.1** and **H_2L2.2**.

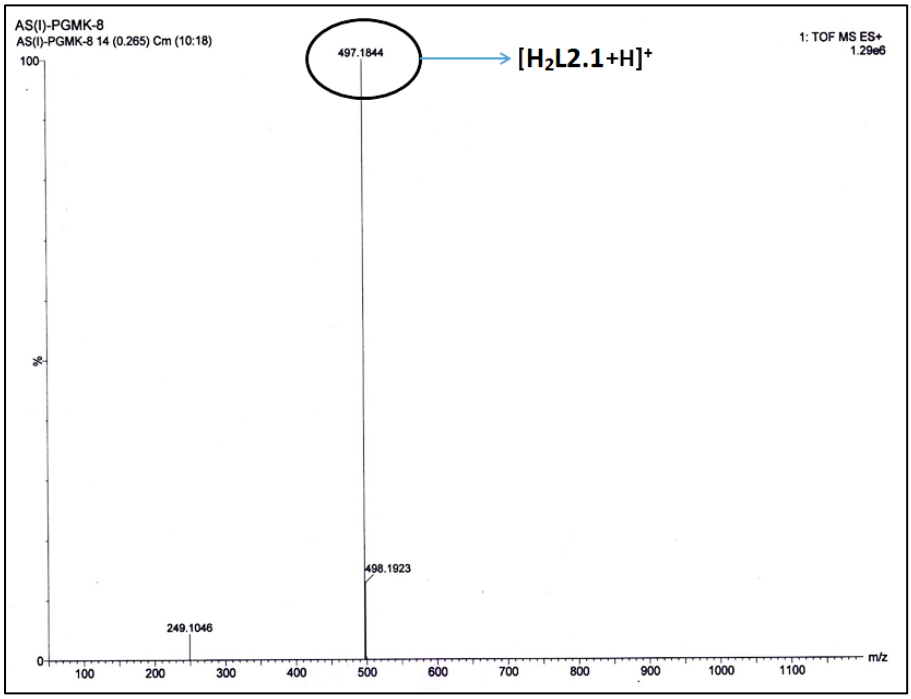

Fig. 2.1. ESI-MS$^+$ spectrum of [**H_2L2.1**+H]$^+$.

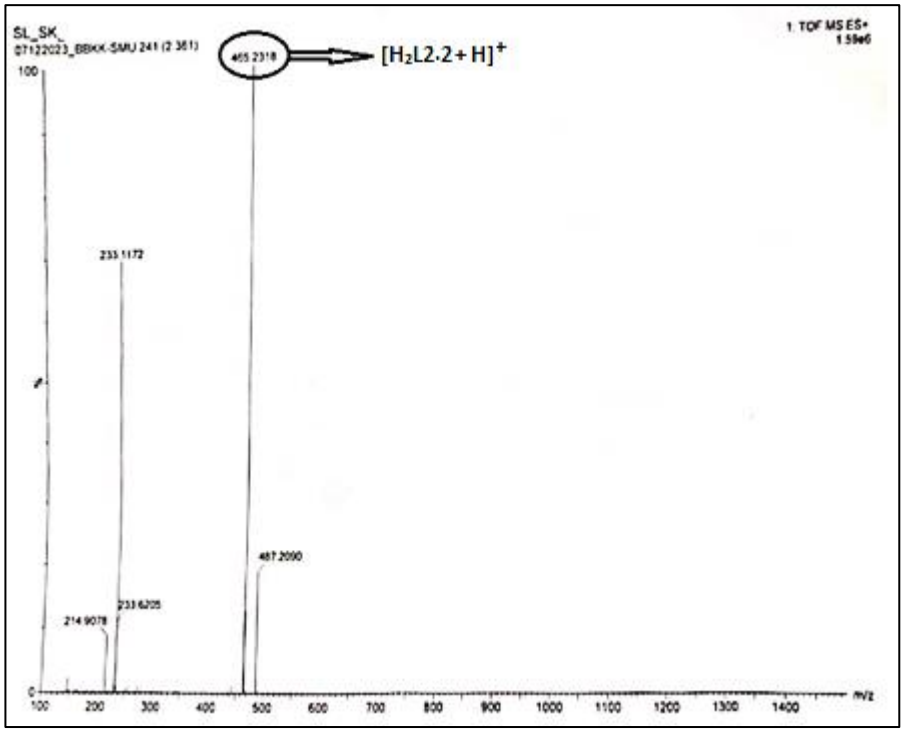

Fig. 2.2. ESI-MS$^+$ spectrum of [**H_2L2.2**+H]$^+$.

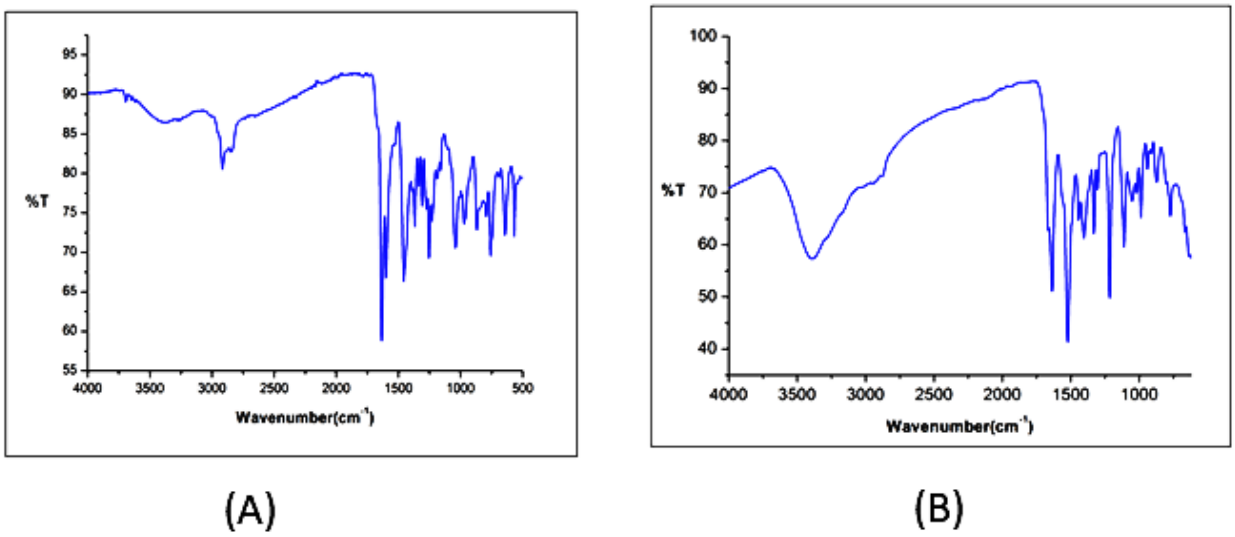

Fig. 2.3. FTIR spectrum of chemosensor (A) **H_2L2.1** & (B) **H_2L2.2**, respectively.

H_2L2.1 and **H_2L2.2** react with respective metal ions (**H_2L2.1**: Zn^{2+}, Al^{3+}, Cr^{3+} and Fe^{3+}; **H_2L2.2**: Zn^{2+}, Al^{3+} and Cr^{3+}) in 1:1 ratio in methanol to produce the complexes **2.1**-**2.7**, respectively (**Scheme 2.2**). Complexes were characterized by different spectroscopic techniques, elemental and ESI-MS^+ analyses. In FT-IR spectra of all seven complexes, **2.1**-**2.7** show characteristic stretching frequencies at ~1640 cm^{-1} υ(C=N), ~770 cm^{-1} υ(C-H) and ~1340 cm^{-1} (υ(NO_3^-, asymmetric stretch) (**Figs. 2.4** and **2.5**). The base peak was detected at *m/z* values of 279.96, 174.85 (molecular ion peak), 527.13 and 539.50 which corresponds to [Zn(**H_2L2.1**)]$^{2+}$ (**Fig. 2.6**), [Al(**H_2L2.1**)]$^{3+}$ (**Fig. 2.7**), [Zn(**L2.2**)+H]+ (**Fig. 2.8**) and [Al(**L2.2**)(H_2O)(CH_3OH)]$^+$ (**Fig. 2.9**), respectively.

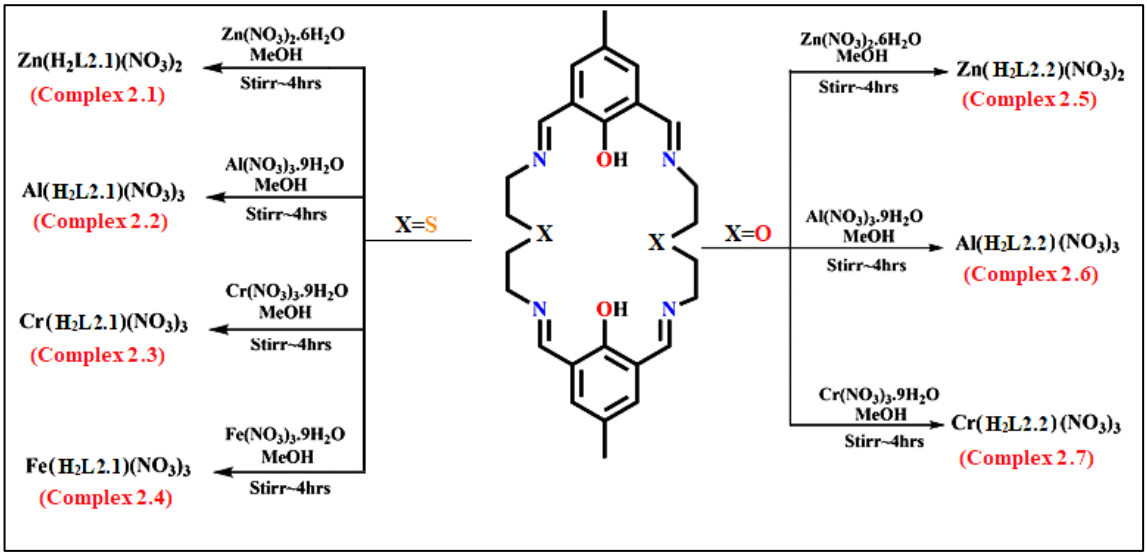

Scheme 2.2. Route to the synthesis of complexes **2.1**-**2.7**.

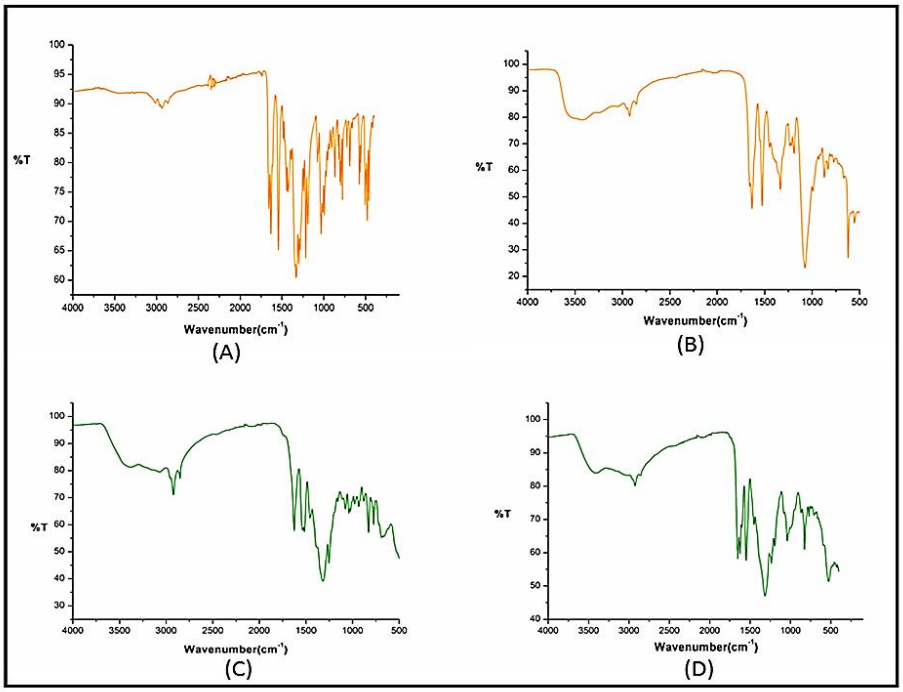

Fig. 2.4. FTIR spectra of (A) complex **2.1** , (B) complex **2.2** , (C) complex **2.3** and (D) complex **2.4**, respectively.

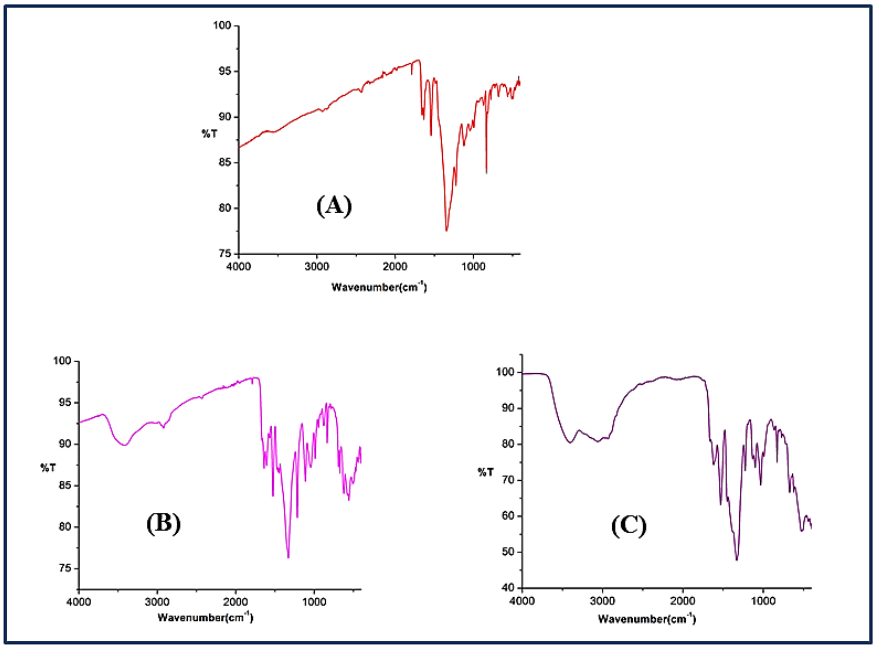

Fig. 2.5. FTIR spectra of (A) complex **2.5** , (B) complex **2.6** and (C) complex **2.7**, respectively.

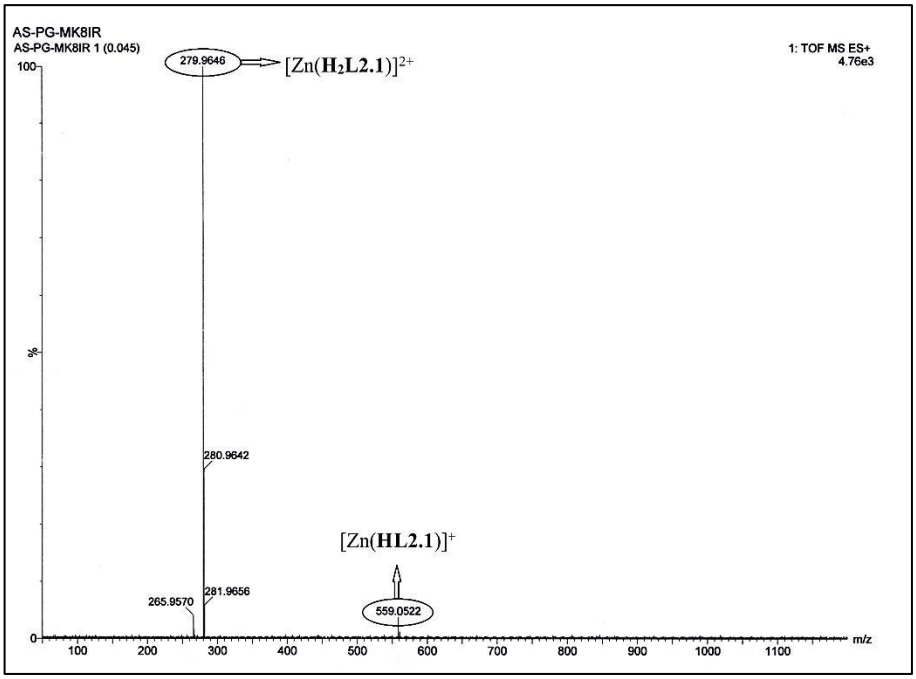

Fig. 2.6. ESI-MS$^+$ spectrum of $[Zn(\mathbf{H_2L2.1})]^{2+}$ and $[Zn(\mathbf{HL2.1})]^+$.

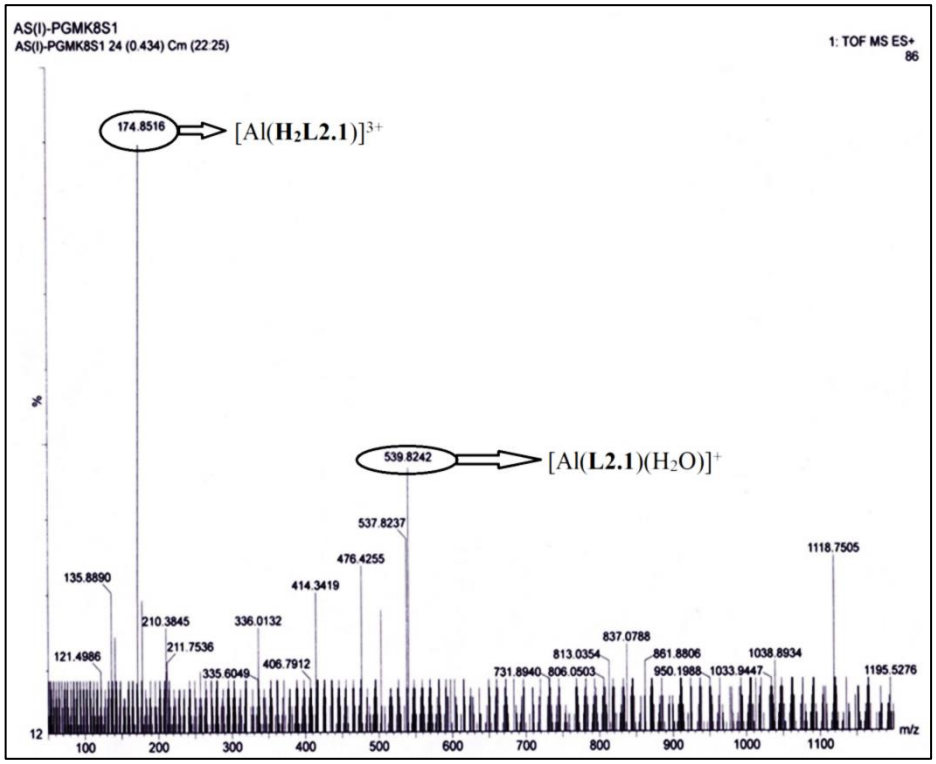

Fig. 2.7. ESI-mass spectrum of $[Al(\mathbf{H_2L2.1})]^{3+}$ and $[Al(\mathbf{L2.1})(H_2O)]^{+}$.

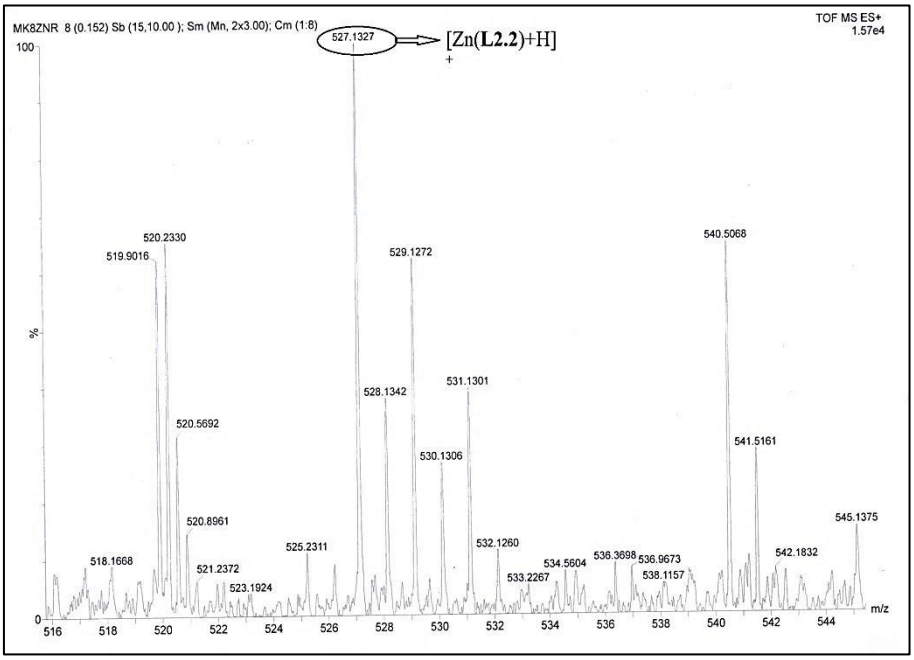

Fig. 2.8. ESI-mass spectrum of $[Zn(\mathbf{L2.2})+H]^{+}$.

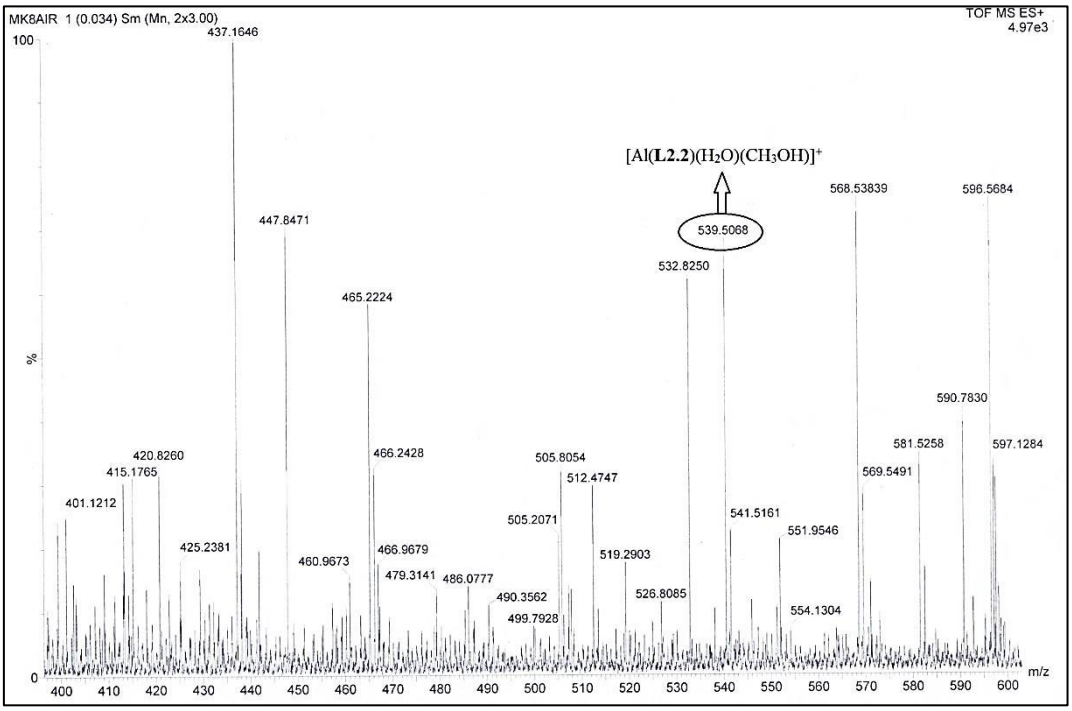

Fig. 2.9. ESI-mass spectrum of $[Al(\mathbf{L2.2})(H_2O)(CH_3OH)]^+$.

2.3.2. Crystal structure description of (2.1) {$[Zn(H_2L2.1)(NO_3)]NO_3$}

We have successfully crystalized $[Zn(\mathbf{H_2L2.1})(NO_3)]NO_3$ (**2.1**) form slow evaporation of a methanolic solution of zinc nitrate hexahydrate and $\mathbf{H_2L2.1}$. Crystals of **2.1** are present in triclinic form with *P*-1 space group (Table 2.1). The crystal structural is shown in Fig. 2.10. Selected bond distances and angles are collected in Table 2.2. The asymmetric unit consists of the whole molecule; the Zn^{2+} bound chemosensor and two nitrate ions, one bound with the metal ion in the first coordination sphere and the other one acting as a counter anion. In **2.1**, the Zn^{2+} centre adopts a distorted octahedral geometry in which the imine nitrogens (N1, N3) are placed in axial positions, while the phenoxido oxygen atoms (O1, O2) and one nitrate anion, coordinated in a bidentate fashion (O6, O7), occupy the equatorial plane. Interestingly, the remaining uncoordinated imine nitrogens (N1, N3) are present in protonated form. Sulphur atoms (S1, S2) also remain uncoordinated. The $Zn–N_{imino}$ and $Zn–O_{phenoxido}$ bond distances are 2.096(4)Å (Zn–N1), 2.094(4)Å (Zn–N3), 2.025(3)Å (Zn–O1) and 2.004(3)Å (Zn–O2),

respectively. The other Zn–O distances are 2.362(4) Å (Zn–O6) and 2.363(4)Å (Zn–O7), respectively. The equatorial angles vary from 54.01(12)° to 112.54(12)°. The axial N1-Zn-N3 angle is 165.64(14)°. Complex **2.1** is further stabilized by different supramolecular interactions including π…π (3.792Å), C-H…π (3.692Å) and chalcogen interaction (3.206Å) to form a one dimensional chain along the '*a*' axis (**Fig. 2.11**).

Importantly, the crystal structure proves the PET-off CHEF-on fluorescence sensing. It also supports the experimentally observed *m/z* value of 279.96, which corresponds to the molecular ion peak of $[Zn(\mathbf{H_2L2.1})]^{2+}$ (**Fig. 2.6**).

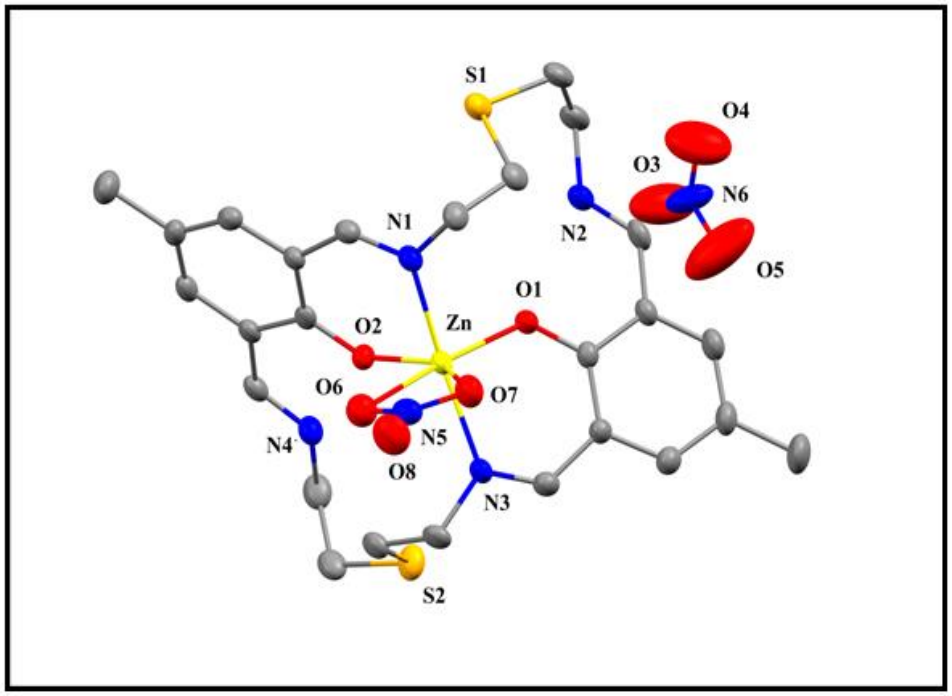

Fig. 2.10. Crystal structure of the asymmetric unit of **2.1**. Atoms are shown as 30% thermal ellipsoids. H atoms are omitted for clarity.

Table 2.1. Crystal parameters and selected refinement details for complex **2.1.**

Complex	**2.1**
Empirical formula	$C_{26}H_{32}N_6O_8S_2Zn$
Formula weight	686.06
Temperature (K)	273(2)
Crystal system	Triclinic
Space group	*P-1*
a (Å)	10.0292(8)
b (Å)	11.0483 (9)
c (Å)	14.5130(12)
α(°)	96.906(2)
β(°)	92.687(2)
γ(°)	104.771(2)
Volume (Å^3)	1538.7(2)
Z	2
D_{calc} (g cm^{-3})	1.481
Absorption coefficient (mm^{-1})	0.991
F(000)	712
θ Range for data collection (°)	1.924-27.150
Reflections collected	52867
Independent reflection / R_{int}	4723/ 0.1058
Data / restraints / parameters	6803/0/398
Goodness-of-fit on F^2	1.088
Final *R* indices [I>2σ(I)]	R1 = 0.0685, wR2 = 0.1219
R indices (all data)	R1 = 0.1109 wR2 = 0.1374
Largest diff. peak / hole (e Å^{-3})	0.777/ -0.504

Table 2.2. Selected bond lengths (Å) and bond angles (°) for complex **2.1**.

Complex **2.1**			
Zn-O1	2.025(3)	O1-Zn-O2	102.74(12)
Zn-O2	2.004(3)	O1-Zn-O7	112.54(12)
Zn-O6	2.362(4)	O2-Zn-O6	90.70(12)
Zn-O7	2.363(4)	O6-Zn-O7	54.01(12)
Zn-N1	2.096(4)	N1-Zn1-N3	165.64(14)
Zn-N3	2.094(4)		

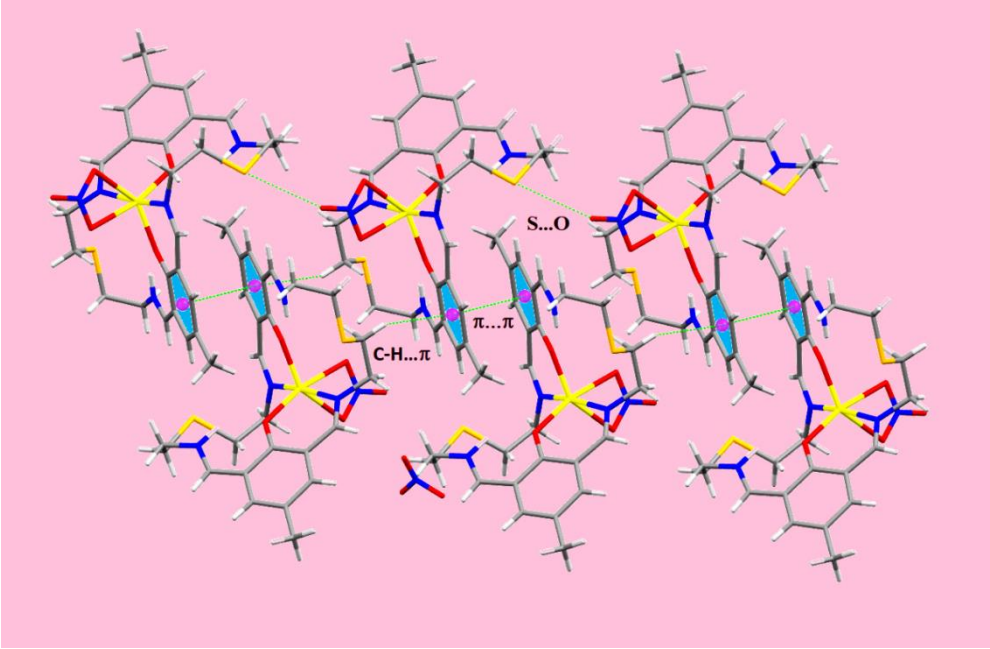

Fig. 2.11. One dimensional chain structure of complex **2.1** with π…π (3.792Å), C-H… π (3.692Å) and chalcogen interaction (3.206Å) along the 'a' axis.

2.3.3. NMR studies

^{1}H and ^{13}C NMR of **H_2L2.1**, **H_2L2.2** and of complexes **2.1**, **2.2**, **2.5** and **2.6** were recorded in DMSO-d_6 solvent. In ^{1}H NMR of **H_2L2.1**, the imine (H-C=N) protons give a peak at 8.48 ppm. The aromatic protons appear at 7.35 ppm, while the aliphatic protons appear at 3.74 ppm and 2.87 ppm, respectively. Methyl protons are found at 2.19 ppm (Fig. 2.12). Aromatic OH protons give a broad signal at 13.98 ppm. In the ^{13}C NMR (Fig. 2.13) the imine carbon atoms appear at 167.10 ppm and 161.94 ppm whereas aromatic carbon atoms appear in the range 139.93-119.42 ppm. Aliphatic carbon atoms appear in the range 55.61-32.38 ppm and methyl carbon atoms appear at 20.34 ppm and 20.06 ppm. Similar type of ^{1}H and ^{13}C NMR spectral pattern were found for **H_2L2.2** also (Figs. 2.14 and 2.15).

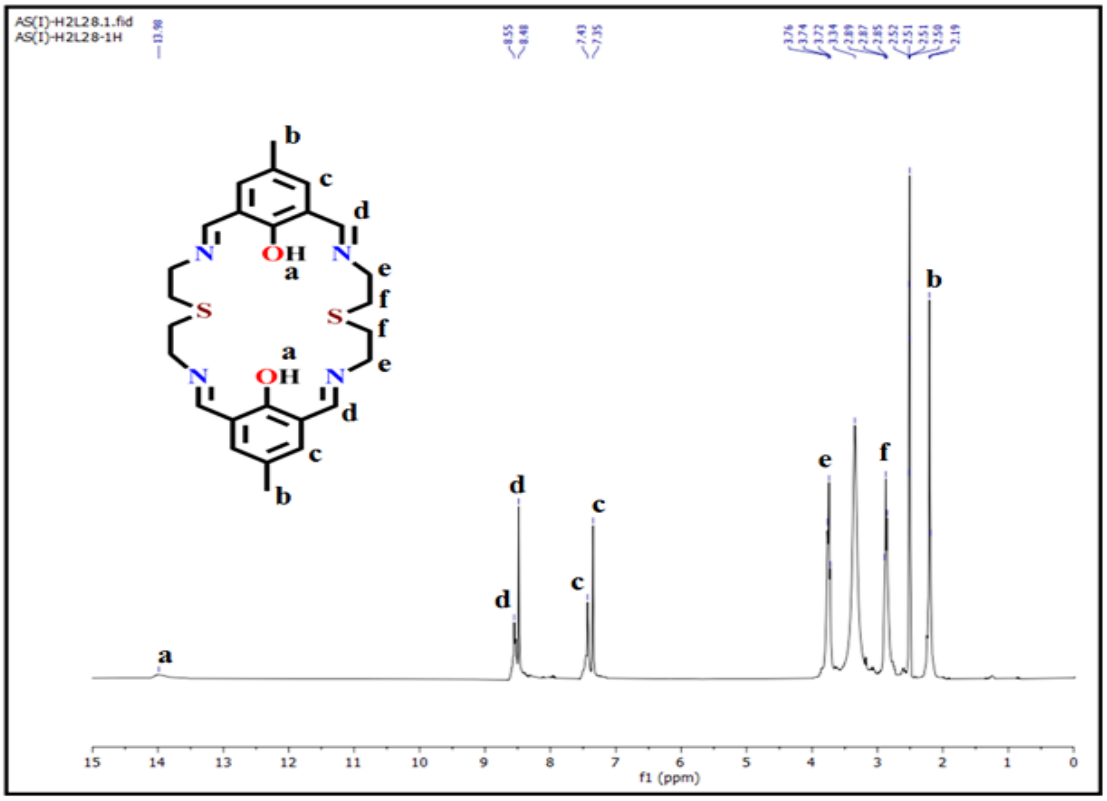

Fig. 2.12. ^{1}H NMR spectrum of **H_2L2.1** in DMSO-d_6 solvent.

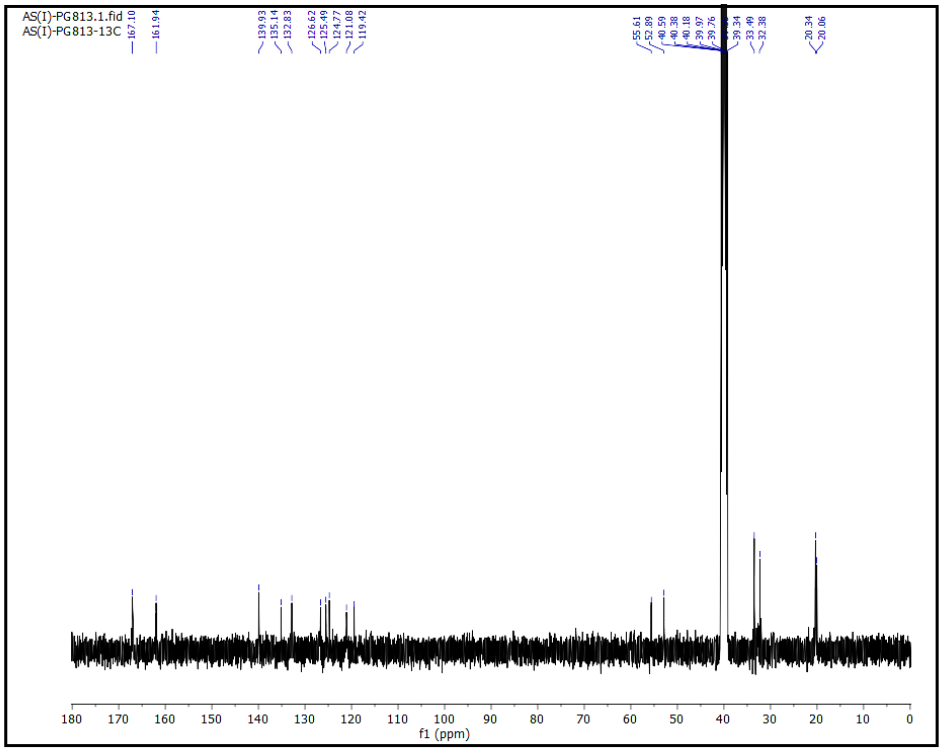

Fig. 2.13. ^{13}C NMR spectrum of **H_2L2.1** in DMSO-d_6 solvent.

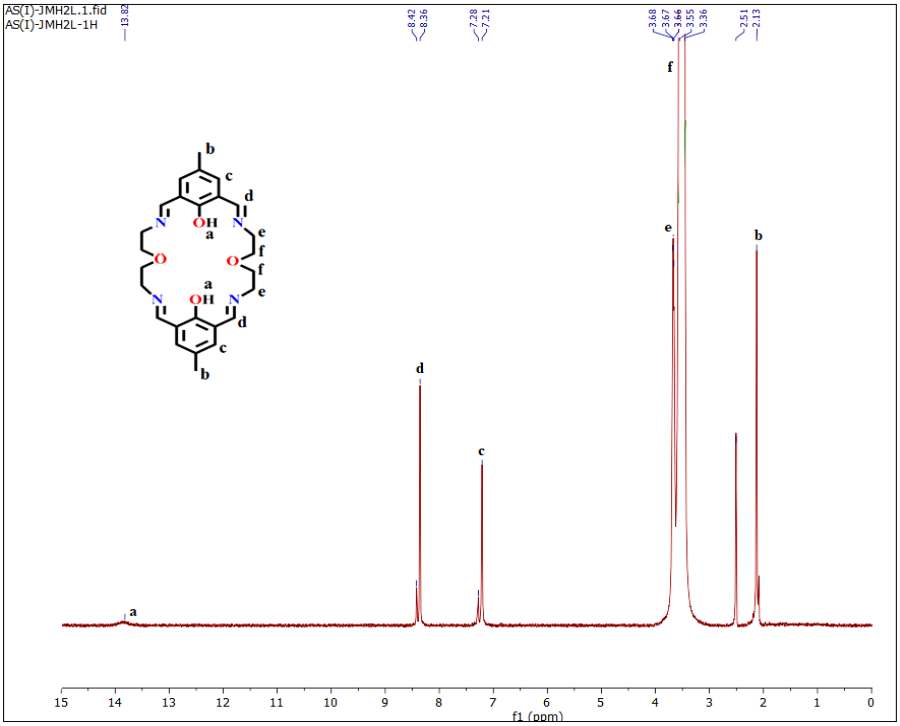

Fig. 2.14. ^{1}H NMR spectrum of **H_2L2.2** in DMSO-d_6 solvent.

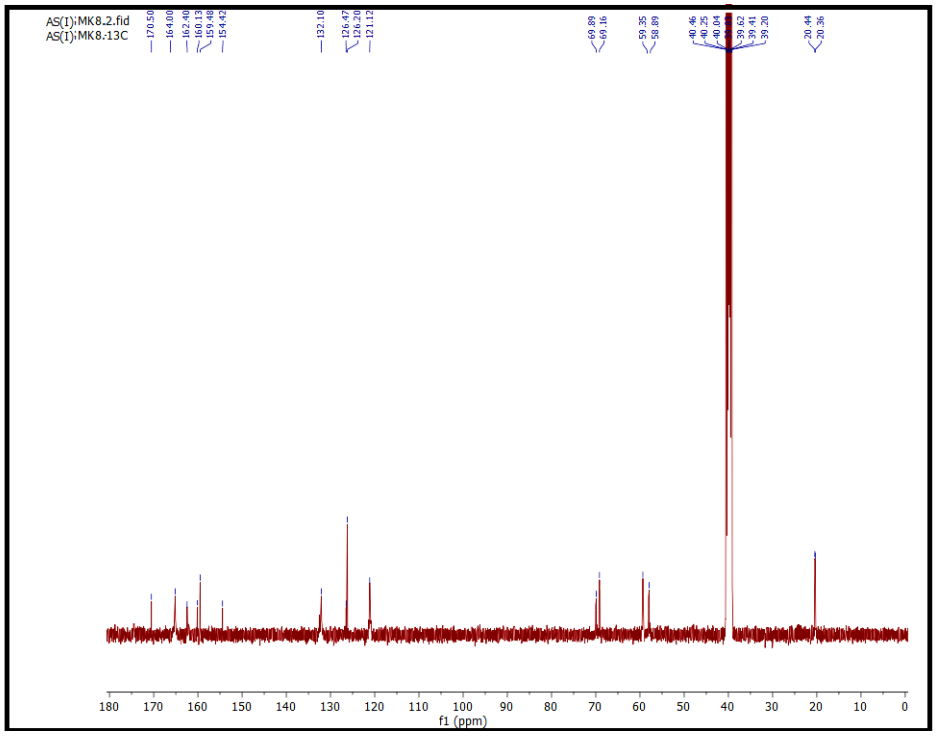

Fig. 2.15. ^{13}C NMR spectrum of **H_2L2.2** in DMSO-d_6 solvent.

Interaction of Zn^{2+} and Al^{3+} with **H_2L2.1** is well explained with the help of NMR spectroscopy. In the ^{1}H NMR of **2.1** (Fig. 2.16) the disappearance of phenolic –OH peaks prove the binding of the phenoxido oxygens to Zn^{2+}. The signal of the imine protons splits into two signals at 8.68 ppm and 8.40 ppm, indicating coordinated and uncoordinated imine nitrogens. Aromatic protons appear downfield at 7.78 ppm and 7.53 ppm. In the ^{13}C NMR spectrum of **2.1** (Fig. 2.17), the signals of the imine carbons appear at 170.94 ppm and 169.96 ppm, while the aromatic carbon atoms appear in the range 147.62-116.55 ppm. Aliphatic carbon atoms are observed in the range 60.50-30.62 ppm.

In the ^{1}H NMR of **2.2** (Fig. 2.18) the disappearances of the phenolic –OH peaks support the binding of the phenoxido oxygens to Al^{3+}. The imine protons appear downfield shifted at 8.76 ppm and 8.61 ppm. Both aromatic and aliphatic protons are also undergoing broadening and appear at 7.86 ppm, 7.70 ppm, 3.95 ppm, and 3.00 ppm, respectively. In the ^{13}C NMR spectrum

of **2.2** (**Fig. 2.19**), imine and aromatic carbons appear in the ranges 168.98-167.12 ppm and 146.40-117.30 ppm, respectively. Aliphatic carbon atoms are shown in the range 52.00-28.14 ppm. ^{1}H and ^{13}C NMR spectral data of complexes **2.5** and **2.6** are collected in experimental section (**Figs. 2.20-2.23**).

We have also performed ^{1}H NMR titration experiments of **H_2L2.1** and **H_2L2.2** with Zn^{2+} or Al^{3+} in DMSO-d_6 solvent (**Figs. 2.24-2.27**). Upon gradual addition of (0 to 1 equivalent) metal ions to one equivalent of chemosensor, disappearance of phenolic -OH protons, significant splitting and downfield shift of imine protons, broadening and splitting of aromatic and aliphatic protons prove strong interaction between chemosensor and corresponding metal ions. The X-ray crystallographic data of complex **2.1** agrees with the ^{1}H NMR titration data.

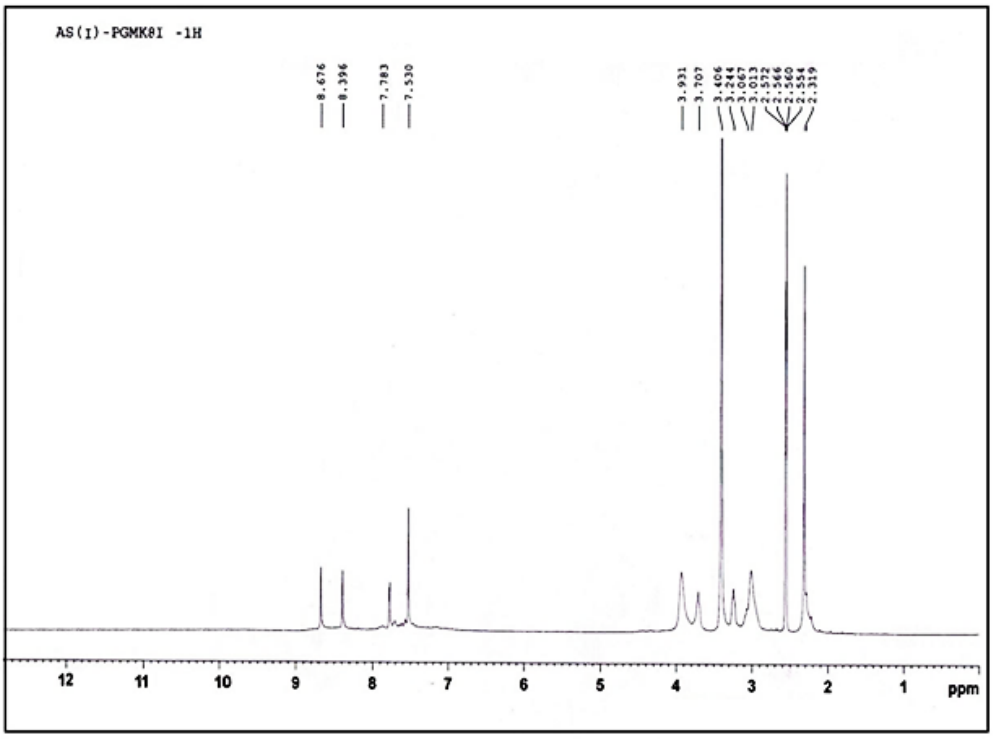

Fig. 2.16. ^{1}H-NMR of complex **2.1** in DMSO-d_6 solvent.

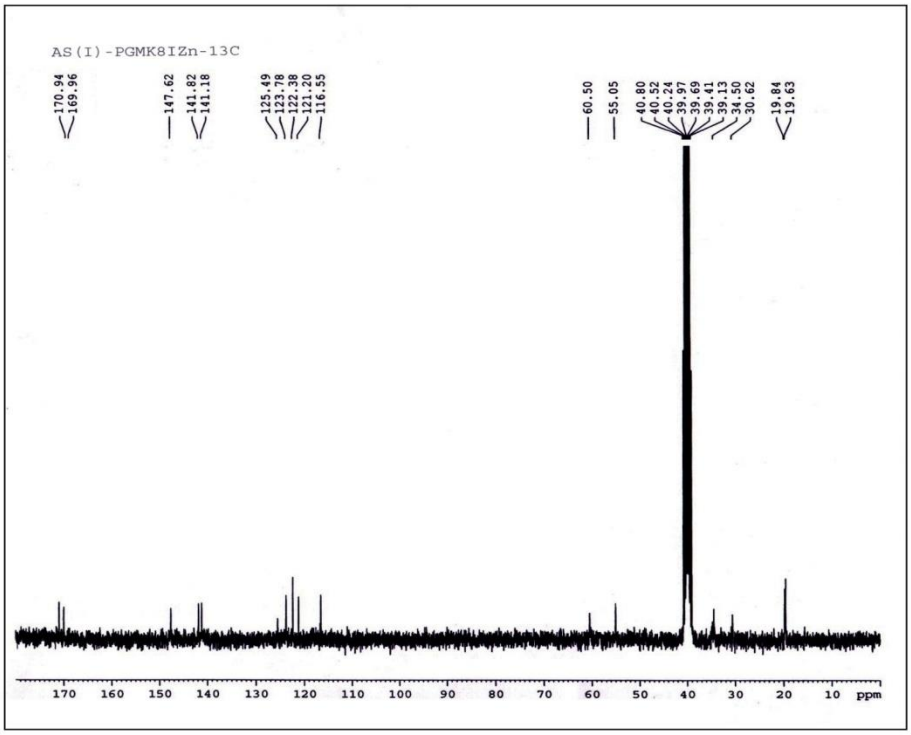

Fig. 2.17. ^{13}C NMR of complex **2.1** in DMSO-d_6 solvent.

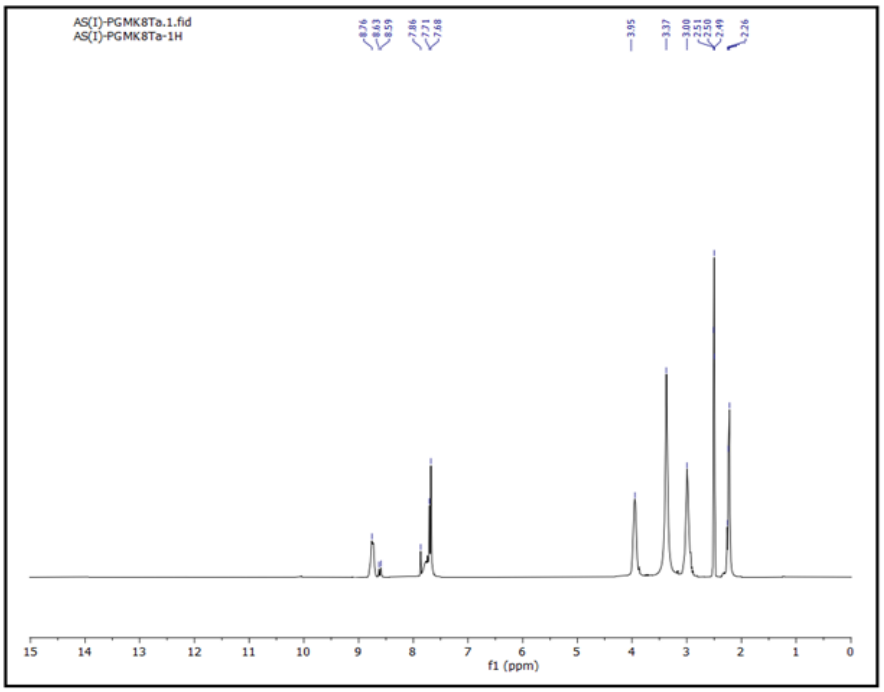

Fig. 2.18. ^{1}H-NMR of complex **2.2** in DMSO-d_6 solvent.

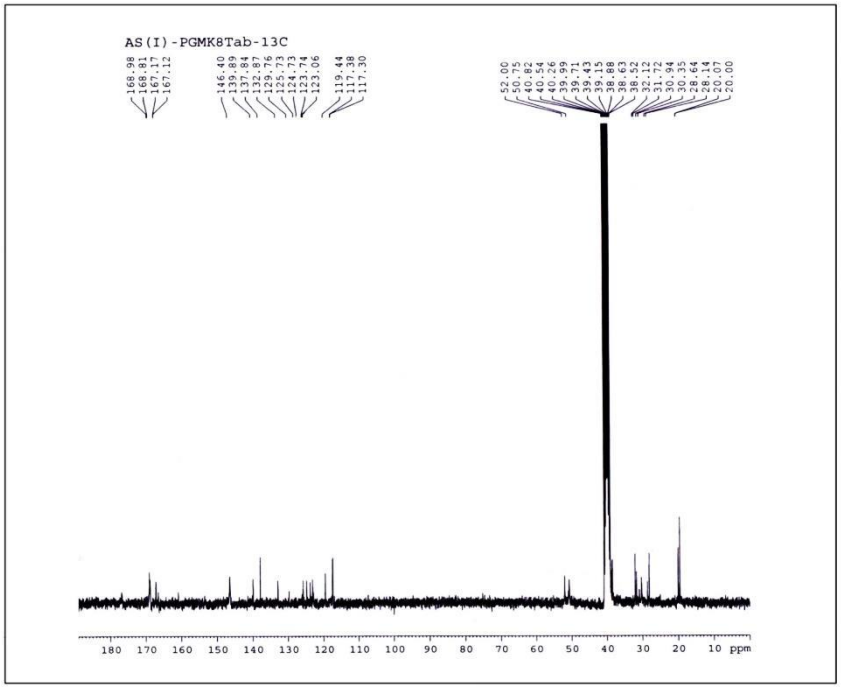

Fig. 2.19. ^{13}C-NMR of complex **2.2** in DMSO-d_6 solvent.

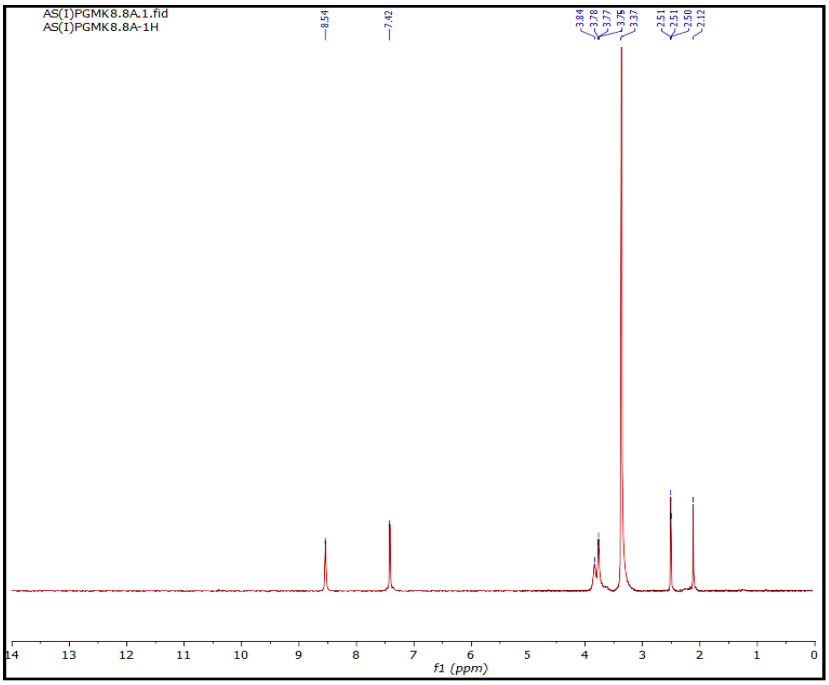

Fig. 2.20. ^{1}H-NMR of complex **2.5** in DMSO-d_6 solvent.

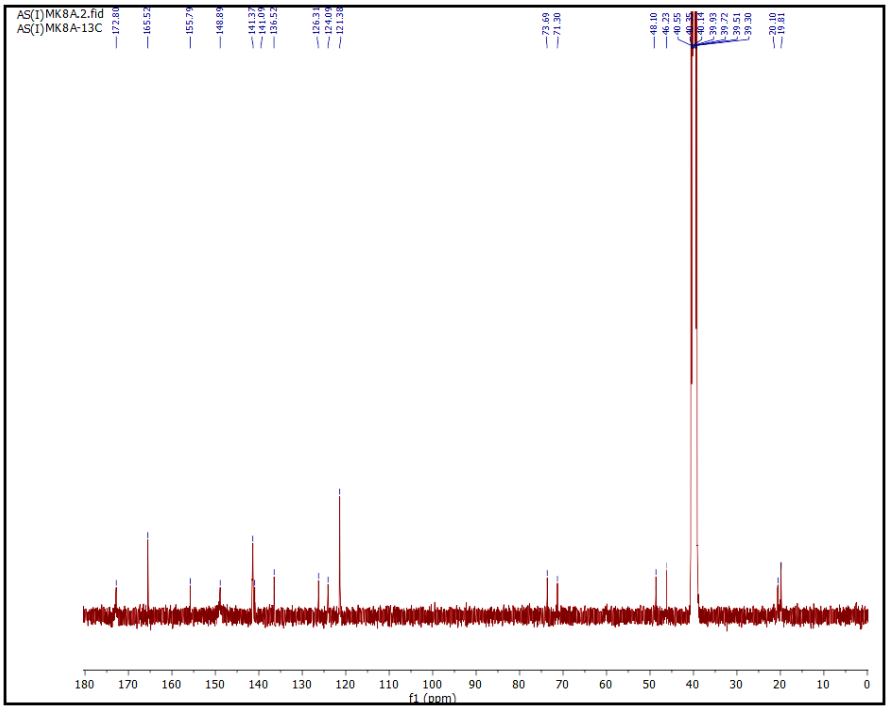

Fig. 2.21. ^{13}C NMR of complex **2.5** in DMSO-d_6 solvent.

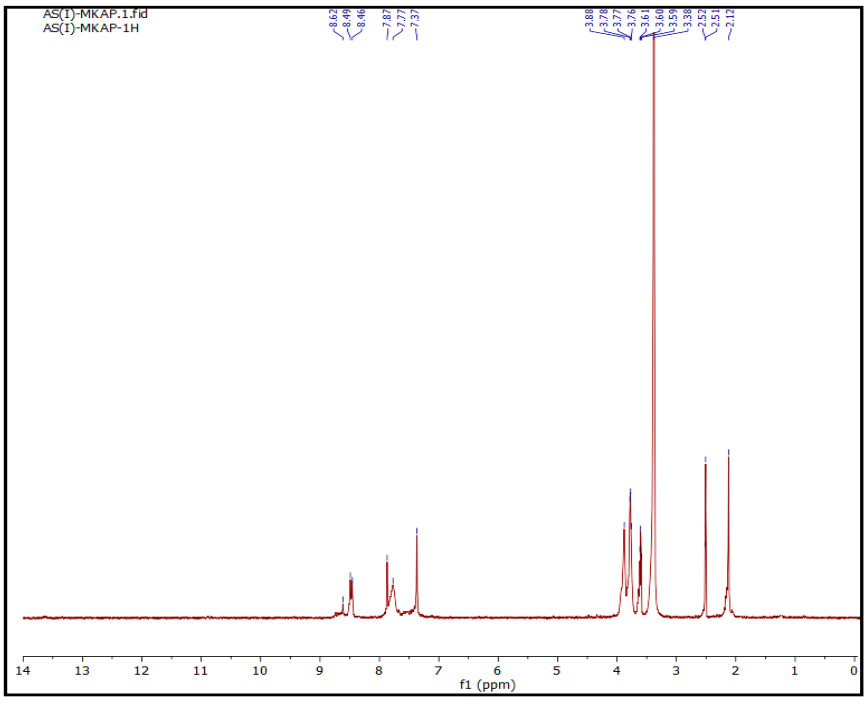

Fig. 2.22. ^{1}H-NMR of complex **2.6** in DMSO-d_6 solvent.

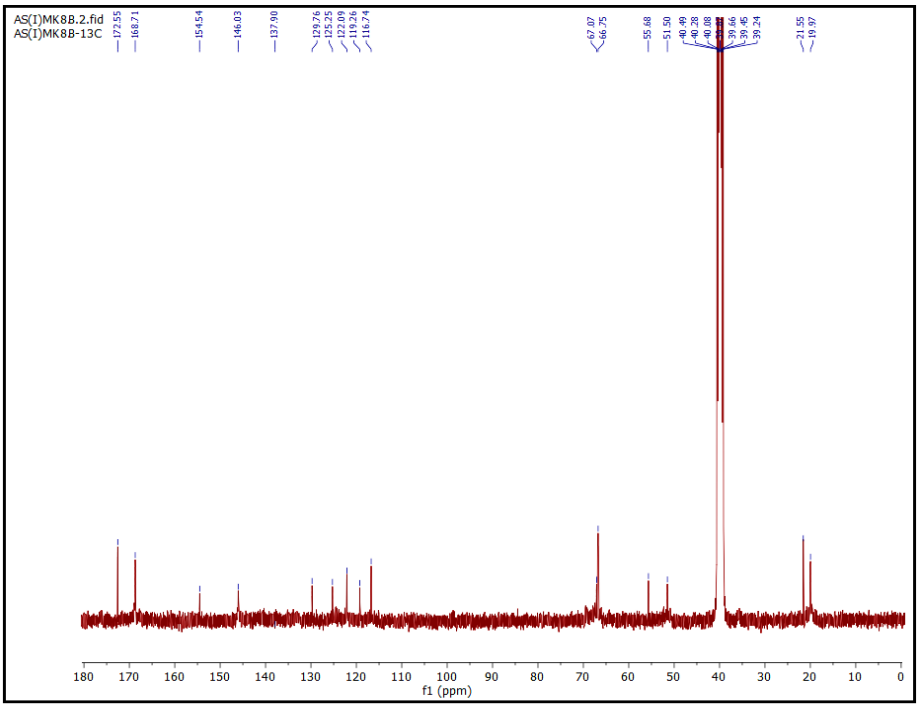

Fig. 2.23. ^{13}C-NMR of complex **2.6** in in DMSO-d_6 solvent.

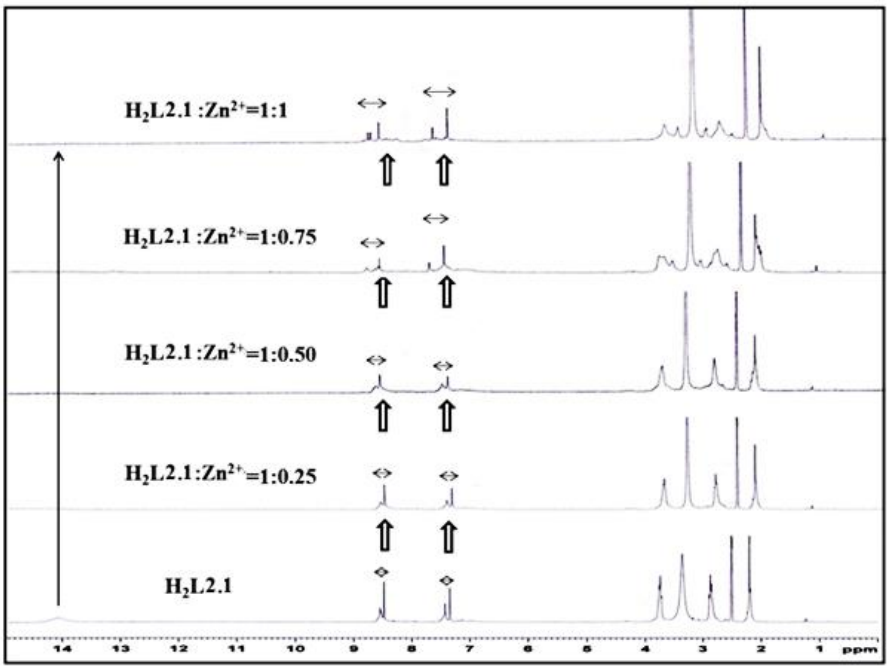

Fig. 2.24. ^{1}H-NMR titration of the free ligand (**H_2L2.1)** and with the addition of 0.25, 0.50, 0.75 and 1 equivalent of Zn^{2+} in DMSO-d_6 solvent.

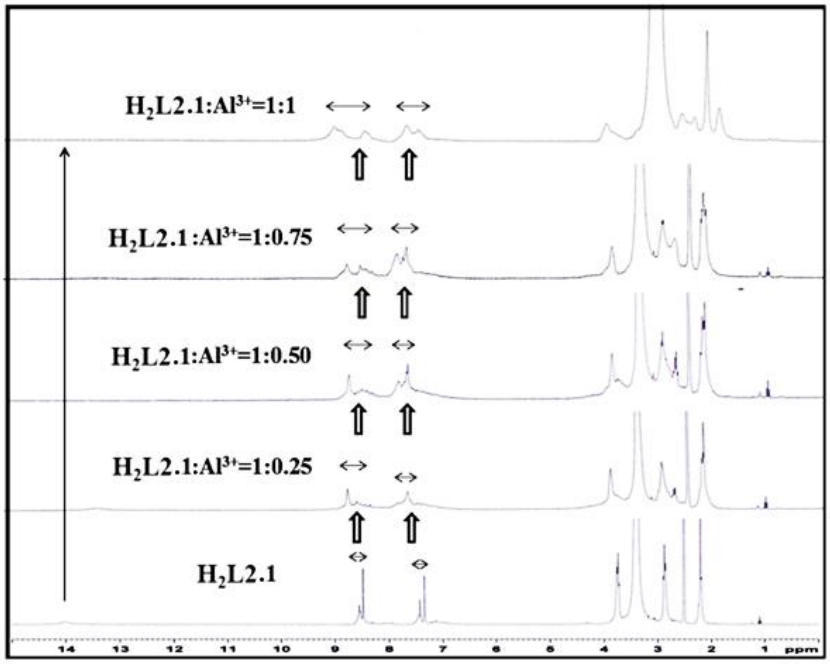

Fig. 2.25. ^{1}H-NMR titration of the free ligand (**H_2L2.1)** and with the addition of 0.25, 0.50, 0.75 and 1 equivalent of Al^{3+} in DMSO-d_6 solvent.

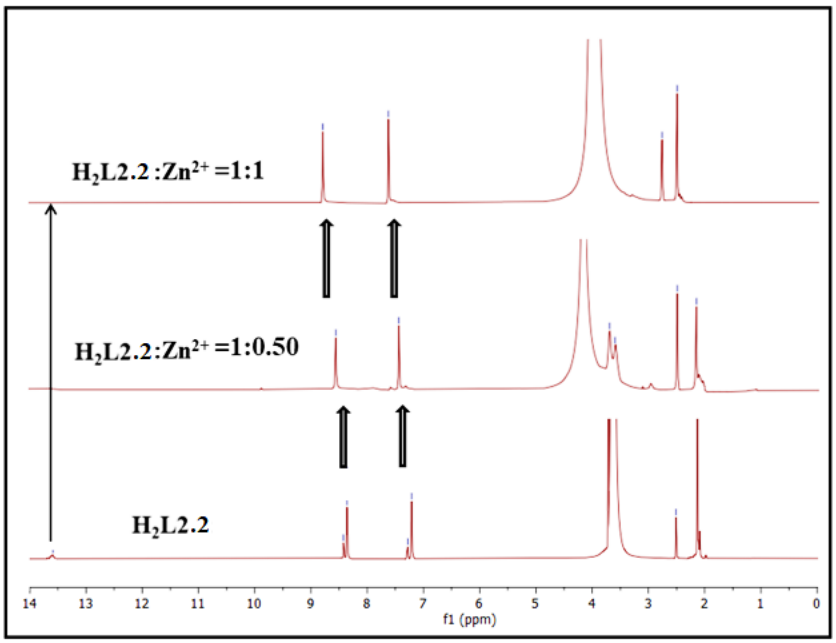

Fig. 2.26. ^{1}H-NMR titration of the free ligand (**H_2L2.2)** and with the addition of 0.50 and 1 equivalent of Zn^{2+} in DMSO-d_6 solvent.

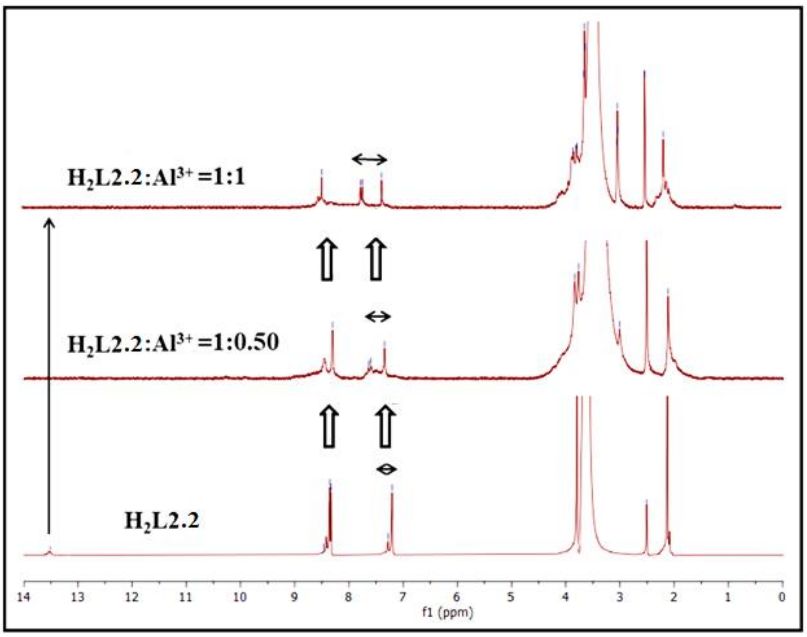

Fig. 2.27. ^{1}H-NMR titration of the free ligand (**H_2L2.2)** and with the addition of, 0.50 and 1 equivalent of Al^{3+} in DMSO-d_6 solvent.

2.3.4. Absorption spectral studies

The UV-Vis absorption spectrum of both **H_2L2.1** and **H_2L2.2** were studied in 1X PBS buffer (pH 7.4) medium. The same buffer medium was chosen for both spectroscopic studies and biological work in order to avoid experimental errors. Characteristic bands around 435 nm and 265 nm suggest n→π* and π →π* type of transitions within the probes. The gradual addition of a Zn^{2+} (0-20 µM) solution to a 20 µM **H_2L2.1** solution results in a decrease in the intensity of the peak at 435 nm and a concomitant increase in absorbance at around 265 nm (**Fig. 2.28**). Both the signals at 435 nm and at 265 nm do not further change after the addition of one equivalent of Zn^{2+}, suggesting 1:1 binding stoichiometry. A similar situation was observed for the trivalent cations, Al^{3+}, Cr^{3+} and Fe^{3+} (**Fig. 2.28**). In case of chemosensor **H_2L2.2**, upon gradual addition of metal ion (Zn^{2+}, Al^{3+} and Cr^{3+} ; 0-20µM) result enhancement of intensity at 440 nm (**Fig. 2.29**).

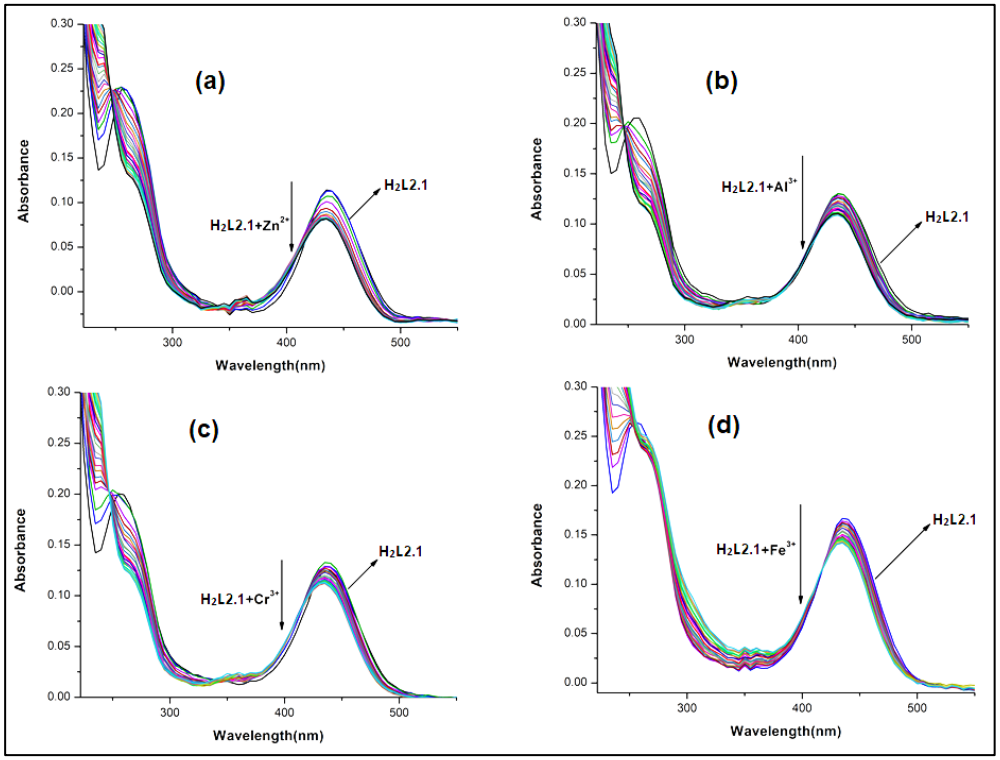

Fig. 2.28. Absorbance titration of **H_2L2.1** (20 µM) with gradual addition of (a) Zn^{2+} (0-20µM); (b) Al^{3+}(0-20µM); (c) Cr^{3+}(0-20µM) and (d) Fe^{3+}(0-20µM) in 1X PBS buffer medium.

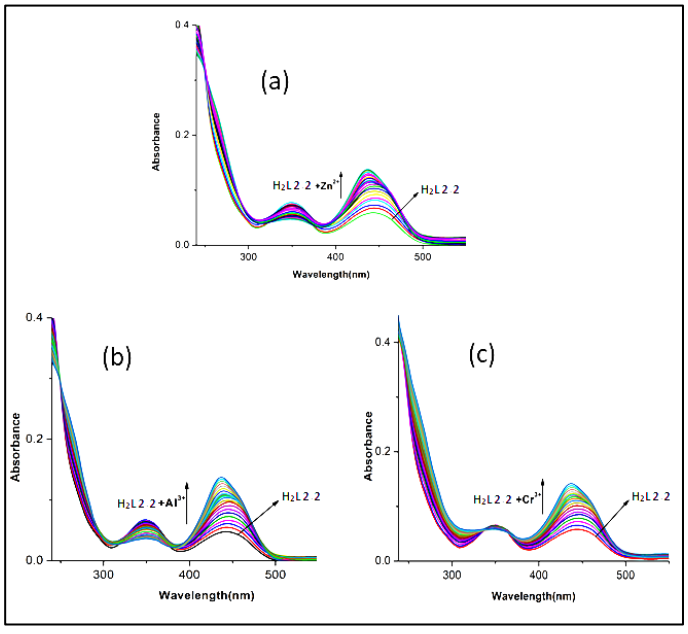

Fig. 2.29. Absorbance titration of **H_2L2.2** (20 µM) with gradual addition of (a) Zn^{2+} (0-20µM); (b) Al^{3+}(0-20µM) and (c) Cr^{3+}(0-20µM) in 1X PBS buffer medium.

2.3.5. Fluorescence properties

The fluorescence spectra were recorded in 1X PBS buffer medium at ambient conditions. Upon excitation at 435 nm, **H_2L2.1** exhibits weak fluorescence at 505 nm, probably due to a PET (Photo Induced Electron Transfer) process. Photoinduced intramolecular electron transfer (PET) from the HOMO of the donor imine nitrogen atoms to the excited fluorophoric moiety results excited state quenching. Addition of Zn^{2+} (0-22 µM, excitation wavelength 435 nm) to a 20 µM solution of **H_2L2.1** produces a gradual increase of the emission intensity and a red shift of the peak at 530 nm (**Fig. 2.30**), which reaches 6-fold enhancement and a plateau for a ~1:1 [Zn^{2+}]/ [**H_2L2.1**] molar ratio (**Fig. 2.30**). The 1:1 binding stoichiometry has been confirmed by Job's plot analysis (**Fig. 2.31**). Coordination of Zn^{2+} to **H_2L2.1**, increases the rigidity of the molecule via restriction of free rotation of **H_2L2.1** around the H–C=N bond. Moreover the PET process could not continue further due to donation of the lone pair of electrons by the imine nitrogen. Both these effects are jointly responsible for the fluorescence enhancement (CHEF effect). The apparent binding constant for the 1:1 Zn^{2+}/**H_2L2.1** complex was calculated using the Benesi− Hildebrand equation:[2.75a]

$$\{(F_{max} - F_0)/(F_x - F_0)\} = \{1 + (1/K)\,(1/[Zn^{2+}])\}$$

Where, K represents the metal to chemosensor binding constant. F_{max}, F_0, and F_x are fluorescence intensities in the presence of maximum [Zn^{2+}] (1 equiv. for 1:1 Zn^{2+}: **H_2L2.1**), free ligand [**H_2L2.1**] (1 equiv.) and any intermediate Zn^{2+} concentration (0–1.0 equiv.), respectively. The binding constant (K) was estimated to be ~1.67 × 10^5 M^{-1} (**Fig. 2.32, Table 2.3**). The stability constant calculated with the program HypSpec ((1.22 ± 0.01) × 10^5 M^{-1}) which permits the use of multiple wavelengths to make the fitting, is in good agreement with the value obtained [2.75b,c].

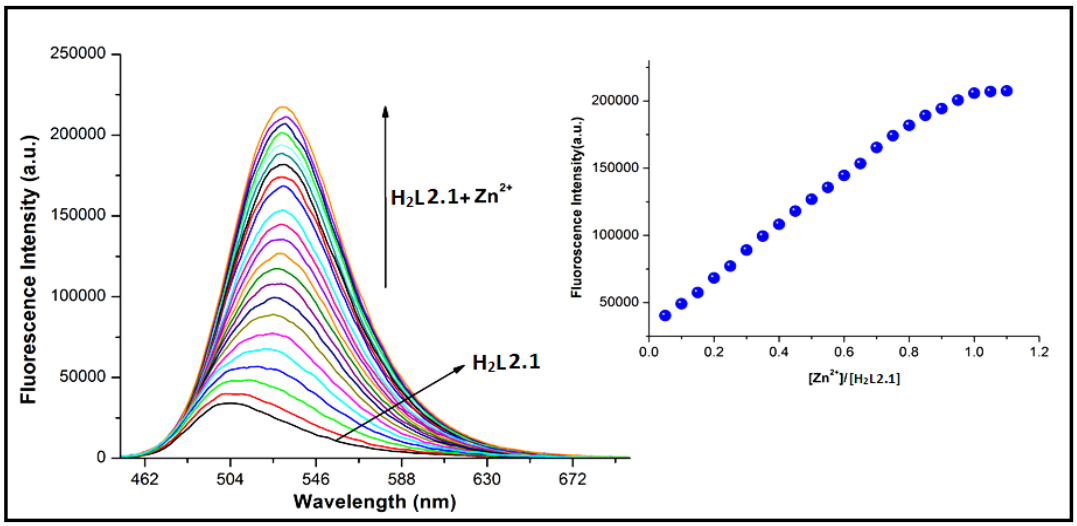

Fig. 2.30. Fluorescence titration of **H_2L2.1** (20μM) with gradual addition of Zn^{2+} (0-22μM) in 1X PBS buffer medium and corresponding fluorescence intensity versus molar ratio plot ($\lambda_{ex.}$= 435 nm).

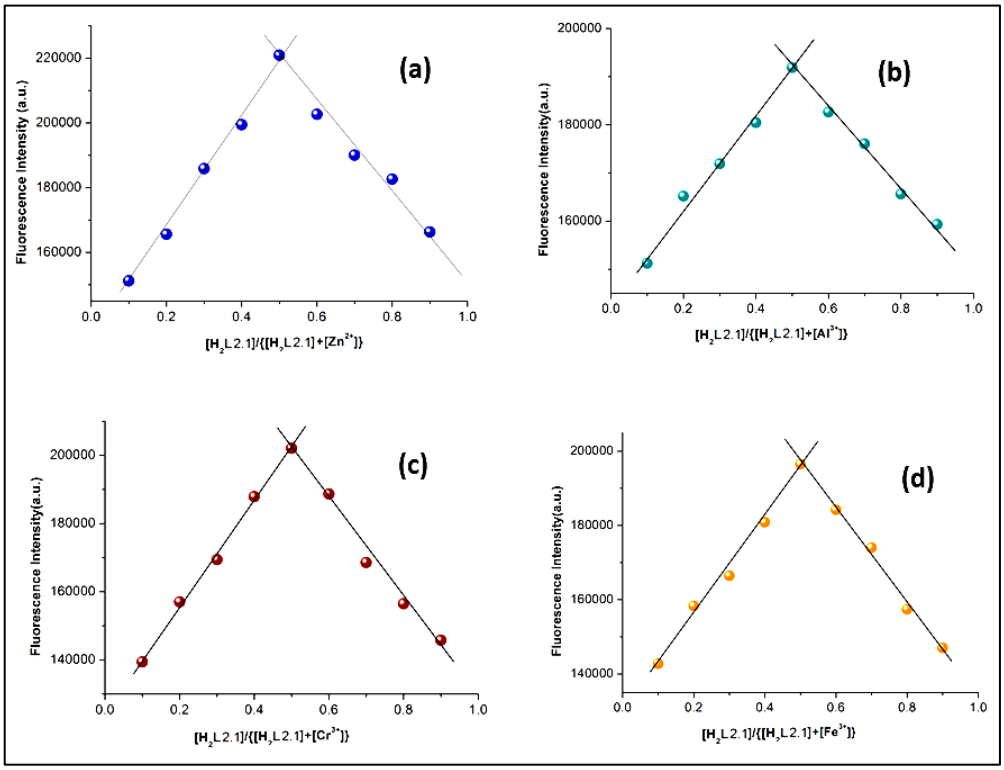

Fig. 2.31. 1:1 binding stoichiometry has shown by Job's plot for (a) complex **2.1**, (b) complex **2.2**, (c) complex **2.3** and (d) complex **2.4**. Symbols and solid lines represent the experimental and simulated profiles, respectively.

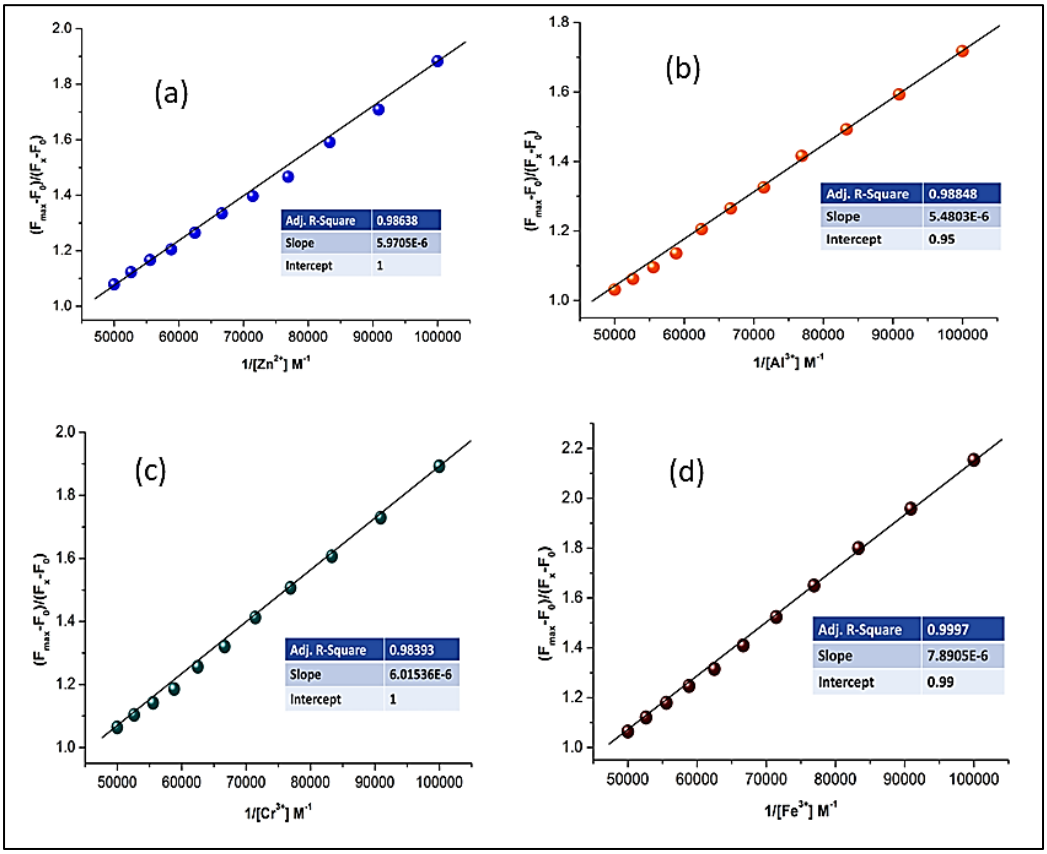

Fig. 2.32. Benesi-Hildebrand plot for (a) [**H_2L2.1**-Zn^{2+}], (b) [**H_2L2.1**-Al^{3+}], (c) [**H_2L2.1**-Cr^{3+}] and (d) [**H_2L2.1**-Fe^{3+}] systems. The linear plot is obtained after adding 1 equivalent Zn^{2+}, Al^{3+}, Cr^{3+} and Fe^{3+} ions to the probe in 1X PBS buffer medium, respectively.

Table 2.3. Apparent binding constant (K) values of complexes **2.1**-**2.7** from spectrofluorometric measurement.

	K (M^{-1})
Complex **2.1**	1.67×10^5
Complex **2.2**	1.82×10^5
Complex **2.3**	1.66×10^5
Complex **2.4**	1.26×10^5
Complex **2.5**	1.27×10^5
Complex **2.6**	1.59×10^5
Complex **2.7**	1.53×10^5

Similarly, addition of the trivalent metal ions Al^{3+}, Cr^{3+} and Fe^{3+} leads to a red-shift of the **H_2L2.1** band at 505 nm that now appears at 530 nm and to remarkable ca. 6-fold enhancement of the emission (**Figs. 2.33-2.35**). A plateau of the emission is reached in all cases for 1:1 [M^{3+}]:[**H_2L2.1**] molar ratio. The 1:1 M^{3+}: **H_2L2.1** binding stoichiometry of these trivalent metal ions towards the chemo sensing probe **H_2L2.1** was further confirmed by Job's plot analysis (**Fig. 2.31**). The selective response towards Zn^{2+}, Al^{3+}, Cr^{3+} and Fe^{3+} can be ascribed based on the Pearson principle which allows them to better fit into the macrocyclic coordination framework and coordinate with imine nitrogens and phenoxido oxygens. Again, paramagnetic metal ions like Cr^{3+} or Fe^{3+} are well known fluorescence quencher [2.76a,b]. Here, electron or energy transfer between the metal ions and fluorophores cause very fast and efficient non-radiative decay of the excited states resulting quenching of the fluorescence. Example of fluorescence enhancement in presence of paramagnetic centers via chelation enhanced fluorescence (CHEF) mechanism is uncommon. Design of chemosensor with suitable multi dentate chelating units, which can effectively coordinate to the metal centre resulting CHEF effect depends on the selection of ionophore [2.76c,d,e]. Turn-on fluorescent sensors for Cr^{3+} or Fe^{3+} ions are less reported due to the lack of selective ionophores [2.76f-h]. In presence of chemosensor **H_2L2.1** and **H_2L2.2**, Cr^{3+} (both **H_2L2.1** and **H_2L2.2**) and Fe^{3+} (only **H_2L2.1**) form stable complexes with the nitrogens and oxygens resulting enhancement of the rigidity of the complex. The 6-fold fluorescence enhancement at 530 nm is a result of chelation-enhanced fluorescence (CHEF) [2.76i]. Further, **H_2L2.1** and **H_2L2.2** are Schiff base ligands where C=N bond undergoes isomerization in the excited state resulting weak fluorescence. Coordination of metal ions with imine nitrogen inhibits C=N isomerization and decreased non-radiative decay of the excited-state, leading to fluorescence enhancement. In the present work, we observed an obvious enhancement of fluorescence intensity in the presence of Zn^{2+} and Al^{3+} as well as

paramagnetic metal ions Cr^{3+} and Fe^{3+}. Therefore, there is a competition between the fluorescence enhancement due to the inhibition of C=N isomerization and quenching of fluorescence from the metal ion-induced electron or energy transfer processes. Our results shows that the C=N isomerization plays a predominant role [2.76j-l].

Interestingly, other metal ions fail to exhibit fluorescence enhancement probably due to several reasons such as the suitable coordination geometry, conformation of the Schiff base sensor, the appropriate ion radius and sufficient binding energy of the Zn^{2+}, Al^{3+}, Cr^{3+} and Fe^{3+}, leading to selective recognition of Zn^{2+}, Al^{3+}, Cr^{3+} and Fe^{3+}. The apparent binding constants for trivalent metal bound chemosensor **H_2L2.1** complexes were calculated using the Benesi−Hildebrand equation [2.75a]. The apparent binding constant (K) values for Al^{3+}, Cr^{3+} and Fe^{3+} were estimated to be 1.82×10^5 M^{-1}, 1.66×10^5 M^{-1} and $1.26 \times 10^5 M^{-1}$, respectively (**Fig. 2.32, Table 2.3**). The limit of detection (LOD) is an important parameter of a chemosensor **H_2L2.1** for real sample analysis. LOD of the chemosensor towards Zn^{2+}, Al^{3+}, Cr^{3+} and Fe^{3+} were calculated using the 3σ method [2.77]. The LODs for the Zn^{2+}, Al^{3+}, Cr^{3+} and Fe^{3+} are 7.99×10^{-8} M, 9.65×10^{-8} M, 8.86×10^{-8} M and 8.43×10^{-8} M, respectively, indicating that these metal ions could be detected quantitatively.

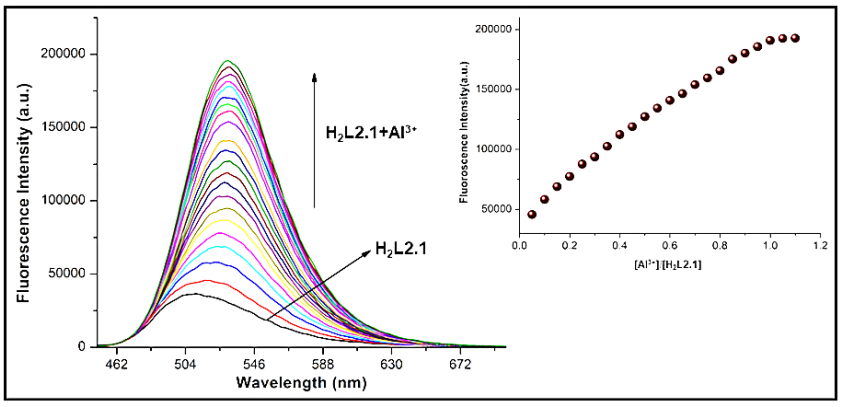

Fig. 2.33. Fluorescence titration of **H_2L2.1** (20 µM) with gradual addition of Al^{3+} (0-22µM) ion in 1X PBS buffer medium and corresponding fluorescence intensities versus molar ratio plot.

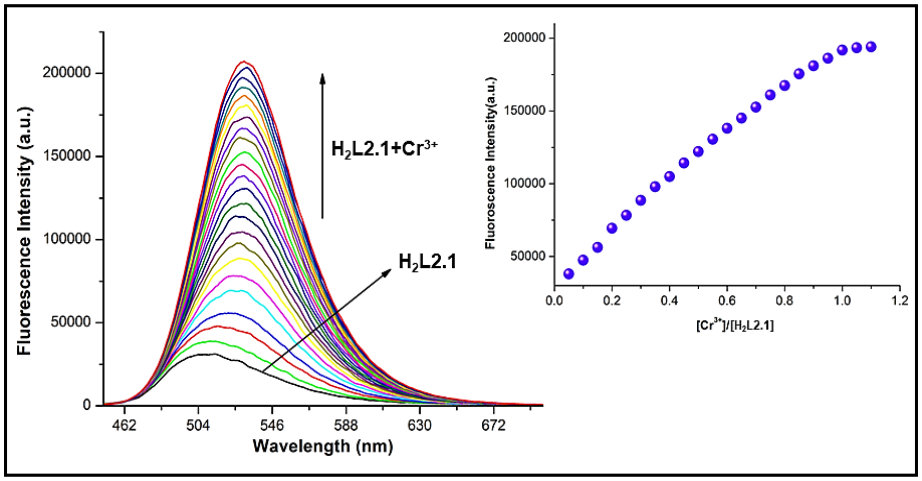

Fig. 2.34. Fluorescence titration of **H_2L2.1** (20 µM) with gradual addition of Cr^{3+} (0-22µM) in 1X PBS buffer medium and corresponding fluorescence intensities versus molar ratio plot.

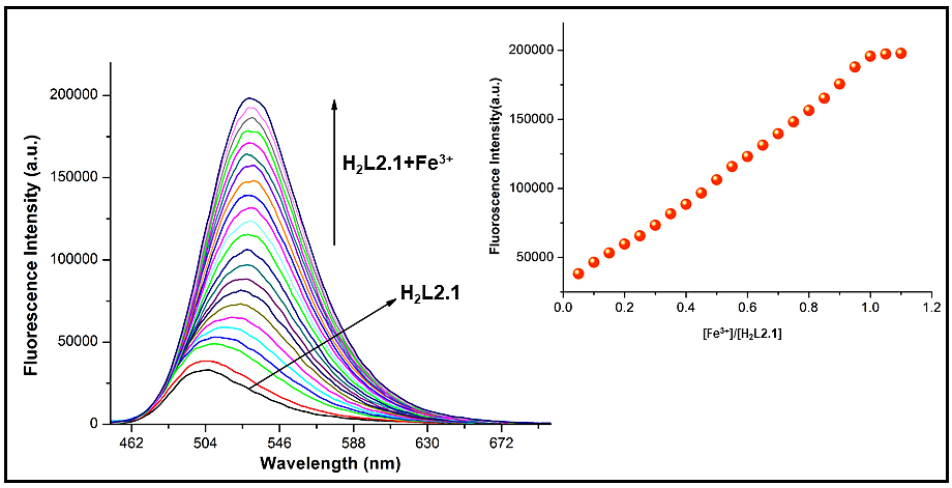

Fig. 2.35. Fluorescence titration of **H_2L2.1** (20 µM) with gradual addition of Fe^{3+} (0-22µM) in 1X PBS buffer medium and corresponding fluorescence intensities versus molar ratio plot.

Interestingly, chemosensor **H_2L2.2** exhibits similar type of fluorescence properties towards Zn^{2+}, Al^{3+} and Cr^{3+} ions. Free chemosensor exhibits weak fluorescence at 540 nm upon excitation at 440 nm. Addition of different metal ions (Zn^{2+}, Al^{3+} and Cr^{3+}) results 6-fold

enhancement of fluorescence intensity at 530 nm (**Figs. 2.36-2.38**). The 1:1 M^{2+}/ M^{3+}: **H_2L2.2** binding stoichiometry was also confirmed by Job's plot analysis (**Fig. 2.39**). The apparent binding constant (K) values and LOD values towards Zn^{2+}, Al^{3+} and Cr^{3+} were estimated to be 1.27×10^5 M^{-1}, 1.59×10^5 M^{-1} and 1.53×10^5 M^{-1}, respectively and 10^{-7} M range (**Fig. 2.40, Table 2.3**).

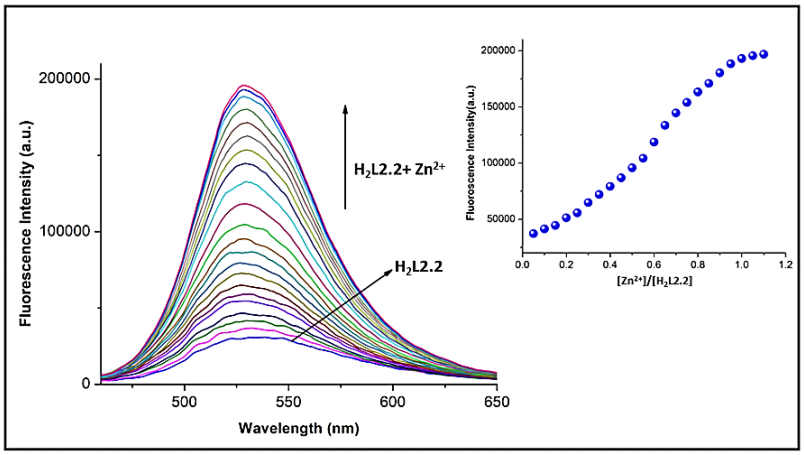

Fig. 2.36. Fluorescence titration of **H_2L2.2** (20 µM) with gradual addition of Zn^{2+} (0-22µM) ion in 1X PBS buffer medium and corresponding fluorescence intensities versus molar ratio plot.

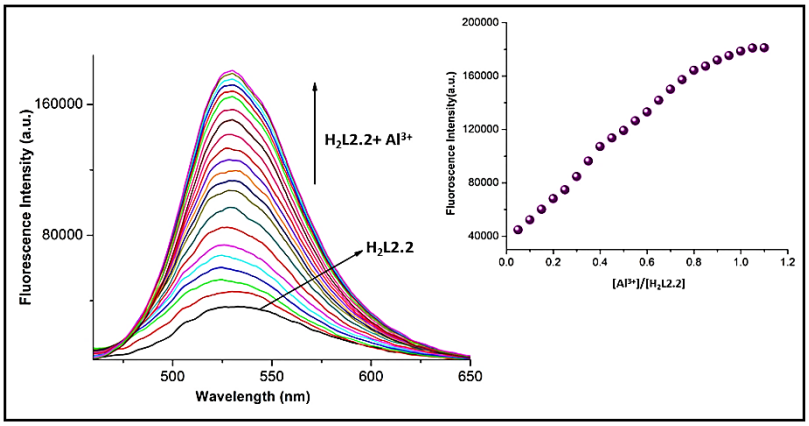

Fig. 2.37. Fluorescence titration of **H_2L2.2** (20 µM) with gradual addition of Al^{3+} (0-22µM) in 1X PBS buffer medium and corresponding fluorescence intensities versus molar ratio plot.

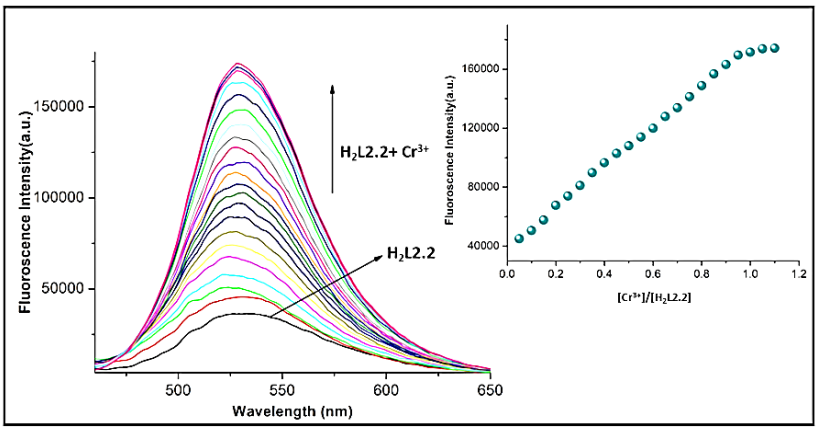

Fig. 2.38. Fluorescence titration of **H_2L2.2** (20 µM) with gradual addition of Cr^{3+} (0-22µM) in 1X PBS buffer medium and corresponding fluorescence intensities versus molar ratio plot.

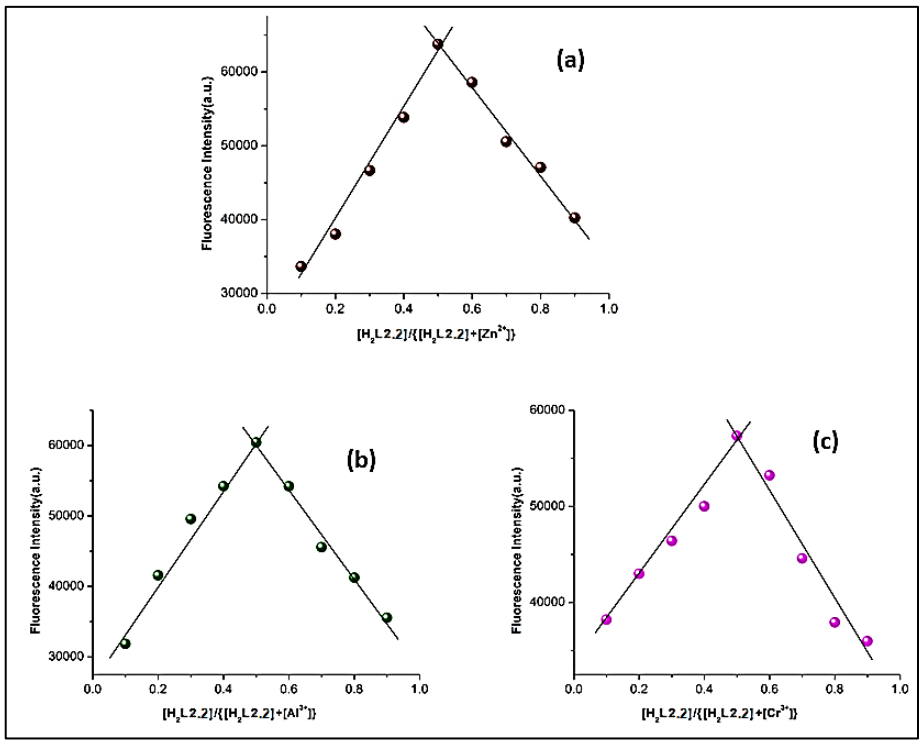

Fig. 2.39. 1:1 binding stoichiometry has shown by Job's plot for (a) complex **2.5**, (b) complex **2.6** and (c) complex **2.7**. Symbols and solid lines represent the experimental and simulated profiles, respectively.

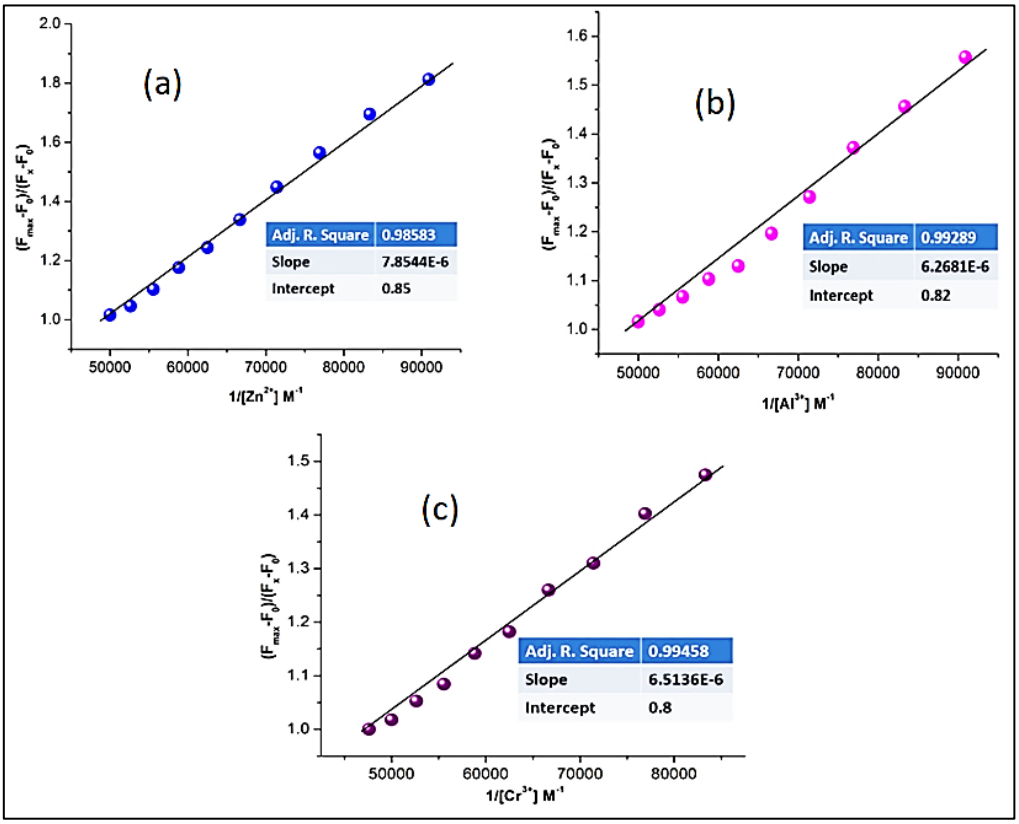

Fig. 2.40. Benesi-Hildebrand plot for (a) [$\mathbf{H_2L2.2}$-Zn^{2+}], (b) [$\mathbf{H_2L2.2}$-Al^{3+}] and (c) [$\mathbf{H_2L2.2}$-Cr^{3+}] systems. The linear plot is obtained after adding 1 equivalent Zn^{2+}, Al^{3+}, Cr^{3+} and Fe^{3+} ions to the probe in 1X PBS buffer medium, respectively.

Selectivity of $\mathbf{H_2L2.1}$ towards Zn^{2+}, Al^{3+}, Cr^{3+} and Fe^{3+} and $\mathbf{H_2L2.2}$ towards Zn^{2+}, Al^{3+} and Cr^{3+} over other common competitive species was examined by fluorescence titration experiments in presence of different alkali metals (Na^+ and K^+), alkaline-earth metals (Mg^{2+} and Ca^{2+}) and various transition-metal ions (Mn^{2+}, Fe^{2+}, Co^{2+}, Ni^{2+}, Cu^+, Cd^{2+} and Hg^{2+}) (**Fig. 2.41**). Upon addition of different common anions like $S_2O_3^{2-}$, S^{2-}, SO_3^{2-}, HSO_4^-, SO_4^{2-}, SCN^-, N_3^-, OCN^-, AsO_4^{3-}, PO_4^{3-}, ClO_4^-, AcO^-, Cl^-, NO_3^-, $P_2O_7^{4-}$ (PPi), PF_6^-, F^- and some important bio molecules such as L-Histidine, L-Cysteine, ATP, Glutathione (**Fig. 2.41**) in 1X PBS buffer medium to the chemosensor no significant fluorescence enhancement was noticed.

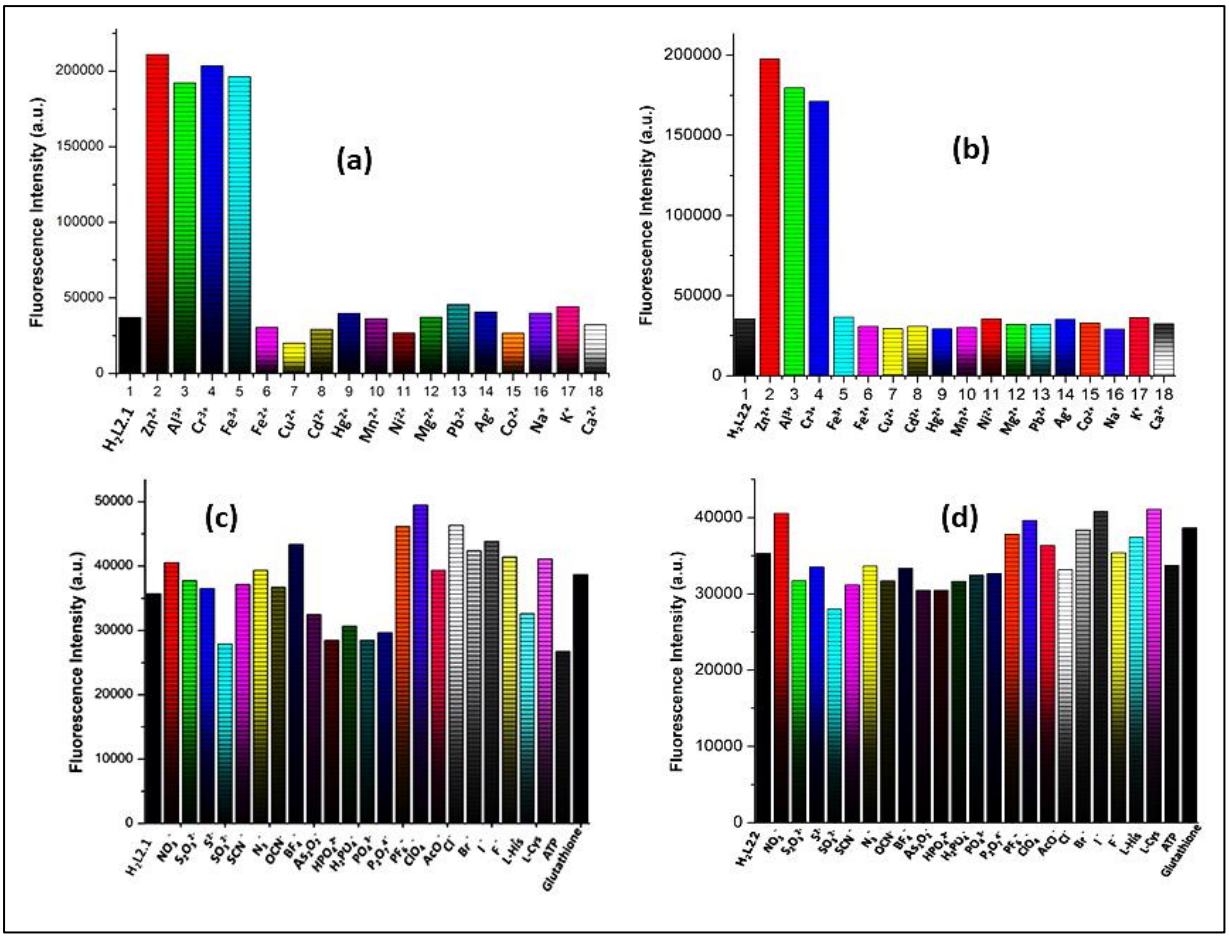

Fig. 2.41. Relative fluorescence intensity profile of (a) **H_2L2.1**, (b) **H_2L2.2** in the presence of different cations (1 equiv.) and (c) **H_2L2.1**, (d) **H_2L2.2** in presence of different common anions (1 equiv.) and biomolecules (1 equiv.) in 1X PBS buffer medium, respectively.

The competition assay experiments were performed either individually for Zn^{2+} (1.0 equiv.) and trivalent metal ions (Al^{3+}, Cr^{3+} and Fe^{3+}) (1.0 equiv.) or in presence of other metal ions (5.0 equiv.) and common anions in 5-fold excess (5.0 equivalents) in the same solvent system. Experimental results show that negligible enhancement or quenching occur either in presence of common cations (**Figs. 2.42, 2.43**) or common anions and some important bio molecules (**Figs. 2.44, 2.45**).

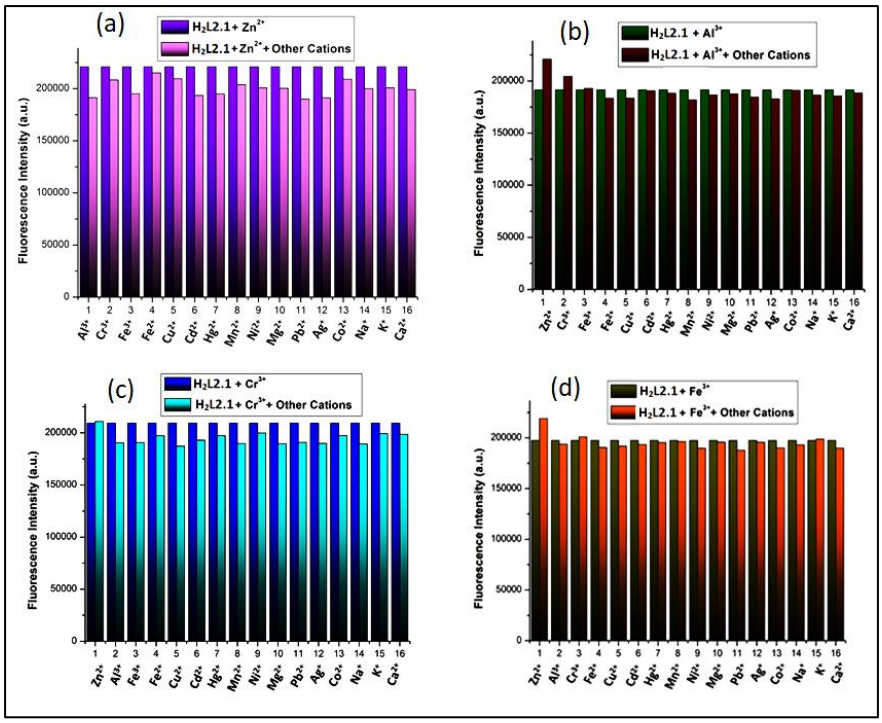

Fig. 2.42. Relative fluorescence intensity profile of (a) [**H_2L2.1**-Zn^{2+}], (b) [**H_2L2.1**-Al^{3+}], (c) [**H_2L2.1**-Cr^{3+}] and (d) [**H_2L2.1**-Fe^{3+}] systems in the presence of different cations in 1X PBS buffer medium [**H_2L2.1** (20µM); Zn^{2+}/ Al^{3+}/ Cr^{3+}/Fe^{3+} (20µM), other cations (100µM)].

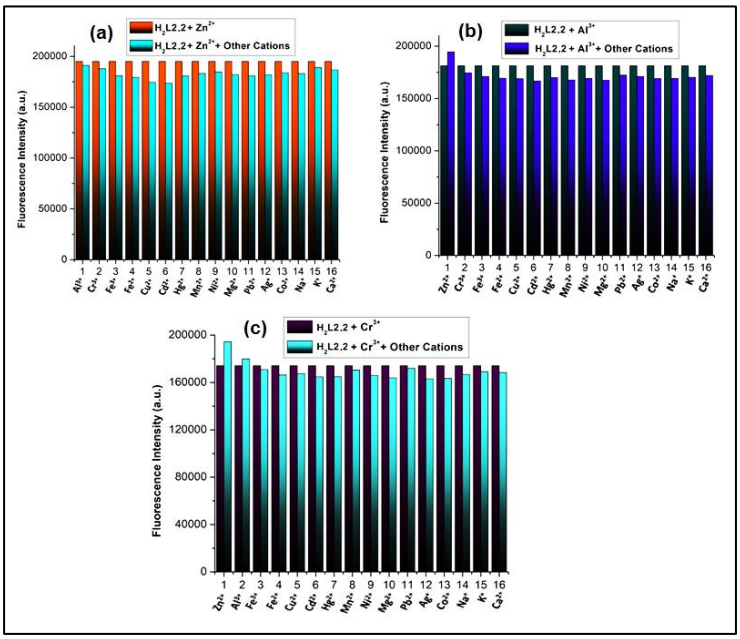

Fig. 2.43. Relative fluorescence intensity profile of (a) [**H_2L2.2.2**-Zn^{2+}], (b) [**H_2L2.2.2**-Al^{3+}] and (c) [**H_2L2.2.2**-Cr^{3+}] systems in the presence of different cations in 1X PBS buffer medium [**H_2L2.2.2** (20µM); Zn^{2+}/ Al^{3+}/ Cr^{3+}/Fe^{3+} (20µM), other cations (100µM)].

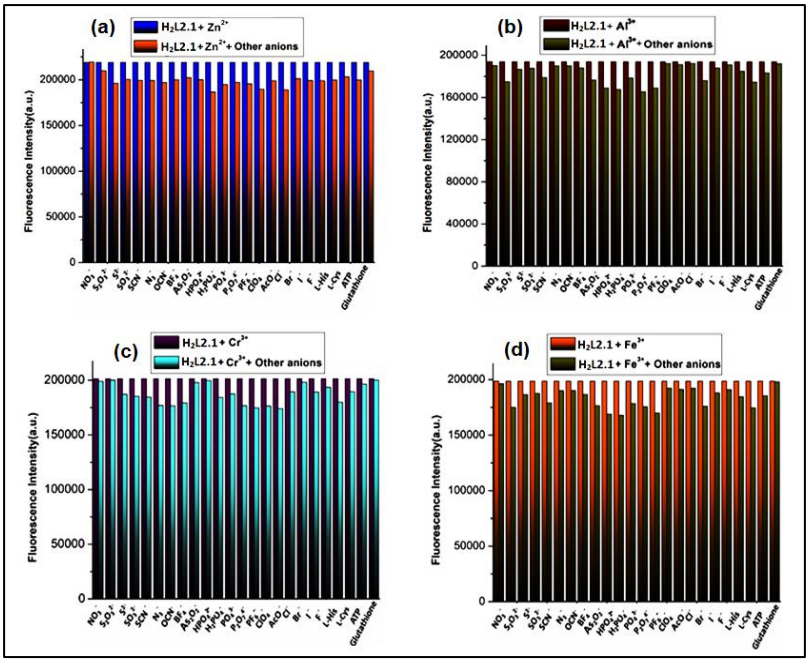

Fig. 2.44. Relative fluorescence intensity profile of (a) [**H_2L2.1**-Zn^{2+}], (b) [**H_2L2.1**-Al^{3+}], (c) [**H_2L2.1**-Cr^{3+}] and (d) [**H_2L2.1**-Fe^{3+}] systems in the presence of different anions and biomolecules in 1X PBS buffer medium [**H_2L2.1** (20µM); Zn^{2+}/ Al^{3+}/ Cr^{3+}/Fe^{3+} (20µM), other anions/ biomolecules (100µM)].

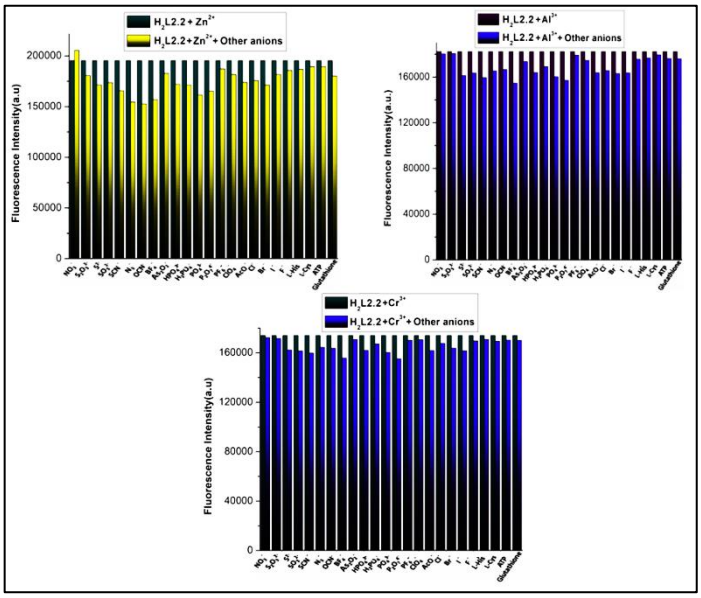

Fig. 2.45. Relative fluorescence intensity profile of (a) [**H_2L2.2**-Zn^{2+}], (b) [**H_2L2.2**-Al^{3+}] and (c) [**H_2L2.2**-Cr^{3+}] systems in the presence of different anions and biomolecules in 1X PBS buffer medium [**H_2L2.2** (20µM); Zn^{2+}/ Al^{3+}/ Cr^{3+} (20µM), other anions/ biomolecules (100µM)].

H_2L2.1 shows distinct colour change under UV light in presence of Zn^{2+} and trivalent cations (Al^{3+}, Cr^{3+} and Fe^{3+}) in 1X PBS buffer medium. **H_2L2.1** shows greenish-yellow fluorescence in presence of Zn^{2+} and trivalent cations (Al^{3+}, Cr^{3+} and Fe^{3+}) (**Fig. 2.46**).

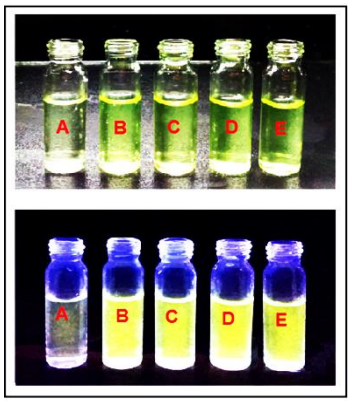

Fig. 2.46. Visual colour changes of chemosensors (**H_2L2.1**) in presence of Zn^{2+}, Al^{3+}, Cr^{3+} and Fe^{3+} ions in 1X PBS buffer medium. Here, A = **H_2L2.1** (20μM), B= **H_2L2.1** (20μM) +Zn^{2+} (20μM), C-E = **H_2L2.1** (20μM) +M^{3+} (M=Al, Cr and Fe) (20μM), respectively. Above images taken under normal light and below images taken under UV lamp.

Reversibility and regeneration of the free chemosensor are two important aspects for real time applications. In this experiment, the sodium salt of ethylenediaminetetraacetic acid (Na_2EDTA) is used as strong chelating ligand. After the addition of 1 equiv. of Na_2EDTA to a solution of Zn^{2+} and **H_2L2.1** the fluorescence changes from greenish-yellow to colourless with obvious decrease in fluorescence intensity confirming the regeneration of the free probe. Similarly, in presence of either Al^{3+} or Cr^{3+} or Fe^{3+} and **H_2L2.1**, addition of 1 equiv. Na_2EDTA results a change of the fluorescence from greenish-yellow to colourless indicating again regeneration of the free probe (**Fig. 2.47**). Again, in the same way reversibility and regeneration of the free chemosensor **H_2L2.2** is also tested (**Fig. 2.48**).

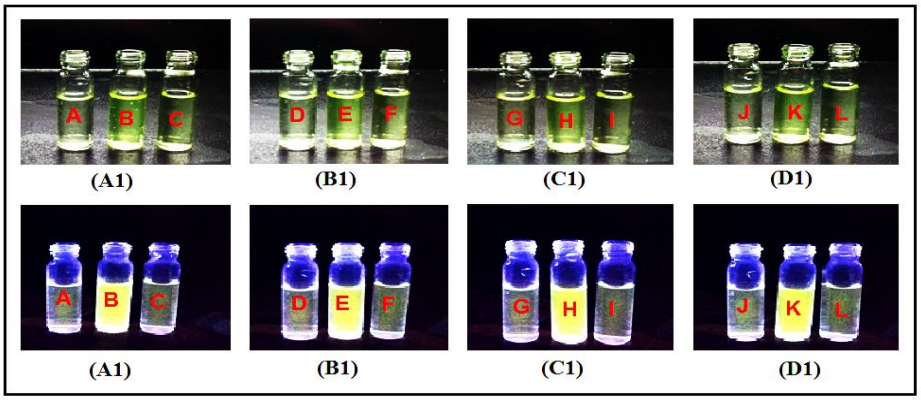

Fig. 2.47. Visual colour changes in reversibility experiments in 1X PBS buffer medium. Here, (A1)A = **H_2L2.1** (20μM), B = **H_2L2.1** (20μM) + Zn^{2+} (20μM), C= **H_2L2.1** (20μM) + Zn^{2+}(20μM) + $EDTA^{2-}$ (20μM), (B1)D= **H_2L2.1** (20μM), E = **H_2L2.1** (20μM) + Al^{3+} (20μM), F= **H_2L2.1** (20μM) + Al^{3+}(20μM) + $EDTA^{2-}$ (20μM), (C1)G= **H_2L2.1** (20μM), H = **H_2L2.1** (20μM) + Cr^{3+} (20μM), I= **H_2L2.1** (20μM) + Cr^{3+}(20μM) + $EDTA^{2-}$ (20μM), and (D1)J= **H_2L2.1** (20μM), K = **H_2L2.1** (20μM) + Fe^{3+} (20μM), L= **H_2L2.1** (20μM) + Fe^{3+}(20μM) + $EDTA^{2-}$ (20μM),respectively. Above images are taken under normal light and below images are taken under UV lamp.

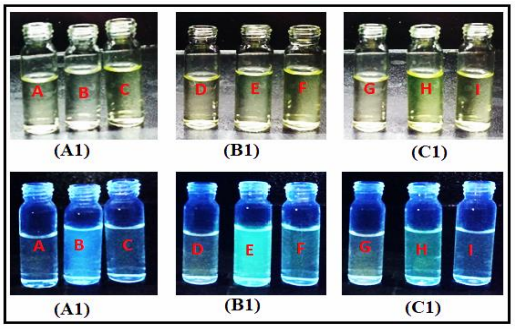

Fig. 2.48. Visual colour changes in reversibility experiments in 1X PBS buffer medium. Here, (A1)A = **H_2L2.2** (20μM), B = **H_2L2.2** (20μM) + Zn^{2+} (20μM), C= **H_2L2.2** (20μM) + Zn^{2+}(20μM) + $EDTA^{2-}$ (20μM), (B1)D= **H_2L2.2** (20μM), E = **H_2L2.2** (20μM) + Al^{3+} (20μM), F= **H_2L2.2** (20μM) + Al^{3+}(20μM) + $EDTA^{2-}$ (20μM) and (C1)G= **H_2L2.2** (20μM), H = **H_2L2.2** (20μM) + Cr^{3+} (20μM), I= **H_2L2.2** (20μM) + Cr^{3+}(20μM) + $EDTA^{2-}$ (20μM), respectively. Above images are taken under normal light and below images are taken under UV lamp.

2.3.6. Life time and quantum yield measurements

Lifetime experiment of **H_2L2.1**, **H_2L2.2** and complexes **2.1-2.7** were performed at 298 K in 1X PBS buffer medium (**Fig. 2.49**). The average fluorescence decay lifetimes of all the compounds were determined by using the formula $\tau_f = a_1\tau_1 + a_2\tau_2$, where a_1 and a_2 are relative amplitude of decay process. The average fluorescence lifetime of **H_2L2.1**, **H_2L2.2** and complexes **2.1-2.7** are in the **Table 2.4**.

Fluorescence quantum yields (Φ) of free **H_2L2.1**, **H_2L2.2** and complexes **2.1-2.7** were calculated using the following formula:

$$\Phi_{sample} = \{(OD_{standard} \times A_{sample} \times \eta^2_{sample})/(OD_{sample} \times A_{standard} \times \eta^2_{standard})\} \times \Phi_{standard}$$

Where, A is the area under the emission spectral curve, OD is the optical density of the compound at the excitation wavelength and η is the refractive index of the solvent. Here the value of $\Phi_{standard}$ is taken as 0.52 (for Quinine Sulfate). The values of Φ for **H_2L2.1**, **H_2L2.2** and complexes **2.1-2.7** were listed in **Table 2.4**.

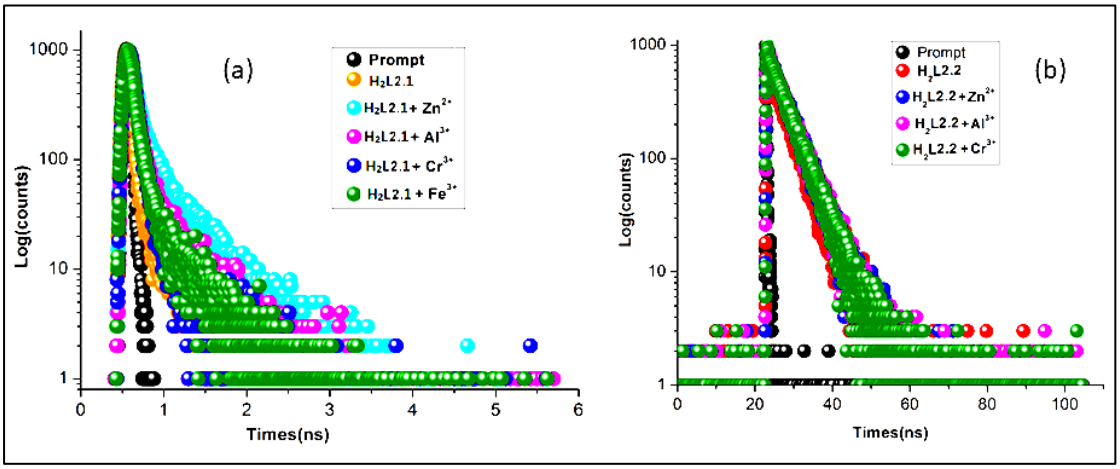

Fig. 2.49. Time-resolved fluorescence decay curve (logarithm of normalized intensity vs. time in ns) of (a) **H_2L2.1** and **H_2L2.1**+M^{n+} (M^{n+}= Zn^{2+}, Al^{3+}, Cr^{3+} and Fe^{3+}), respectively; (b) **H_2L2.2** and **H_2L2.2**+M^{n+} (M^{n+}= Zn^{2+}, Al^{3+} and Cr^{3+}), respectively.

Table 2.4. Data of lifetime (τ_f) and quantum yield (Φ) of **H_2L2.1** and **H_2L2.2** and complexes **2.1- 2.7.**

	τ_f (ns) (average)	χ^2	Φ
H_2L2.1	0.39	1.115859	0.04
H_2L2.2	4.58	0.96904	0.13
Complex **2.1**	1.30	1.120712	0.15
Complex **2.2**	1.06	1.017881	0.19
Complex **2.3**	1.18	0.9973537	0.13
Complex **2.4**	1.47	1.029217	0.12
Complex **2.5**	4.75	1.136785	0.27
Complex **2.6**	4.72	1.055282	0.25
Complex **2.7**	4.73	1.04918	0.23

2.3.7. Cell imaging study

A fluorescence microscopic study was performed to envisage the cellular uptake of both ligands (**H_2L2.1** and **H_2L2.2**) (10μM), Zn^{2+} salt (10μM), Al^{3+} salt (10μM**)**,Cr^{3+} salt (10μM**)** and Fe^{3+} salt (10μM), in *HepG2* cells. A moderate green signal is observed in the case of the cells treated with the ligand. The intensity of the green signal gets enhanced significantly when the cells were treated with **H_2L2.1** or **H_2L2.2** and respective metal salts. No fluorescence was observed in case of the untreated cells. Thus we can conclude that the cells readily uptake **H_2L2.1** and **H_2L2.2** as well as its Zn^{2+}, Al^{3+}, Cr^{3+} and Fe^{3+}complexes, which results in prominent green fluorescent signals (**Fig. 2.50**).

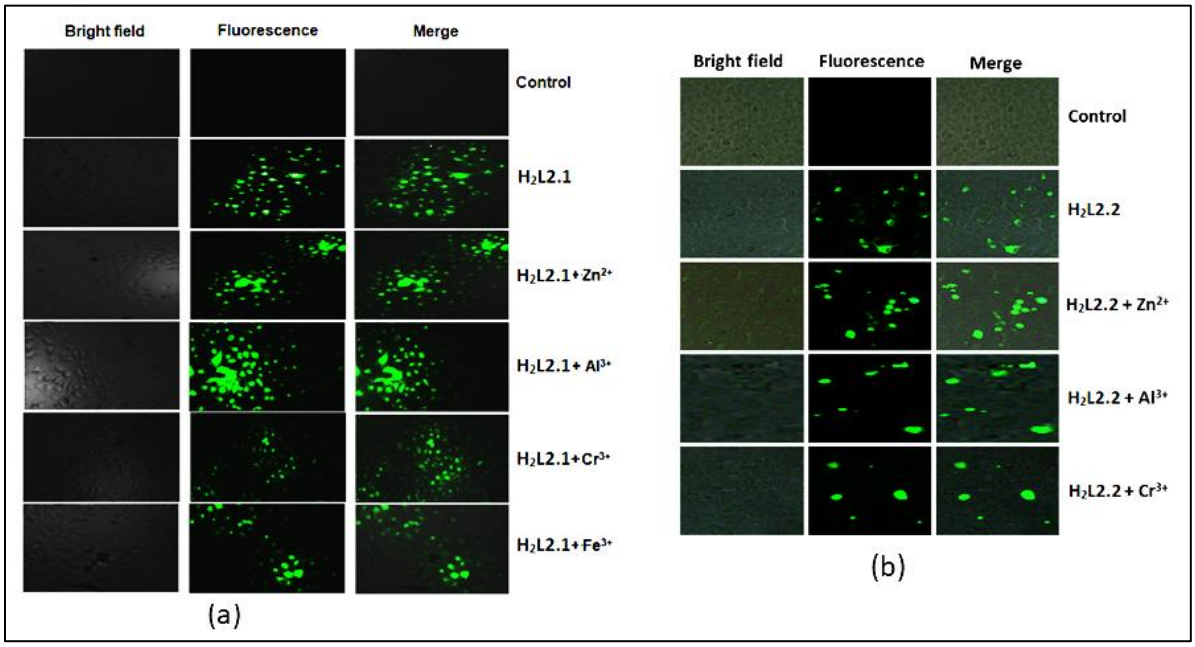

Fig. 2.50. Bright field, fluorescence and merged microscopic images of untreated *HepG2* (Control), cells treated with (a) **H_2L2.1**(10μM), **H_2L2.1**(10μM)+ Zn^{2+}(10μM), **H_2L2.1**(10μM) + Al^{3+}(10μM), **H_2L2.1**(10μM) + Cr^{3+}(10μM) and **H_2L2.1**(10μM) + Fe^{3+}(10μM) ; (b) **H_2L2.2**(10μM), **H_2L2.2**(10μM)+ Zn^{2+}(10μM), **H_2L2.2**(10μM) + Al^{3+}(10μM), **H_2L2.2**(10μM) + Cr^{3+}(10μM), respectively.

2.3.8. Cell survivability assay

The in vitro cytotoxicity of the ligands was estimated for checking the biocompatibility on *WI-38* cell lines. The cells were treated with five different concentrations (20μg/ml, 40μg/ml, 60μg/ml, 80μg/ml and 100μg/ml) of ligand for 24 h and followed by MTT assay. It was observed that both the ligands exhibited no significant toxicities even at the highest concentration of 100μg/ml (**Fig. 2.51**). Therefore, the ligands are biocompatible and highly conducive for biological applications.

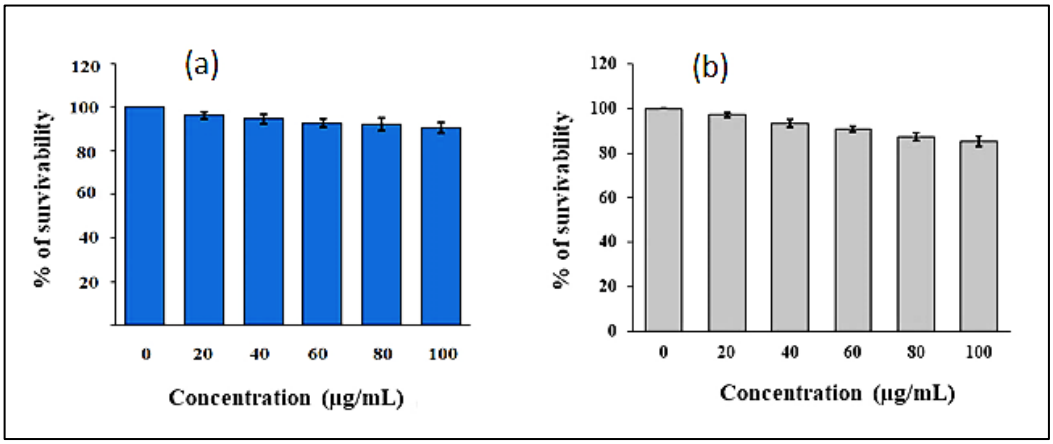

Fig. 2.51. Cell survivability of WI-38 cells exposed to the ligands (a) **H_2L2.1** and (b) **H_2L2.2**.

2.4. Conclusion

In this work we have successfully developed two aza-phenol based macrocyclic fluorescence probes, **H_2L2.1** and **H_2L2.2** as a "turn-on" fluorescence receptor towards multiple metal ions (**H_2L2.1** for Zn^{2+}, Al^{3+}, $Cr^{3+}$and Fe^{3+}ions; **H_2L2.2** for Zn^{2+}, Al^{3+} and Cr^{3+} ions). Fluorescence enhancement originates from a CHEF effect owing to the coordination of metal ions with the macrocyclic ligand through the imine nitrogens and phenoxido oxygens. In presence of above metal ions around 6-fold enhancement of emission intensity in 1X PBS buffer mediumis observed.1:1 chemosensor: metal binding stoichiometry both in solid and solution phase has been proven by different techniques viz. X-ray crystallography, ESI-Mass analysis and fluorescence spectroscopy. Important parameters like reversibility and regeneration of the chemosensors have been examined in the presence of Na_2EDTA. The large Stoke shifts of the chemosensors in presence of metal ions (~100 nm) and low LOD values make them suitable for bio-imaging studies. Indeed, we have successfully performed bio-imaging studies of the chemosensors using *HepG2* cells along with MTT assay. Therefore, phenol based macrocyclic probes able to behave as multi-analyte detectors constitute a unique class of chemosensors. Moreover, the tuning of the macrocyclic framework and donor sites can lead to chemosensors able to accommodate different analytes with varying stoichiometries.

2.5. References

[2.1] K. P. Carter, A. M. Young, A. E. Palmer, Chem. Rev. 114 (2014) 4564–4601.

[2.2] T. McKee, J. R. McKee, Biochemistry: An Introduction, McGraw-Hill Companies, Inc., China Science Press, New York, 2nd edn, (1999).

[2.3] C. K. Mathews, K. E. Van Holde, Biochemistry, The Benjamin/Cummings Publishing Company, Inc., Menlo Park, 2nd edn, (1996).

[2.4] C. S. Bonnet, E. Toth, Future Med. Chem. 2 (2010) 367–384.

[2.5] R. Y. Tsien, Czarnik, A. Ed.; American Chemical Society, Washington DC (1993).

[2.6] (a) M. Schmittel, H. W. Lin, Angew. Chem. Int. Ed. 46 (2007) 893–896; (b) P. N. Basa, A. G. J. Sykes, , Org. Chem. 77 (2012) 8428–8434; (c) J. F. Zhang, Y. Zhou, J. Yoon, Y. Kim, S. J. Kim, J. S. Kim, Org. Lett. 12 (2010) 3852–3855; (d) D. Maity, T. Govindaraju, Chem. Commun. 48 (2012) 1039–1041; (e) N. Kaur, S. Kumar, Chem. Commun. (2007) 3069–3070; (f) V. Luxami, S. Kumar, RSC Adv. 2 (2012) 8734–8740; (g) L. Wang, J. Yan, W. Qin, W. Liu, R. Wang, Dye. Pigm. 92 (2012) 1083–1090.

[2.7] J. Wang, Y. Li, N. G. Patel, G. Zhang, D. Zhoub, Y. Pang, Chem. Commun. 50 (2014) 12258–12261

[2.8] S. Paul, A. Manna, S. Goswami, Dalton Trans. 44 (2015) 11805–11810.

[2.9] Y. Liu, D. Wang, X. J. Zheng, L. P. Jin, RSC Adv. 5 (2015) 36987–36992.

[2.10] M. Shellaiah, T. Simon, V. Srinivasadesikan, C. M. Lin, K. W. Sun, F. H. Ko, M. C. Linc, H. C. Linb, J. Mater. Chem. C 4 (2016) 2056–2071.

[2.11] D. Das, R. Alam, A. Katarkarb, M. Ali, Photochem. Photobiol. Sci. 18 (2019) 242–252.

[2.12] R. Chandra, A. K. Manna, K. Rout, J. Mondal, G. K. Patra, RSC Adv. 8 (2018) 35946–35958.

[2.13] S. Janakipriya, N. R. Chereddy, P. Korrapati, S. Thennarasu, Spectrochim. acta 153 (2016) 465–470.

[2.14] D. Singha, T. Das, L. Satyanarayana, P. Roy, M. Nandi, New J. Chem. 43 (2019) 15563–15574.

[2.15] J. Wang, Y. Li, N. G. Patel, G. Zhang, D. Zhoub, Y. Pang, Chem. Commun. 50 (2014) 12258–12261.

[2.16] (a) P. Ghorai, K. Pal, P. Karmakar, A. Saha, Dalton Trans. 49 (2020) 4758–4773; (b) J. Mandal, K. Pal, S. G. Chowdhury, P. Karmakar, A. Panja, S. Banerjee, A. Saha, Dalton Trans. 51 (2022) 15555-15570.

[2.17] G. T. Sfrazzetto, C. Satriano, G. A. Tomaselli, E. Rizzarelli, Coord. Chem. Rev. 311 (2016) 125–167.

[2.18] (a) B. D'Autréaux, N. P. Tucker, R. Dixon, S. Spiro, Nature 437 (2005) 769–772; (b) N. Ercal, H. Gurer-Orhan, N. Aykin-Burns, Curr. Top. Med. Chem. 1 (2001) 529–539; (c) J. Wang, K. Pantopoulos, Biochem. J. 434 (2011) 365–381.

[2.19] J. M. Berg, H. A. Godwin, Annu. Rev. Biophys. Biomol. Struct. 26 (1997) 357–371.

[2.20] A. S. Pithadia, M. H. Lee, Curr. Opin, Chem. Biol. 16 (2012) 67–73.

[2.21] J. B. Vincent, The Journal of Nutrition 147 (2017) 2212–2219.

[2.22] D. M. Stearns, Bio. Factors 11 (2000) 149–162.

[2.23] S. C. Bondy, Neurotoxicology 31 (2010) 575–581.

[2.24] G. D. Fasman, Coord. Chem. Rev. 149 (1996) 125–165.

[2.25] D. P. Perl, D. C. Gajdusek, R. M. Garruto, R. T. Yanagihara, C. J. Gibbs, Science 217 (1982) 1053–1055.

[2.26] S. H. Park, N. Kwon, J. H. Lee, J. Yoon, I. Shin, Chem. Soc. Rev. 49 (2020) 143–179.

[2.27] H. Zhu, J. Fan, B. Wang, X. Peng, Chem. Soc. Rev. 44 (2015) 4337–4366.

[2.28] D. Wu, A. C. Sedgwick, T. Gunnlaugsson, E. U. Akkaya, J. Yoon, T. D. James, Chem. Soc. Rev. 46 (2017) 7105–7123.

[2.29] A. C. Sedgwick, L. Wu, H. H. Han, S. D. Bull, X. P. He, T. D. James, J. L. Sessler, B. Z. Tang, H. Tian, J. Yoon, Chem. Soc. Rev. 47 (2018) 8842–8880.

[2.30] L. Wu, C. Huang, B. P. Emery, A.C. Sedgwick, S. D. Bull, X. P. He, H. Tian, J. Yoon, J. L. Sessler, T. D. James, Chem. Soc. Rev. 49 (2020) 5110–5139.

[2.31] Y. Lu, S. Huang, Y. Liu, S. He, L. Zhao, X. Zeng, Org. Lett. 13 (2011) 5274–5277.

[2.32] (a) Y. Tachapermpon, S. Thavornpradit, A. Charoenpanich, J. Sirirak, K. Burgess, N. Wanichacheva, Dalton Trans. 46 (2017) 16251–16256; (b) T. Liu, Y. Dong, X. Wan, W. Li, Y. Yao, RSC Adv. 5 (2015) 76939–76942.

[2.33] (a) L. Hou, J. Feng, Y. Wang, C. Dong, S. Shuang, Y. Wang, Sens. Actuators B 247 (2017) 451–460; (b) J. C. Qin, L. Fan, B. D. Wang, Z. Y. Yang, T. R. Li, Anal. Methods 7 (2015) 716–722.

[2.34] X. Chen, T. Pradhan, F. Wang, J. S. Kim, J. Yoon, Chem. Rev. 112 (2012) 1910–1956.

[2.35] H. N. Kim, M. H. Lee, H. J. Kim, J. S. Kim, J. Yoon, Chem. Soc. Rev. 37 (2008) 1465–1472.

[2.36] V. Dujols, F. Ford, A. W. Czarnik, J. Am. Chem. Soc. 119 (1997) 7386–7387.

[2.37] D. T. Quang, J. S. Kim, Chem. Rev. 110 (2010) 6280–6301.

[2.38] B. A. Wong, S. Friedle, S. J. Lippard, J. Am. Chem. Soc. 131 (2009) 7142–7152.

[2.39] X. Zhang, D. Hayes, S. J. Smith, S. Friedle, S. J. Lippard, J. Am. Chem. Soc. 130 (2008) 15788–15789.

[2.40] L. Xue, G. Li, D. Zhu, Q. Liu, H. Jiang, Inorg. Chem. 51 (2012) 10842–10849.

[2.41] L. Xue, Q. Liu, H. Jiang, Org. Lett. 11 (2009) 3454–3457.

[2.42] H. Liua, Y. Dongc, B. Zhanga, F. Liua, C. Tana, Y. Tana, Y. Jianga, Sens. Actuators B 234 (2016) 616–624.

[2.43] Z. Xu, J. Yoon, D. R. Spring, Chem. Soc. Rev. 39 (2010) 1996–2006.

[2.44] Y. Fu, C. Fan, G. Liu, S. Cui, S. Pu, Dye. Pigm. 126 (2016) 121–130.

[2.45] (a) Y. Zhang, X. Guo, W. Si, L. Jia, X. Qian, Org. Lett. 10 (2008) 473–476; (b) C. He, Z. Lin, Z. He, C. Duan, C. Xu, Z. Wang, C. Yan, Angew. Chem., Int. Ed. 47 (2008) 877–881.

[2.46] I. Ravikumar, P. Ghosh, Inorg. Chem. 50 (2011) 4229–4231.

[2.47] D. Maity, T. Govindaraju, Chem. Commun. 48 (2012) 1039–1041.

[2.48] S. Anbu, R. Ravishankaran, M. Fátima, C. G. da Silva, A. A. Karande, A. J. L. Pombeiro, Inorg. Chem. 53 (2014) 6655−6664.

[2.49] S. Lohar, A. Sengupta, A. Chattopadhyay, J. S. Matalobos, D. Das, Eur. J. Inorg. Chem. (2014) 5675–5682.

[2.50] Y. Wang, Z. G. Wang, X. Q. Song, Q. Chen, H. Tian, C. Z. Xie, Q. Z. Li, J. Y. Xu, Analyst 144 (2019) 4024–4032.

[2.51] R. Purkait, S. Dey, C. Sinha, New J. Chem. 42 (2018) 16653–16665.

[2.52] P. Ghorai, S. Banerjee, D. Nag, S. K. Mukhopadhyay, A. Saha, J. Luminescence 205 (2019) 197–209.

[2.53] J. Mandal, P. Ghorai, K. Pal, P. Karmakar, A. Saha, J. Luminescence 205 (2019) 14–22.

[2.54] R. Alam, T. Mistri, R. Bhowmick, A. Katarkar, K. Chaudhuri, M. Ali, RSC Adv. 5 (2015) 53940–53948.

[2.55] A. K. Bhanja, C. Patra, S. Mondal, S. Mishra, K. D. Saha, C. Sinha, Sens. Actuators B 252 (2017) 257–267.

[2.56] R. Alam, T. Mistri, A. Katarkar, K. Chaudhuri, S. K. Mandal, A. R. Khuda-Bukhsh, K. K. Das, M. Ali, Analyst 139 (2014) 4022–4030.

[2.57] S. B. Maity, P. K. Bharadwaj, J. Luminescence 155 (2014) 21–26.

[2.58] A. Roy, S. Das, S. Sacher, S. K. Mandal, P. Roy, Dalton Trans. 48 (2019) 17594–17604.

[2.59] (a) C. T. L. Ma, M. J. MacLachlan, Angew. Chem. Int. Ed. 44 (2005) 4178–4182; (b) W. Huang, H. B. Zhu, S. H. Gou, Coord. Chem. Rev. 250 (2006) 414–423; (c) S. Anbu, M. Kandaswamy, P. Suthakaran, V. Murugan, B. Varghese, J. Inorg. Biochem. 103 (2009) 401–410; (d) D. P. Singh, K. Kumar, C. Sharma, Eur. J. Med. Chem. 44 (2009) 3299–3304; (e) J. K. Hui, P. D. Frischmann, C. H. Tso, C. A. Michal, M. J. Maclachlan, Chem. Eur. J. 16 (2010) 2453–2460; (f) J. Janczak, D. Prochowicz, J. Lewinski, D. Fairen-Jimenez, T. Bereta, J. Lisowski, Chem. Eur. J. 22 (2016) 598–609; (g) S. Matsunaga, M. Shibasaki, Chem. Commun. 50 (2014) 1044–1057; (h) B. L. Vallee, R. J. P. Williams, Proc. Natl. Acad. Sci. USA 59 (1968) 498–505.

[2.60] (a) Y. Qin, X. Liu, P. P. Jia, L. Xu, H. B. Yang, Chem. Soc. Rev. 49 (2020) 5678–5703; (b) P. Ghorai, S. G. Chowdhury, K. Pal, J. Mandal, P. Karmakar, A. Franconetti, A. Frontera, S. Blasco, E. G. España, P. P. Parui, A. Saha, Inorg. Chem. 61 (2022) 1982−1996; (c) F. Pina, M. A. Bernardo, E. G. España, , Eur. J. Inorg. Chem. (2000) 2143−2157; (d) R. Martınez-Manez, F. Sancenon, Chem. Rev. 103 (2003) 4419−4476; (e) B. Verdejo, M. Inclán, M. P. Clares, I. B. Sabater, M. R. Gasent, E. G. España, Chemosensors 21 (2022) 1; (f) L. Pla, B. Lozano-Torres, R. Martínez-Máñez, F. Sancenón, J. V. Ros-Lis, Sensors 19 (2019) 5138.

[2.61] S. A. Nepogodiev, J. F. Stoddart, Chem. Rev. 98 (1998) 1959–1976.

[2.62] X. Ji, X. Chi, M. Ahmed, L. Long, J. L. Sessler, Acc. Chem. Res. 52 (2019) 1915–1927.

[2.63] K. Jie, Y. Zhou, E. Li, F. Huang, Acc. Chem. Res. 51 (2018) 2064–2072.

[2.64] A. Bianchi, E. G. España, John Wiley & Sons, Ltd. (2012), DOI: 10.1002/9780470661345.smc048.

[2.65] (a) H. Ōkawa, H. Furutachi, D. E. Fenton, Coord. Chem. Rev. 174 (1998) 51–75; (b) C. Fraser, L. Johnson, A. L. Rheingold, B. S. Haggerty, G. K. Williams, J. Whelan, B. Bosnish,

Inorg. Chem. 31 (1992) 1835–1844; (c) D. G. McCollum, G. P. A. Yap, A. L. Rheingold, B. Bosnish, J. Am. Chem. Soc. 118 (1996) 1365–1379; (d) S. Karunakaran, M. Kandaswamy, J. Chem. Soc., Dalton Trans. (1994) 1595–1599; (e) E. V. Rybak-Akimova, N. W. Alcock, D. H. Busch, Inorg. Chem. 37 (1998) 1563–1574.

[2.66] (a) M. Yonemura, Y. Matsumura, H. Furutachi, M. Ohba, H. Ōkawa, D. E. Fenton, Inorg. Chem. 36 (1997) 2711–2717; (b) M. Yonemura, M. Ohba, K. Takahashi, H. Ōkawa, D. E. Fenton, Inorg. Chim. Acta 283 (1998) 72–79.

[2.67] (a) M. Yonemura, Y. Nakamura, N. Usuki, H. Ōkawa, Proc. Ind. Acad. Sci. (Chem. Ser.) 112 (2000) 291–310; (b) M. Yonemura, Y. Nakamura, N. Usuki, H. Ōkawa, J. Chem. Soc. Dalton Trans. (2000) 3624–3631; (c) M. Yonemura, K. Arimura, K. Inoue, N. Usuki, M. Ohba, H. Ōkawa, Inorg. Chem. 41 (2002) 582–589.

[2.68] (a) Z. Wang, A. E. Martell, R. J. Motekaitis, J. H. Reibenspies, J. Chem. Soc. Dalton Trans. (1999) 2441–2449; (b) G. Q. Shangguan, A. E. Martell, Z. R. Zhang, J. Reibenspies, Inorg. Chim. Acta 299 (2000) 47–58; (c) D. Y. Kong, A. E. Martell, R. J. Motekaitis, Ind. Eng. Chem. Res. 39 (2000) 3429–3435; (d) D. Kong, J. Reibenspies, A. E. Martell, R. J. Motekaitis, Inorg. Chim. Acta 324 (2001) 35–45; (e) J. D. Wang, A. E. Martell, R. J. Motekaitis, Inorg. Chim. Acta 322 (2001) 47–55; (f) J. D. Wang, D. Y. Kong, A. E. Martell, R. J. Motekaitis, J. H. Reibenspies, Inorg. Chim. Acta 324 (2001) 194–202; (g) J. Gao, A. E. Martell, R. J. Motekaitis, Inorg. Chim. Acta 325 (2001) 164–170; (h) D. Y. Kong, A. E. Martell, J. H. Reibenspies, Inorg. Chim. Acta 333 (2002) 7–14; (i) D. Kong, J. Reibenspies, J. Mao, A. Clearfield, A. E. Martell, Inorg. Chim. Acta 342 (2003) 158–170.

[2.69] (a) G. Ambrosi, M. Micheloni, D. Paderni, M. Formica, L. Giorgi, V. Fusi, Supramolecular Chemistry (2020) 32139–32149; (b) B. Ghanbari, M. Zarepour-jevinani, J. Luminescence 205 (2019) 219–227; (c) S. Goswami, S. Maity, A. C. Maity, A. K. Das, K.

Khanra, T. K. Mandal, N. Bhattacharyya, Tetrahedron Letters 55 (2014) 5993–5997; (d) A. K. Bhanjaa, C. Patra, S. Mondal, S. Mishra, K. D. Saha, C. Sinha, Sensors and Actuators B 252 (2017) 257–267; (e) B. S. Kumar, B. Chandra, K. V. J. Jose, P. K. Panda, J. Org. Chem. 86 (2021) 10536−10543; (f) R. Azadbakht, N. Chehrib, New J. Chem. 42 (2018) 17690–17699; (g) S. Das, J. Adhikary, P. Chakraborty, T. Chakraborty, D. Das, RSC Adv. 6 (2016) 98620–98631; (h) D. Paderni, L. Giorgi, M. Voccia, M. Formica, L. Caporaso, E. Macedi, V. Fusi, Chemosensors 10 (2022) 188-205; (i) S. Patra, V. P. Boricha, P. Paul, Eur. J. Inorg. Chem. (2019) 199–205;

[2.70] R. R. Gagne, C. L. Spiro, T. J. Smith, C. A. Hamann, W. R. Thies, A. K. Schiemke, J. Am. Chem. Soc. 103 (1981) 4073–4081.

[2.71] G. M. Sheldrick, SAINT, Version 6.02, SADABS, Version 2.03, Bruker AXS Inc., Madison, Wisconsin (2002).

[2.72] G. M. Sheldrick, SADABS, University of Gottingen, Institute fur Anorganische Chemieder Universitat, Gottingen, Germany (1999–2003).

[2.73] G. M. Sheldrick, SHELXL, Acta Cryst. C71 (2015) 3–8.

[2.74] (a) A. Pramanik, D. Laha, S. Chattopadhyay, S. K. Dash, S. Roy, P. Pramanik. P. Karmakar, Materials Science and Engineering C 65 (2016) 327–337; (b) D. Laha, A. Pramanik, S. Chattopadhyay, S. K. Dash, S. Roy, P. Pramanik, P. Karmakar, RSC Adv. 5 (2015) 68169–68178.

[2.75] (a) H. A. Benesi, J. H. Hildebrand, J. Am. Chem. Soc. 71 (1949) 2703–2707; (b) P. Gans, A. Sabatini, A. Vacca, Annali di Chimica 89 (1999) 45–49; (c) L. Alderighi, P. Gans, A. Ienco, D. Peters, A. Sabatini, A. Vacca, Coord. Chem. Rev. 184 (1999) 311–318.

[2.76] B. Tang, T. J. Wu, Y. Dong, Y. Ding, H. Wang, Talanta 64 (2004) 955–960; (b) J. H. Chang, Y. M. Choi, Y. K. Shin, Bull. Korean Chem. Soc. 22 (2001) 527–530; (c) E. M. Nolan, J.

Jaworski, M. E. Racine, M. Sheng, S. J. Lippard, Inorg. Chem. 45 (2006) 9748–9757; (d) D. Y. Wu, L. X. Xie, C. L. Zhang, C. Y. Duan, Y. G. Zhao, Z. J. Guo, Dalton Trans. (2006) 3528–3533; (e) D. Y. Wu, W. Huang, C. Y. Duan, Z. H. Lin, Q. J. Meng, Inorg. Chem. 46 (2007) 1538–1540; (f) J. Mao, L. N. Wang, W. Dou, X. L. Tang, Y. Yan, W. S. Liu, Org. Lett. 9 (2007) 4567-4570; (g) K. Huang, H. Yang, Z. Zhou, M. Yu, F. Li, X. Gao, T. Yi, C. Huang, Org. Lett. 10 (2008) 2557-2560; (h) Z. Zhou, M. Yu, H. Yang, K. Huang, F. Li, T. Yi, C. Huang, Chem. Commun. (2008) 3387–3389; (i) S. Aoki, D. Kagata, M. Shiro, K. Takeda, E. Kimura, J. Am. Chem. Soc. 126 (2004) 13377-13390, (j) D. Maity, T. Govindaraju, E. J. Inorg. Chemistry (2011) 5479–5485; (k) J. S. Wu, W. M. Liu, X. Q. Zhuang, F. Wang, P. F. Wang, S. L. Tao, X. H. Zhang, S. K. Wu, S. T. Lee, Organic Letters 9 (2007) 33–36; (l) H. S. Jung, K. C. Ko, J. H. Lee, S. H. Kim, S. Bhuniya, J. Y. Lee, Y. Kim, S. J. Kim, J. S. Kim, Inorg. Chem. 49 (2010) 8552–8557.

[2.77] A. B. Pradhan, S. K. Mandal, S. Banerjee, A. Mukherjee, S. Das, A. R. K. Bukhsh, A. Saha, Polyhedron 94 (2015) 75–82.

Chapter 3

Design and synthesis of a hydrazinopthalazine derived chemosensor to detect metal ions Zn^{2+}, Al^{3+} via CHEF effect with biological study and theoretical calculation

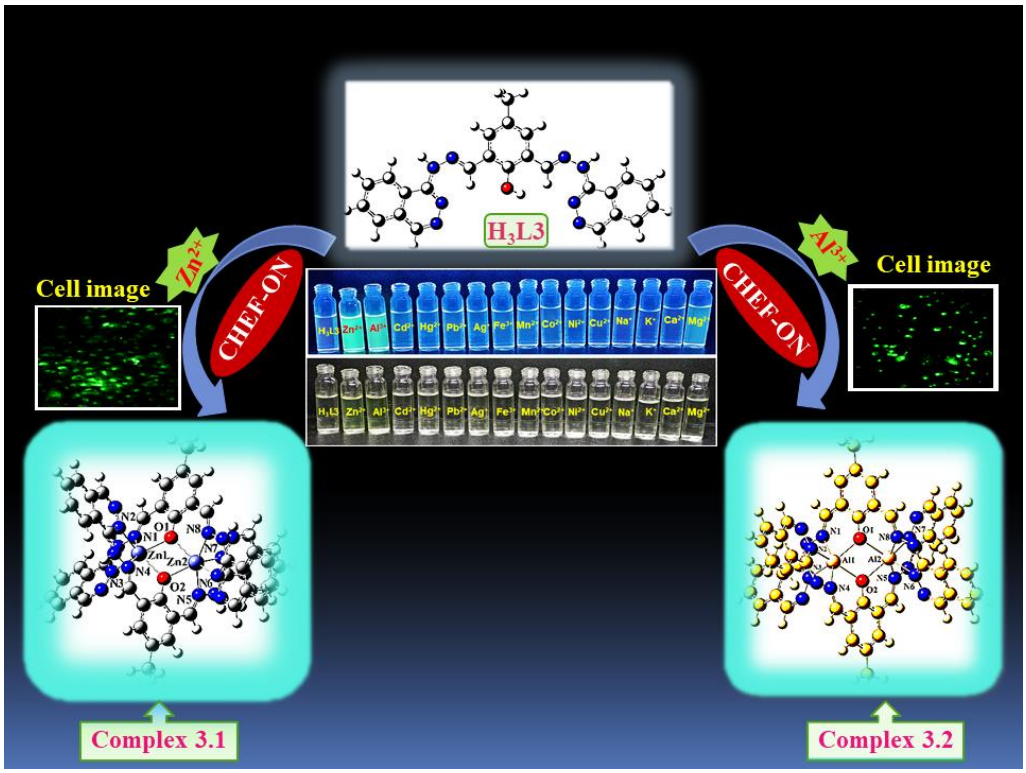

Journal of Photochemistry & Photobiology, A: Chemistry 446 (2024) 115145

Abstract

A multiple metal ion detector, **H_3L3** [**H_3L3**=4-methyl-2,6-bis((E)-(2-(phthalazin-1-yl)hydrazono)methyl)phenol] has been synthesized upon mixing 2,6-diformyl-4-methylphenol (DFP) and hydrochloride salt of hydrazinopthalazine in 1:2 ratio. **H_3L3** successfully detects Zn^{2+} and Al^{3+} ions through fluorescence enhancement in HEPES buffer (1:9, MeOH:H_2O, v/v, pH 7.4). The fluorescent probe and its metal-bound compounds (**3.1** and **3.2**) are characterized using different spectroscopy and mass spectrometric techniques. The turn-on fluorescence response towards Zn^{2+} and Al^{3+} was explained based on PET OFF, and chelation enhanced fluorescence (CHEF) ON processes. The binding mode and sensing mechanism of compounds **3.1** and **3.2** were confirmed using DFT calculations. **H_3L3** exhibits low detection limits and strong binding constants towards Zn^{2+} (2.37×10^{-6} M and 3.49×10^{4} M^{-1}) and Al^{3+} (1.32×10^{-6} M and 2.67×10^{4} M^{-1}) ions. It is successfully used in paper strips for the detection of Zn^{2+} and Al^{3+}. Biocompatible **H_3L3** also applied as a visual probe for the practical determination of Zn^{2+} and Al^{3+} on cervical cancer cells.

3.1. Introduction

The use of fluorescence spectroscopy has uplifted scientific research enormously due to its simplicity, high selectivity, and sensitivity, together with the advantage of rapid and real-time monitoring [3.1-3.3]. Fluorescent chemosensors are frequently used in environmental and biological sample analysis, molecular catalysis, etc [3.4-3.8]. They not only analyze but also accurately measure the number of guest species and biologically important species in vitro and in vivo [3.9-3.11]. Design and synthesis of a multi-analyte detector over a single analyte detector is far more advantageous from a practical point of view since they are more efficient and save preparation time and cost [3.12-3.15]. Zn^{2+} and Al^{3+}, biologically and environmentally important metal ions, have attracted considerable attention in research [3.16]. Literature reports on fluorescent turn-on probes of Zn^{2+} and Al^{3+} ions are not common. We have done a literature survey on some recently published works (**Chart 3.1**). K. Xu *et al.* have reported two quinoline based chemosensors for the detection of Zn^{2+} and Al^{3+} ions. In one work, fluorescent probe, 7-Hydroxy-8-(((2-(hydroxymethyl)quinolin-8-yl)imino)methyl)-coumarin was used for dual detection of Zn^{2+} and Al^{3+} ions. It exhibited strong binding affinity (1.27×10^5 M^{-1} and 5.28×10^5 M^{-1}) and low detection limits (3.75×10^{-8} and 1.14×10^{-8} M) towards Zn^{2+} and Al^{3+} ions. The probe was used to study fluorescence bio-imaging of Zn^{2+}, Al^{3+} and PPi, F^- in PC12 cells [3.16a]. In other work, they used an 8-aminoquinoline based "turn-on" dual fluorescence probe for selective detection of Zn^{2+} and Al^{3+} ions. It showed different colours and low detection limits (11.5 and 23.5 nM) in presence of Zn^{2+} and Al^{3+} ions. The chemosensor exhibited a preference for Al^{3+} over Zn^{2+} by displacing it from the chemosensor-bound Zn^{2+} complex. The probe was further utilized in monitoring of Al^{3+}, Zn^{2+} and F^- ions in living PC12 cells [3.16b]. J. Y. Xu and his group have developed a fluorescence probe, N'-((1-hydroxynaphthalen-2-yl)methylene)isoquinoline-3-carbohydrazide for selectively monitoring Al^{3+} and Mg^{2+}. The

fluorescence enhancement is based on the PET off, and CHEF on effects. The detection limit of probe for Al^{3+} and Mg^{2+} was low (1.20×10^{-8} M and 7.69×10^{-8} M). They had also performed fluorescence bioimaging of Al^{3+} and Mg^{2+} in MCF-7 cells in presence of the probe [3.16c]. Z. Y. Xing *et al.* have reported a naphthalene based dual probe for the recognition of Zn^{2+} and Al^{3+} both by fluorescence enhancement and colour changes through the naked eye, respectively. The probe showed a low limit of detection (3.02×10^{-7} M and 7.55×10^{-8} M) for Zn^{2+} and Al^{3+}, respectively. It was further used in logic gate construction, monitoring Zn^{2+} in plant roots and detecting Zn^{2+} and Al^{3+} in river water and test strips [3.16d]. S. Pu and coworkers have prepared a diarylethene derivative containing a purine unit that showed high selectivity and sensitivity towards Zn^{2+} and Al^{3+} in THF and methanol, respectively. Its fluorescence intensity increased by 18-fold in presence of Zn^{2+} whereas a 98-fold fluorescence enhancement was found with the addition of Al^{3+}. They have also explored the practical applicability of the probe [3.16e]. P. Li *et al.* have reported a fluorescent chemosensor for the detection of Zn^{2+} and Al^{3+} where the aggregation-induced emission (AIE)-based fluorescence enhancement was investigated in aqueous media and ethanol. Importantly, the probe had been successfully applied for the accurate detection of prostate cancer [3.16f]. Y. Zhang *et al.* have successfully reported an imidazo[2,1-b]thiazole and 2-hydroxy-1-naphthaldehyde-based chemosensor that detects Al^{3+} in methanol buffer solution and Zn^{2+} in ethanol buffer solution. The detection limits are found to be 1.45×10^{-7} M and 1.29×10^{-8} M, respectively. Furthermore, DFT/TDDFT calculations are performed in order to study the binding mode and sensing mechanism of the probe with metal ions [3.16g]. Zn^{2+} and Al^{3+}, biologically and environmentally important metal ions, have attracted considerable attention in research [3.16h-n] (**Chart 3.1**).

Aluminium, the richest metal in the earth's crust, is an essential part of our daily lives and its vast applicability is found in pharmaceutical products, utensils, electronic and electrical parts,

building equipment, different packaging systems, water treatment, food additives, etc. The World Health Organization (WHO) has restricted its maximum daily intake to 10 mg. Neurotoxic Al^{3+} inevitability accumulates in the human body through drinking water and food nutrients, thus causing neurogenic disorders like Alzheimer's disease and Parkinson's disease [3.17], osteomalacia [3.18] and breast cancer [3.19]. On the other hand, zinc, the second most abundant metal found in human body, is a key player in many cellular functions [3.20], like gene expression [3.21], apoptosis [3.22] and neurotransmission [3.23]. Zn contains some important metalloproteins and metalloenzymes, including zinc finger proteins (ZFPs), histone deacetylases (HDACs) and carbonic anhydrases (CAs) [3.24]. Zinc ion deficiency causes mental retardation and digestive dysfunction [3.25] whereas excessive accumulation of "free zinc" is responsible for Alzheimer's and Parkinson's diseases [3.26]. Thus, detection of both these ions in environmental and biological samples at trace levels like ppb, ppm, or nanomolar concentrations is a challenging task.

Both Zn^{2+} and Al^{3+} are spectroscopically silent ($3d^{10}4s^0$ and $3s^0$ electronic configurations, respectively) therefore, utilization of fluorescence spectroscopy will be a wise choice in comparison with traditional instrumental and analytical methods. However, poor coordination ability and strong tendency to hydration in the case of Al^{3+} and similar chemical properties and fluorescent responses of Zn^{2+} and its heavier congeners (Cd^{2+}, Hg^{2+}) hinder the preparation of suitable chemosensors for these ions. Keeping all these facts in mind design and synthesis of a multi-ion responsive chemosensor with a suitable coordination environment which anchor Zn^{2+} and Al^{3+} with different response signals is a challenging task. Some common fluophoric units for the detection of Al^{3+} ions are rhodamine, anthraquinone, BODIPY, salicylaldehyde, fluorescein, and coumarin [3.27-3.33] while for Zn^{2+} sensing the most frequently used chemosensors contain di-2-picolylamine (DPA) [3.34-3.37], quinoline [3.38-3.43], bipyridyl [3.39], etc. The design of

a new multi-ion detector chemosensor should achieve certain criteria, such as an easy synthetic route, solubility in nontoxic solvents, and high sensitivity, along with successful analysis of environmental and biological samples (**Chart 3.1**).

In continuation of our efforts to design a new fluorescent chemosensor with 2,6-diformyl-4-methyl phenol (DFP) as the fluophoric unit [3.12], we have prepared a Schiff base ligand (**H_3L3**) using the hydrochloride salt of hydrazinopthalazine and DFP. Hydrazinophthalazine is used as an antihypertensive drug all over the world for the treatment of high blood pressure-related diseases such as stroke, heart failure, kidney failure, and myocardial infarction. An extensive conjugation within the ligand framework exhibits photo-induced electron transfer (PET) which is responsible for its very weak fluorescence emission. **H_3L3** shows rapid response towards Zn^{2+} and Al^{3+} with high (~54 and 47 fold, respectively) fluorescence enhancement. Complexation with respective metal ions through a rigid chelate ring destabilizes the PET processes, and it is well reflected in UV–vis absorbance and fluorescence spectral changes. The LOD values of **H_3L3** towards Zn^{2+} and Al^{3+} ions are 2.37×10^{-6} and 1.32×10^{-6} M, respectively, lower than the WHO's guideline (5 mg/L for Zn^{2+} and 0.1 mg/L for Al^{3+} daily intake). Job′s plot analysis reveals 1:1 binding proportions of **H_3L3** with both the ions Zn^{2+} and Al^{3+}. ESI-MS analysis also confirmed the result. The binding constant values of the metal-bound probes (**3.1** and **3.2**) are found to be 3.49×10^{4} and 2.67×10^{4} M^{-1}. Both real-sample analysis (paper strips) and biological cell imaging studies of the chemosensor present a reliable method for the detection of Zn^{2+} and Al^{3+} in environmental and biological samples. We have also performed theoretical calculations to study the electronic spectra and binding mode of the chemosensor around the metal centre.

Chart 3.1. Literature survey of multi analytes sensing.

Sl. No.	Probe	Sensing mechanism	Sensing of metal ion(s)	Sensing media	Excitation(nm)/ Emission (nm)	Limit of detection (LOD) (M)	Binding constant (M^{-1})	Biological study	Refs.
1.	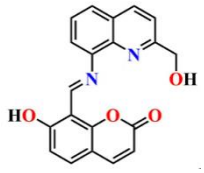	CHEF ICT	Zn^{2+} Al^{3+}	MeOH-H_2O (4/1, v/v)	430/535 420/518	3.75×10^{-8} 1.14×10^{-8}	1.27×10^{5} 5.28×10^{5}	Cell imaging	**3.16a**
2.	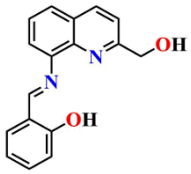	CHEF ICT	Zn^{2+} Al^{3+} F^{-}	EtOH–H_2O solution (v/v = 4/1, 0.01 M, Tris-HCl buffer, pH = 7.30)	252, 425/530 252/500	11.5×10^{-9} 23.5×10^{-9}	2.06×10^{4} 6.83×10^{4}	Cell imaging	**3.16b**
3.	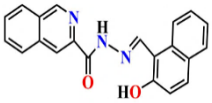	ESIPT and CHEF	Al^{3+} Mg^{2+}	Ethanol	439/460,487 432/543	1.20×10^{-8} 7.69×10^{-8}	3.6×10^{4} 5.8×10^{4}	Cell imaging	**3.16c**
4.	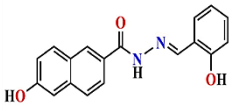	C=N isomerization and PET process	Zn^{2+} Al^{3+}	C_2H_5OH solution	380/456 380/503	3.02×10^{-7} 7.55×10^{-8}	8.48×10^{4} 4.45×10^{5}	Cell imaging	**3.16d**
5.	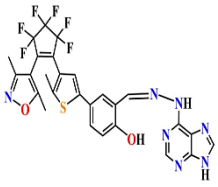	CHEF	Zn^{2+} Al^{3+}	THF MeOH	370/545 370/534	7.02×10^{-8} 6.72×10^{-9}	2.06×10^{4} 4.61×10^{4}	None	**3.16e**

6.	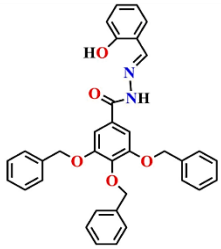	AIE, PET	Zn^{2+} Al^{3+}	DMF/H_2O	400/510 385/450	0.25×10^{-6} 0.039×10^{-6}	----	Cell imaging	**3.16f**
7.	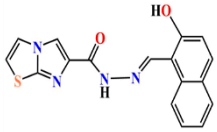	off–on–off	Zn^{2+} Al^{3+}	EtOH/ H_2O Methanol/H_2O [buffer solution (v/v = 9 : 1, Tris = 10 mM, and pH = 7.4)]	413,430/484 405,428/472	1.29×10^{-8} 1.45×10^{-7}	1.19×10^{5} 1.94×10^{4}	None	**3.16g**
8.	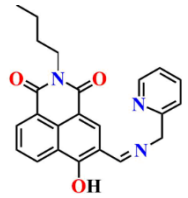	CHEF PET	Zn^{2+} Al^{3+}	CH_3CN /water (7:3, v/v)	380/492 380/458	14.4×10^{-6} 74.0×10^{-6}	4.89 ± 0.12) $\times 10^4$ (5.37 ± 0.08) $\times 10^4$	None	**3.16h**
9.	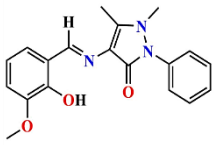	CHEF	Al^{3+} Zn^{2+}	EtOH-water	406/520 425/535	1.05×10^{-9} 2.35×10^{-9}	-----	None	**3.16i**
10	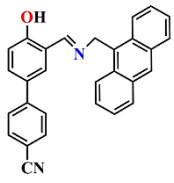	PET, C=N isomerization	Zn^{2+} Al^{3+}	EtOH-H_2O (v/v, 95/5)	365/477 365/390,410,435	78.8×10^{-9} 52.2×10^{-9}	$\log K_a$=2.81 $\log K_a$=6.24	None	**3.16j**
11.	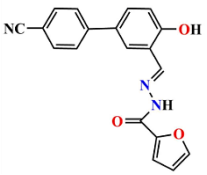	Fluorescence off-on	Al^{3+} Zn^{2+}	ACN/H_2O (v/v=80/20, 1 μM, pH = 7.0)	355/464 355/512	1.27×10^{-9} 1.02×10^{-9}	12.8×10^5 5.05×10^5	Cell imaging	**3.16k**

12.	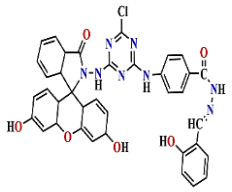	Fluorescence turn-on	Al^{3+} Zn^{2+}	EtOH-H_2O (v/v ¼ 9/1, 10.0mM PBS, pH 7.0)	384/446 406/500	5.37×10^{-8} 7.90×10^{-8}	1.5×10^{5} 6.0×10^{5}	Cell imaging	**3.16l**
13.	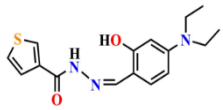	C=N isomerization, CHEF	Al^{3+} Zn^{2+}	DMSO/H_2O (1/1, v/v)	375/475 375/475	3.7×10^{-9} 3.0×10^{-8}	1.16×10^{4} 2.08×10^{4}	Cell imaging	**3.16m**
14.	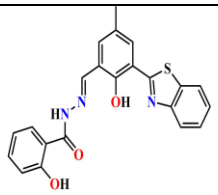	ESIPT	Zn^{2+} Al^{3+}	DMF/H_2O (1/1, v/v, 0.01 M HEPES, pH = 6.0).	440/494 435/508	1.27×10^{-7} 1.42×10^{-7}	3.19×10^{4} 7.78×10^{4}	No	**3.16n**
16.	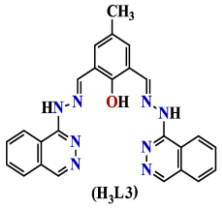	**CHEF**	**Zn^{2+} Al^{3+}**	**HEPES buffer medium (1:9, MeOH: H_2O, v/v, pH 7.4)**	**448/510 472/505**	**2.37×10^{-6} 1.32×10^{-6}**	**3.49×10^{4} 2.67×10^{4}**	**Cell imaging**	**This work**

3.2. Experimental section

3.2.1. Chemicals and instrumentations involved in this work

Chemicals and solvents are of analytical grade, brought from commercial suppliers, and used without further purification. C, H, N analysis has been performed by Perkin–Elmer 240C elemental analyzer. Electron spray ionization mass (ESI-MS positive) and infrared spectral data (400–4000 cm^{-1}) were collected from the MICROMASS Q-TOF mass spectrometer and the Nicolet Magna IR 750 series-II FTIR spectrophotometer, respectively. Absorption spectroscopy has been studied using a Shimadzu UV 1800 spectrophotometer with a 10-mm-path-length quartz cell. Fluromax-4 spectrofluorometer was utilised to collect emission spectral data at

normal temperature (298 K) in HEPES buffer (1:9, MeOH:H_2O, v/v, pH 7.4). Fluorescence lifetime data were collected from a time-resolved spectrofluorometer from IBH, UK. Bruker 400 spectrometer was used for recording ^{1}H and ^{13}C NMR spectra in d_6-DMSO solvent.

3.2.2. Synthesis

3.2.2.1. Procedure for synthesis of 2,6-diformyl-4-methylphenol

2,6-Diformyl-4-methylphenol (DFP) was prepared as usual by following a published procedure [3.44].

3.2.2.2. Procedure for synthesis of chemosensor [H_3L3= 4-methyl-2,6-bis((E)-(2-(phthalazin-1-yl)hydrazono)methyl)phenol]

To the hydrochloride salt of hydrazinopthalazine (2.0 mmol, 0.194g), sodium acetate (6.0 mmol, 0.492 g) was added to neutralize the solution. Solution turned into a light yellow colour. Then to the mixture DFP (1.0 mmol, 0.164 g) in methanol was added, and instantaneous precipitation was observed. After stirring for 4h at room temperature, the precipitate was filtered and washed with methanol for three times. A deep yellow solid mass was used directly for characterization and complexation.

Yield: 0.408g (91%). Anal. Calc. For $C_{25}H_{20}N_8O$: C 66.95%; H 4.50%; N 24.99%. Found: C 66.90%; H 4.46%; N 24.97%. IR (cm^{-1}, KBr): (υ_{O-H}) 3323; ($\upsilon_{C=N}$) 1609; (υ_{C-H}) 776. ESI-MS (positive) in MeOH: *m/z* = 449.13 (base peak, [**H_3L3**+H]$^+$). UV-Vis, λ_{max} (nm), (ε ($dm^3mol^{-1}cm^{-1}$)) in HEPES buffer (1:9, MeOH:H_2O, v/v, pH 7.4): 295 (24380) and 400 (30235), respectively.

^{1}H NMR (solvent used: d_6-DMSO, 400 MHz) δ ppm: 2.31 (-CH_3) (s, 3H), 7.76 (Ar-H) (d, 4H, J=8 Hz), 7.96 (Ar-H) (s, 2H), 8.34 (Ar-H) (d, 4H, *J* = 8Hz), 8.43 (Ar-H) (s, 2H), 8.74 (-HC=N) (s, 2H), 10.99 (-HN=N) (s, 2H), 12.88 (-OH) (s, 1H).

^{13}C NMR (solvent used: d_6-DMSO, 75 MHz) δ ppm: 20.63, 114.30, 122.40, 123.76, 125.78, 127.26, 129.52, 131.57, 132.35, 134.38, 138.30, 140.54, 149.29 and 163.00.

3.2.2.3. Synthesis of complex 3.1 [Zn(H_2L3)](NO_3)

Zinc nitrate hexahydrate (0.5 mmol, 0.148 g) was initially dissolved in 2 mL methanol and added dropwise to the chemosensor, **H_3L3** in 20 mL methanol (0.5 mmol, 0.224 g). 2-3 drops of triethylamine (0.5 mmol, ~0.1 mL) also added to it, and the resultant reaction mixture was stirred for ca. 4 h. Complex **3.1** was finally obtained as an orange-coloured solid mass.

Yield: 0.488g (85%). Anal. Calc. For $C_{25}H_{19}N_9O_4Zn$: C 52.23%; H 3.33%; N 21.93%. Found: C 52.20%; H 3.31%; N 21.89%. IR (cm^{-1}, KBr): ($\upsilon_{C=N}$) 1542; (υ_{NO3^-}) 1311; (υ_{C-H}) 758. ESI-MS (positive) in MeOH: at *m/z* = 513.03, (base peak, $[Zn_2(\mathbf{H_2L3})_2]^{2+}$). UV-Vis, λ_{max} (nm), (ε ($dm^3mol^{-1}cm^{-1}$)) in HEPES buffer (1:9, MeOH:H_2O, v/v, pH 7.4): 448 (15940) and 473 (14410).

^{1}H NMR (solvent used: d_6-DMSO, 400 MHz) δ ppm: 2.34 (-CH_3) (s, 3H), 7.98 (Ar-H) (s, 2H), 8.16 (Ar-H) (d, 4H, J=24 Hz), 8.47 (Ar-H) (s, 2H), 8.57 (Ar-H) (s, 2H), 8.71 (Ar-H) (s, 2H), 9.18 (-HC=N) (s, 2H), 12.48 (-HN=N) (s, 2H).

^{13}C NMR (solvent used: d_6-DMSO, 75 MHz) δ ppm: 20.81, 117.02, 122.08, 123.03, 124.51, 126.82, 127.02, 132.57, 133.93, 135.14, 145.02, 149.81, 151.82, 164.07.

3.2.2.4. Synthesis of complex 3.2 [Al(H_2L3)](NO_3)$_2$

Aluminium nitrate nonahydrate (0.5 mmol, 0.187 g) was first dissolved in 2 mL methanol and added drop by drop to a 20 mL methanolic solution of **H_3L3** (0.5 mmol, 0.224 g). 2-3 drops of triethylamine (0.5 mmol, ~0.1 mL) also added to it, and the resultant reaction mixture was stirred for ca. 4 h. Complex **3.2** was finally obtained as a light orange-coloured solid mass.

Yield: 0.514 g (86%). Anal. Calc. For $C_{25}H_{19}N_{10}O_7Al$: C 50.17%; H 3.20%; N 23.40%. Found: C 50.14%; H 3.18%; N 23.35%. IR (cm^{-1}, KBr): ($\upsilon_{C=N}$) 1545; (υ_{NO3^-}) 1323; (υ_{C-H}) 772. ESI-MS (positive) in MeOH: *m/z* = 321 $[Al(\mathbf{H_2L3})+NO_3^{-}+2H_2O+CH_3OH+K^{+}]^{2+}$, 473.23 (base peak,

$[Al(\mathbf{H_2L3})\text{-}H]^+$), and 963.49 $[Al_2(\mathbf{H_2L3})_2+H_2O\text{-}3H]^+$, respectively. UV-Vis, λ_{max} (nm), (ε ($dm^3mol^{-1}cm^{-1}$)) in HEPES buffer (1:9, MeOH:H_2O, v/v, pH 7.4): 472 (24250).

^{1}H NMR (solvent used: d_6-DMSO, 400 MHz) δ ppm: 2.39 (-CH_3) (s, 3H), 8.07 (Ar-H) (s, 4H), 8.56 (Ar-H) (t, 2H, J_1=J_2=8Hz), 8.74 (Ar-H) (s, 2H), 8.94 (Ar-H) (s, 2H), 9.16 (Ar-H) (s, 2H), 9.36 (-HC=N) (s, 2H).

^{13}C NMR (solvent used: d_6-DMSO, 75 MHz) δ ppm: 21.60, 116.40, 123.38, 124.08, 125.34, 126.35, 126.83, 128.24, 130.38, 132.35, 133.50, 136.63, 151.56, 164.02.

3.2.3. Absorbance and emission spectral analysis

Chemosensor (**H_3L3**) (1×10^{-3} M) and individual analyte (1×10^{-3} M) solutions were prepared carefully in methanol solvent as stock solutions. After that, stock solution of **H_3L3** was diluted to 2×10^{-5} M for experimental purposes. Absorbance and fluorescence experiments, along with competitive assays with various analytes, done in HEPES buffer (1:9, MeOH:H_2O, v/v, pH 7.4). For absorbance measurements, a quartz optical cell with a 10 mm optical path length was first filled with a 60 µL solution of **H_3L3** (1×10^{-3} M) and mixed gradually with stock solution of analytes (Zn^{2+} and Al^{3+}) resulting in a final concentration at 2×10^{-5} M. In competitive assay experiments, we followed the same procedure. During emission spectral studies, the solution of the chemosensor was excited at 400 nm, and spectra were recorded between the range of 415-700 nm.

3.2.4. Determination of binding stoichiometry (Job′s plot)

Binding stoichiometry of the chemosensor with that of Zn^{2+} and Al^{3+} ions had been determined by Job′s plot using UV-visible as well as fluorescence spectroscopic techniques at room temperature (25ºC). During this study, absorbance and fluorescence intensity were recorded for both chemosensor and Zn^{2+} or Al^{3+} ions with varied concentrations while keeping

the summation of the whole concentration fixed at 2×10^{-5} M. Next relative change in absorbance ($\Delta A/A_0$) and fluorescence ($\Delta I/I_0$) were plotted against the mole fraction of the chemosensor. The stoichiometry was calculated from the break point. The value of stoichiometry was the average value of these experiments, which were done at least three times.

3.2.5. Computational method

The geometry of chemosensor **H_3L3**, complexes **3.1** and **3.2** were optimized by density functional theory (DFT) using the basis set B3LYP/6-31+G* level in their ground state [3.45]. Time-dependent DFT (TDDFT) [3.46] for energy calculations had been set up using the conductor-like polarizable continuum model (CPCM) [3.47]. Electronic density plots for the frontier molecular orbitals have been calculated using Gauss View 5.0 software. Gaussian09 software package is used for calculation purposes [3.48].

3.2.6. Cell imaging experiment

The *Hela* cells were grown in cover slips, and the time required was 24 h. Further, mock-treatment or treatment of the cells with 20 µM of ligand **H_3L3** and Zn^{2+} salt (20 µM), Al^{3+} salt (20 µM) for 24 h at 37ºC was done. PBS buffer was used for washing the cells. Glass slides were used for mounting the cells and finally they were observed under a fluorescence microscope (Leica) using a filter with a power of excitation 450-500 nm (blue) and emission 500-570 nm (green).

3.2.7. Cell survivability assay

Cell survivability experiment of **H_3L3** was studied in presence of WI-38 cells, following a standard protocol [3.49]. Here, the capability of experimental cells in the presence of various concentrations of **H_3L3** was checked by MTT assay. 96-well plates were used for cell seeding, where 1×10^4 cells per well were exposed to **H_3L3** with concentration limits of 0, 20, 40, 60, 80 and 100 µM for 24 h, respectively. Finally obtained formazan crystals were dissolved in an MTT

solubilization buffer, followed by absorbance measurement at 570 nm using a spectrophotometer (BioTek) and the obtained result was compared with control cells.

3.3. Results and discussion

3.3.1. Discussion on synthesis and characterization

The chemosensor **H_3L3** has been prepared in a single step process where 2,6-diformyl-4-methylphenol (DFP) reacts with hydrazinopthalazine under stirring conditions at room temperature. The solid organic compound was obtained in good yield (**Scheme 3.1**). Spectroscopic methods such as UV-Vis absorbance, FT-IR, ^{1}H NMR, and ^{13}C NMR are utilised for its complete characterization. The base peak of the chemosensor in the ESI-mass analysis was found at *m/z* = 449.13, suggesting [**H_3L3**+H]$^{+}$ species (**Fig. 3.1**). 1:1 reaction between $Zn(NO_3)_2.6H_2O$ and $Al(NO_3)_3.9H_2O$ with **H_3L3** in methanol medium under stirring conditions generate complexes **3.1** [Zn(**H_2L3**)](NO_3) and **3.2** [Al(**H_2L3**)]$(NO_3)_2$ in high yield (**Scheme 3.2**). Similar to free chemosensor, compounds were characterized by different spectroscopic methods, CHN and mass analysis. The characterized ESI-mass data of complexes **3.1** and **3.2** were found at m/z = 513.03, 473.23 and 963.49 correspond to various species like, $[Zn_2(\mathbf{H_2L3})_2]^{2+}$, [Al(**$H_2L3$**)-H]$^{+}$ and $[Al_2(\mathbf{H_2L3})_2+H_2O\text{-}3H]^{+}$, respectively (**Figs. 3.2 and 3.3**). In FT-IR spectrum of **H_3L3** two characteristic bands at 3323 and 1609 cm^{-1} give an idea of phenolic OH and C=N (azomethine) groups. Also for complexes **3.1** and **3.2,** important stretching frequencies are generated around ~1545 cm^{-1} for ($\upsilon_{C=N}$), 765 cm^{-1} for (υ_{C-H}), respectively.

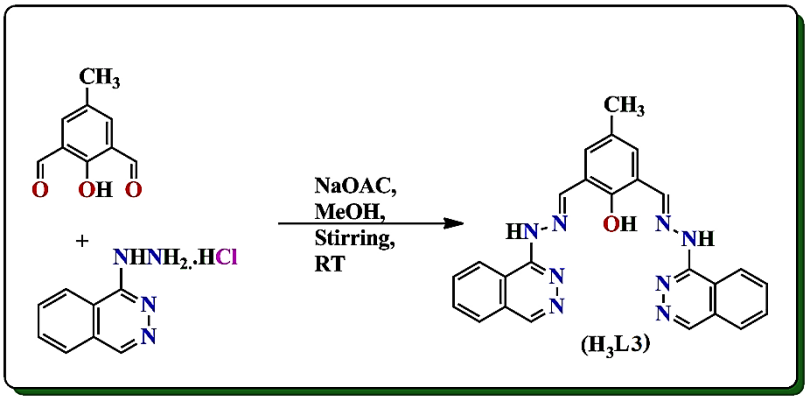

Scheme 3.1. Route to synthesis of chemosensor (**H_3L3**).

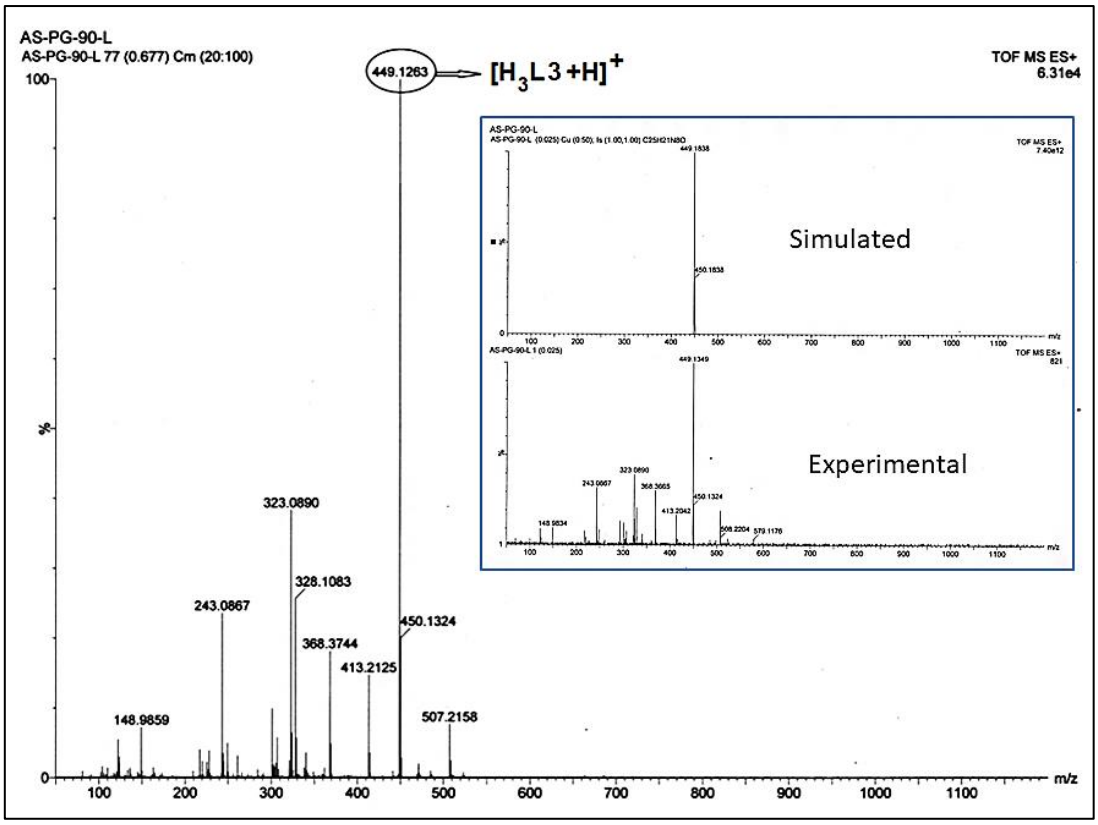

Fig. 3.1. ESI-MS$^+$ spectrum of [**H_3L3**+H]$^+$.

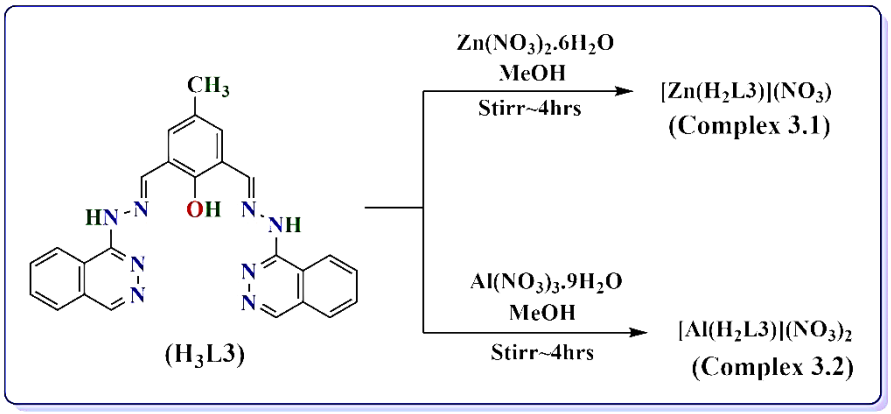

Scheme 3.2. Route to synthesis of complexes **3.1** and **3.2**.

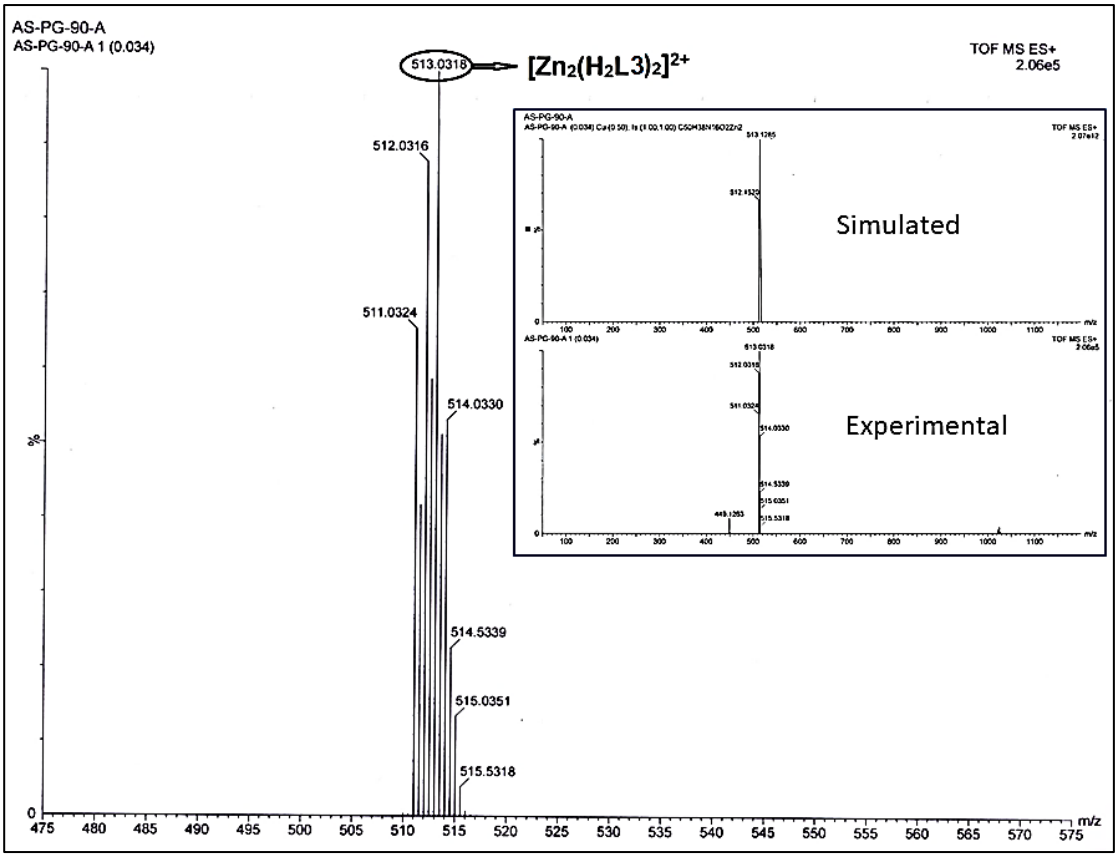

Fig. 3.2. ESI-MS$^+$ spectrum of $[Zn_2(\mathbf{H_2L3})_2]^{2+}$.

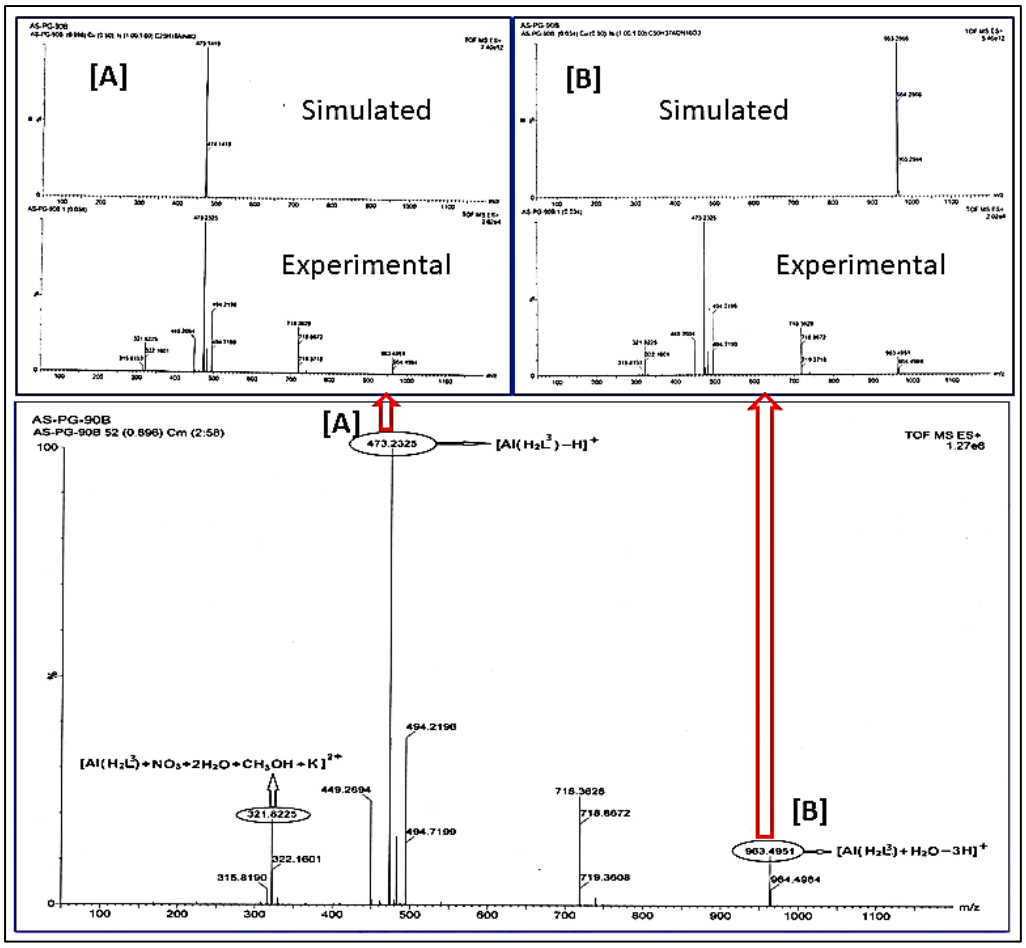

Fig. 3.3. ESI-MS$^+$ spectrum of [Al**(H$_2$L3)**-H]$^+$ and [Al$_2$**(H$_2$L3)**$_2$+H$_2$O-3H]$^+$.

3.3.2. Selectivity experiment of probe H$_3$L3 towards Zn^{2+} and Al^{3+} ions

3.3.2.1. Analysis of absorption spectral data

The selectivity of the chemosensor, **H$_3$L3** (2 × 10^{-5}M) among different metal ions was examined in HEPES buffer (1:9, MeOH:H$_2$O, v/v, pH 7.4) medium. In the UV-vis spectrum, free chemosensor **H$_3$L3** displayed well-defined bands at 295 and 400 nm, respectively, probably due to intramolecular π →π* or n→π* type transitions. As represented in **Fig. 3.4**, upon gradual addition of Zn^{2+} (0–1.2 equiv.), bands at 295 and 400 nm of free chemosensor **H$_3$L3** exhibited a significant decrease with the concomitant generation of two closely spaced absorption peaks at 448 and 473 nm. Whereas, for Al^{3+} ion (0–1.2 equiv.), a new peak appeared at 472 nm (**Fig. 3.5**). It suggests a strong interaction between **H$_3$L3** and Zn^{2+}/Al^{3+}. Different charge densities and radii

of the metal ion caused different spectral patterns. However, various metal ions, like Na^{+}, K^{+}, Ca^{2+}, Mg^{2+}, Ag^{+}, Mn^{2+}, Fe^{3+}, Co^{2+}, Ni^{2+}, Cu^{2+} , Pb^{2+}, Hg^{2+} and Cd^{2+} ions did not make notable changes on the absorption spectrum of probe **H_3L3**. Spectral data further used to establish the 1:1 binding stoichiometry of **H_3L3** in the presence of Zn^{2+}/Al^{3+} through Job′s plot analysis (**Fig. 3.6**).

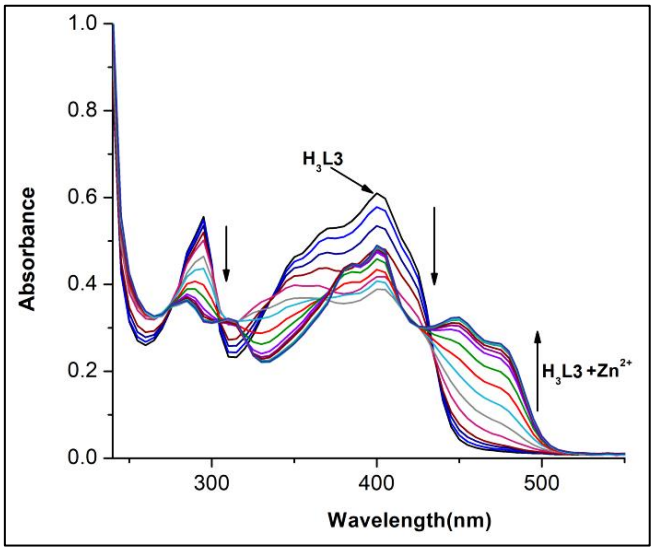

Fig. 3.4. Absorption titration study. Here, in **H_3L3** (20 µM) gradually Zn^{2+} (0-24µM in HEPES buffer, 1:9, MeOH:H_2O, v/v, pH 7.4) was added.

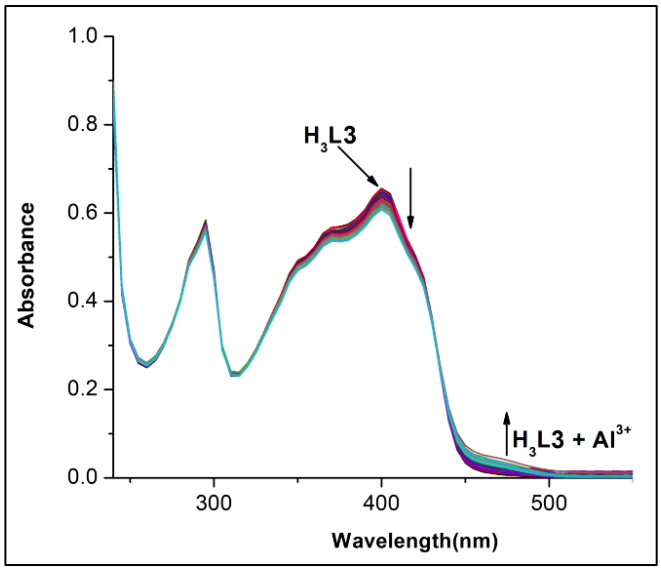

Fig. 3.5. Absorption titration study. Here, in **H_3L3** (20 µM) gradually Al^{3+} (0-24µM in HEPES buffer, 1:9, MeOH:H_2O, v/v, pH 7.4) was added.

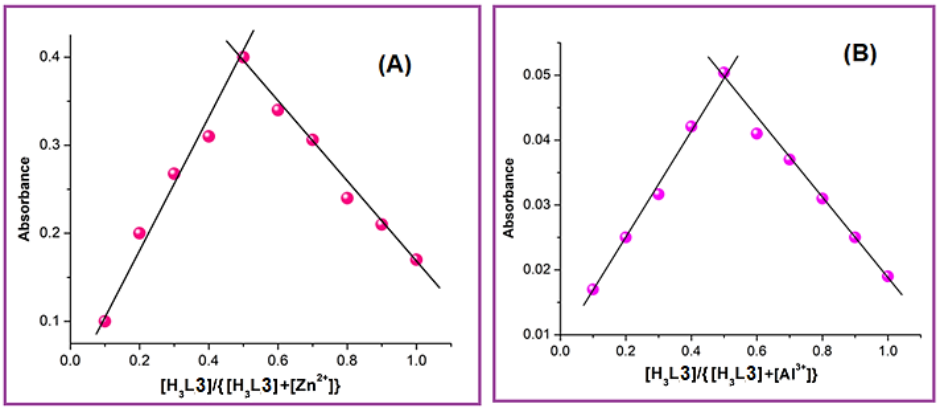

Fig. 3.6. 1:1 binding stoichiometry showed by Job's plot of complexes (A) **3.1** and (B) **3.2**, respectively. Symbols and solid lines represent the experimental and simulated profiles, respectively.

3.3.2.2. Fluorescence spectral studies

Free probe **H_3L3** was faintly fluorescent. A weak fluorescence peak was found at 610 nm when excited at 400 nm, (Fig. 3.7). This was probably due to the photo-induced electron transfer (PET) and -C=N isomerization processes. Here, photo-induced intra-molecular electron transfer (PET) from the HOMO of the donor imine nitrogen atoms to the excited fluorophoric moiety was responsible for excited state quenching. On gradual addition of Zn^{2+} and Al^{3+} metal ions (0–1.2 equiv.) to the **H_3L3** solution, huge enhancements of fluorescence intensity (~54 folds for Zn^{2+} and ~47 folds forAl^{3+}) have been observed. In the presence of Zn^{2+} the original emission peak has been blue-shifted to 510 nm whereas, in presence of Al^{3+} fluorescence maxima blue shifted to 505 nm (Fig. 3.8). In presence of Zn^{2+}/Al^{3+} ion rigidity of the molecule increases via metal coordination, which restricts free rotation around the H–C=N bond. Transfer of the imine-nitrogen lone pair to the metal centre also holds for the PET process. These two simultaneous effects are jointly accountable for fluorescence enhancement (CHEF effect). A significant enhancement of the quantum yield value of free **H_3L3** (0.03) to its metal-bound form (0.38 for **H_3L3** + Zn^{2+} and 0.26 for **H_3L3** + Al^{3+}) also supports the above fact (Table 3.1). Importantly,

the presence of other metal ions did not produce any significant fluorescence responses. A plot of fluorescence enhancement at 510 nm (505 nm for Al^{3+}) against increasing concentration of Zn^{2+} (or Al^{3+}) in the presence of probe gave a clear enhancement up to 1 equivalent of Zn^{2+} (or Al^{3+}) suggesting 1:1 binding between the probe and Zn^{2+} (or Al^{3+}). Fluorescence data was further utilized for Job′s plot analysis, which again proves 1:1 binding stoichiometry of these divalent and trivalent metal ions towards the chemosensor probe **H_3L3** (**Fig. 3.9**). Mass spectrometric data (Figs.S1-S3) also confirmed the formation of 1:1 complexes between **H_3L3** and the two metal ions, respectively. The binding constant values for Zn^{2+} and Al^{3+} ions were calculated using the Benesi–Hildebrand equation [3.50] which were 3.49×10^4 and 2.67×10^4 M^{-1}, respectively (**Fig. 3.10**). The detection limits towards Zn^{2+} and Al^{3+} ions were estimated to be 2.37×10^{-6} and 1.32×10^{-6} M (**Table 3.2**). The average fluorescence lifetime of the chemosensor **H_3L3**, complexes **3.1** and **3.2** were 0.17, 0.96, and 1.05 nS, respectively (**Fig. 3.11**, **Table 3.1**).

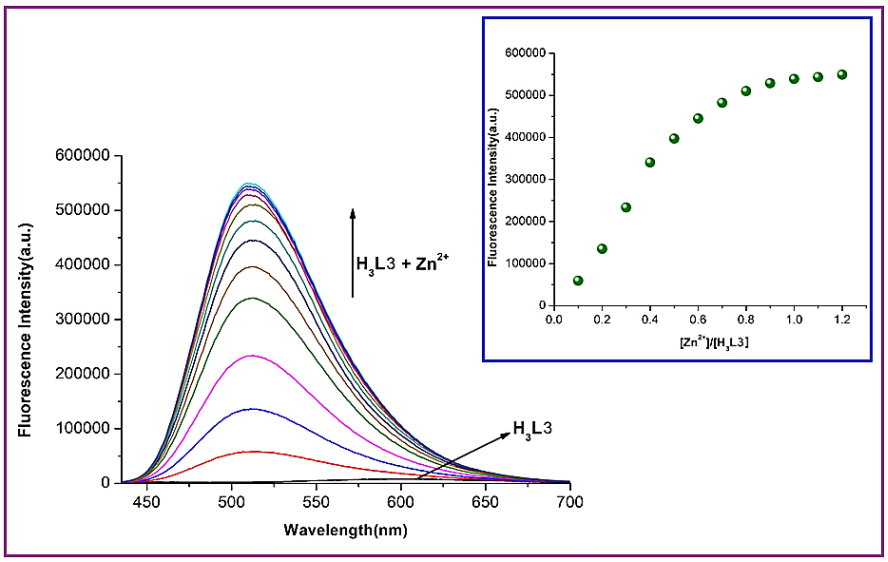

Fig. 3.7. Fluorescence titration experiment where **H_3L3** (20 μM) in HEPES buffer (1:9, MeOH:H_2O, v/v, pH 7.4) are gradually mixed with Zn^{2+} (0–24 μM) with λ_{em} = 510 nm (λ_{ex} = 400 nm). Inset: non-linear plot of fluorescence intensity vs. concentration of Zn^{2+} ion.

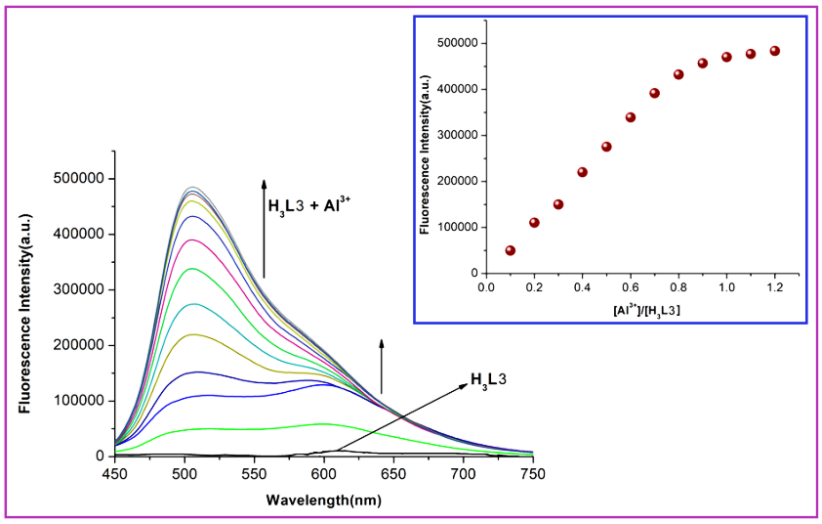

Fig. 3.8 Fluorescence titration experiment where **H_3L3** (20 μM) in HEPES buffer (1:9, MeOH:H_2O, v/v, pH 7.4) are gradually mixed with Al^{3+} (0–24μM) with λ_{em}= 510 nm (λ_{ex}= 400 nm). Inset: non-linear plot of fluorescence intensity vs. concentration of Al^{3+} ion.

Table 3.1. Data of lifetime (τ_f) and quantum yield (Φ) of **H_3L3** and complexes **3.1** and **3.2**.

	τ_f (ns) (average)	χ^2	Φ
H_3L3	0.17	1.115859	0.03
Complex **3.1**	0.96	1.120712	0.38
Complex **3.2**	1.05	1.017881	0.26

Table 3.2. Apparent binding constant (K) and LOD values of complexes **3.1** and **3.2** from spectrofluorometric measurement.

	K (M^{-1})	**LOD (M)**
Complex **3.1**	3.49×10^4	2.37×10^{-6}
Complex **3.2**	2.67×10^4	1.32×10^{-6}

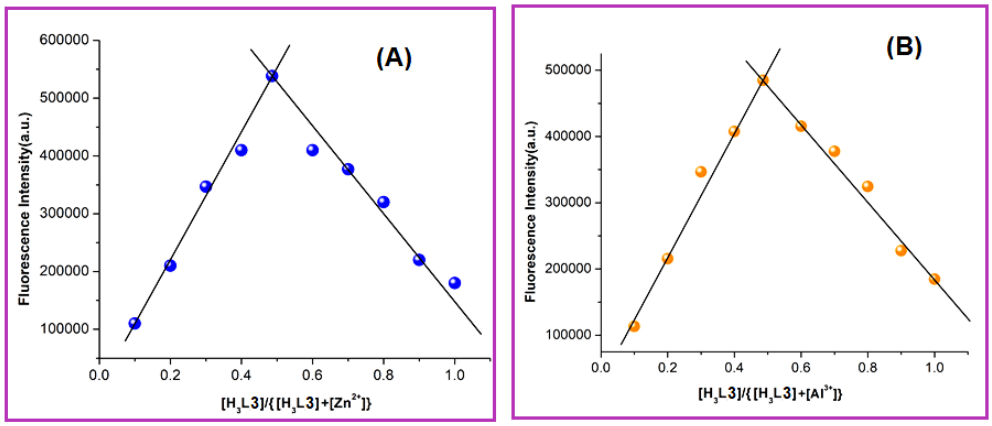

Fig. 3.9. Binding stoichiometry (1:1) has shown by Job's plot of complexes (A) **3.1** and (B) **3.2**, respectively. Symbols and solid lines represent the experimental and simulated profiles, respectively (λ_{ex} = 400 nm).

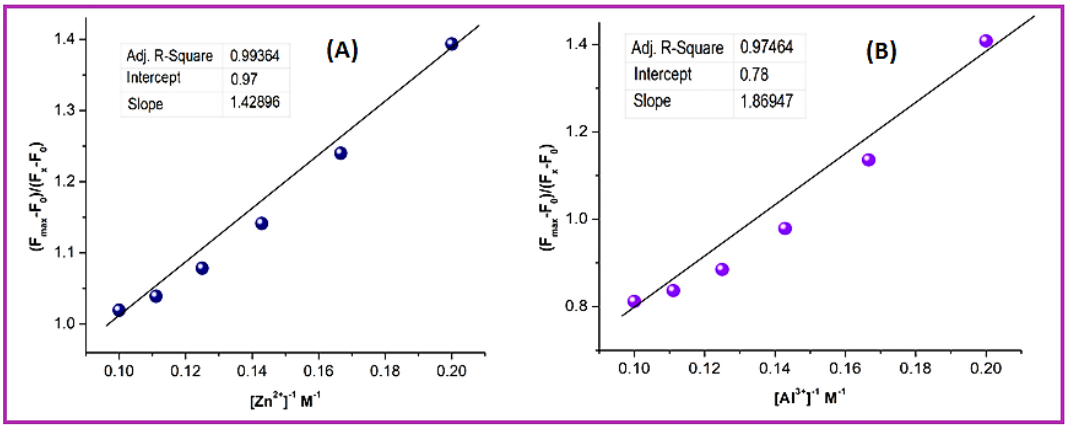

Fig. 3.10. Benesi-Hildebrand equation: A plot of $(F_{max} - F_0)/(F_x - F_0)$ vs 1/[M] for complexes (A) **3.1** and (B) **3.2**, respectively. Symbols and solid lines represent the experimental and simulated profiles, respectively.

The selectivity of the probe towards Zn^{2+} and Al^{3+} ions are also examined by performing a competition assay. When Zn^{2+} or Al^{3+} ions were added to **H_3L3** in large excess (5 equiv.) of other metal ions (Fig. 3.12), apart from the Cu^{2+} ion, where a small quenching has been observed, most of the ions showed fluorescence intensity unchanged (Figs. 3.13 and 3.14). This clearly indicates that the presence of most of the metal ions do not influence the fluorescence property of the probe.

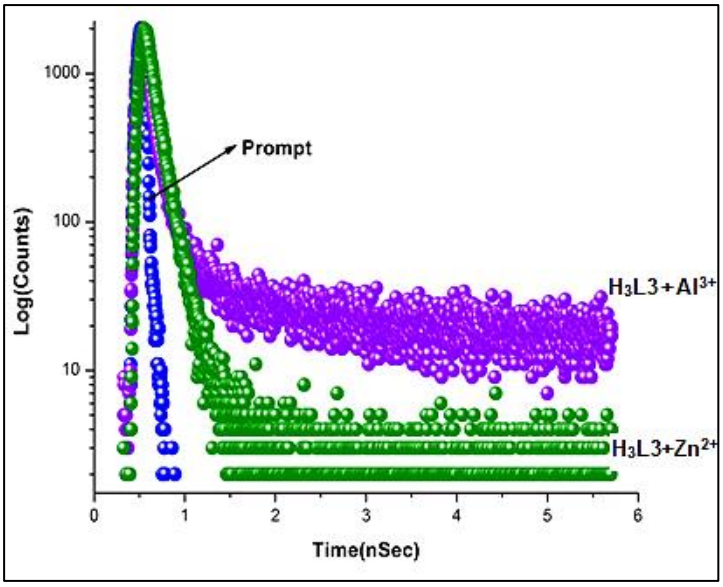

Fig. 3.11. Time-resolved fluorescence decay curves (logarithm of normalized intensity vs time in ns) of **H_3L3** in presence of ( ) Zn^{2+} ion and ( ) Al^{3+}ion, ( ) indicates decay curve for the scattered.

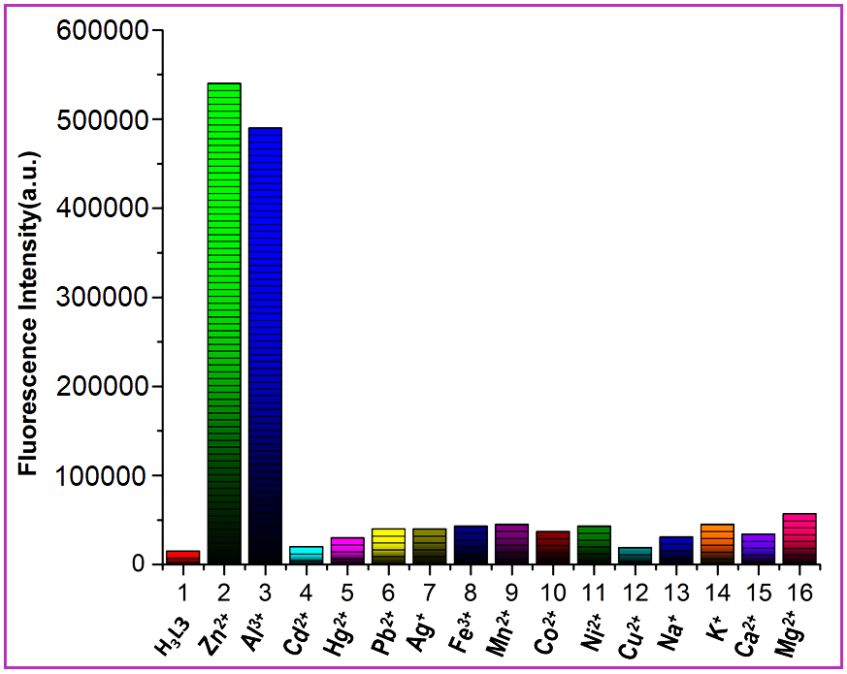

Fig. 3.12. Relative fluorescence intensity diagram of chemosensor (**H_3L3**) along with different cations in HEPES buffer (1:9, MeOH:H_2O, v/v, pH 7.4) medium (λ_{ex}= 400 nm). 1 = only **H_3L3** (20 µM); **H_3L3** (20 µM) + M^{n+} (100 µM), where M^{n+} = (2-Zn^{2+}, 3-Al^{3+}, 4-Cd^{2+}, 5-Hg^{2+}, 6-Pb^{2+}, 7-Ag^{+}, 8-Fe^{3+}, 9-Mn^{2+}, 10-Co^{2+}, 11-Ni^{2+}, 12-Cu^{2+}, 13-Na^{+}, 14-K^{+}, 15-Ca^{2+} and 16-Mg^{2+} respectively).

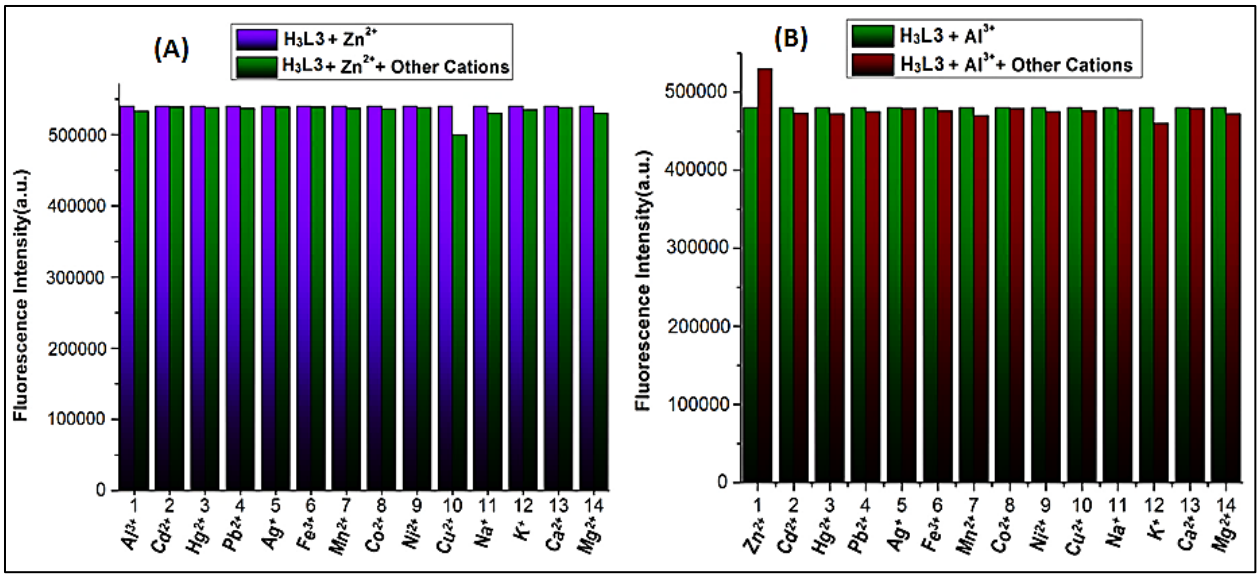

Fig. 3.13. Relative fluorescence intensity diagram of (A) [$\mathbf{H_3L3}$-Zn^{2+}] and (B) [$\mathbf{H_3L3}$-Al^{3+}] along with different cations in HEPES buffer medium (1:9, MeOH:H_2O, v/v, pH 7.4) (λ_{ex}= 400 nm), where 1-14=$\mathbf{H_3L3}$ (20 µM) + Zn^{2+}/Al^{3+} (20 µM) + M^{n+}(other metal ions) (100 µM) respectively).

The influence of different anions such as ATP^{2-}, $P_2O_7^{2-}$, PO_4^{3-}, HPO_4^{2-}, $H_2PO_4^-$, NO_3^-, Br^-, I^-, Cl^-, F^-, S^{2-}, $S_2O_3^{2-}$, $S_2O_8^{2-}$, SO_4^{2-}, HSO_3^-, PF_6^-, SCN^-, N_3^-, OCN^-, AcO^- on $\mathbf{H_3L3}$ had been examined in HEPES buffer (1:9, MeOH:H_2O, v/v, pH 7.4) medium. No significant fluorescence enhancement or quenching was found (**Fig. 3.14**). In competition assays where different common anions are added in presence of $\mathbf{H_3L3}$ and Zn^{2+} or Al^{3+} ions, similar observations have been noticed (**Fig. 3.15**).

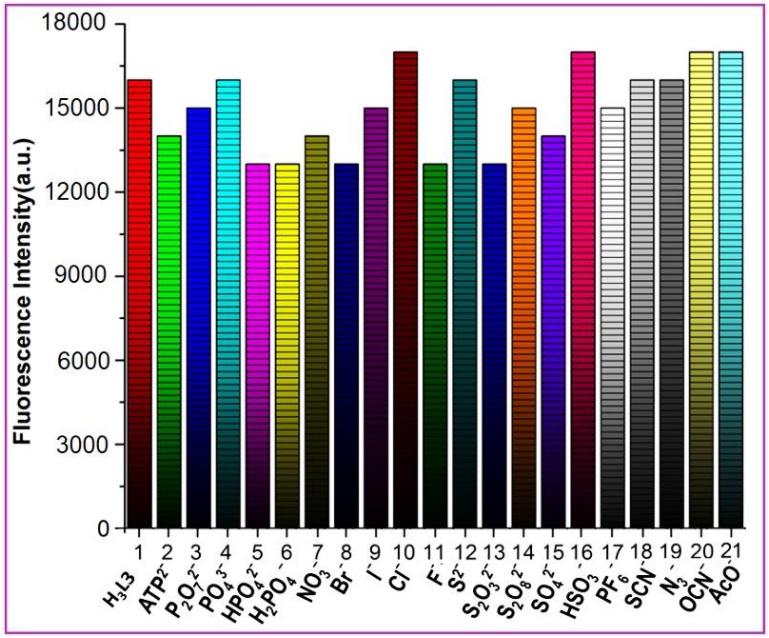

Fig. 3.14. Relative fluorescence intensity diagram of chemosensor (**H_3L3**) along with different anions in HEPES buffer (1:9, MeOH:H_2O, v/v, pH 7.4) (λ_{ex}= 400 nm) where 1=only **H_3L3** (20 µM); and 2-21=**H_3L3** (20 µM) + M^{n-} (anions/biomolecules) (100 µM).

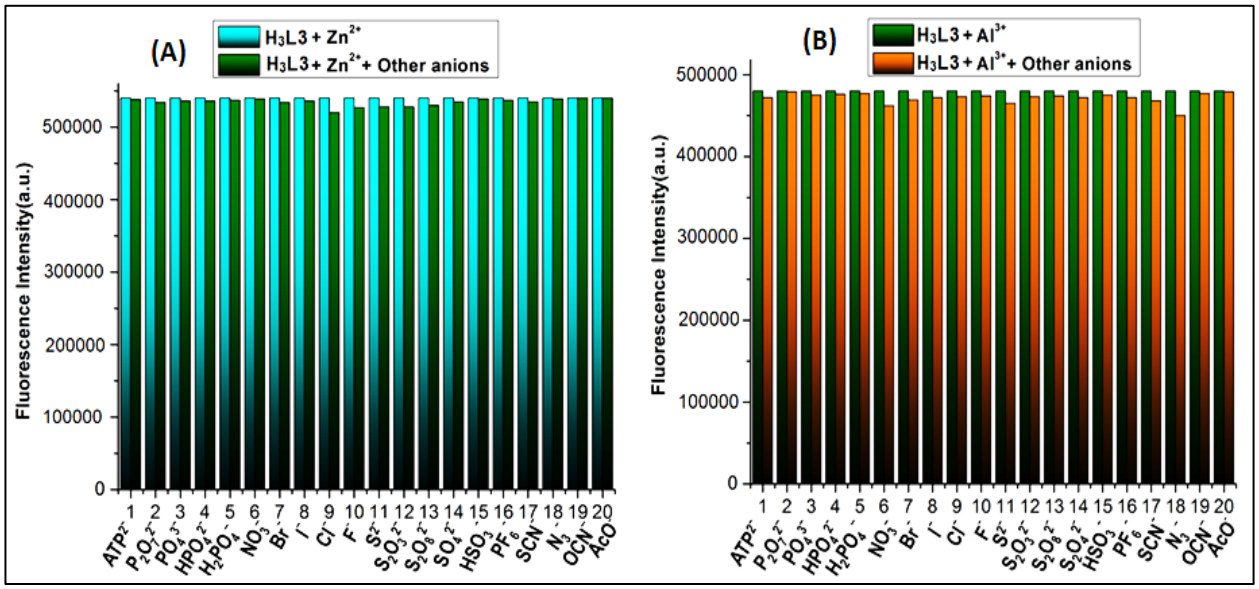

Fig. 3.15. Relative fluorescence intensity diagram of (A) [**H_3L3**-Zn^{2+}] and (B) [**H_3L3**-Al^{3+}] along with different anions in HEPES buffer medium (1:9, MeOH:H_2O, v/v, pH 7.4) (λ_{ex}= 400 nm). 1-20 = **H_3L3** (20 µM) + Zn^{2+}/ Al^{3+} (20 µM) + M^{n-} (anions/biomolecules) (100 µM).

The reversibility test and regeneration of the free probe are two important parameters to check its applicability as real-sample analysis. Where a strong chelating ligand such as, 1 equiv. of Na_2EDTA (sodium salt of ethylenediaminetetraacetic acid) solution was mixed with **H_3L3** and 1 equiv. of a Zn^{2+}/Al^{3+} ions solution. Initial green fluorescence vanished with generation of a colourless solution with very weak fluorescence due to the formation of a free probe and a metal-bound EDTA complex. Upon addition of extra 1 equiv. of metal ions, the initial green fluorescence was recovered instantaneously (**Fig. 3.16**). The colour of chemosensor (**H_3L3**) in the presence of different metal ions under UV and visible light is shown in **Fig. 3.17**.

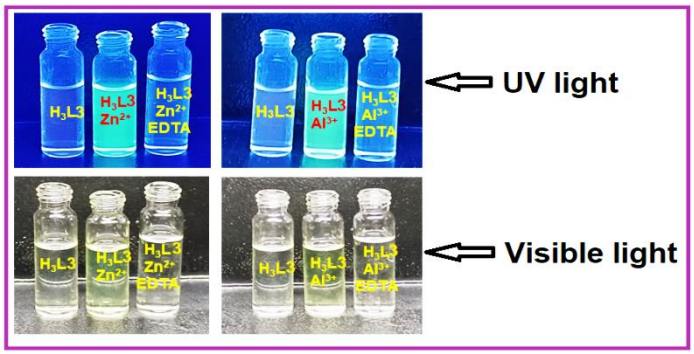

Fig. 3.16. Visual colour changes in reversibility experiment in HEPES buffer medium (1:9, MeOH:H_2O, v/v, pH 7.4). Here, **H_3L3** (20μM), **H_3L3** (20μM) + M^{n+} (Zn^{2+}/Al^{3+}) (20μM), **H_3L3** (20μM) + M^{n+} (Zn^{2+}/Al^{3+}) (20μM) + $EDTA^{2-}$ (20μM), respectively. Below images are taken under visible light and above images are taken under UV lamp.

Fig. 3.17. Colour changes of chemosensor (**H_3L3**) (20μM) under UV and Visible light when different metal ions in HEPES buffer (1:9, MeOH:H_2O, v/v, pH 7.4) medium are present.

As a part of the on-field applicability of the probe, we have utilised paper strip experiment to support its fluorescence sensing property. In this experiment, paper strips are dipped in free chemosensor and then charged with Zn^{2+} and Al^{3+} solutions separately. A significant colour change of the strips from light yellow to fluorescent green under UV light had been noticed (**Fig. 3.18**). Importantly, colour intensity remains unaffected by presence of different cations. The low detection limit of this paper-based chemosensor **H_3L3** (~10^{-6} M) suggests that this simple process could be effectively used for fast and selective fluorescence detection of Zn^{2+} and Al^{3+} for environmental sample analysis in remote areas where analytical instrumentation are limited.

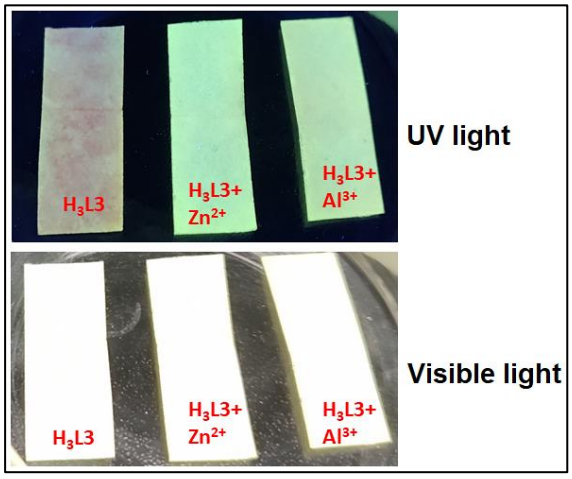

Fig. 3.18. Colour change of paper strips under visible light (below) and UV light (above) when absorbed with chemosensor **H_3L3** , **H_3L3** + Zn^{2+} and **H_3L3** + Al^{3+} , respectively.

3.3.2.3. Binding mode analysis

Experimental evidence for a strong interaction between probe **H_3L3** and Zn^{2+}/Al^{3+} ions had been achieved through several spectroscopic studies, such as FT-IR, UV–vis absorbance titration, and ^{1}H NMR titration. Binding of chemosensor **H_3L3** with Zn^{2+}/Al^{3+} generates noticeable changes in its IR spectrum, where the vibration band of –HC=N– group has been shifted to a lower wavenumber from 1609 to ~1545 cm^{-1}. These changes suggest coordination of

the imine N of **H_3L3** with Zn^{2+}/Al^{3+} centre. The appearance of a new peak around 1311 and 1323 cm^{-1} also confirmed the association of the nitrate ion (NO_3^-) in complexes **3.1** and **3.2**. Again in UV-Vis absorption titration of free **H_3L3** against Zn^{2+}/Al^{3+}, there is a gradual disappearance of bands at 295 and 400 nm with the evolution of new absorption peaks at 448 and 473 nm for Zn^{2+} and 472 nm for Al^{3+} ion. ^{1}H NMR studies were used in order to establish the complexation behaviour of probe **H_3L3** with the respective metal ions. The free chemosensor gives phenolic –OH, amine (H-NR) and imine (H-C=N) proton peaks at 12.88, 10.99 and 8.74 ppm, respectively. Aromatic protons appeared in the usual position, 8.43-7.75 ppm. Methyl protons were found at 2.31 ppm as expected (**Fig. 3.19**). In ^{13}C NMR, **H_3L3** imine carbon atoms appeared at 163.00 ppm. Aromatic carbon atoms appeared in the usual range 149.29-114.30 ppm (**Fig. 3.20**). In ^{1}H NMR of complex **3.1** phenolic –OH disappeared, amine and imine protons have shifted downfield and appeared at 12.48 and 9.18 ppm which is a clear indication of bonding between phenoxido oxygen, amine and imine nitrogens with metal. Aromatic protons shifted downfield in the range of 8.71-7.98 ppm also support the above facts (**Fig. 3.21**). In the ^{13}C NMR spectrum of complex **3.1**, imine carbon shifted downfield and appeared at 164.07 ppm. Aromatic carbon atoms were observed in the range 151.82-117.02 ppm (**Fig. 3.22**). On the contrary, in ^{1}H NMR of complex **3.2** both phenolic –OH and amine (H-NR) protons disappeared, and imine protons have shifted downfield and appear at 9.36 ppm. Aromatic protons are found within the range 9.16-8.07 ppm (**Fig. 3.23**). In ^{13}C NMR spectrum of complex **3.2** imine and aromatic carbon atoms appear at 163.02 ppm and within the range 151.56-116.40 ppm (**Fig. 3.24**). ^{1}H NMR titration experiments of the probe along with Zn^{2+} or Al^{3+} ions also confirmed the above observations (**Figs. 3.25** and **3.26**).

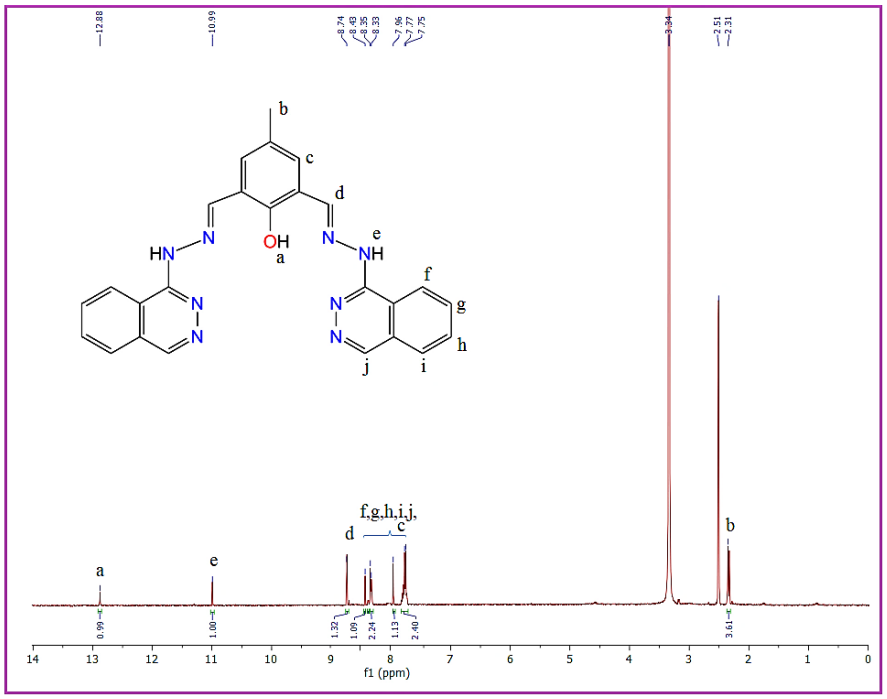

Fig. 3.19. ^{1}H NMR spectrum of **H_3L3** in DMSO-d_6 solvent.

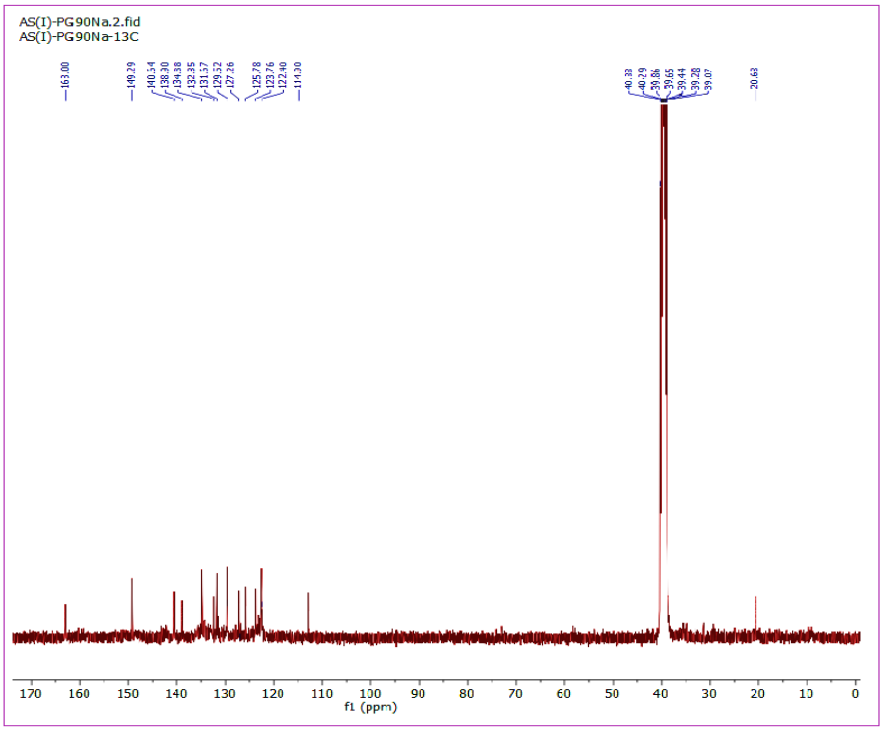

Fig. 3.20. ^{13}C NMR spectrum of **H_3L3** in DMSO-d_6 solvent.

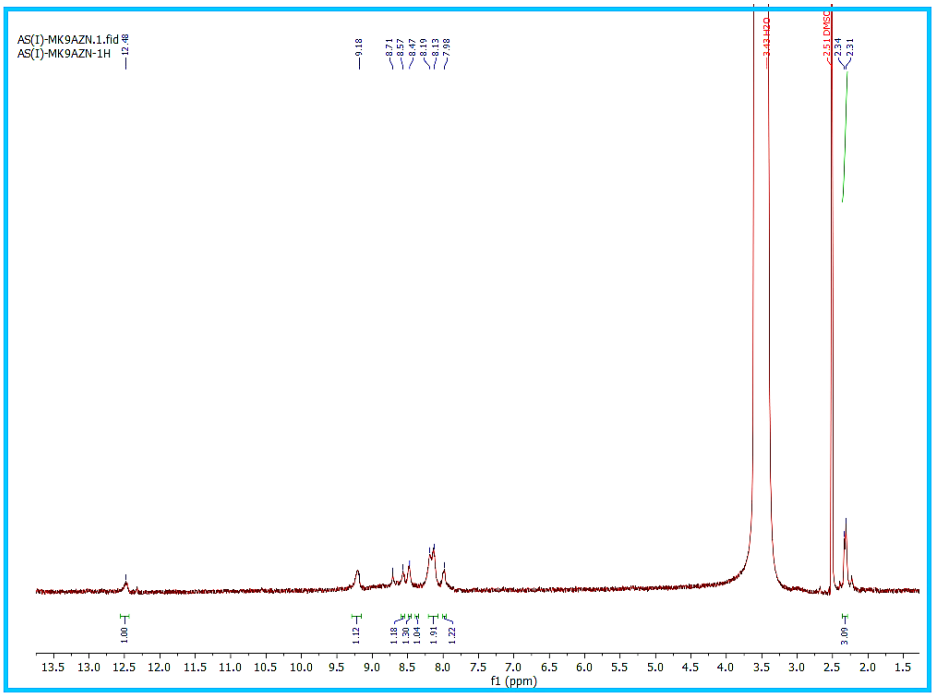

Fig. 3.21. ^{1}H NMR spectrum of complex **3.1** in DMSO-d_6 solvent.

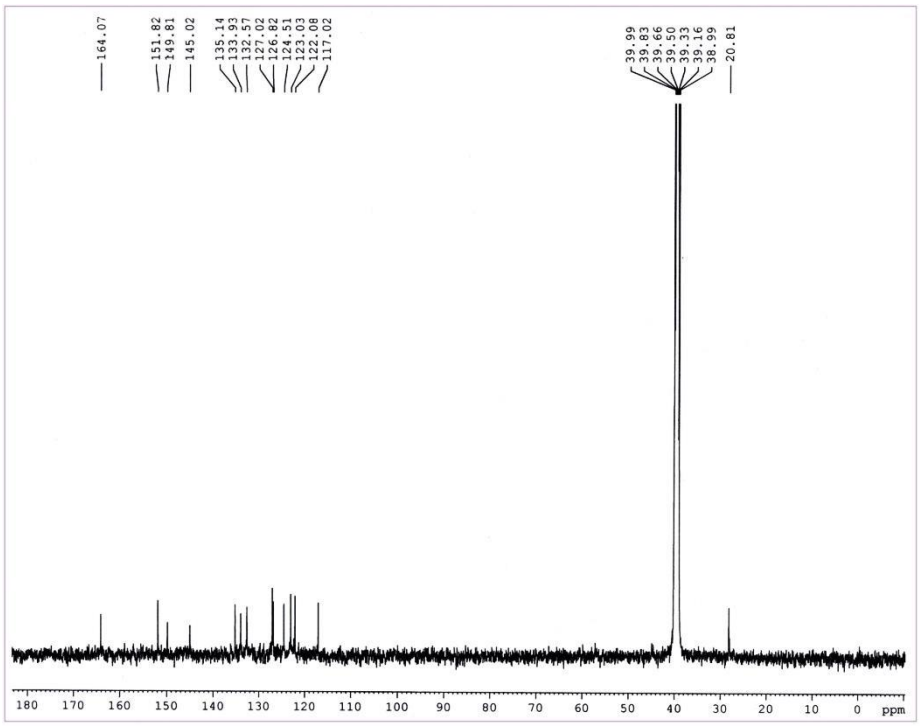

Fig. 3.22. ^{13}C NMR spectrum of complex **3.1** in DMSO-d_6 solvent.

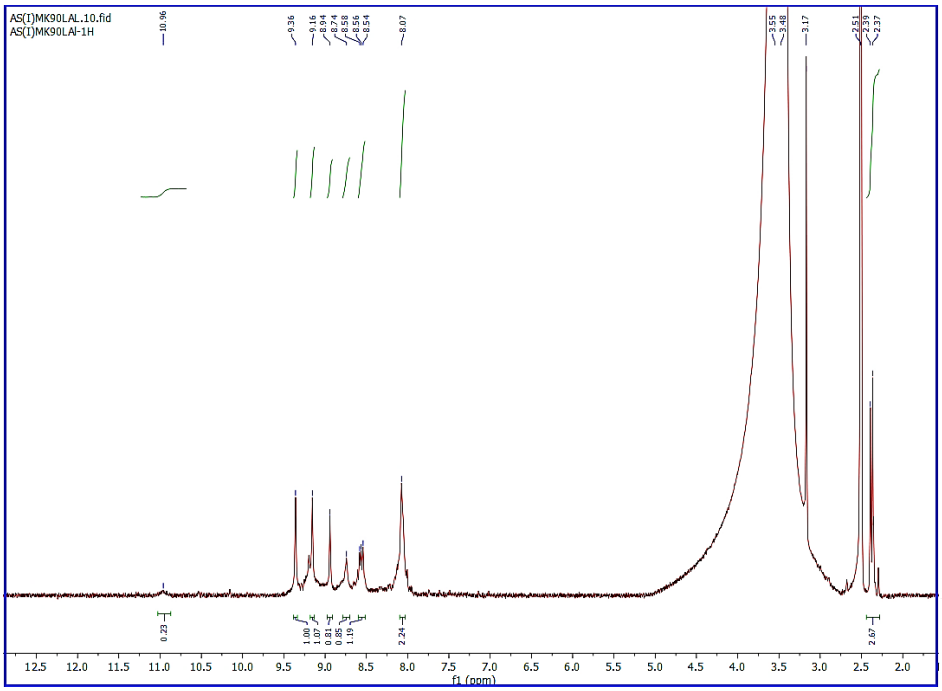

Fig. 3.23. ^{1}H NMR spectrum of complex **3.2** in DMSO-d_6 solvent.

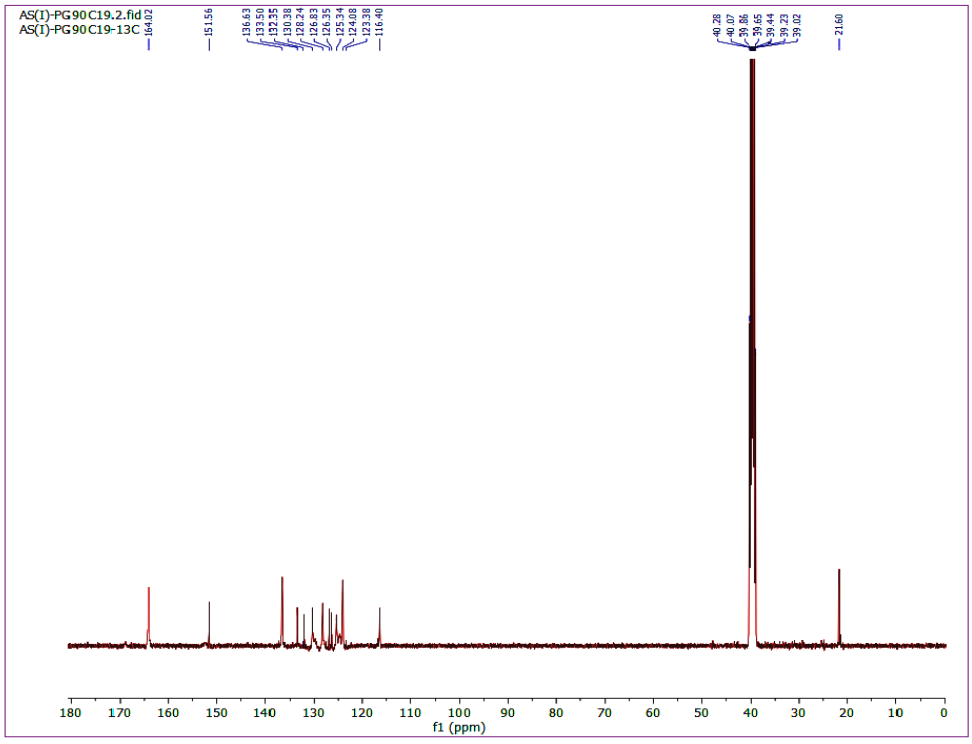

Fig. 3.24. ^{13}C NMR spectrum of complex **3.2** in DMSO-d_6 solvent.

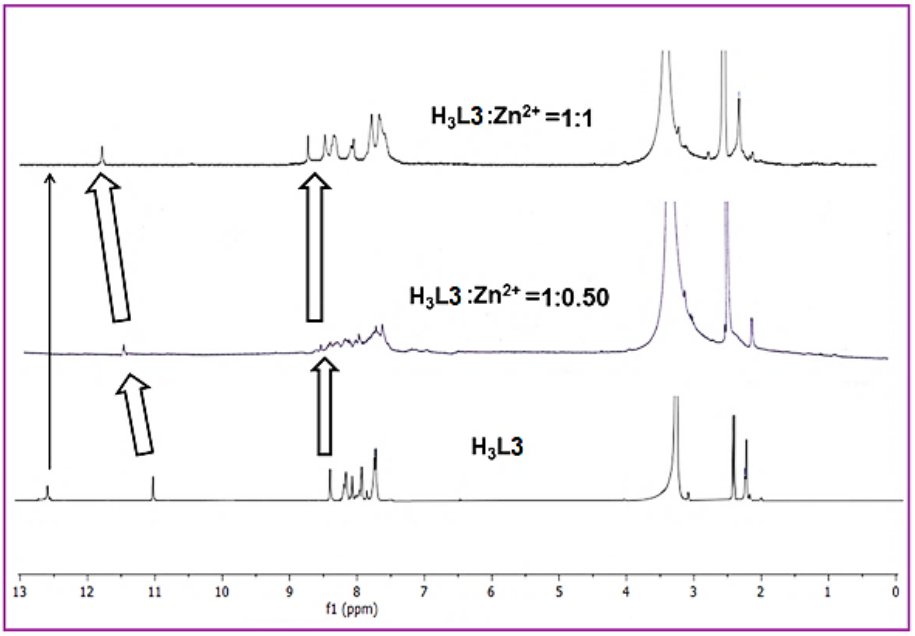

Fig. 3.25. ^{1}H-NMR titration of the free ligand (**H_3L3)** and with the addition of 0.50 and 1 equivalent of Zn^{2+} in DMSO-d_6 solvent.

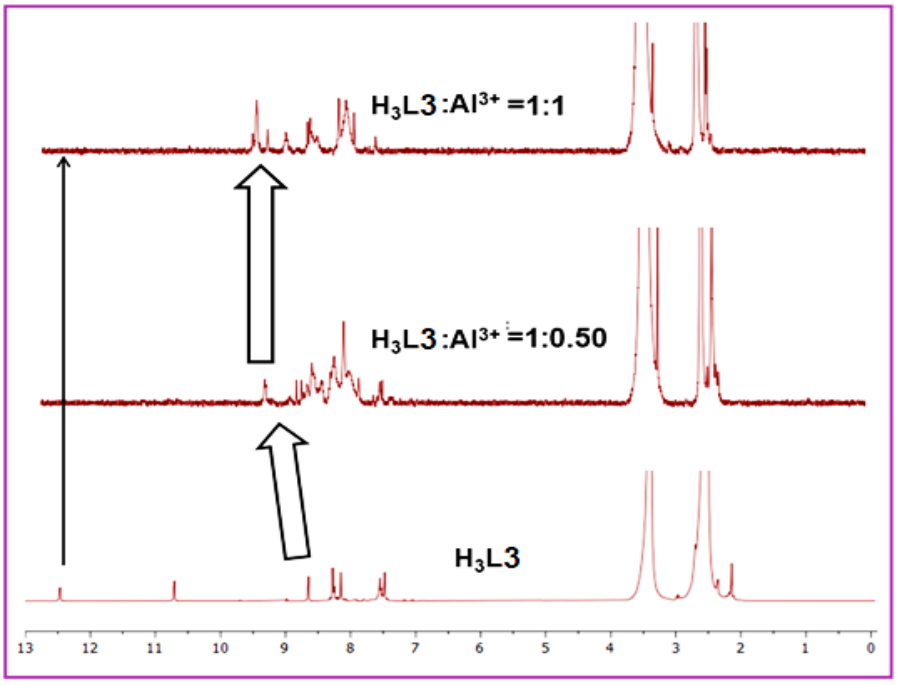

Fig. 3.26. ^{1}H-NMR titration of the free ligand (**H_3L3)** and with the addition of 0.50 and 1 equivalent of Al^{3+} in DMSO-d_6 solvent.

Study of emission intensity of the chemosensor (**H_3L3**) in free state and metal bound form at different pH were important in order to study their live cell imaging and environmental sample analysis. Fluorescence intensity of the free chemosensor has been found to be unchanged throughout pH window (**Fig. 3.27**). In presence of Zn^{2+}/Al^{3+} ions, up to pH 6 no complex formation occur resulting no fluorescence enhancement. On the pH scale 6-7 fluorescence intensity increased abruptly indicating metal-chemosensor complex formation. Fluorescence intensity remains unchanged up to pH 12, indicating stability of the compounds at pH 12. Within pH scale 6-7, fluorescence enhancement is probably due to deprotonation of the phenolic proton followed by coordination of amine, imine N and phenoxido O with the metal centre, where photo-induced electron transfer (PET) process has been restricted, followed by the initiation of CHEF process, resulting in the fluorescence enhancement. Therefore, **H_3L3** can act as a selective fluorescent probe for Zn^{2+}/Al^{3+} ions in biological cell imaging under physiological conditions.

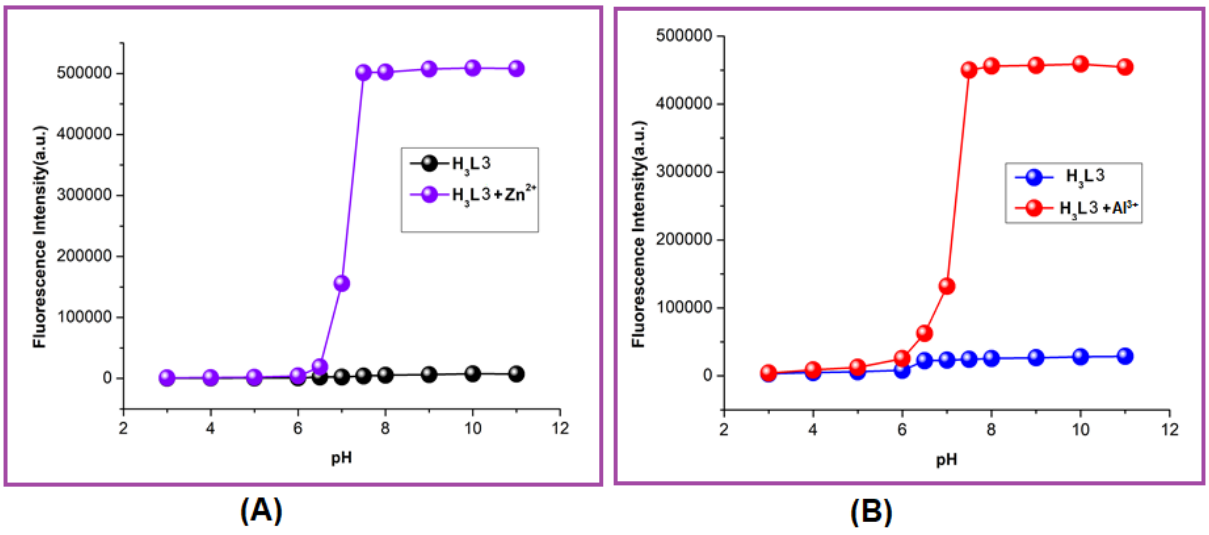

Fig. 3.27. Effect of pH on fluorescence intensity of **H_3L3** (20 µM) in absence and presence of (A) Zn^{2+} (20 µM) and (B) Al^{3+} (20 µM) ions, respectively in HEPES buffer medium.

3.3.3. DFT and TDDFT

DFT calculations were performed in order to better understand the complexation between the chemosensor (**H_3L3**) with Zn^{2+} and Al^{3+} ions as well as their structural parameters. Furthermore, contributions of M.O.s which are participated in electronic transitions were analyzed by TDDFT studies. Using TDDFT analysis, we get an idea of the quantity of energy associated with different transitions and the contribution from ligand and metal centres in the respective M.O.s. DFT/B3LYP method had been performed to optimize the geometries of chemosensor (**H_3L3**), complexes **3.1** and **3.2**. Interestingly, bisphenoxido-bridged dinuclear (Zn^{2+}/Al^{3+}) structures had been optimised for both complexes **3.1** and **3.2**. In complexes **3.1** and **3.2** metal centres, (Zn^{2+}/Al^{3+}) are connected by two $\mu_{1,1}$ phenoxido bridged O, two pthalazino N and two imine N atoms of the chemosensor in N_4O_2 fashion, giving rise to a distorted octahedral structure (**Figs. 3.28** and **3.29**). Some calculated bond distances and bond angles of **3.1** and **3.2** are found in **Table 3.3**. In free chemosensor, the electron density of LUMO is basically concentrated over one of the pthalazino unit, the imine bond and 4-methyl phenol. In complexes **3.1** and **3.2** electron density in both LUMO and HOMO were found to be ligand based. Energy of important M.O.s of **H_3L3**, complexes **3.1** and **3.2** are listed in **Table 3.4**.

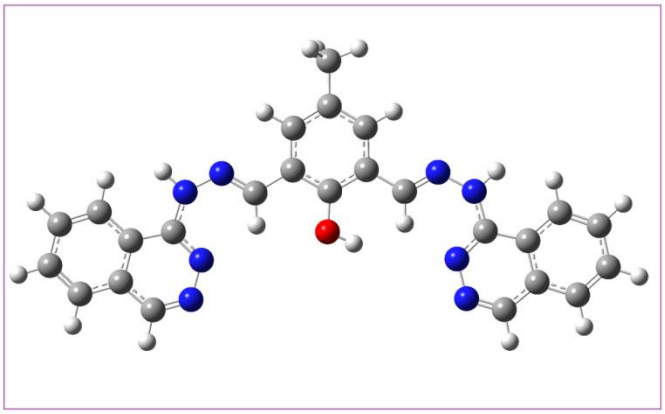

Fig. 3.28. DFT optimized structure of chemosensor **H_3L3**.

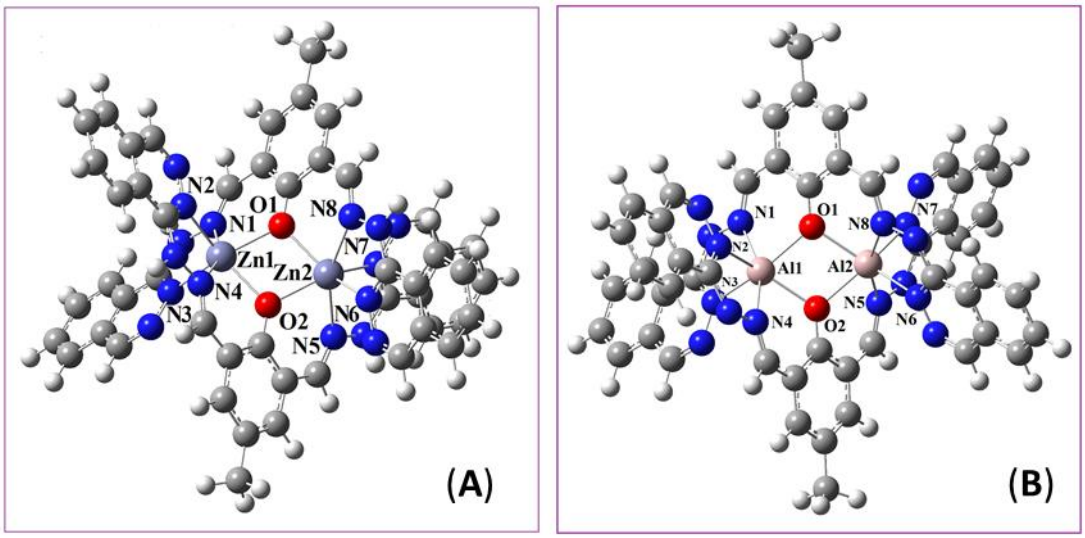

Fig. 3.29. DFT optimized structure of (A) complex **3.1** and (B) complex **3.2**, respectively.

Table 3.3. Bond lengths (Å) and bond angles (°) of optimized structure of complexes **3.1** and **3.2** (B3LYP/6-31+G(d) basis set).

Complex **3.1**	Calculated	Complex **3.2**	Calculated
Zn1-O1	2.116	Al1-O1	1.963
Zn1-O2	2.116	Al1-O2	1.963
Zn2-O1	2.117	Al2-O1	1.963
Zn2-O2	2.117	Al2-O2	1.963
Zn1-N1	2.284	Al1-N1	2.149
Zn1-N2	2.204	Al1-N2	2.025
Zn1-N3	2.204	Al1 -N3	2.025
Zn1-N4	2.284	Al1-N4	2.149
Zn2-N5	2.282	Al2-N5	2.148
Zn2-N6	2.205	Al2-N6	2.024

Zn2-N7	2.204	Al2-N7	2.024
Zn2-N8	2.282	Al2-N8	2.148
Zn1⋯ Zn2	3.354	Al1⋯ Al2	3.201
N1- Zn1-O1	76.41	N1-Al1-O1	78.31
N4- Zn1-O2	76.40	N4- Al1-O2	78.31
N1- Zn1-N2	93.85	N1- Al1-N2	92.44
N2- Zn1-N3	102.09	N2- Al1-N3	102.65
N3- Zn1-N4	93.86	N3- Al1-N4	92.43
N8- Zn2-O1	76.42	N8- Al2-O1	78.40
N5- Zn2-O2	76.42	N5- Al2-O2	78.40
N5- Zn2-N6	93.98	N5- Al2-N6	92.51
N6- Zn2-N7	102.04	N6- Al2-N7	102.45
N7- Zn2-N8	93.98	N7- Al2-N8	92.51
Zn1-O1-Zn2	104.79	Al1-O1-Al2	109.17
Zn1-O2-Zn2	104.79	Al1-O2-Al2	109.17

Table 3.4. Energy (eV) of selected M.O.s of chemosensor (**H_3L3**), complexes **3.1** and **3.2**.

	H_3L3	Complex **3.1**	Complex **3.2**
LUMO+4	-1.05	-5.57	-6.01
LUMO+3	-1.22	-5.89	-6.11
LUMO+2	-1.29	-5.99	-6.13
LUMO+1	-1.66	-6.01	-6.9
LUMO	-1.87	-6.13	-6.91
HOMO	-5.57	-9.44	-8.86
HOMO-1	-5.62	-9.5	-8.9
HOMO-2	-6.46	-10.01	-10.09
HOMO-3	-6.48	-10.03	-10.09
HOMO-4	-6.53	-10.59	-10.2

We used the B3LYP/CPCM method with same basis sets in water for TDDFT calculations. Theoretically obtained electronic transitions for **H_3L3** and complexes **3.1**, **3.2** are given in **Table 3.5**, and contour plots of relevant molecular orbitals are given in **Table 3.6**. Theoretically obtained electronic transitions for the chemosensor (**H_3L3**), complexes **3.1** and **3.2** match well with the experimental data. From theoretical calculations, we found that in the case of **H_3L3** absorption bands appeared at 308 and 393 nm (**Fig. 3.30**). These bands are assigned as HOMO-1→LUMO+2 (33%), HOMO→LUMO+3 (34%) and HOMO→ LUMO (81%). In complex **3.1** important transitions are HOMO→LUMO (99%) and HOMO-1→LUMO (80%) (**Fig. 3.31** and **Table 3.5**). For complex **3.2** major peaks appeared at 473 nm for transitions HOMO-3→LUMO (10%), HOMO-3→LUMO+1 (22%) (**Table 3.5** and **Fig. 3.31**). It has been observed that HOMO and LUMO of free chemosensor were better stabilised in their metal-

bound form. The HOMO-LUMO energy gap of free probe (3.7 eV) decreased appreciably in its Zn^{2+} or Al^{3+} bound complexes (3.31 and 1.95 eV, respectively).

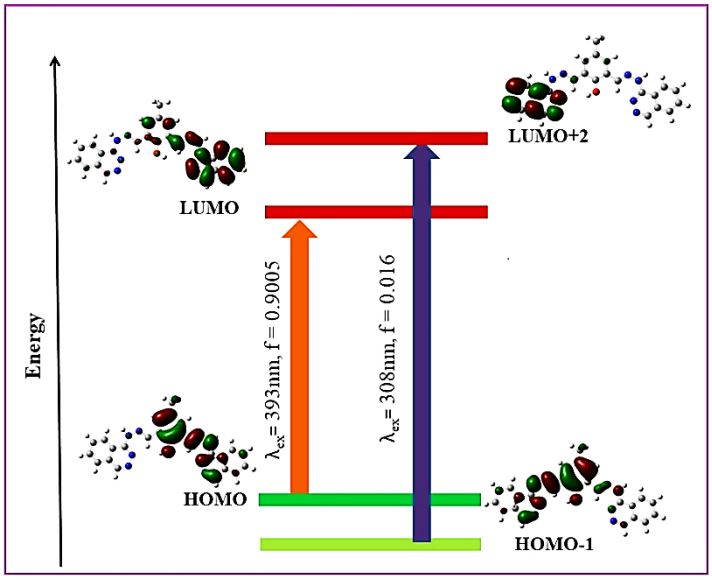

Fig. 3.30. Pictorial representation of key transitions of chemosensor **H_3L3**.

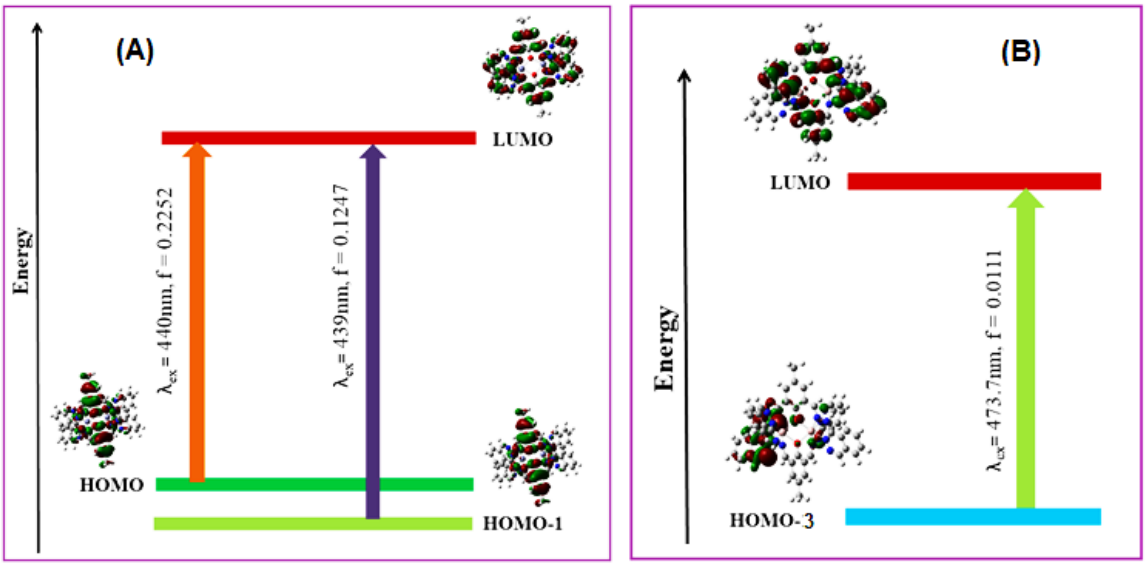

Fig. 3.31. Pictorial representation of key transition of complexes (A) **3.1** and (B) **3.2**, respectively.

Table 3.5. Electronic transition calculated by TDDFT using B3LYP/CPCM method in water solvent of chemosensor (**H_3L3**), complexes **3.1** and **3.2**.

	$E_{ex.}$ (ev)	$\lambda_{ex.}$ (nm)	Osc. Strength (f)	Key transition	Transition assigned
H_3L3	3.15	393	0.9005	HOMO→ LUMO (81%) HOMO-1→LUMO (13%)	$n\rightarrow\pi^*$
	4.02	308	0.016	HOMO-1→ LUMO+2 (33%) HOMO→LUMO+3 (34%)	$\pi\rightarrow\pi^*$
Complex **3.1**	2.82	440	0.2252	HOMO→LUMO (99%)	$n\rightarrow\pi^*$ or $\pi\rightarrow\pi^*$
	2.84	439	0.1247	HOMO-1→LUMO (80%) HOMO→LUMO+1 (17%)	$n\rightarrow\pi^*$ or $\pi\rightarrow\pi^*$
Complex **3.2**	2.62	473	0.0111	HOMO-3→ LUMO (10%) HOMO-3→LUMO+1 (22%)	$n\rightarrow\pi^*$ or $\pi\rightarrow\pi^*$

Table 3.6. Contour plots of some selected molecular orbital of **H_3L3**, complexes **3.1** and **3.2**.

	H_3L3	**Complex 3.1**	**Complex 3.2**
LUMO+4	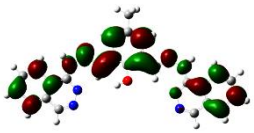	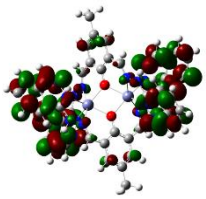	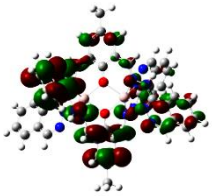
LUMO+3		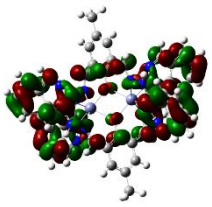	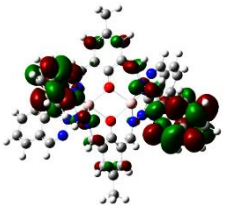

LUMO+2	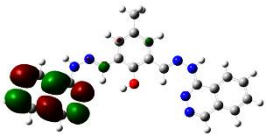	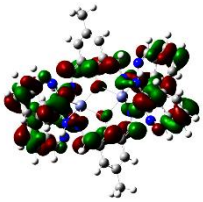	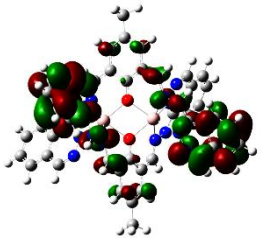
LUMO+1	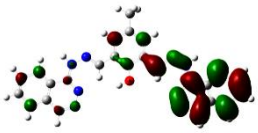	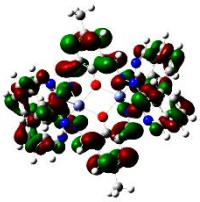	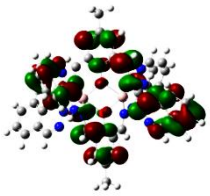
LUMO	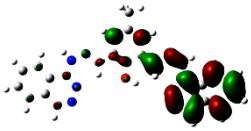	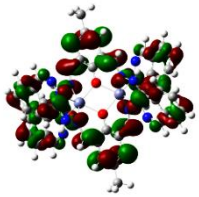	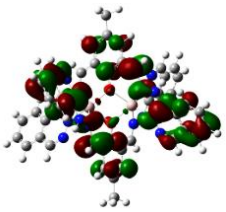
HOMO	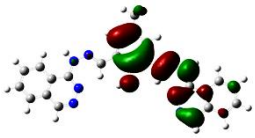		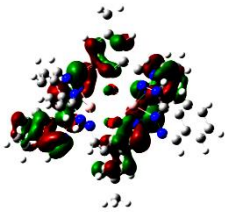
HOMO-1		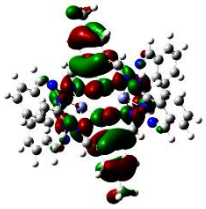	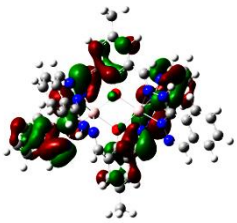

HOMO-2	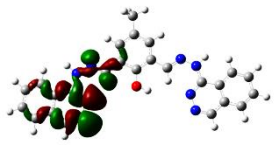	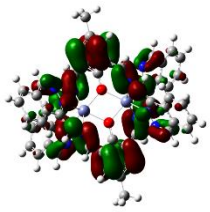	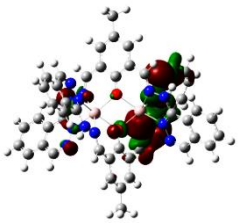
HOMO-3	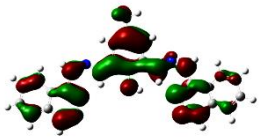	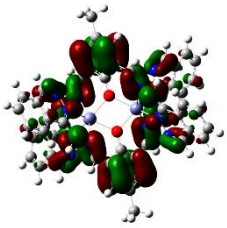	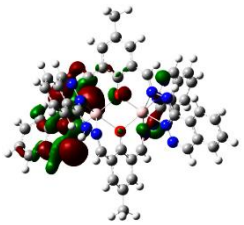
HOMO-4	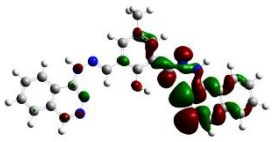	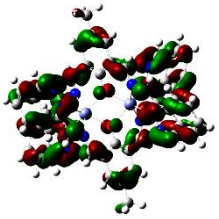	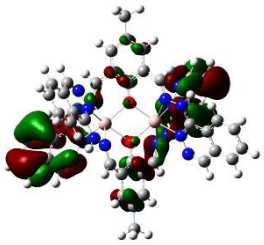

3.3.4. Application of H_3L3 in living cell imaging studies

Cell imaging study has been examined with *HeLa* cells where the probe **H_3L3** serves as an efficient luminescent bio-probe towards Zn^{2+} and Al^{3+} ions (**Fig. 3.32**). Initially, MTT assay was performed to evaluate the toxicity of probe **H_3L3** at different levels of concentrations in the WI-38 cell line. The probe **H_3L3** was amicable towards cells viability upto100 μM concentration (**Fig. 3.33**). In fluorescence microscopy the cells are non-fluorescent in the presence of free **H_3L3**. Green fluorescence is detected when cells are treated with Zn^{2+} or Al^{3+} ions.

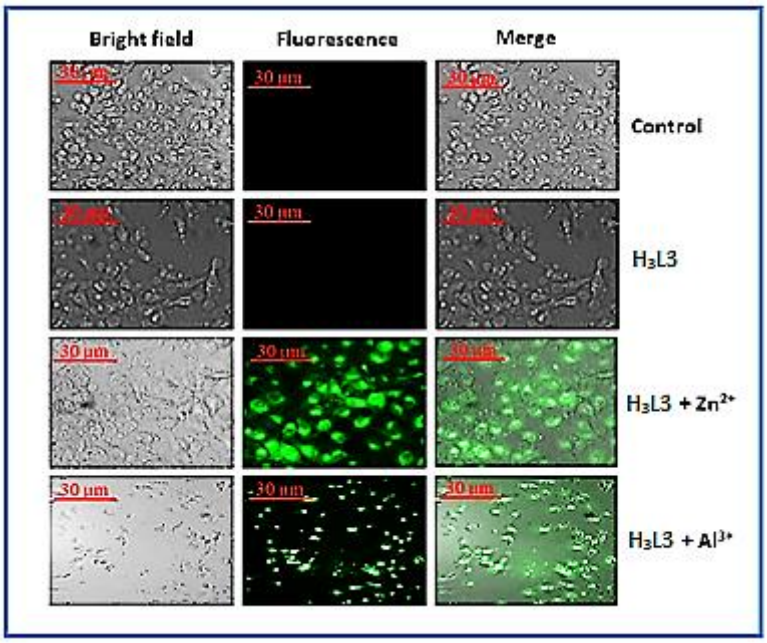

Fig. 3.32. Microscopic images (bright field, fluorescence and merged) of free HeLa (Control), HeLa cells in presence of **H_3L3** (20 µM), **H_3L3** (20 µM) + Zn^{2+} (20 µM), **H_3L3** (20 µM) + Al^{3+} (20 µM).

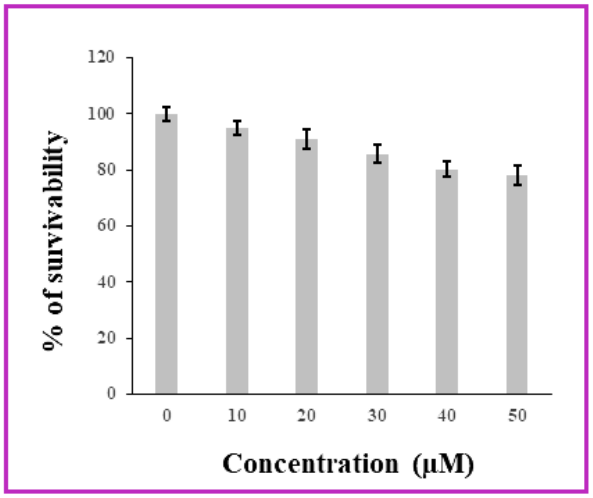

Fig. 3.33. Cell survivability of WI-38 cells exposed to the ligand (**H_3L3**).

3.4. Conclusion

In this work, the development of a DFP-pthalazine based multiple metal ions detector **H_3L3** has been described. Chemosensor (**H_3L3)** is used for detection of metal ions Zn^{2+} and Al^{3+}, respectively. **H_3L3** exhibits remarkable fluorescence sensing properties towards Zn^{2+} (~54-fold) and Al^{3+} (~47-fold) ions in HEPES buffer (1:9 MeOH:H_2O, v/v, pH 7.4) medium. Strong emission at 510 and 505 nm has been found in the presence of Zn^{2+} and Al^{3+} ions when excited at 400 nm, which is attributed to the arrest of the photo-induced electron transfer (PET) process with the simultaneous generation of chelation-enhanced fluorescence (CHEF). 1:1 binding stoichiometry between **H_3L3** and metal ions has been calculated from Job′s plot analysis. It is further supported by ESI-Mass analysis and DFT calculations. Theoretical calculations show coordination of metal ions with phenoxido oxygens, imine nitrogens, and pthalazine nitrogens which also support fluorescence enhancement due to CHEF mechanism. We have successfully proved the reversibility and regeneration behaviour of the chemosensor in presence of Na_2EDTA. Low limit of detection (LOD), stronger association constant of **H_3L3** towards Zn^{2+} (2.37×10^{-6} M and 3.49×10^{4} M^{-1}) and Al^{3+} (1.32×10^{-6} M and 2.67×10^{4} M^{-1}) ions indicate its high level of sensitivity towards bio-imaging studies. **H_3L3** successfully used in paper strip for identification of Zn^{2+} and Al^{3+} ions. It is further used in biological samples (cervical cancer cell) for detection of Zn^{2+} and Al^{3+} ions.

3.5. References

[3.1] P. Wang, J. X. Fu, K. Yao, Y. X. Chang, K. X. Xu, Y. Q. Xu, Sens. Actuators B: Chem. 273 (2018) 1070–1076.

[3.2] H. N. Kim, W. X. Ren, J. S. Kim, J. Yoon, Chem. Soc. Rev. 41 (2012) 3210–3244.

[3.3] G. Aragay, J. Pons, A. Merkoçi, Chem. Rev. 111 (2011) 3433–3458.

[3.4] A. T. Wright, E. V. Anslyn, Chem. Soc. Rev. 35 (2006) 14-28.

[3.5] V. Amendola, L. Fabbrizzi, Chem. Commun. (2009) 513-531.

[3.6] L. Prodi, New J. Chem. 29 (2005) 20-31.

[3.7] J. Yoon, S. K. Kim, N. J. Singh, K. S. Kim, Chem. Soc. Rev. 35 (2006) 355-360.

[3.8] A. W. Czarnik, ACS Symposium Series; American Chemical Society: Washington, DC, 1993.

[3.9] B. C. Dickinson, D. Srikun, C. J. Chang, Curr. Opin. Chem. Biol. 14 (2010) 50-56.

[3.10] H. Kobayashi, M. Ogawa, R. Alford, P. L. Choyke, Y. Urano, Chem. Rev. 110 (2010) 2620-2640.

[3.11] R. W. Sinkeldam, N. J. Greco, Y. Tor, Chem. Rev. 110 (2010) 2579-2619.

[3.12] (a) P. Ghorai, S. Banerjee, D. Nag, S. K. Mukhopadhyay, A. Saha, J. Luminescence 205 (2019) 197–209; (b) J. Mandal, P. Ghorai, K. Pal, P. Karmakar, A. Saha, J. Luminescence 205 (2019) 14–22; (c) P. Ghorai, S. G. Chowdhury, K. Pal, J. Mandal, P. Karmakar, A. Franconetti, A. Frontera, S. Blasco, E. G. Espana, P. P. Parui, A. Saha, Inorg. Chem. 61 (2022) 1982−1996; (d) M. Khatun, P. Ghorai, J. Mandal, S. G. Chowdhury, P. Karmakar, S. Blasco, E. G. Espana, A. Saha, ACS Omega 8 (2023) 7479−7491.

[3.13] Y. J. Lee, C. Lim, H. Suh, E. J. Song, C. Kim, Sens. Actuators B: Chem. 201 (2014) 535–544.

[3.14] S. Erdemir, O. Kocyigit, Sens. Actuators B Chem. 273 (2018) 56–61.

[3.15] S. A. Lee, G. R. You, Y. W. Choi, H. Y. Jo, A. R. Kim, I. Noh, S. J. Kim, Y. Kim, C. Kim, Dalton Trans. 43 (2014) 6650–6659.

[3.16] (a) J. Fu, Y. Chang, B. Li, X. Wang, X. Xie, K. Xu, Spectrochim. Acta Part A: Mol. Biomol. Spectroscopy 225 (2020) 117493; (b) J. Fu, Y. Chang, B. Li, H. Mei, L. Yang, K. Xu, Analyst 144 (2019) 5706; (c) X. J. Yan, Y. Y. Gao, H. B. Liu, X. Qiao, C. Z. Xie, Q. Z. Li, W. Z. Gao, H. B. Sun, J. Y. Xu, Spectrochim. Acta Part A: Mol. Biomol. Spectroscopy 261 (2021) 120067; (d) X. J. Sun, T. T. Liu, N. N. Li, S. Zeng, Z. Y. Xing, Spectrochim. Acta Part A: Mol. Biomol. Spectroscopy 228 (2020) 117786; (e) Z. Wang, S. Cui, S. Qiu, S. Pu, J. Photochem. Photobiol. A: Chemistry 376 (2019) 185–195; (f) X. Lu, M. Wu, S. Wang, J. Qin, P. Li, Dye. Pigm. 203 (2022) 110372; (g) Y. Xu, H. Wang, J. Zhao, X. Yang, M. Pei, G. Zhang, Y. Zhang, New J. Chem. 43 (2019) 14320; (h) Y. R. Chiou, J. H. Chen, C. H. Hu, A. T. Wu, Inorg. Chim. Acta 502 (2020) 119295; (i) S. Maity, M. Shyamal, R. Maity, N. Mudi, P. Hazra, P. K. Giri, S. S. Samanta, S. Pyne, A. Misra, Photochem. Photobiol. Sci. 19 (2020) 681; (j) S. Erdemir, O. Kocyigit, Sensors & Actuators: B. Chemical 273 (2018) 56–61; (k) D. Aydin, Talanta 210 (2020) 120615; (l) G. Zhao, G. Wei, Z. Yan, B. Guo, S. Guang, R. Wu, H. Xu, Analytica Chimica Acta 1095 (2020) 185–196; (m) Y. Li, Q. Niu, T. Wei, T. Li, Analytica Chimica Acta 1049 (2019) 196; (n) T. T. Liu, J. Xu, C. Liu, S. Zeng, Z. Y. Xing, X. J. Sun, J. L. Li, J. Mol. Liquids 300 (2020) 112250.

[3.17] (a) D. R. Crapper, S. S. Krishnan, A. J. Dalton, Science 180 (1973) 511–513; (b) D. P. Perl, A. R. Brody, Science 208 (1980) 297–299; (c) E. House, J. Collingwood, A. Khan, O. Korchazkina, G. Berthon, C. J. Exley, J. Alzheimer's Dis. 6 (2004) 291–301.

[3.18] G. C. Woodson, Bone 22 (1998) 695–698.

[3.19] P. D. Darbre, J. Inorg. Biochem. 99 (2005) 1912–1919.

[3.20] B. L. Vallee, K. H. Falchuk, Psychol. Rep. 73 (1993) 79–118.

[3.21] A. Klug, Annu. Rev. Biochem. 79 (2010) 213–231.

[3.22] A. Adamo, M. Zago, G. Mackenzie, L. Aimo, C. Keen, A. Keenan, P. Oteiza, Neurotoxic. Res.17 (2010) 1–14.

[3.23] K. Tóth, Annu. Rev. Nutr. 31 (2010) 139–153.

[3.24] W. Kaim, B. Schwederski, in Bioinorganic Chemistry, Wiley & Sons 4 (1994) 242–272.

[3.25] A. Krezel, W. Maret, J. Biol. Inorg. Chem. 11 (2006) 1049–1062.

[3.26] (a) A. I. Bush, Trends in Neurosciences 26 (2003) 207–214; (b) D. Noy, I. Solomonov, O. Sinkevich, T. Arad, K. Kjaer, I. Sagi, J. Am. Chem. Soc. 130 (2008) 1376–1383.

[3.27] Y. Lu, S. Huang, Y. Liu, S. He, L. Zhao, X. Zeng, Org. Lett.13 (2011) 5274–5277.

[3.28] (a) Y. Tachapermpon, S. Thavornpradit, A. Charoenpanich, J. Sirirak, K. Burgess,N. Wanichacheva, Dalton Trans.46 (2017) 16251–16256; (b) T. Liu, Y. Dong, X. Wan, W. Li, Y. Yao, RSC Adv. 5 (2015) 76939–76942.

[3.29] (a) L. Hou, J. Feng, Y. Wang, C. Dong, S. Shuang, Y. Wang, Sens. Actuators B247 (2017) 451–460; (b) J. Qin, L. Fan, B. Wang, Z. Yang, T. Li, Anal. Methods 7 (2015) 716–722.

[3.30] X. Chen, T. Pradhan, F. Wang, J. S. Kim, J. Yoon, Chem. Rev. 112 (2012) 1910–1956.

[3.31] H. N. Kim, M. H. Lee, H. J. Kim, J. S. Kim, J. Yoon, Chem. Soc. Rev. 37 (2008) 1465–1472.

[3.32] V. Dujols, F. Ford, A. W. Czarnik, J. Am. Chem. Soc. 119 (1997) 7386–7387.

[3.33] D. T. Quang, J. S. Kim, Chem. Rev. 110 (2010) 6280–6301.

[3.34] B. A. Wong, S. Friedle, S. J. Lippard, J. Am. Chem. Soc. 131 (2009) 7142–7152.

[3.35] X. Zhang, D. Hayes, S. J. Smith, S. Friedle, S. J. Lippard, J. Am. Chem. Soc. 130 (2008) 15788–15789.

[3.36] L. Xue, G. Li, D. Zhu, Q. Liu, H. Jiang, Inorg. Chem. 51 (2012) 10842–10849.

[3.37] L. Xue, Q. Liu, H. Jiang, Org. Lett. 11 (2009) 3454–3457.

[3.38] H. Liu, Y. Dong, B. Zhang, F. Liu, C. Tan, Y. Tan, Y. Jiang, Sens. Actuators B 234 (2016) 616–624.

[3.39] Z. Xu, J. Yoon, D. R. Spring, Chem. Soc. Rev. 39 (2010) 1996–2006.

[3.40] Y. Fu, C. Fan, G. Liu, S. Cui, S. Pu, Dyes Pigm. 126 (2016) 121–130.

[3.41] (a) Y. Zhang, X. Guo, W. Si, L. Jia, X. Qian, Org. Lett. 10 (2008) 473–476; (b) C. He, Z. Lin, Z. He, C. Duan, C. Xu, Z. Wang, C. Yan, Angew. Chem. Int. Ed. 47 (2008) 877–881.

[3.42] I. Ravikumar, P. Ghosh, Inorg. Chem. 50 (2011) 4229–4231.

[3.43] D. Maity, T. Govindaraju, Chem. Commun. 48 (2012) 1039–1041.

[3.44] R. R. Gagne, C. L. Spiro, T. J. Smith, C. A. Hamann, W. R. Thies, A. D. Shiemke, J. Am. Chem. Soc. 103 (1981) 4073–4081.

[3.45] L. A. Burns, Á. V. Mayagoitia, B. G. Sumpter, C. D. Sherri, J. Chem. Phys. 134 (2011) 084107–084132.

[3.46] (a) M. E. Casida, C. Jamoroski, K. C. Casida, D. R. Salahub, J. Chem. Phys. 108 (1998) 4439−4449; (b) R. Bauernschmitt, R. Ahlrichs, Chem. Phys. Lett. 256 (1996) 454−464.

[3.47] (a) M. Cossi, N. Rega, G. Scalmani, V. Barone, J. Comput. Chem. 24 (2003) 669−681; (b) M. Cossi, V. Barone, J. Chem. Phys. 115 (2001) 4708−4717; (c) V. Barone, M. Cossi, J. Phys. Chem. A102 (1998) 1995−2001.

[3.48] M. J. Frisch, G. W. Trucks, H. B. Schlegel, G. E. Scuseria, M. A. Robb, J. R. Cheeseman, G. Scalmani, V. Barone, B. Mennucci, G. A. Petersson, H. Nakatsuji, M. Caricato, X. Li, H. P. Hratchian, A. F. Izmaylov, J. Bloino, G. Zheng, J. L. Sonnenberg, M. Hada, M. Ehara, K. Toyota, R. Fukuda, J. Hasegawa, M. Ishida, T. Nakajima, Y. Honda, O. Kitao, H. Nakai, T. Vreven, J. A. Jr. Montgomery, J. E. Peralta, F. Ogliaro, M. Bearpark, J. J. Heyd, E. Brothers, K. N. Kudin, V. N. Staroverov, R. Kobayashi, J. Normand, K. Raghavachari, A. Rendell, J. C.

Burant, S. S. Iyengar, J. Tomasi, M. Cossi, N. Rega, J. M. Millam, M. Klene, J. E. Knox, J. B. Cross, V. Bakken, C. Adamo, J. Jaramillo, R. Gomperts, R. E. Stratmann, O. Yazyev, A. J. Austin, R. Cammi, C. Pomelli, J. W. Ochterski, R. L. Martin, K. Morokuma, V. G. Zakrzewski, G. A. Voth, P. Salvador, J. J. Dannenberg, S. Dapprich, A. D. Daniels, Ö. Farkas, J. B. Foresman,J. V. Ortiz, J. Cioslowski, D. J. Fox, GAUSSIAN 09, Rev. C.01; Gaussian, Inc. 2009.

[3.49] (a) A. Pramanik, D. Laha, S. Chattopadhyay, S. K. Dash, S. Roy, P. Pramanik. P. Karmakar, Materials Science and Engineering C 65 (2016) 327–337; (b) D. Laha, A. Pramanik, S. Chattopadhyay, S. K. Dash, S. Roy, P. Pramanik, P. Karmakar, RSC Adv. 5 (2015) 68169–68178.

[3.50] H. A. Benesi, J. H. Hildebrand, J. Am. Chem. Soc. 71 (1949) 2703–2707.

Chapter 4

A pyridoxal based bio-compatible fluorometric chemosensor for recognition of Zn^{2+} ion: theoretical approaches and application in live cell imaging

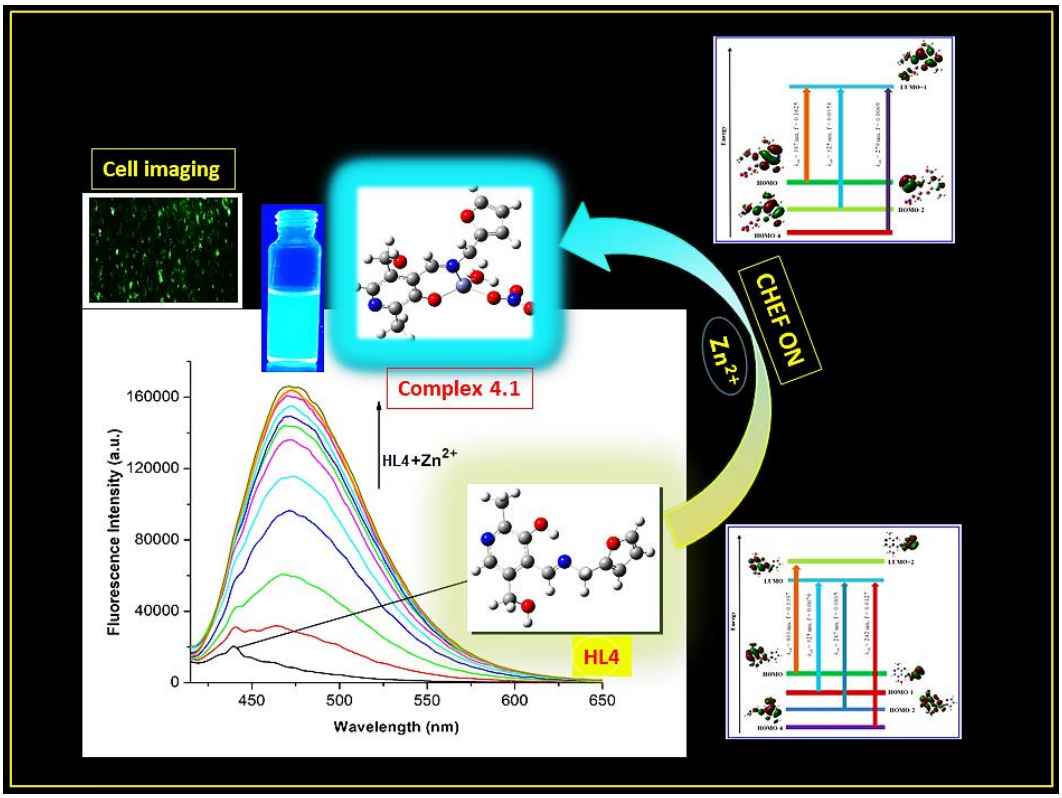

Journal of Photochemistry & Photobiology, A: Chemistry 447 (2024) 115231

Abstract

A simple pyridoxal-based chemosensor (**HL4**=4-(((furan-2-ylmethyl)imino)methyl)-5-(hydroxymethyl)-2-methylpyridin-3-ol) was synthesized which selectively detects Zn^{2+} ion in HEPES buffer at pH = 7.4 (MeOH:H_2O, 9:1, (v/v)) among other competitive metal ions. Around 10-fold increase in fluorescence intensity was seen at 472 nm after excition at 390 nm. **HL4** displays blue fluorescence with a large stoke′s shift (~80 nm) in presence of Zn^{2+} ion. A 1:1 binding stoichiometry between **HL4** and metal ions (Zn^{2+}) and the PET-OFF-CHEF-ON mechanism had been established by different spectroscopic techniques and theoretical studies. Low LOD value of the chemosensor towards Zn^{2+} (lower than the WHO's guideline of 76.5 μM) and strong binding constant ($K = 1.54 \times 10^5$ M^{-1}) suggest the applicability of **HL4** towards biological cell imaging studies under physiological conditions. MTT assay was carried out to evaluate the toxicity of probe **HL4** up to maximum concentrations with PC3 cell line.

4.1. Introduction

In vitro and in vivo detection of metal ions that have actively taken part in vital physiological processes continue to be an important part of research [4.1,4.2]. Fluorescence spectroscopy has been frequently used for this purpose due to its sensitivity, simplicity, and real-time monitoring [4.3]. During the design of chemosensors, two important factors; binding-selectivity of the receptor part towards the target molecule and their stability under illumination conditions are considered. Furthermore, environmental interference such as, photo bleaching, temperature, pH of the medium, solvent polarity, etc. needs to be controlled. Zinc, the second-most transition metal present in the human body after iron, is found as structural cofactors of many enzymes like carboxypeptidase A and carbonic anhydrases (CAs) and as DNA-binding proteins [4.4]. Zinc also associated with several biological processes such as brain function, gene transcription, immune function, and mammalian reproduction [4.5]. It is related to several diseases such as Alzheimer's disease, epilepsy, ischemic stroke, and infantile diarrhoea [4.6]. In enzymes, Zn^{2+} is present in a tightly bound form, and in the brain, intestine, pancreas, and retina, free zinc pools are found. Among different fluorescence turn-on mechanisms for the detection of Zn^{2+} ions; two major pathways, photo-induced electron transfer (PET) and intermolecular charge transfer (ICT), are mostly used [4.7]. Both of these processes result in fluorescence enhancement signals in the presence of Zn^{2+} ions.

Among well-known receptors for the detection of Zn^{2+} ions, secondary amine nitrogen atom of di-2- picolylamine (DPA) or its derivatives, such as N,N-di-(2-picolyl)ethylenediamine (DPEN) and N,N,N'-tris(pyridin-2-ylmethyl)ethylenediamine (TRPEN), act as a good reaction site for binding with various fluorophoric units [4.8-4.10]. Fluorogenic cheaters like 8-hydroxyquinoline and 8-aminoquinoline combine with aryl sulfonamide units to generate chemosensors, which are frequently used for detecting Zn^{2+} in biological samples [4.11-4.13].

Bipyridyl like biaryl fluorophore, upon coordination with Zn^{2+} ions result in an increase in fluorescence intensity. Here, fluorescence enhancement occurs through binding-induced conformational restriction and intramolecular charge transfer [4.14]. Chemosensors containing acyclic and cyclic polyamines as the receptor are capable of forming strong bonds with the Zn^{2+} centre and show fluorescence enhancement through inhibition of the PET process [4.15]. Iminodiacetic acid [4.16, 4.17] and triazole [4.18] suitably connect with the fluorophoric units also act as a Zn^{2+} ion receptors. Zinc has strong coordination affinity towards the N atom of C=N bond present in schiff base-type of ligands. Such a type of compound is frequently used as a zinc chemosensor. Free chemosensors are non-fluorescent due to C=N isomerization driven excited state decay process. This C=N isomerization process is restricted when Zn^{2+} ions are covalently linked with C=N bonds resulting in a dramatic increase of fluorescence intensity [4.19].

A literature survey on pyridoxal based fluorescent turn on probes of Zn^{2+} ion are presented in **Chart 4.1** [4.20]. From **Chart 4.1** we found that most of the pyridoxal based chemosensors selectively detect Zn^{2+} ions. Majority of the reported sensors have been synthesized from Schiff base condensation using pyridoxal hydrochloride and different amines. We also noticed that they exhibit strong affinity towards Zn^{2+} ion. Due to high binding constant values it was impossible to replace Zn^{2+} from the ligand core. S. K. Sahoo and his group have synthesized a chemosensor involving pyridoxal and 3-hydroxy-2-naphthoic hydrazide. The organic molecule showed an instantaneous ratiometric fluorescence response in the presence of Zn^{2+} ions (binding constant value, $6.1\times10^5\ M^{-1}$) due to coordination of imine-N, pyridoxal-OH and carbonyl-O of the ligand with zinc ions [4.20a]. A. G. Sykes *et al.* have used tris(hydroxymethyl)aminomethane to prepare a pyridoxal based chemosensor which selectively detects Zn^{2+}. They have elucidated crystal structure of the Zn-chemosensor where Zn bound with the chemosensor in 1:2 stoichiometric ratio (binding constant $1.2 \times 10^9\ M^{-1}$) [4.20b]. Y. S.

Marfin and coworker in a very recent work reported a chemosensor, pyridoxal 5′-phosphate 2-methyl-3-furoylhydrazone for selective detection of Zn^{2+} ion. The value of stability constant is also high (log β2′ = 8.96 ± 0.09) [4.20c]. A. Tamilselvi *et al.* have prepared a flexible cyclohexane and pyridoxal-based sensor which selectively detects Zn^{2+} ion in solid and solution medium. The binding constant of the probe with Zn^{2+} was found to be 7.9080 ± 0.0097 × 10^5 M^{-2} [4.20d]. In one of our recent work we have also reported two pyridoxal based fluoresence turn on Zn^{2+} chemosensors. Both the chemosensors have strong binding constant values (3.47 × 10^5 and 3.12 × 10^5 M^{-1}. We have successfully crystallized one of the Zn bound chemosensor [4.20e]. In an interesting work, D. F. Back *et al.* have reported study of superoxide dismutase mimicking catalytic activity, cytotoxicity and interaction with CT-DNA of three pyridoxal based Cu(II) compounds. In this work different Schiff base ligands are prepared upon condensation between different aromatic amines like furfurylamine, 2-thiophenethylamine, and 2-thiophenemethylamine with pyridoxal hydrochloride. McCord-Fridovich assay indicates that among all the compounds, 2-thiophenethylamine-pyridoxal hydrochloride based Cu(II) compound showed the safest reactive oxygen species generation level and also best antioxidant activity with low cytotoxicity value. Interactions of all three compounds with CT-DNA are studied using absorption and emission spectroscopy which is further theoretically supported by molecular docking. Interaction between Cu(II) compounds and CT-DNA occur probably through π-stacking and secondary hydrogen bonding. Theoretical data also support the minor groove interaction [4.21].

All these results prompted us to prepare pyridoxal based chemosensor for selective detection of Zn^{2+} ion. Pyridoxal is a vitamer of vitamin B6. It is a water-soluble, naturally occurring compound. Pyridoxal 5'-phosphate (PLP) has been found to be the most active vitamer which involves around 140 enzymatic processes and actively takes part in decarboxylation,

transamination, and racemization [4.22-4.24]. Bioactivity, high solubility in aqueous medium, chelating ability, and interesting photo-physical properties make this anticancer agent a well-known probe in the areas of sensing and bio-sensing [4.25]. Chemosensor **HL4** is feebly fluorescent due to –C=N bond isomerization and the PET process. Around a 10 fold fluorescence intensity increment of **HL4** was observed in the presence of Zn^{2+} ions. Different spectroscopic techniques, elemental analysis and ESI-MS^{+} spectrometry are deployed to study the interaction between Zn^{2+} and chemosensor. Jobs plot analysis proves a 1:1 metal:chemosensor binding stoichiometry. The large Stokes shift (~80 nm), micromolar range LOD value (4.12×10^{-6} M) and strong binding constant ($K=1.54 \times 10^{5}$ M^{-1}) of the probe towards Zn^{2+} suggest its applicability to biological studies. Theoretical calculations were performed in order to support the electronic spectra and binding mode of the chemosensor around the metal centre.

Chart 4.1. Literature survey of pyridoxal based Zn^{2+} sensors.

Sl. No.	Probe	Sensing mechanism	Sensing of metal ion(s)	Sensing media	Excitation(nm)/ Emission (nm)	Limit of detection (LOD) (M)	Binding constant (M^{-1})	Biological study	Refs.
1.	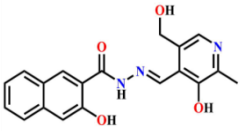	Push-pull effect	Zn^{2+}	(2 mL, 5×10^{-5} M, DMSO: 50 µL, 1×10^{-3} M, H_2O	375/475	8.73×10^{-7}	6.1×10^{5}	Cell imaging	**4.20a**
2.	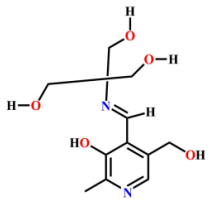	Fluorescent turn-on	Zn^{2+}	MeOH, H_2O(0.1 M HEPES buffer, pH =7.3)	385/470	2.77×10^{-8}	1.2×10^{9} M^{-2}	Cell imaging	**4.20b**
3.	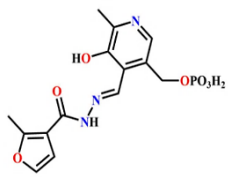	CHEF	Zn^{2+}	DMSO-aqueous Tris-HCl (90:10, vol. %)	412/501	18×10^{-9}	$\log \beta_2' =$ 8.96 ± 0.09.	Cell imaging	**4.20c**

4.	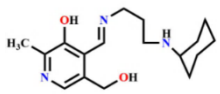	CHEF	Zn^{2+}	Aqueous ethanolic (9:1, v/v) HEPES buffer (pH = 7.0)	322/464	$(9.5850 \pm 0.38\times10^{-9}$	$(7.908 \pm 0.0097)\times 10^{5}\ M^{-2}$	Cell imaging	**4.20d**
5.	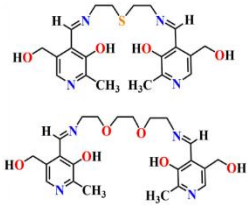	CHEF	Zn^{2+}	H_2O in HEPES buffer at pH 7.4	385/472	7.47×10^{-8} 6.95×10^{-8}	3.47×10^{5} 3.12×10^{5}	Cell imaging	**4.20e**
6.	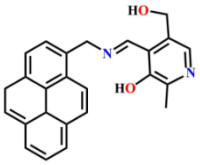	CHEF	Zn^{2+} $H_2PO_4^-$ cysteine	50 µL H_2O, 1950 µL DMSO, 2.5 × 10^{-5} M	378/485 398/485 417/485	2.3×10^{-6} 2.18×10^{-7} 1.59×10^{-7}	log β = 10.03(1)	None	**4.20f**
7.	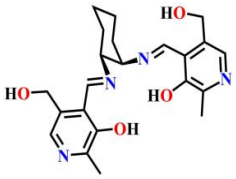	CHEF	Zn^{2+}	$EtOH/H_2O$ (4:1, v/v, 25 mM HEPES buffer, pH 7.4)	416/476	5.9×10^{-6}	9.6×10^{3}	Cell imaging	**4.20g**
8.		CHEF	Zn^{2+}	$EtOH/H_2O$ (4 : 1, v/v, 25 mM Tris buffer, pH 7.4)	411/483	40.78×10^{-7}	1.18×10^{4}	Cell imaging	**4.20h**
9.		OFF-ON, LMCT	Zn^{2+} Cu^{2+}	Methanol: water (1:1 (v/v), HEPES buffer, pH 7.4)	400/526 400/498	2.1×10^{-8} 0.15×10^{-8}	---- 1.17×10^{5}	Cell imaging	**4.20i**
10	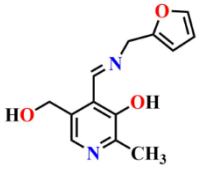	**CHEF**	**Zn^{2+}**	**HEPES buffer at pH 7.4 ($MeOH:H_2O$, 9:1, (v/v))**	**390/472**	**4.12×10^{-6}**	**1.54×10^{5}**	**Cell imaging**	**This work**

4.2. Experimental section

4.2.1. Chemicals and instrumentations involved in this work

Pyridoxal hydrochloride and furan-2-ylmethanamine were purchased from commercial suppliers (Alfa-Aesar). Also other necessary chemicals or reagents are of analytical grade, and the solvents were purchased from commercial sources. These chemicals were used without further purification. Elemental analysis (C, H and N) was carried out using a Perkin–Elmer 240C elemental analyser. Electron spray ionization mass (ESI-MS positive) spectra and infrared spectra (400–4000 cm^{-1}) were recorded by a MICROMASS Q-TOF mass spectrometer and FTIR spectrophotometer with KBr pellets on a Nicolet Magna IR 750 series-II, respectively. Using a Shimadzu UV 1800 spectrophotometer with a 10-mm-path-length quartz cell, absorption spectra were measured within the wavelength range 200-800 nm. A Fluromax-4 spectrofluorometer was used to measure emission spectra at room temperature (298 K) in HEPES buffer at pH 7.4 (MeOH:H_2O, 9:1, (v/v)). Fluorescence lifetime was conducted using time-resolved spectrofluorometer from IBH, UK. Bruker 400 spectrometer was used for measuring ^{1}H and ^{13}C NMR spectra in d_6-DMSO solvent.

4.2.2. Synthesis

4.2.2.1. Procedure for synthesis of chemosensor HL4 [HL4=4-(((furan-2-ylmethyl)imino)methyl)-5-(hydroxymethyl)-2-methylpyridin-3-ol]

Firstly, 1 mmol pyridoxal hydrochloride (0.203 g) and 4 mmol sodium acetate (0.328 g) were taken in a beaker and stirred ~30 minutes in a 20 mL methanol solution for neutralization of the solution. After stirring, a light yellow colour solution of free pyridoxal was observed with a precipitation of NaCl. Then the solution was filtered, and 5 ml methanolic solution of 1 mmol furan-2-ylmethanamine (0.097 g) was added. Stirring was continued for another ~3 hours, and a

yellow colour clear solution was observed. Evaporation of the solvent results in a yellow-coloured crystalline solid.

Yield: 0.216 g (88%). Anal. Calc. for $C_{13}H_{14}N_2O_3$: C 63.40%; H 5.73%; N 11.38%. Found: C 63.37%; H 5.71%; N 11.34%. IR (cm^{-1}, KBr): υ(C=N) 1630s; υ(O-H) 3149. ESI-MS (positive) in MeOH: The base peak was detected at *m/z* = 247.10, corresponding to $[\mathbf{HL4}+H]^+$. UV-Vis, λ_{max} (nm), (ε ($dm^3mol^{-1}cm^{-1}$)) in HEPES buffer at pH 7.4 (MeOH:H_2O, 9:1, (v/v)): 252 (4420), 283 (3080), 331 (2210) and 415 (360), respectively.

^{1}H NMR (solvent used: d_6-DMSO, 400 MHz) δ ppm: 2.35 (-CH_3) (s, 3H), 3.44 (-CH_2) (s, 2H), 4.63 (-CH_2) (s, 2H), 4.89 (-CH_2 and -OH) (s, 2H), 6.42 (Ar-H) (s, 1H), 6.46 (Ar-H) (s, 1H), 7.66 (Ar-H) (s, 1H), 7.86 (-HC=N) (s, 1H), 9.04 (-OH) (s, 1H).

^{13}C NMR (solvent used: d_6-DMSO, 75 MHz) δ ppm: 18.60, 55.62, 60.39, 108.20, 110.54, 120.08, 131.66, 137.53, 142.73, 150.37, 150.62, 154.81, 163.99.

4.2.2.2. Synthesis of complex 4.1 [Zn(L4)(NO_3)(H_2O)]

A methanolic solution of 1.0 mmol of zinc nitrate hexahydrate (0.297 g) was added drop-wise to solution of **HL4** (1.0 mmol, 0.246 g) followed by the addition of triethylamine (2.0 mmol, ~0.4 mL) and the resultant reaction mixture was stirred for ca. 4 h. A yellow colour solid was obtained in high yield after slow evaporation of the solvent.

Yield: 0.346 g (89%). Anal. Calc. for $C_{13}H_{15}N_3O_7Zn$: C 39.97%; H 3.87%; N 10.76%. Found: C 39.92%; H 3.86%; N 10.72%. IR (cm^{-1}, KBr): υ(C=N) 1621s, υ(NO_3^-) 1316 s. ESI-MS (positive) in MeOH: The base peak was detected at *m/z* = 309.02, corresponding to $[(\mathbf{L4})Zn]^+$. UV-Vis, λ_{max} (nm), (ε ($dm^3mol^{-1}cm^{-1}$)) in HEPES buffer at pH 7.4 (MeOH:H_2O, 9:1, (v/v)): 278 (3915), 325 (2590) and 390 (945), respectively.

^{1}H NMR (solvent used: d_6-DMSO, 400 MHz) δ ppm: 2.30 (-CH_3) (s, 3H), 4.53 (-CH_2) (d, 2H, J=8 Hz) 4.79 (-CH_2) (s, 2H), 5.28 (-OH) (t, 1H, J_1=J_2=8 Hz), 6.39 (Ar-H) (s, 2H), 7.45 (Ar-H) (s, 1H), 7.60 (Ar-H) (s, 1H), 8.78 (-HC=N) (s, 1H).

^{13}C NMR (solvent used: d_6-DMSO, 75 MHz) δ ppm: 20.68, 46.13, 59.58, 109.83, 111.12, 117.74, 131.64, 134.89, 143.10, 143.64, 150.62, 155.32, 169.15.

4.2.3. Absorbance and emission spectral analysis

Nitrate salts of different metal ions were prepared in MeOH (1×10^{-3} M) as stock solutions. Also, a stock solution of the chemosensor (**HL4**) was ready to be prepared in methanol at concentration 1×10^{-3} M. The solution of **HL4** was then diluted to 1×10^{-5} M as per necessity. All the spectroscopic experiments, including competitive assays of various cations and anions, were performed in HEPES buffer at pH 7.4 (MeOH:H_2O, 9:1, (v/v)). For titration experiments, a quartz optical cell with a 1.0 cm optical path length was filled with 60 µL solution of **HL4** (1×10^{-3} M) and mixed gradually with the ion stock solutions to maintain a concentration of 2×10^{-5} M. For fluorescence measurements, the excitation wavelength was fixed at 390 nm and emission was recorded between the range of 415-700 nm. For pH metric titration, different range of pH solutions (pH=2-12) were prepared using HEPES buffer, 1N HCl and 1N NaOH solutions in water.

4.2.4. Determination of binding stoichiometry (Job's plot)

Job's technique was used to check out the binding ratio of the chemosensor (**HL4**):Zn^{2+} ions with absorption as well as emission spectroscopy. By changing the concentration of both the chemosensor (**HL4**) and metal ions (Zn^{2+}), absorbance and fluorescence intensity were recorded, but overall concentrations were fixed at 2×10^{-5} M at room temperature (25ºC). Then mole fraction {[**HL4**]/([**HL4**]+[Zn^{2+}])} vs relative change in absorbance ($\Delta A/A_0$) or fluorescence

($\Delta I/I_0$) was plotted. After a certain point, the resulting plot broke corresponded to {[**HL4**]/([**HL4**]+[Zn^{2+}])} which confirmed the stoichiometric ratio of the chemosensor with respect to the metal ion.

4.2.5. LOD and binding constant calculations

The IUPAC approved equation for calculating the limit of detection (LOD) was:

$$LOD = \frac{3\sigma}{\text{slope}}$$ where σ represents the curve′s standard deviation of the curve.

Using the equation (1) LOD was calculated from fluorescence titration data. Binding constant (K) of the chemosensor (**HL4**) towards Zn^{2+} was calculated using web support: https://supramolecular.org [4.26].

4.2.6. Cell imaging experiment

The PC3 cells were allowed to grow in coverslips for 24 h. The cells were then treated or mock-treated with 20 µM Zn^{2+} ions at 37ºC for 24 h followed by a wash with 1X PBS. These cells were mounted on glass slides for observation under the fluorescence microscope (Leica) [4.27].

4.2.7. Cell survivability test by MTT assay

The cell survivability of **HL4** over PC3 cells was monitored by MTT assay following the reported procedure. 48 well plates were used to seed the cells at 2×10^4 for each well. They were then exposed to a ligand concentration of 0 µM, 20 µM, 40 µM, 60 µM, 80 µM, 100 µM for 24 hrs. The resulting formazan crystals were dissolved in an MTT solubilization buffer, and the absorbance was measured at 570 nm by using a spectrophotometer (BioTek) and the value was compared with that of control cells. The cytotoxicity of **HL4** was checked towards the PC3 cells by the MTT assay protocol [4.27].

4.2.8. Theoretical calculations based on computational methods

For optimization, the compounds were initially set at the B3LYP/6-31+G* level of theory in their ground state [4.28]. We also performed the time-dependent DFT (TDDFT) [4.29] calculations by setting the same level of theory associated with the conductor-like polarizable continuum model (CPCM) [4.30]. Using Gauss View 5.0 software, electronic density plots for the frontier molecular orbitals were calculated. All these calculations were performed with the Gaussian 09 software package [4.31].

4. 3. Results and discussion

4.3.1. Discussion on synthesis and characterization

Initially, the pyridoxal hydrochloride and CH_3COONa were mixed at 1:4 ratio in methanol to neutralize the medium. Then a methanolic solution of furan-2-ylmethanamine was added drop-wise to the reaction mixture. Three hours stirring at room temperature result a yellow colored crystalline solid, (**Scheme 4.1**) which was directly used for characterization and different spectroctroscopic analysis such as UV-Vis, FT-IR, ^{1}H NMR, ^{13}C NMR, and elemental analysis, etc. The base peak was detected in ESI-mass spectrometry at *m/z* = 247.10, corresponding to $[\mathbf{HL4}+H]^+$ (**Fig. 4.1**). In the FT-IR spectrum of **HL4**, a broad and a sharp band at ~3149 and 1630 cm^{-1} represents phenolic OH and C=N stretching frequencies, respectively (**Fig. 4.2**).

Complex **4.1** was prepared upon reaction between **HL4** and $Zn(NO_3)_2.6H_2O$ at 1:1 ratio (**Scheme 4.2**). The yellow colored solid of complex **4.1** was isolated with high yield. It was further characterized by FT-IR, NMR spectroscopy, elemental analysis and mass spectrometry. The molecular ion peak of $[(\mathbf{L4})Zn]^+$ was detected at *m/z* = 309.02 (**Fig. 4.3**). The characteristics stretching frequency for υ(C=N) was found at 1621 cm^{-1} whereas at 1316 cm^{-1} one sharp peak appeared which represent asymmetric stretching frequencies for NO_3^- group (**Fig. 4.2**).

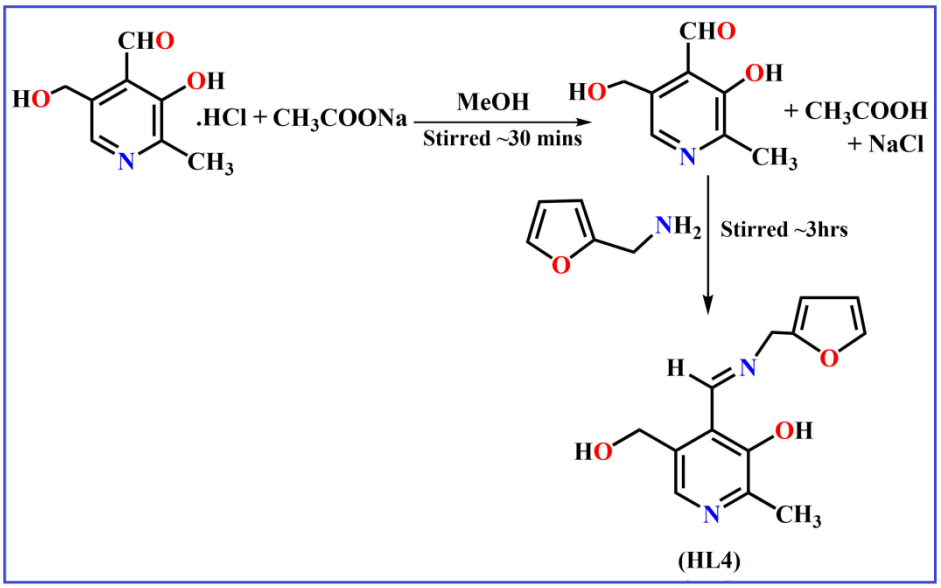

Scheme 4.1. Synthesis route of chemosensor (**HL4**).

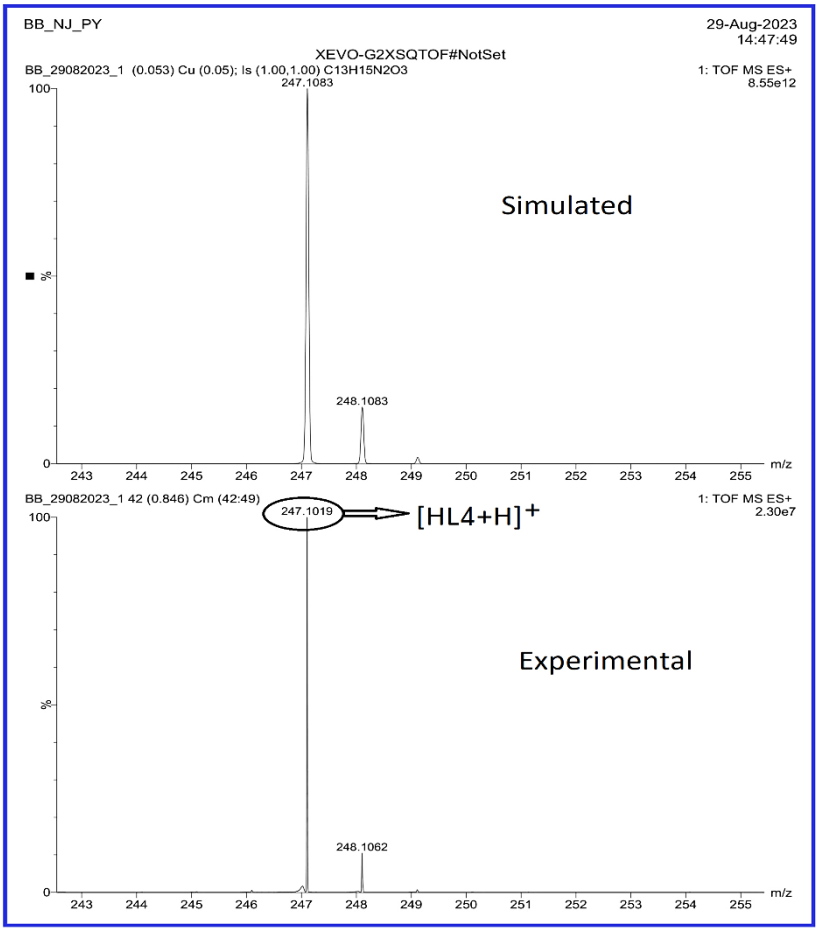

Fig. 4.1. ESI-MS$^+$ spectrum of [**HL4**+H]$^+$.

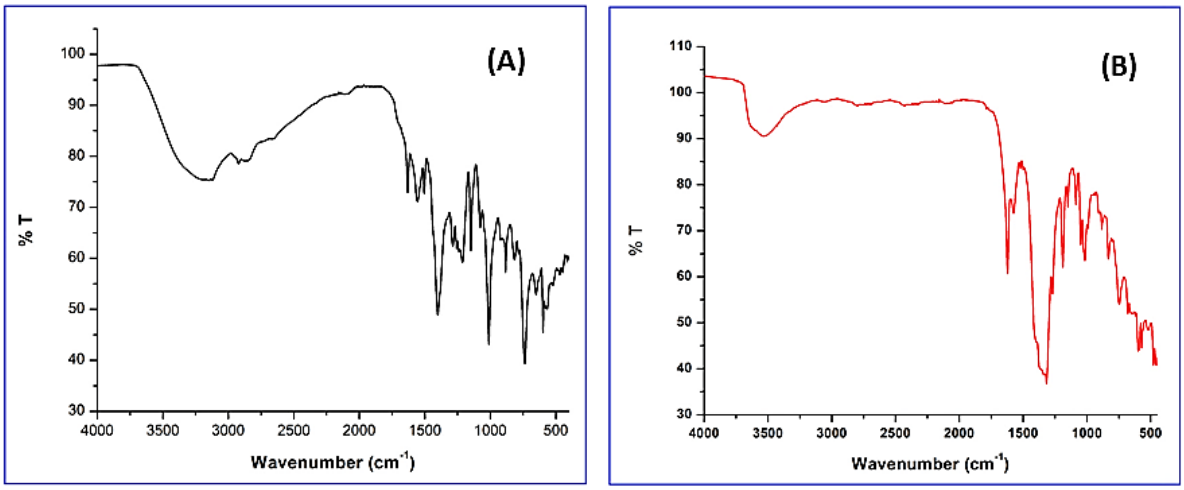

Fig. 4.2. FTIR spectra of (A) chemosensor **HL4** and (B) complex **4.1**, respectively.

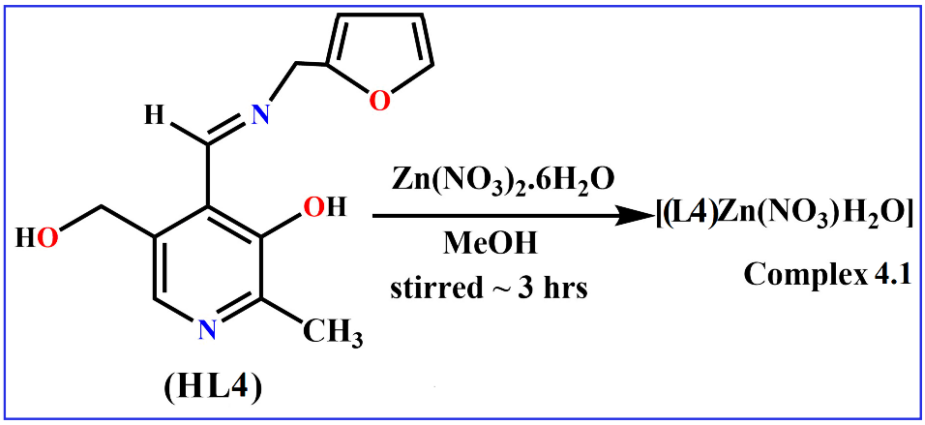

Scheme 4.2. Route to the synthesis of complex **4.1**.

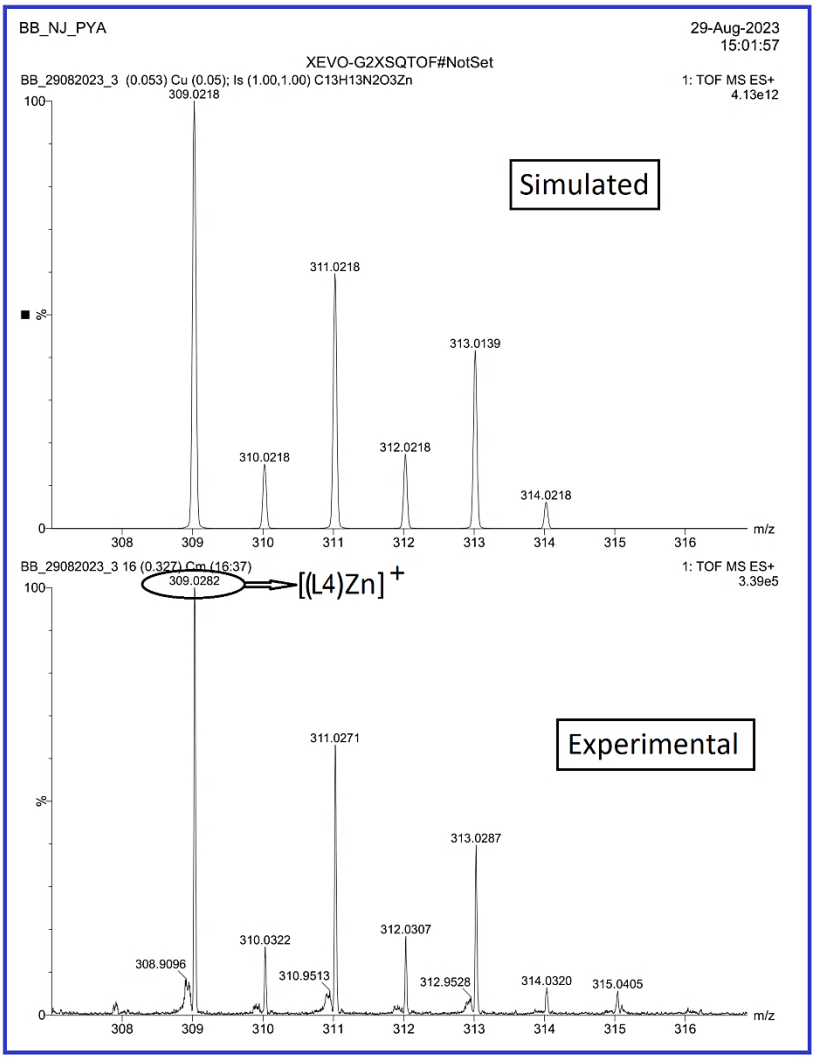

Fig. 4.3. ESI-MS^{+} spectrum of [(**L4**)Zn]$^{+}$.

4.3.2. Analysis of absorption spectral data

Absorption measurements for the free chemosensor and with Zn^{2+} ions were carried out in HEPES buffer at pH 7.4 (MeOH:H_2O, 9:1, (v/v)). Free chemosensor (**HL4)** gave well-defined bands at 252, 283, 331, and 415 nm, respectively responsible for intramolecular π →π* and n→π* type of transitions, respectively. In presence of Zn^{2+} ions a significant change in the spectrum of chemosensor is observed. Upon gradual addition of Zn^{2+} ion solution (0-22 µM), broadening of the peak at 415 nm observed, and finally it was blue-shifted to 390 nm. Rest of the peaks are also blue shifted and appear at 325 and 278 nm, respectively (**Fig. 4.4**). Hypsochromic shift of the peaks is a strong indication of bonding between **HL4** and Zn^{2+}. This could be

assigned as coordination of imine N and phenolate O to the metal centre. No further enhancement of the intensity of peaks after a 1.1 equivalent addition of Zn^{2+} suggests a 1:1 binding stoichiometry between the chemosensor and Zn^{2+} ion, which is also supported by Job's plot analysis (**Fig. 4.5**). The binding constant of the chemosensor towards Zn^{2+} ions has been calculated involving absorbance titration data, and the value is 1.54×10^5 M^{-1} (**Fig. 4.6**) [4.26]. Importantly, upon addition of other common cations (Al^{3+}, Cd^{2+}, Hg^{2+}, Pb^{2+}, Ag^{+}, Mn^{2+}, Ni^{2+}, Na^{+}, K^{+}, Ca^{2+}, Mg^{2+}, Cr^{3+}, Co^{2+}, Fe^{3+}, and Cu^{2+}) did not make considerable change in the absorption spectrum of the chemosensor (**Fig. 4.4**).

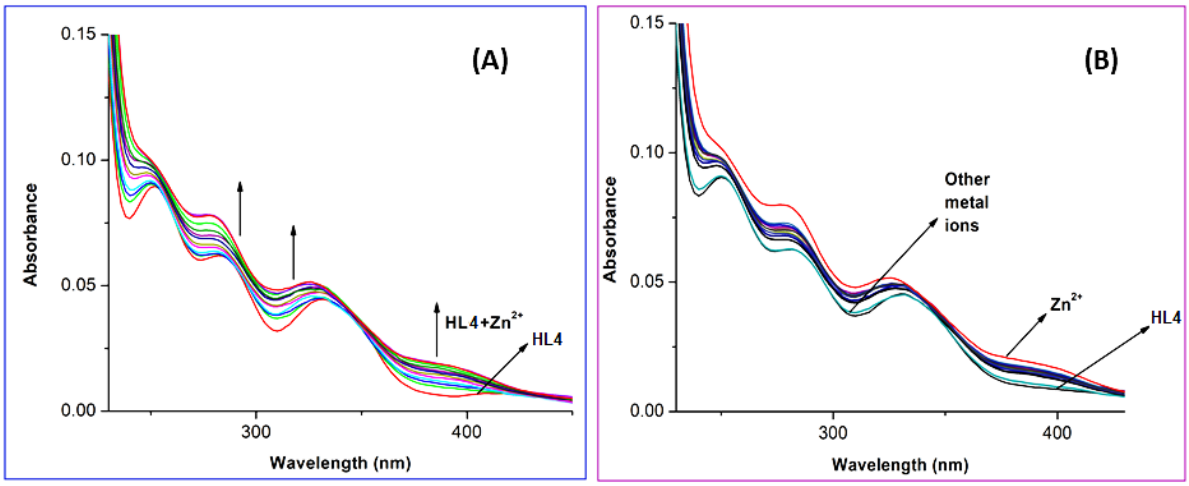

Fig. 4.4. (A) UV-Vis spectra studies of **HL4** (20 µM) with addition of 0-22 µM Zn^{2+}, in HEPES buffer at pH 7.4 (MeOH:H_2O, 9:1, (v/v)), (B) UV-Vis spectra of chemosensor (**HL4**) (20 µM) in the presence of different metal ions in HEPES buffer at pH 7.4 (MeOH:H_2O, 9:1, (v/v)).

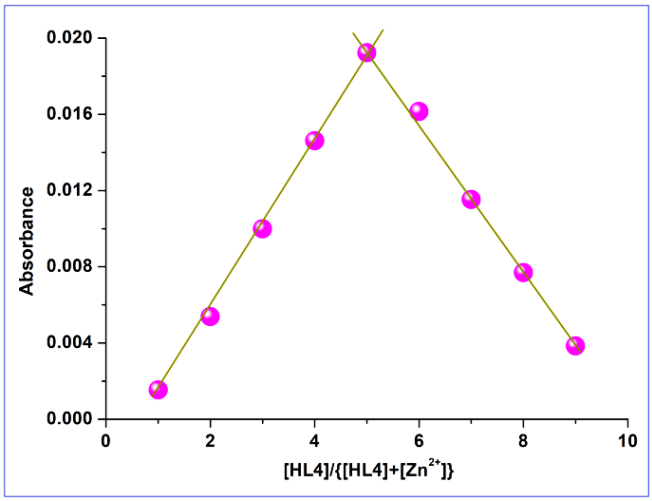

Fig. 4.5. Job's plot experiment to study 1:1 binding stoichiometry of **HL4** and Zn^{2+}. Symbols and solid lines represent the experimental and simulated profiles, respectively.

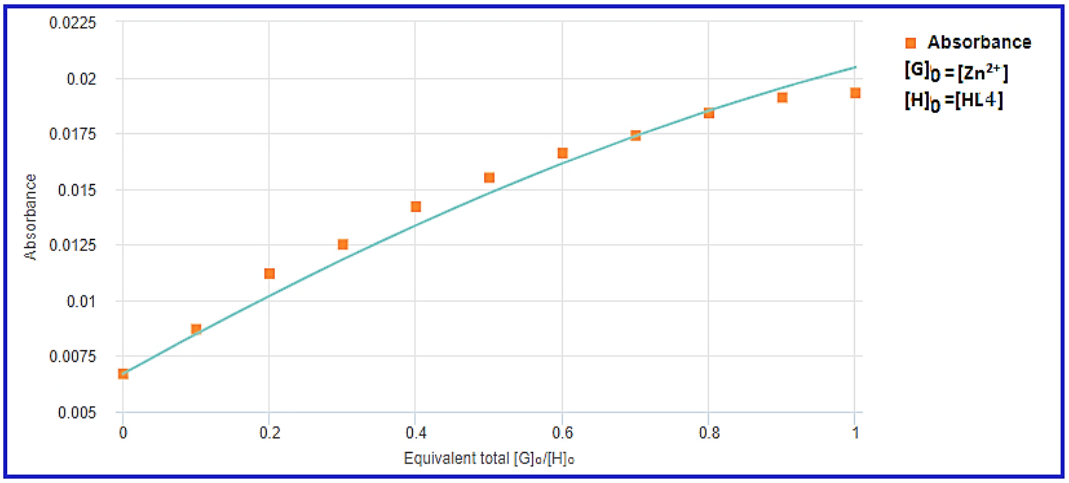

Fig. 4.6. Binding constant calculation for **HL4** (20 µM) with Zn^{2+} (20 µM) ion in HEPES buffer at pH 7.4 (MeOH:H_2O, 9:1, (v/v)). [http://supramolecular.org]. Binding constant=1.54×10^5 M^{-1}.

4.3.3. NMR spectral description

All ^{1}H and ^{13}C NMR spectra of the chemosensor (**HL4**) and its Zn-bound compound (**4.1**) are recorded in d_6-DMSO solvent. The free chemosensor gives phenolate –OH, and imine (H-C=N) proton peaks at 9.04, and 7.86 ppm, respectively. Aromatic protons appear in the usual position, 7.66-6.42 ppm. Aliphatic $–CH_2$ protons, aliphatic –OH proton and methyl protons associated with the pyridoxal part appear at 4.63, 4.89 and 2.35 ppm, respectively, whereas aliphatic $–CH_2$ protons of the furfural moiety appear at 3.44 ppm (**Fig. 4.7**). In ^{13}C NMR of **HL4**, imine carbon atoms appeared at 163.99 ppm. Aromatic carbon atoms appeared in the usual range 154.81-108.20 ppm. Aliphatic carbon and methyl carbon atoms are found at 60.39, 55.62 and 18.60 ppm (**Fig. 4.8**).

In ^{1}H NMR of complex **4.1**, phenolic –OH disappeared, and the imine proton shifted downfield and appeared at 8.78 ppm, which is a clear indication of bonding between phenoxido oxygen and imine nitrogen with metal ion (**Fig. 4.9**). Due to metal coordination shifting of aromatic protons and other aliphatic $–CH_2$ protons, aliphatic –OH proton have been noticed. In the ^{13}C NMR spectrum of complex **4.1**, imine carbon shifted downfield and appeared at 169.15 ppm. Aromatic carbon atoms appeared in the usual range of 155.32-109.83 ppm. Aliphatic carbon and methyl carbon atoms are found at 59.58, 46.13, and 20.68 ppm, respectively (**Fig. 4.10**).

Complex formation between Zn^{2+} and the chemosensor was again studied by ^{1}H NMR titration experiment in d_6-DMSO solvent. Upon gradual addition of Zn^{2+} ions (0.50 mmol to 1 mmol) disappearance of the phenolate –OH proton and the downfield shift of imine and aromatic protons of **HL4** are observed (**Fig. 4.11**).

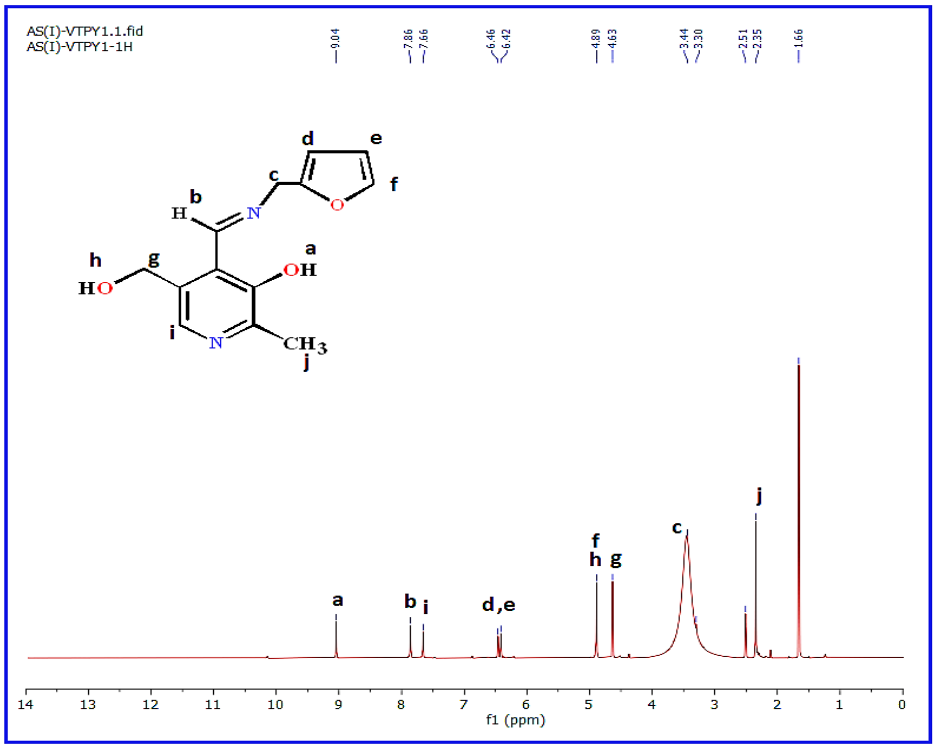

Fig. 4.7. ^{1}H NMR spectrum of **HL4** in DMSO-d_6 solvent.

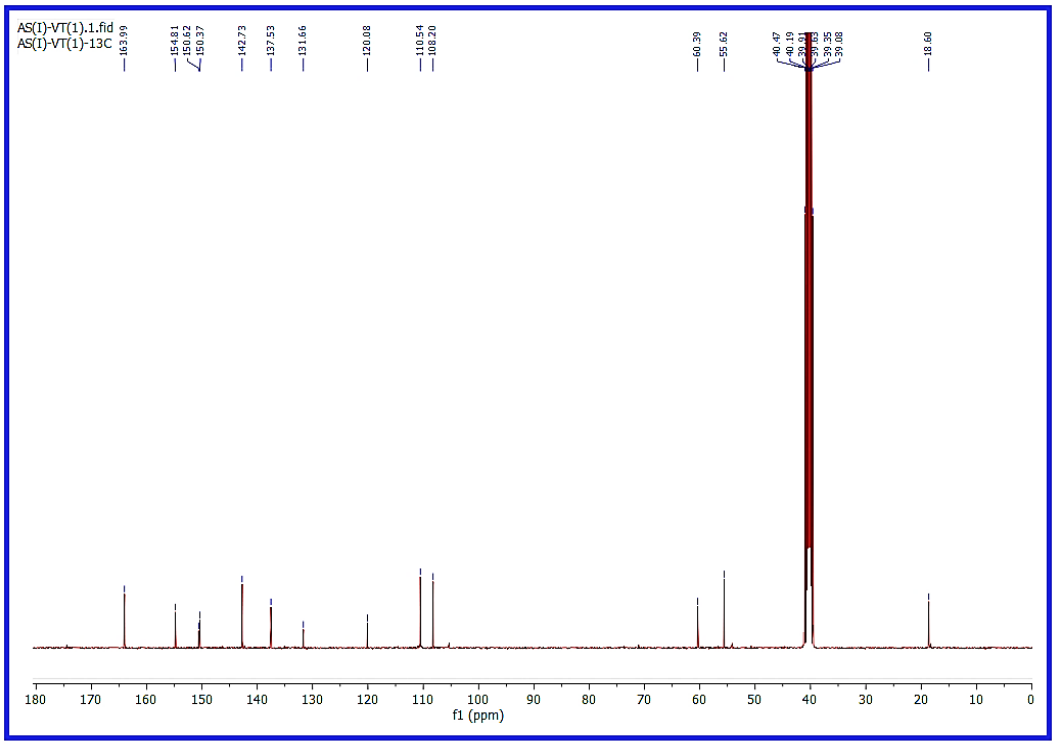

Fig. 4.8. ^{13}C NMR spectrum of **HL4** in DMSO-d_6 solvent.

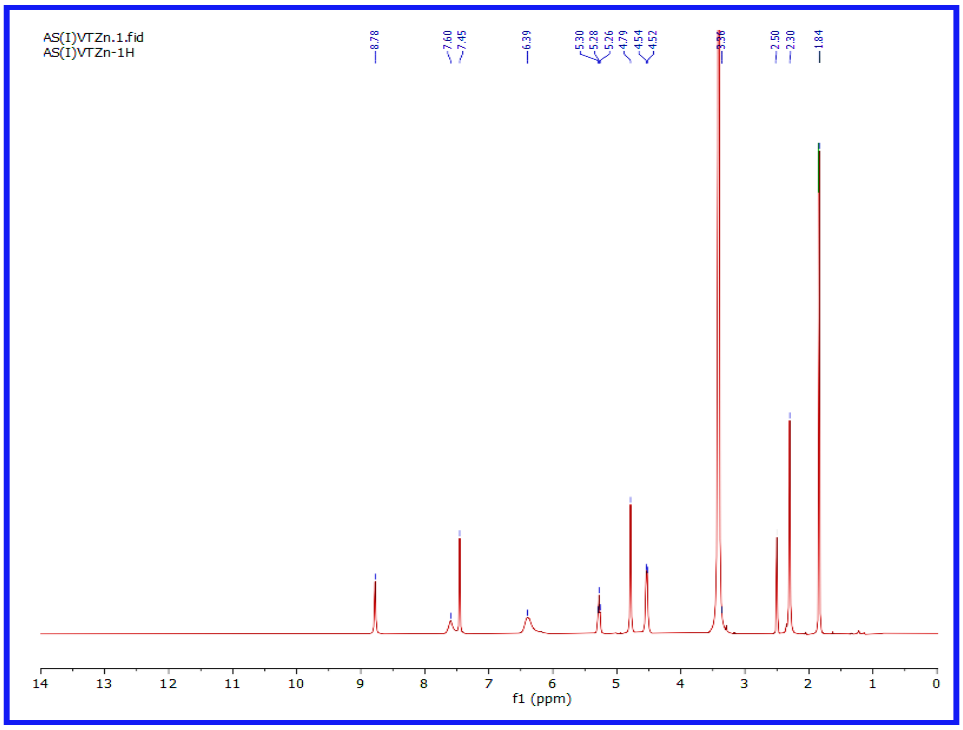

Fig. 4.9. ^{1}H-NMR of complex **4.1** in DMSO-d_6 solvent.

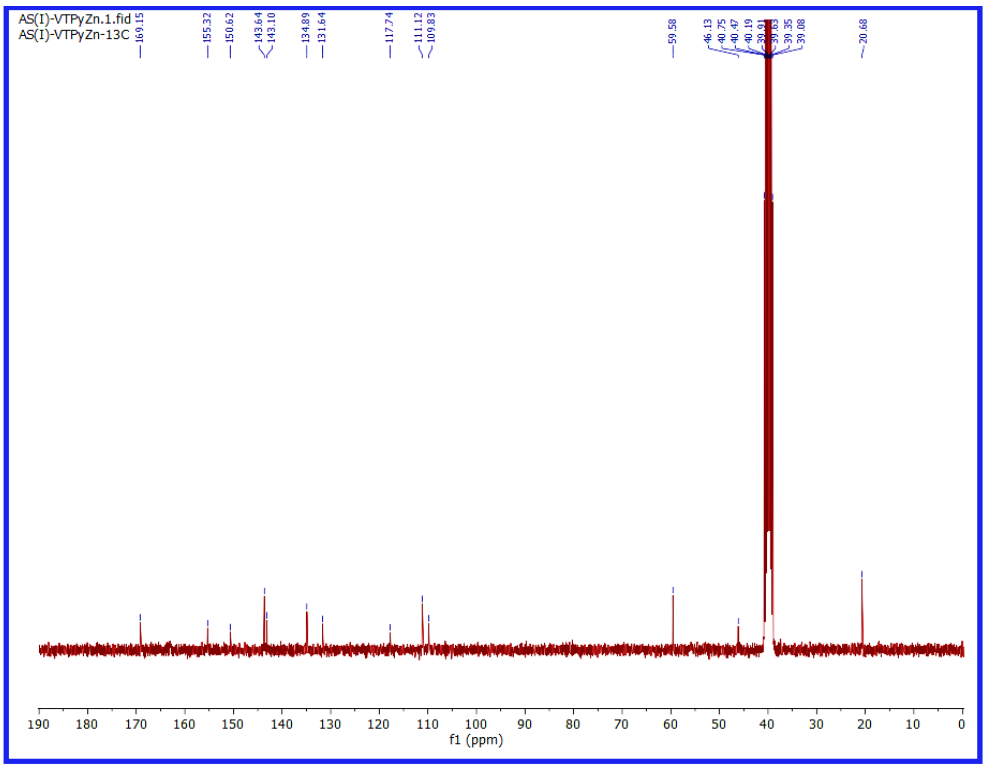

Fig. 4.10. ^{13}C NMR of complex **4.1** in DMSO-d_6 solvent.

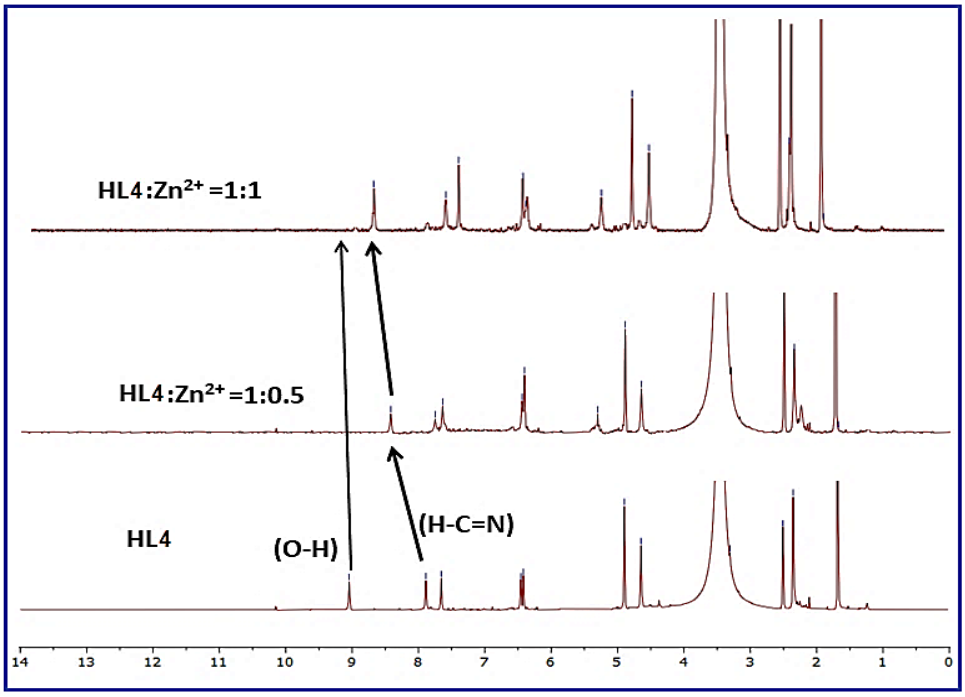

Fig. 4.11. ^{1}H-NMR titration of the free ligand (**HL4)** and with the addition of 0.50, and 1 equivalent of Zn^{2+} in DMSO-d_6 solvent.

4.3.4. Fluorescence spectral studies

Free probe **HL4** was feebly fluorescent. A weak fluorescence peak was found at 440 nm when excited at 390 nm (**Fig. 4.12**). This was probably due to the photo-induced electron transfer (PET) and -C=N isomerization processes. In the PET process, a relatively high-energy non-bonding electron pair of nitrogen atoms present on the receptor part transfers an electron to the excited fluorophore, resulting in fluorescence quenching. In the presence of the Zn^{2+} ions this electron pair is donated to the metal ion via coordination. This results in a raised of redox potential of the receptor part, and the HOMO of the receptor becomes lower in energy than the fluorophore. Metal ions block the PET process from the receptor to the fluorophore, and fluorescence enhancement occurs [4.32].

On gradual addition of the Zn^{2+} metal ion (0–1.1 equiv.) to the **HL4** solution, a large enhancement of fluorescence intensity (~10 folds for Zn^{2+}) has been observed. In the presence of

Zn^{2+} the original emission peak has made a bathochromic shift (red shift) to 472 nm. In the presence of Zn^{2+} ions rigidity of the molecule increases via metal coordination, which restricts free rotation around the H–C=N bond. Transfer of the imine-nitrogen lone pair to the metal centre also holds for the PET process. These two simultaneous effects are jointly accountable for fluorescence enhancement (CHEF effect) (**Fig 4.13**). A significant enhancement of the quantum yield value of free **HL4** (0.04) to its metal-bound form (0.19 for **HL4** + Zn^{2+}) also supports the above fact (**Table 4.1**). The average fluorescence lifetime experiment for the chemosensor (**HL4**) and Zn^{2+} bound chemosensor was studied at 298 K in HEPES buffer at pH = 7.4 (MeOH:H_2O, 9:1, (v/v)) using the formula ($\tau_f = a_1\tau_1 + a_2\tau_2$, where a_1 and a_2 are relative amplitudes of the decay process) and a significant enhancement of lifetime is observed in Zn^{2+} bound chemosensor **(**5.48 nS, and 2.95 nS for **HL4**) (**Fig. 4.14, Table 4.1**). Importantly, the presence of other metal ions did not produce any significant fluorescence responses. A plot of fluorescence intensity at 472 nm against increasing concentrations of Zn^{2+} in the presence of the probe gave a rapid fluorescence enhancement upto 1 equivalent of Zn^{2+} suggesting 1:1 binding between the probe and Zn^{2+}. Fluorescence data was further utilized for Job's plot analysis, which again proves the 1:1 binding stoichiometry of divalent metal ions towards the chemosensing probe **HL4** (**Fig. 4.15**). Limit of detection (LOD) of the chemosensor towards Zn^{2+} ions is calculated using 3σ method. The detection limit of the chemosensor for Zn^{2+} ions is 4.12×10^{-6} M (**Table 4.1**).

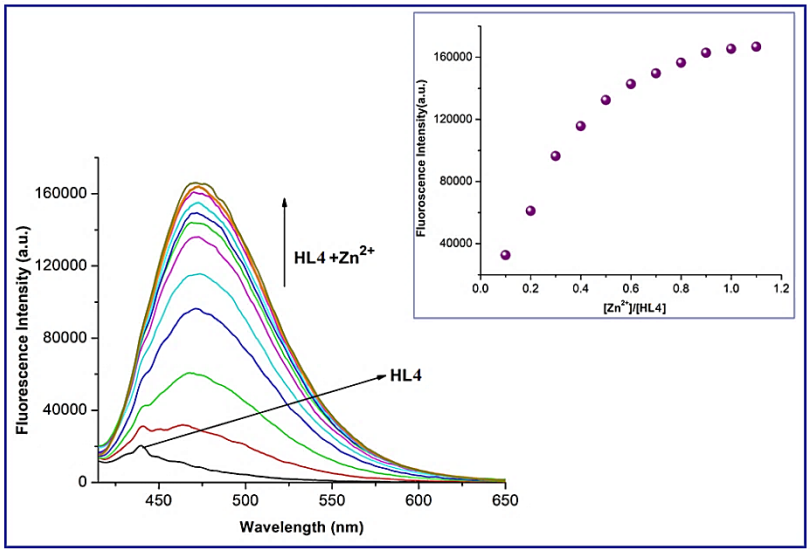

Fig. 4.12. Fluorescence titration of **HL4** (20 µM) in HEPES buffer at pH 7.4 (MeOH:H_2O, 9:1, (v/v)) are gradually mixed with Zn^{2+} (0–22 µM) with λ_{em}= 472 nm. Inset: non-linear plot of fluorescence intensity vs. concentration of Zn^{2+} ions.

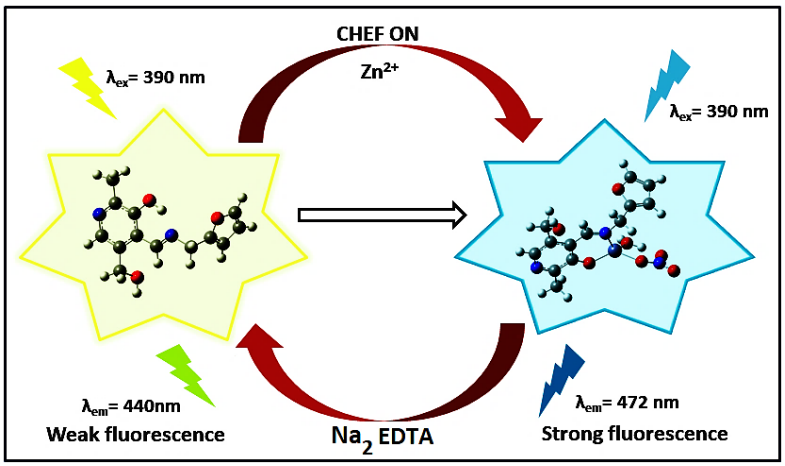

Fig. 4.13. Pictorial representation of 'CHEF-ON' process.

Table 4.1. Apparent binding constant (K), LOD, lifetime (τ_f) and quantum yield (Φ) values of **HL4** and complex **4.1** from spectrofluorometric measurement.

	K (M^{-1})	**LOD** (M)	τ_f (ns) (average)	χ^2	**Φ**
HL4	-		2.95	1.066715	0.04
Complex **4.1**	1.54×10^5	4.12×10^{-6}	5.48	0.9802415	0.19

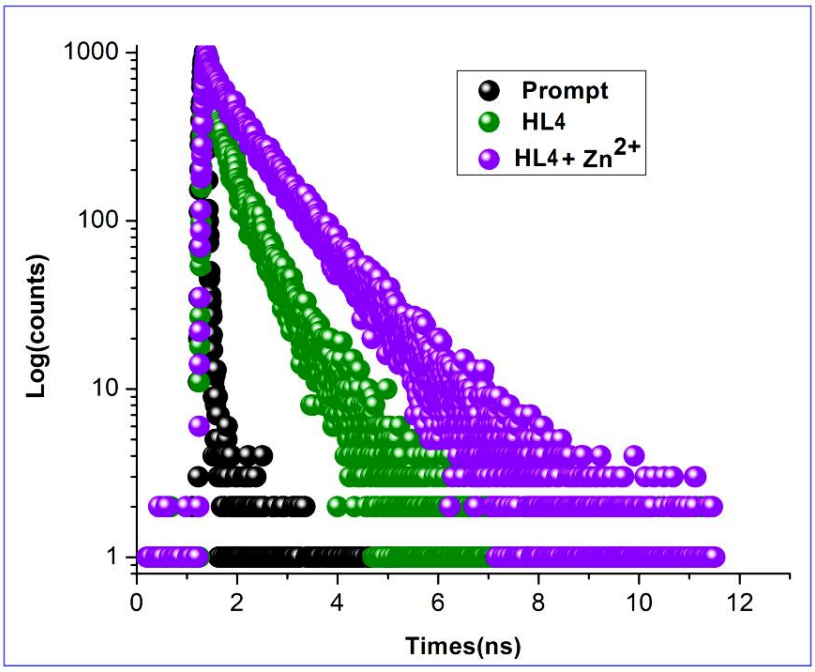

Fig. 4.14. Time-resolved fluorescence decay curves (logarithm of normalized intensity vs time in nS) of **HL4** in the absence (●) and presence (●) of Zn^{2+} ion, (●) indicates decay curve for the scattered.

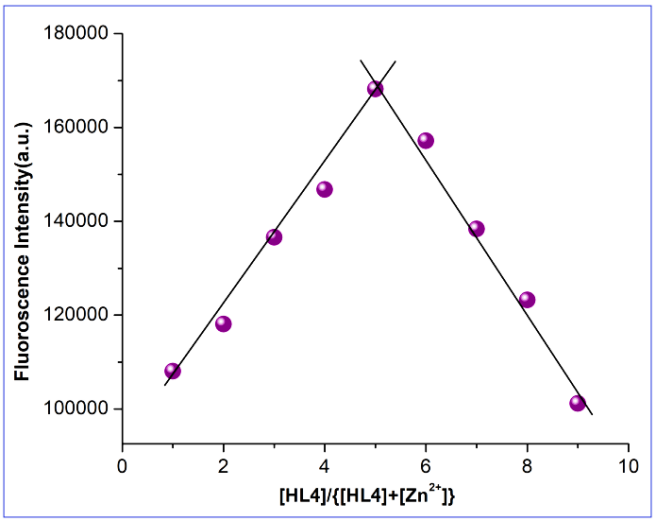

Fig. 4.15. 1:1 binding stoichiometry has shown by Job's plot for complex **4.1**. Symbols and solid lines represent the experimental and simulated profiles, respectively.

The selectivity of the probe towards the Zn^{2+} ions over other competitive metal ions also examined (**Fig. 4.16**). In the competition assay, Zn^{2+} ions added to **HL4** (1 equiv.) in the presence of other metal ions (5 equiv.). Most of the ions showed no change of fluorescence intensity (**Fig. 4.17**). This is a clear indication of the selectivity of the probe towards Zn^{2+} metal ions. The influence of different anions such as AcO^-, OCN^-, F^-, Br^-, I^-, Cl^-, N_3^-, $S_2O_3^{2-}$, SO_3^{2-}, PF_6^-, $P_2O_7^{2-}$, NO_3^-, BF_4^-, ClO_4^-, $H_2PO_4^-$, HPO_4^{2-}, AsO_2^-, S^{2-}, SCN^-, PO_4^{2-}, L-Histidine, L-Cystiene, and ATP on **HL4** had been examined in HEPES buffer at pH 7.4 (MeOH:H_2O, 9:1 (v/v)). No significant fluorescence enhancement or quenching was found (**Figs. 4.16** and **4.17**).

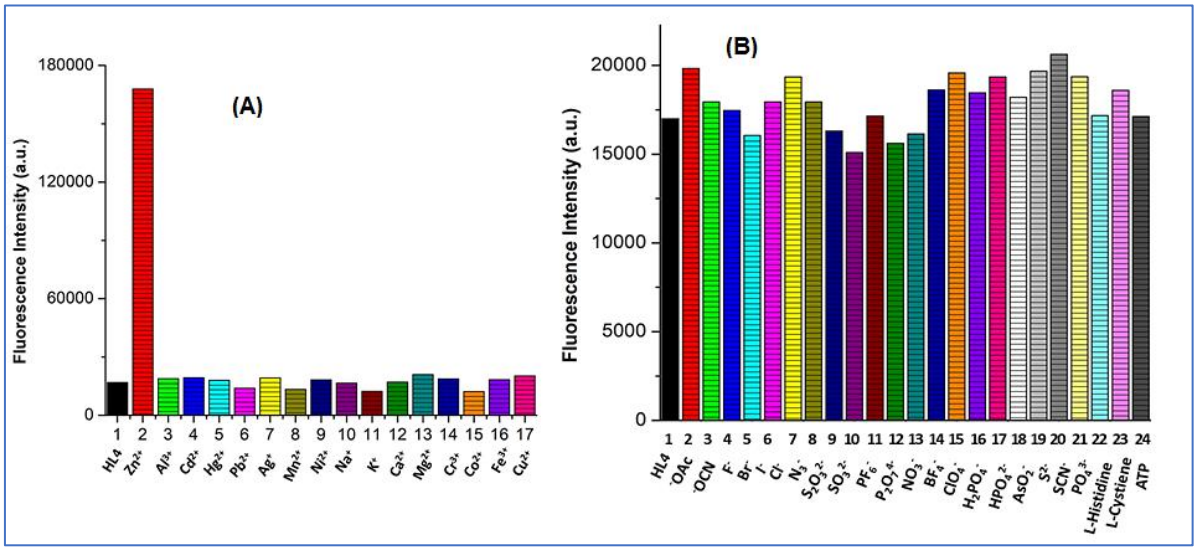

Fig. 4.16. Relative fluorescence intensity profile of **HL4** in the presence of (A) different cations [1=only **HL4** (20 µM); 2-17=**HL4** (20 µM) + M^{n+} (20 µM), where M^{n+}=(Zn^{2+}, Al^{3+}, Cd^{2+}, Hg^{2+}, Pb^{2+}, Ag^+, Mn^{2+}, Ni^{2+}, Na^+, K^+, Ca^{2+} , Mg^{2+}, Cr^{3+}, Co^{2+}, Fe^{3+} and Cu^{2+}, respectively)]; (B) different anions [1=only **HL4** (20 µM); 2-24=**HL4** (20 µM) + M^{n-} (20 µM), where M^{n+}= AcO^-, OCN^-, F^-, Br^-, I^-, Cl^-, N_3^-, $S_2O_3^{2-}$, SO_3^{2-}, PF_6^-, $P_2O_7^{2-}$, NO_3^-, BF_4^-, ClO_4^-, $H_2PO_4^-$, HPO_4^{2-}, AsO_2^-, S^{2-}, SCN^-, PO_4^{3-}, L-Histidine, L- Cystiene and ATP, respectively] in HEPES buffer at pH 7.4 (MeOH:H_2O, 9:1, (v/v)).

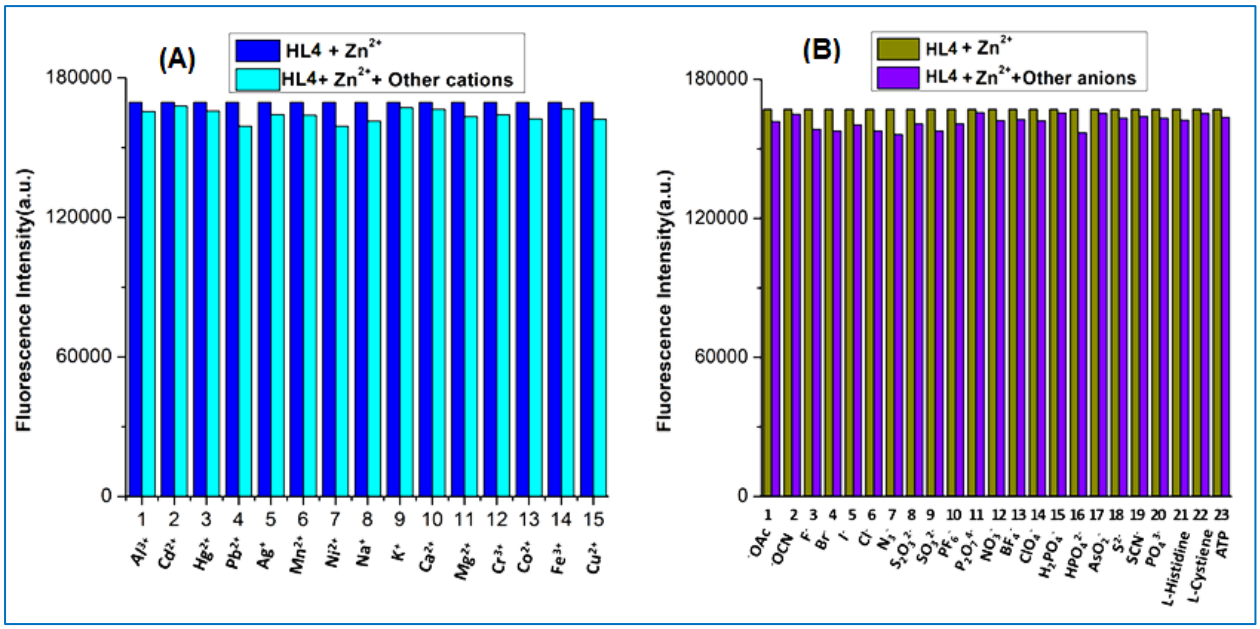

Fig. 4.17. Relative fluorescence intensity diagram of [**HL4**–Zn^{2+}] with (A) different cations (M^{n+}) and (B) different anions (M^{n-}) in HEPES buffer at pH 7.4 (MeOH:H_2O, 9:1, (v/v)) where **HL4** (20 µM) + Zn^{2+}(20 µM) + M^{n+}/ M^{n-} (100 µM), respectively).

The reversibility test and regeneration of the free probe are two vital points to check its applicability in real sample analysis. Where a strong chelating ligand such as 1 equiv. of Na_2EDTA (sodium salt of ethylenediaminetetraacetic acid) solution was used. First, the addition of 1 equiv. of Zn^{2+} ions results in blue fluorescence (**Fig. 4.18**). Initial blue fluorescence vanished with the generation of a colourless solution when Na_2EDTA mixed with **HL4** and 1 equiv. of Zn^{2+} ion solution. Formation of free probe and metal bound EDTA complex is responsible for such incidents. The colour of chemosensor (**HL4**) in the presence of different metal ions under UV and visible light are shown in **Fig. 4.19**.

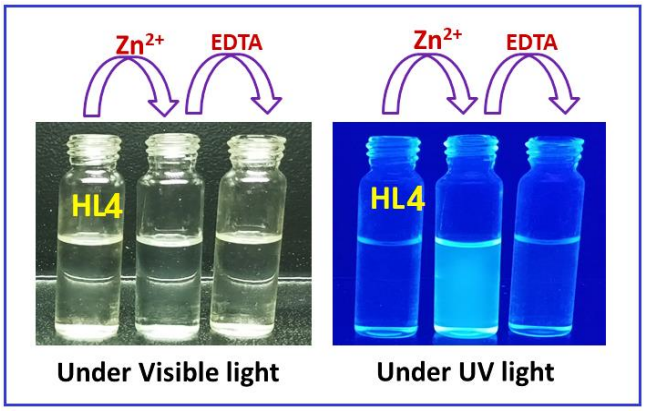

Fig. 4.18. Visual colour changes in reversibility experiment in HEPES buffer at pH 7.4 (MeOH:H_2O, 9:1, (v/v)). Here, **HL4** (20μM), **HL4** (20μM) + Zn^{2+} (20μM), **HL4** (20μM) + Zn^{2+} (20μM) + $EDTA^{2-}$ (20μM), respectively under visible light and UV lamp.

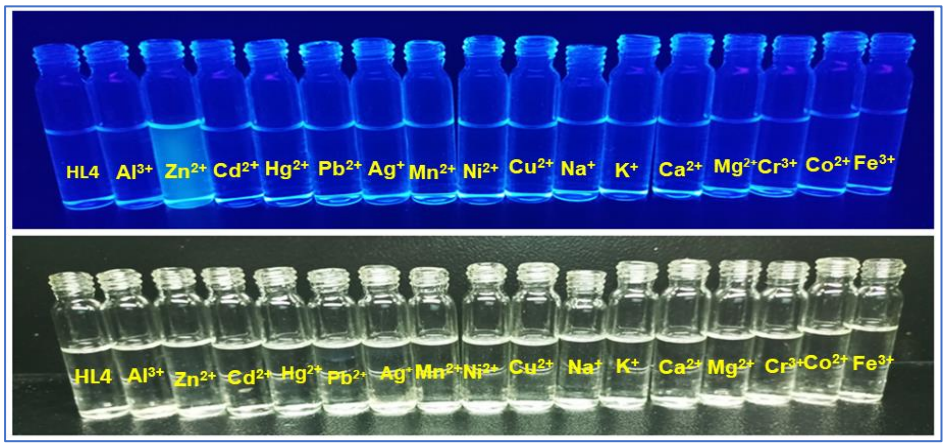

Fig. 4.19. Colour changes of chemosensor (**HL4**) (20μM) under UV and Visible light in HEPES buffer at pH 7.4 (MeOH:H_2O, 9:1, (v/v)).

As a part of the on-field applicability of the probe, we have utilized a paper strip experiment to support its fluorescence sensing property. In this experiment, a paper strip is dipped in free chemosensor and then charged with Zn^{2+} solution. A significant colour change of the strips from colourless to fluorescent blue under UV-light had been noticed (**Fig. 4.20**). Importantly, the colour intensity of the paper strip remains unaffected in presence of different cations. The low detection limit of this paper-based chemosensor **HL4** (~10^{-6} M) suggests that this simple process could be effectively used for fast and selective fluorescence detection of Zn^{2+}

for environmental sample analysis in remote areas where provision of analytical instrumentation is difficult.

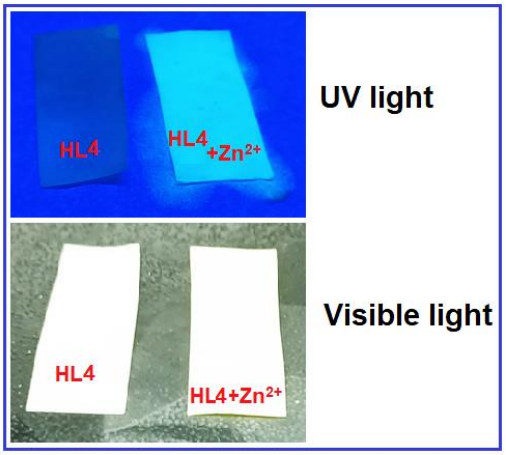

Fig. 4.20. Colour change of paper strips under visible light (below) and UV light (above) in presence of chemosensor **HL4** and **HL4** + Zn^{2+}, respectively.

To study biological and environmental samples, the effect of pH on emission intensity of the free chemosensor (**HL4**) and metal-bound form needs to be analyzed. The weak fluorescence intensity of the free chemosensor has found to be unaffected throughout the pH window (**Fig. 4.21**). In the presence of Zn^{2+} ions, up to pH 3 (strong acidic condition), similar fluorescence patterns suggest no complex formation. On the pH scale, 3.5-6.5 fluorescence intensity increased abruptly, indicating metal-chemosensor complex formation. After that, fluorescence intensity remains unchanged up to pH 8.5, indicating the stability of the compound at pH 8.5. Fluorescence enhancement is probably due to deprotonation of phenolate−OH proton followed by coordination with imine N and phenoxido O with the metal centre. PET and -C=N isomerization processes have been restricted, followed by the initiation of the CHEF process, resulting in fluorescence enhancement. Therefore, **HL4** can act as a selective fluorescent probe for Zn^{2+} ions in biological cell imaging studies under physiological conditions.

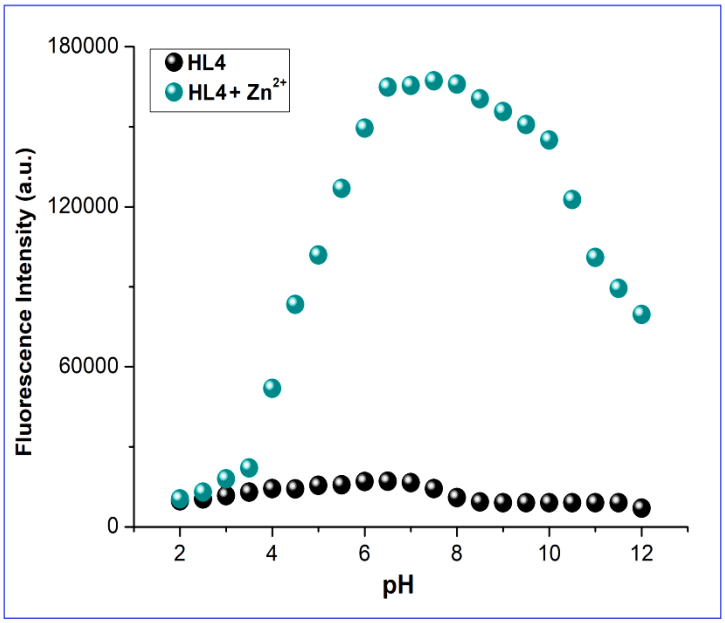

Fig. 4.21. Fluorescence intensity of **HL4** (20 µM) in the absence and presence of Zn^{2+} ions (20 µM) at various pH values in HEPES buffer.

4.3.5. Application of HL4 in living cell imaging studies

Cell imaging study was performed on PC3 cells and the probe **HL4** was used as an efficient luminescent bio-probe towards Zn^{2+} ions (Fig. 4.22). Initially, different concentrations of **HL4** probe were prepared and applied on PC3 cells to evaluate its cytotoxicity by MTT assay (Fig. 4.23). The probe **HL4** was amicable towards cell viability up to 100 µM concentration. Green fluorescence was detected in presence of free **HL4** as well as when the cells were treated with **HL4** and Zn^{2+} ions as evident from fluorescence microscopy.

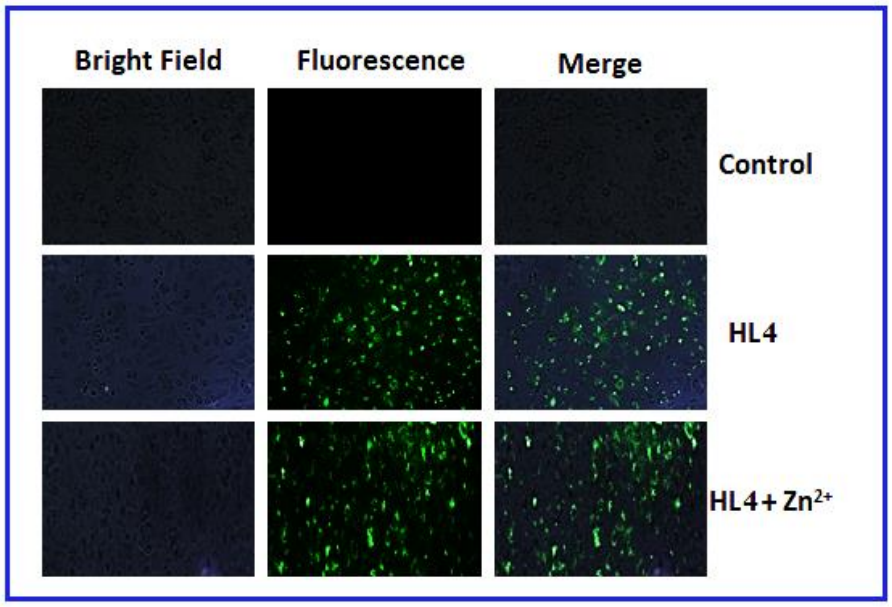

Fig. 4.22. Bright field, fluorescence and merged microscopic images of untreated PC3 (Control), cells treated with **HL4** (20 μM), **HL4** (20 μM) + Zn^{2+} (20 μM), respectively.

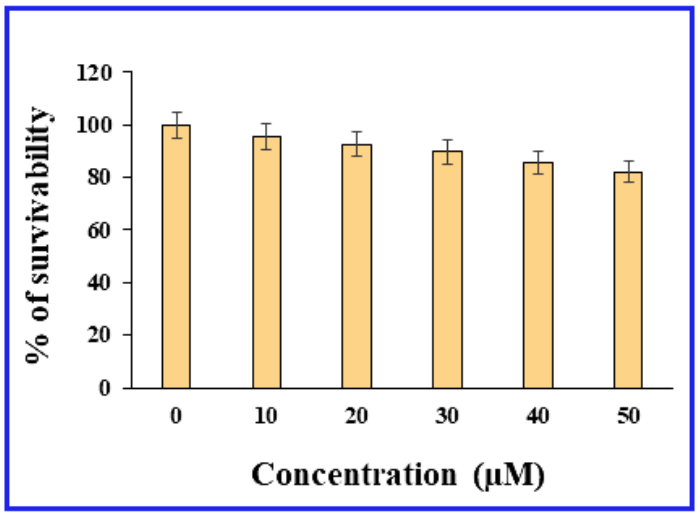

Fig. 4.23. Cell survivability of PC3 cells exposed to the chemosensor **HL4**.

4.3.6. DFT and TDFT studies

DFT calculations were performed in order to better understand the interaction between the chemosensor (**HL4**) and the Zn^{2+} ion as well as their structural parameters. Furthermore, the contributions of M.O.s who participated in electronic transitions were analysed by TDDFT studies. Using TDDFT analysis, we get an idea of the quantity of energy associated with different transitions and the contribution from ligand and metal centres in the respective M.O.s. The DFT/B3LYP method had been performed to optimize the geometries of the chemosensor (**HL4**) and complex **4.1**. Interestingly, the chemosensor-bound mononuclear Zn^{2+} structure had been optimized for complex **4.1**. In complex **4.1**, metal centre (Zn^{2+}) is connected by imine nitrogen, phenolate oxygen, one H_2O molecule, and one NO_3^- ion coordinated with the metal centre (Fig. 4.24). In free chemosensor, electron density of both HOMO and LUMO is basically concentrated over the pyridoxal unit and imine bond. In complex **4.1**, electron densities in both LUMO and HOMO were found to be ligand-based (Fig. 4.24). The energy of important M.O.s of **HL4** and complex **4.1** is listed in Table 4.2.

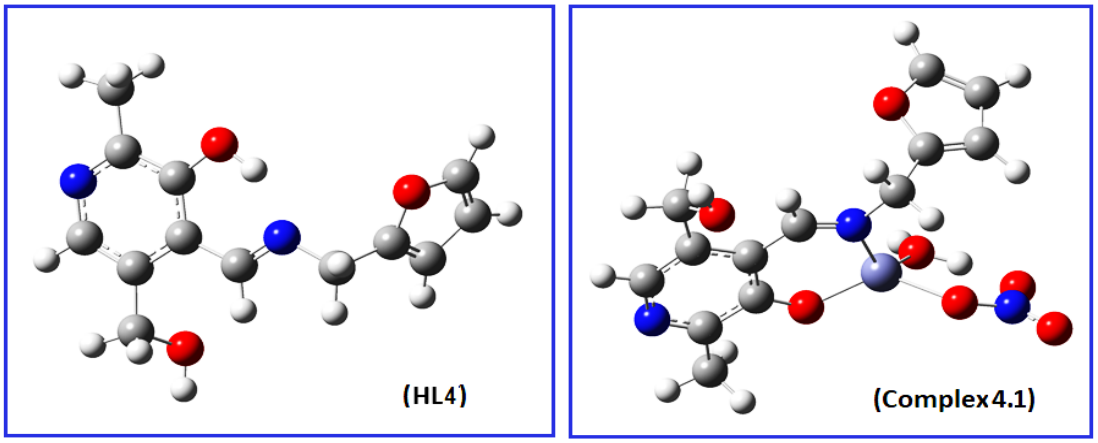

Fig. 4.24. DFT optimized structure of chemosensor **HL4** and complex **4.1**.

Table 4.2. Energy (eV) of selected M.O.s of chemosensor (**HL4**) and complex **4.1**.

M.O.s	HL4	Complex 4.1
LUMO+4	**1.81**	**0.18**
LUMO+3	**0.72**	**0.34**
LUMO+2	**0.08**	**0.52**
LUMO+1	**-0.18**	**-2.27**
LUMO	**-1.52**	**-2.68**
HOMO	**-6.2**	**-6.1**
HOMO-1	**-6.31**	**-6.66**
HOMO-2	**-6.65**	**-6.8**
HOMO-3	**-7.03**	**-7.49**
HOMO-4	**-7.23**	**-7.7**

Table 4.3. Electronic transition calculated by TDDFT using B3LYP/CPCM method in MeOH solvent of chemosensor (**HL4**) and complex **4.1**.

	$E_{ex.}$ (ev)	**$\lambda_{ex.}$ (nm)**	**Osc. Strength (f)**	**Key transition**	**Transition assigned**
HL4	3.07	403	0.0397	HOMO→LUMO+2 (64%), HOMO→LUMO (24%)	$n\rightarrow\pi^*$
	3.80	325	0.0079	HOMO-2→LUMO (41%), HOMO-1→LUMO (57%)	$n\rightarrow\pi^*$ or $\pi\rightarrow\pi^*$
	4.30	287	0.0805	HOMO-2→LUMO (56%), HOMO-1→LUMO (39%)	$\pi\rightarrow\pi^*$
	5.12	242	0.0127	HOMO-4→LUMO (53%), HOMO-3→LUMO (27%)	$\pi\rightarrow\pi^*$
Complex 4.1	2.82	387	0.1625	HOMO→LUMO+1 (85%), HOMO-2→LUMO+1 (6%)	$n\rightarrow\pi^*$
	2.84	325	0.0358	HOMO-2→LUMO+1 (47%), HOMO-1→LUMO+1 (52%)	$n\rightarrow\pi^*$
	4.44	279	0.0069	HOMO-4→LUMO+1 (76%)	$\pi\rightarrow\pi^*$

Table 4.4. Contour plots of some selected molecular orbital of **HL4** and complex **4.1**.

M.O.s	HL4	Complex 4.1
LUMO+4	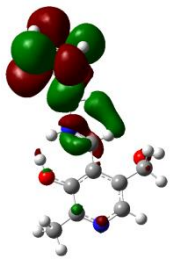	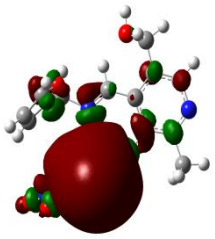
LUMO+3	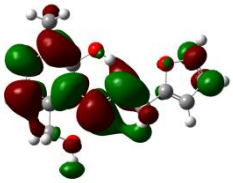	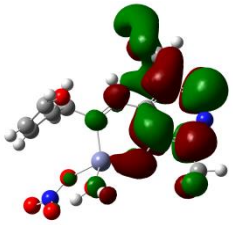
LUMO+2	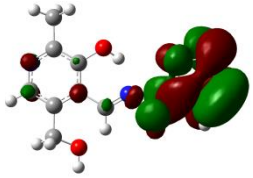	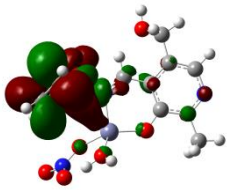
LUMO+1	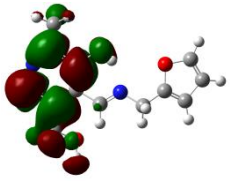	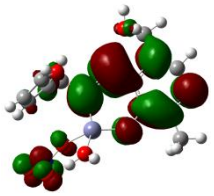
LUMO	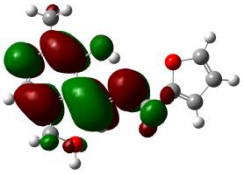	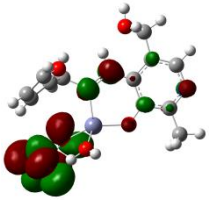

HOMO	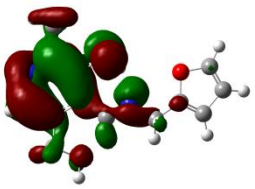	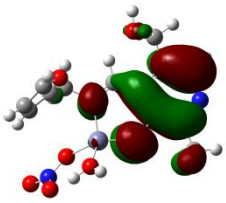
HOMO-1	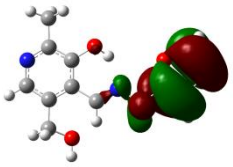	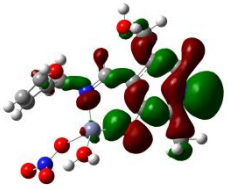
HOMO-2	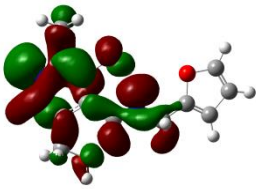	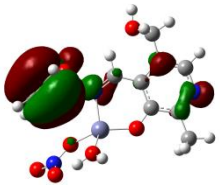
HOMO-3	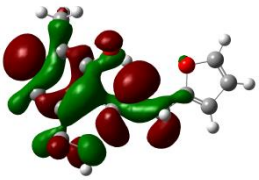	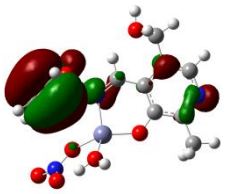
HOMO-4	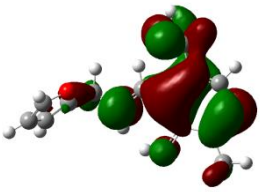	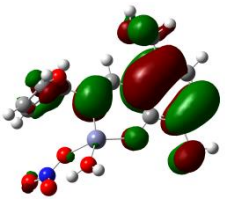

In TDDFT calculations, we have used the B3LYP/CPCM method with the same basis sets in MeOH. Theoretically obtained electronic transitions for **HL4** and complex **4.1** are given in **Table 4.3**, and contour plots of relevant molecular orbitals are given in **Table 4.4**. Theoretically obtained electronic transitions for the chemosensor (**HL4**) and complex **4.1** are well matched with the experimental data. From theoretical calculations, we found that in the case of **HL4** absorption bands appeared at 403, 325, 287 and 242 nm. These bands are assigned as HOMO→LUMO+2 (64%), HOMO→LUMO (24%), HOMO-2→LUMO (41%), HOMO-1→LUMO (57%), HOMO-2→LUMO (56%), HOMO-1→LUMO (39%), HOMO-4→LUMO (53%), HOMO-3→LUMO (27%) (**Fig. 4.25**, **Table 4.3**). In complex **4.1** important transitions are HOMO→LUMO+1 (85%), HOMO-2→LUMO+1 (47%), HOMO-1→LUMO+1 (52%), HOMO-4→LUMO+1 (76%) (**Fig. 4.26** and **Table 4.3**). It has been observed that HOMO and LUMO of the free chemosensor were better stabilized in their metal-bound form. The HOMO-LUMO and energy gap of free probe (4.68 eV) decreased appreciably in its Zn^{2+}-bound complex (3.42 eV).

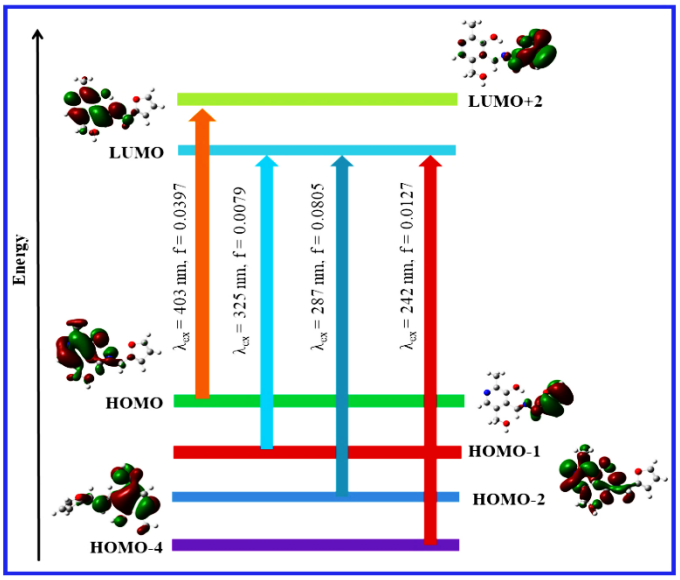

Fig. 4.25. Pictorial representation of key transitions of chemosensor **HL4**.

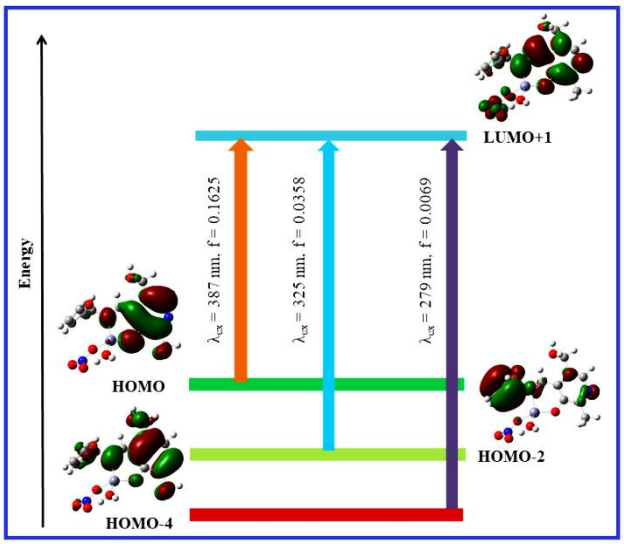

Fig. 4.26. Pictorial representation of key transitions of complex **4.1**.

4. 4. Conclusion

In this work, development of a pyridoxal-based chemosensor (**HL4)** for selective detection of Zn^{2+} ions has been described. **HL4** exhibits remarkable fluorescence enhancement towards the Zn^{2+} (~10-fold) ion in HEPES buffer at pH = 7.4 (MeOH:H_2O, 9:1, (v/v)). Strong emission at 472 nm (λ_{ex} 390 nm) in the presence of Zn^{2+} ion is basically due to arrest of photo-induced electron transfer (PET) and -C=N isomerization processes followed by chelation-enhanced fluorescence (CHEF). A 1:1 binding stoichiometry between **HL4** and metal ions has been established from Jobs plot analysis. The ESI-Mass data also supports this value. Theoretical calculations show coordination of metal ion with phenoxido oxygen and imine nitrogen of the chemosensor, which also support fluorescence enhancement due to CHEF mechanism. Reversibility and regeneration of the chemosensor in presence of Na_2EDTA are also studied. **HL4** shows a low limit of detection (LOD) and strong association constant towards Zn^{2+} ions (4.12×10^{-6} M and 1.54×10^{5} M^{-1}), suggesting its applicability towards bio-imaging studies. **HL4** was successfully used in paper strip for the identification of Zn^{2+} ions. It is further used in biological samples (PC3 cells) for the detection of Zn^{2+} ions.

4.5. References

[4.1] J. Kong, N. R. Franklin, C. Zhou, M. G. Chapline, S. Peng, K. Cho, H. Dai, Science 287 (2000) 622–625.

[4.2] Z. H. Xiang, C. Q. Fang, S. H. Leng, D. P. Cao, J. Mater. Chem. A 2 (2014) 7662–7665.

[4.3] R. Y. Tsien, ed. A. W. Czarnik, American Chemical Society, Washington, DC, 1993, pp. 130–146.

[4.4] J. M. Berg, H. A. Godwin, Annu. Rev. Biophys. Biomol. Struct. 26 (1997) 357–371.

[4.5] C. J. Frederickson, J. Y. Koh, A. I. Bush, Nat. Rev. Neurosci. 6 (2005) 449–462.

[4.6] A. I. Bush, W. H. Pettingell, G. Multhaup, M. Paradis, J. P.Vonsattel, J. F. Gusella, K. Beyreuther, C. L. Masters, R. E. Tanzi, Science 265 (1994) 1464–1467.

[4.7] A. P. de Silva, H. Q. Nimal Gunaratne, T. Gunnlaugsson, A. J. M. Huxley, C. P. McCoy, J. T. Rademacher, T. E. Rice, Chem. Rev. 97 (1997) 1515–1566.

[4.8] S. C. Burdette, G. K. Walkup, B. Spingler, R. Y. Tsien, S. J. Lippard, J. Am. Chem. Soc. 123 (2001) 7831–7841.

[4.9] C. J. Chang, E. M. Nolan, J. Jaworski, S. C. Burdette, M. Sheng, S. J. Lippard, Chem. Biol. 11 (2004) 203–210.

[4.10] E. Kawabata, K. Kikuchi, Y. Urano, H. Kojima, A. Odani, T. Nagano, J. Am. Chem. Soc. 127 (2005) 818–819.

[4.11] C. J. Frederickson, E. J. Kasarskis, D. Ringo, R. E. Frederickson, J. Neurosci. Methods 20 (1987) 91–103.

[4.12] P. D. Zalewski, S. H. Millard, I. J. Forbes, O. Kapaniris, A. Slavotinek, W. H. Betts, A. D. Ward, S. F. Lincoln, I. Mahadevan, J. Histochem. Cytochem. 42 (1994) 877–884.

[4.13] Y. Zhang, X. Guo, W. Si, L. Jia, X. Qian, Org. Lett. 10 (2008) 473–476.

[4.14] A. Ajayaghosh, P. Carol, S. Sreejith, J. Am. Chem. Soc. 127 (2005) 14962–14963.

[4.15] M. E. Huston, K. W. Haider, A. W. Czarnik, J. Am. Chem. Soc. 110 (1988) 4460–4462.

[4.16] L. M. Canzoniero, S. L. Sensi, D. W. Choi, Neurobiol. Dis. 4 (1997) 275–279.

[4.17] K. R. Gee, Z. L. Zhou, D. Ton-That, S. L. Sensi, J. H. Weiss, Cell Calcium 31 (2002) 245–251.

[4.18] L. Zhu, S. Gong, S. Gong, C. Yang, J. Qin, Chin. J. Chem. 26 (2008) 1424–1430.

[4.19] G. Q. Yang, F. Morlet-Savary, Z. K. Peng, S. K. Wu, J. P. Fouassier, Chem. Phys. Lett. 256 (1996) 536–542.

[4.20] (a) T. Anand, A. S. K. Kumar, S. K. Sahoo, Photochem. Photobiol. Sci. 17 (2018) 414–422; (b) A. Hussain, K. Mariappan, D. C. Cork, L. D. Lewandowski, P. K. Shrestha, S. Giri, X. Wang, A. G. Sykes, RSC Adv. 11 (2021) 34181; (c) M. N. Zavalishin, G. A. Gamov, O. A. Pimenov, A. E. Pogonin, V. V. Aleksandriiskii, S. D. Usoltsev, Yu. S. Marfin, J.Photochem. Photobiol., A: Chemistry 432 (2022) 114112; (d) K. A. Karthick, K. Kaleeswari, C. U. Maheswari, G. Sivaraman, B. Shankar, A. Tamilselvi, J. Photochem. Photobiol, A: Chemistry 428 (2022) 113861; (e) J. Mandal, N. C. Jana, S. G. Chowdhury, P. Karmakar, A. Saha, Inorg. Chem. Commun. 156 (2023) 111217; (f) Y. Upadhyaya, T. Anand, L. T. Babu, P. Paira, G. Crisponi, A. K. SK, R. Kumar, S. K Sahoo, Dalton Trans. 47 (2018) 742–749; (g) S. Mandal, Y. Sikdar, D. K. Maiti, R. Sanyal, D. Das, A. Mukherjee, S. K. Mandal, J. K. Biswas, A. Bauzá, A. Frontera, S. Goswami, J. Photochem. Photobiol. A: Chemistry 334 (2017) 86–100; (h) S. Mandal, Y. Sikdar, D. K. Maiti, G. P. Maiti, S. K. Mandal, J. K. Biswas, S. Goswami, RSC Adv. 5 (2015) 72659; (i) L. Qu, C. Yin, F. Huo, J. Chao, Y. Zhang, F. Cheng, Sens. Actuators B 191 (2014) 158–164.

[4.21] J. D. Siqueira, S. F. Pellegrin, L. A. Fontana, B. A. Iglesias, M. R. Sagrillo, P. S. Oliveira, A. Rossato, L. D. S. Silveira, A. Neves, O. A. Chaves, D. F. Back, Inorg. Chim. Acta 526 (2021) 120530.

[4.22] C. Lee, W. Yang, R.G. Parr, Phys. Rev. B 37 (1988) 785–789.

[4.23] P. J. Hay, W. R. Wadt, J. Chem. Phys. 82 (1985) 270–283.

[4.24] W. R. Wadt, P. J. Hay, J. Chem. Phys. 82 (1985) 284–298.

[4.25] P. J. Hay, W. R. Wadt, J. Chem. Phys. 82 (1985) 299–310.

[4.26] (a) A. B. Pradhan, S. K. Mandal, S. Banerjee, A. Mukherjee, S. Das, A. R. K. Bukhsh, A. Saha, Polyhedron 94 (2015) 75–82; (b) D. B. Hibbert, P. Thordarson, Chem. Commun. 52 (2016) 12792–12805.

[4.27] (a) A. Pramanik, D. Laha, S. Chattopadhyay, S. K. Dash, S. Roy, P. Pramanik. P. Karmakar, Materials Science and Engineering C 65 (2016) 327–337; (b) D. Laha, A. Pramanik, S. Chattopadhyay, S. K. Dash, S. Roy, P. Pramanik, P. Karmakar, RSC Adv. 5 (2015) 68169–68178.

[4.28] L. A. Burns, Á. V. Mayagoitia, B. G. Sumpter, C. D. Sherri, J. Chem. Phys. 134 (2011) 084107–084132.

[4.29] (a) M. E. Casida, C. Jamoroski, K. C. Casida, D. R. Salahub, J. Chem. Phys. 108 (1998) 4439−4449; (b) R. Bauernschmitt, R. Ahlrichs, Chem. Phys. Lett. 256 (1996) 454−464.

[4.30] (a) M. Cossi, N. Rega, G. Scalmani, V. Barone, Energies, J. Comput. Chem. 24 (2003) 669−681; (b) M. Cossi, V. Barone, J. Chem. Phys. 115 (2001) 4708−4717; (c) V. Barone, M. Cossi, J. Phys. Chem. A 102 (1998) 1995−2001.

[4.31] M. J. Frisch, G. W. Trucks, H. B. Schlegel, G. E. Scuseria, M. A. Robb, J. R. Cheeseman, G. Scalmani, V. Barone, B. Mennucci, G. A. Petersson, H. Nakatsuji, M. Caricato, X. Li, H. P. Hratchian, A. F. Izmaylov, J. Bloino, G. Zheng, J. L. Sonnenberg, M. Hada, M. Ehara, K. Toyota, R. Fukuda, J. Hasegawa, M. Ishida, T. Nakajima, Y. Honda, O. Kitao, H. Nakai, T. Vreven, J. A. Jr. Montgomery, J. E. Peralta, F. Ogliaro, M. Bearpark, J. J. Heyd, E. Brothers, K. N. Kudin, V. N. Staroverov, R. Kobayashi, J. Normand, K. Raghavachari, A. Rendell, J. C.

Burant, S. S. Iyengar, J. Tomasi, M. Cossi, N. Rega, J. M. Millam, M. Klene, J. E. Knox, J. B. Cross, V. Bakken, C. Adamo, J. Jaramillo, R. Gomperts, R. E. Stratmann, O. Yazyev, A. J. Austin, R. Cammi, C. Pomelli, J. W. Ochterski, R. L. Martin, K. Morokuma, V. G. Zakrzewski, G. A. Voth, P. Salvador, J. J. Dannenberg, S. Dapprich, A. D. Daniels, Ö. Farkas, J. B. Foresman, J. V. Ortiz, J. Cioslowski, D. J. Fox, GAUSSIAN 09, Rev. C.01; Gaussian, Inc. 2009.

[4.32] Z. Xu, J. Yoon, D. R. Spring, Chem. Soc. Rev. 39 (2010) 1996–2006.

Chapter 5

Derivative of clove oil used as chemosensor for colorimetric and fluorometric detection of Al^{3+}: crystal structure description and live cell imaging

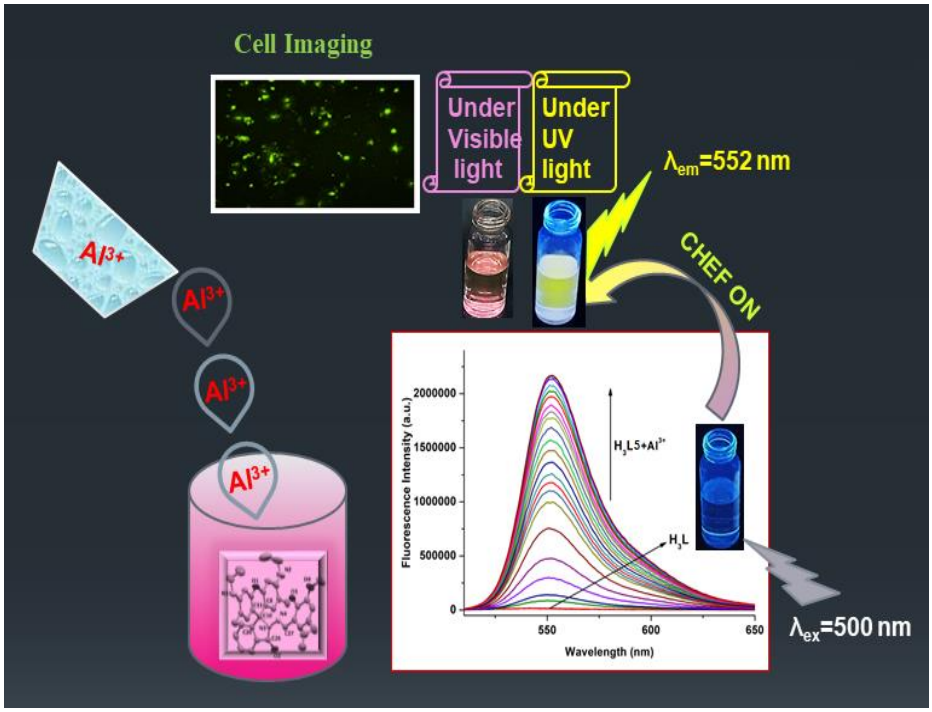

Abstract

Eugenol, popularly known as Clove oil, has been treated as an important natural ingredient from ancient times due to its versatile pharmacological properties. Till date use of derivatives of clove oil as chemosensors for recognition of metal ions has been unexplored. Here, an eugenol-rhodamine based dual sensor (colorimetric and fluorometric), **H_3L5** has been synthesized via condensation reaction between N-(rhodamine-6G)lactam-hydrazine and eugenol-5-aldehyde which selectively detect Al^{3+} ion in HEPES buffer at pH = 7.4 (MeOH:H_2O, 9:1, (v/v)). Crystal structure of chemosensor (**H_3L5**) validates Schiff base condensation reaction and formation of closed spirolactum ring. Upon excitation at 500 nm **H_3L5** generate pink coloration and strong fluorescence enhancement (~138 times at 552 nm) in presence of Al^{3+}. 1:1 **H_3L5**, metal ion binding stoichiometry has been established using ESI-MS value, NMR, IR spectroscopic data. Strong association constant (2.01×10^5 M^{-1}) and low value of limit of detection (LOD) of **H_3L5** against Al^{3+} ($\sim 2.82 \times 10^{-6}$ M) permit us to use it in real world applications and cell imaging studies.

5.1. Introduction

In the field of environmental science and biology, chemical sensing plays an important role. It is a process where the interaction between an analyte and a receptor molecule is monitored by an easily detectable changes [5.1]. In optical sensing, the chemosensors are designed in such a way so that the detection process is based on photophysical changes [5.2]. Among different photophysical techniques, fluorescence spectroscopy is frequently used for detection of different cations, anions, biomolecules and neutral species due to its easy operational technique, low cost, real-time response, along with high selectivity and sensitivity [5.3,5.4].

Aluminium, the third most abundant element present on the earth crust, is indispensible in our life. According to WHO guideline weekly intake of Al^{3+} ion by humans is about 7 mg per kg of the body weight [5.5,5.6]. It is used in our daily life in numerous way, utensils, medicines, electric materials etc. Enormous use of aluminium in different industries, food additives and pharmaceutical products makes its exposure to the environment [5.7,5.8]. Apart from that acid rain causes increase of Al^{3+} ions in the soil and water which damage crops and growing plants [5.11]. Aluminium acts as a neurotoxic agent. It affects our central nervous system and causes Alzheimer's disease, Parkinson's disease and amyotrophic lateral sclerosis [5.9-5.12]. Therefore, detection of aluminium is crucial for environment and human health [5.7–5.15]. Different sophisticated techniques such as atomic absorption and emission spectroscopy, electrochemiluminescence and electrochemical are available for the detection of Al^{3+} ions [5.16–5.19]. However, many limitations like high cost of the instruments, trained technicians, delicate procedures and lack of selectivity make these techniques difficult to use. In this context fluorescence spectroscopy is best alternative choice. However, synthesis of fluorescent

chemosensors of non-transition metal ion like Al^{3+} is difficult due to its high hydration energy and poor coordination ability.

Our group has been devoted in the development of new chemosensors for selective detection of biologically and environmentally important cations [5.20]. In this work, we have used an eugenol-rhodamine based luminescent sensor for selective detection of Al^{3+} ion. Eugenol is a versatile natural ingredient with a wide spectrum of biological and functional properties. Different pharmacological properties like anti-carcinogenic effects, anaesthetic activity, antioxidant, antimicrobial, anti-inflammatory action make eugenol an important therapeutic tool. It belongs to Phenylpropanoids class of family. It was extracted from the leaves and buds of Eugenia caryophyllata commonly named as clove. WHO (World Health Organization) declared Eugenol as GRAS (generally recognized as safe) compound [5.21,5.22]. Importantly, sensing study and coordination chemistry on eugenol platform is still unexplored. Among different chemosensors (**Chart 5.1**) [5.23a-k] rhodamine-based chemosensors are well known optical sensors. Interesting photophysical properties like emission and absorption wavelengths in visible region and high fluorescence quantum yield make rhodamine derivatives as excellent examples of fluorophoric and chromophoric units [5.24]. They work as ‘‘off–on’’ fluorescent or colorimetric switch chemosensors. They are non-fluorescent and colourless due to closed form spirolactam ring. Presence of external stimuli like H^+ ions, metal ions and mechanical force initiates ring-opening, giving rise to strong fluorescence and a pink colouration [5.25]. Rhodamine-based chemosensors are deployed for detection of different metal ions which have huge impact on the environment and human health for example alkali metal like Al(III) [5.26] heavy and transition-metal ions [5.27] like Cu(II) [5.28], Zn(II) [5.29], Hg(II) [5.30], and Fe(II/III) [5.31].

The synthesized eugenol-rhodamine based optical sensor (**H_3L5**) exhibits huge fluorescence enhancement (~138 times) and color change in presence of Al^{3+} ion. The Schiff base ligand has been synthesized using N-(rhodamine-6G)lactam-hydrazine and eugenol-5-aldehyde. Eugenol-5-aldehyde with an electron rich aromatic unit and hydroxyl group which can provide a lone pair of electrons to the metal centre. Chemosensor **H_3L5** selectively detects Al^{3+} ion. The permissible limit of Al^{3+} ions in water is 2.9 mg. L^{-1}. Therefore, strong binding ability ($2.01 \times 10^5\ M^{-1}$) and low detection limit (LOD) of **H_3L5** against Al^{3+} ($\sim 10^{-6}$ M order) will allow us to use it in practical and biological applications. We have successfully explained the X-ray crystal structure of the chemosensor. X-ray crystal structure of **H_3L5** confirms the Schiff base formation reaction and presence of closed spirolactum ring within the ligand framework. This structurally characterized optical chemosensor will act as a promising tool for the identification of Al^{3+} ion in real world and biological samples due to its easy synthetic procedure, high response rate and dual sensing character (colorimetric and fluorescence).

Chart 5.1. Literature survey of rhodamine based metal ion sensors.

Sl. No.	Probe	Sensing metal	Solvent used	Excitation/Emission (nm)	Limit of detection (LOD) (M)	Binding constant (M^{-1})	Fluorescent intensity enhancement	Crystal structure	Biological study	Refs.
1.	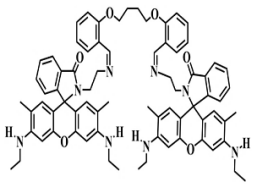	Fe^{3+} Al^{3+} Cr^{3+}	H_2O/CH_3CN (7 : 3, v/v, pH 7.2)	502/558	2.57×10^{-6} 0.78×10^{-6} 0.47×10^{-6}	K_d=1.94×10^{-5} 3.15×10^{-5} 2.26×10^{-5}	669 653 667	No	None	**5.23a**

2.	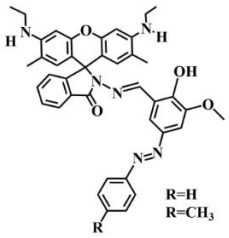	Al^{3+} Cr^{3+} Fe^{3+}	Britton – Robinson buffer solution (H_2O/MeOH 1 : 9 v/v; pH 7.4)	525/555	For R=H 2.86×10^{-8} 2.67×10^{-8} 5.62×10^{-6} For R=CH_3 2.78×10^{-8} 2.61×10^{-8} 6.14×10^{-6}	For R=H (M^{-2}) 5.14×10^{5} 4.91×10^{5} 3.37×10^{4} For R=CH_3 5.03×10^{5} 4.86×10^{5} 3.95×10^{4}	400 400 100	Yes	Cell imaging	**5.23 b**
3.	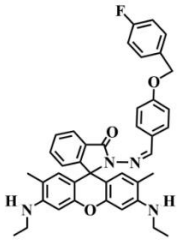	Al^{3+} Ga^{3+} In^{3+} Tl^{3+}	10 mM HEPES buffer in (1:9, v/v) H_2O:EtOH (pH =7.4)	530/555 530/553 530/553 530/558	2.66×10^{-8} 10.4×10^{-8} 8.19×10^{-8} 3.10×10^{-8}	5.01×10^{4} 4.79×10^{4} 4.57×10^{4} 5.75×10^{4}	96 26 32 80	No	None	**5.23c**
4.	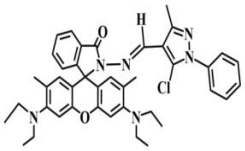	Al^{3+} Fe^{3+} Cr^{3+}	HEPES buffer at pH 7.4 in H_2O/ MeOH (9:1, v/v)	510/575	1.74×10^{-5} 1.86×10^{-5} 3.45×10^{-5}	1.44×10^{6} 1.52×10^{6} 4.01×10^{7}	~10 ~8 ~4	Yes	Cell imaging	**5.23 d**
5.	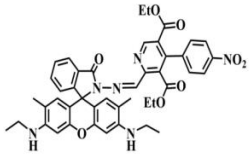	Cr^{3+}	10 mM, CH_3CN –PBS (9 : 1 v/v, pH = 7.4)	531/558	0.21×10^{-6}	1.56×10^{4}	~7	Yes	None	**5.23e**
6.	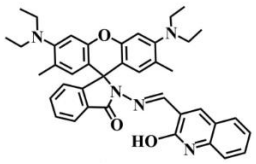	Al^{3+} Cr^{3+} HSO_4^-	H_2O-CH_3CN (1:9, v/v)	500/585 500/583 500/587	2.20×10^{-8} 2.12×10^{-8} 8.63×10^{-7}	1.79×10^{5} 1.79×10^{4}	341 292 136	No	Cell imaging	**5.23f**
7.	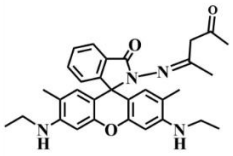	Cu^{2+}	1 mM PBS buffer in an CH_3CN /PBS (v/v, 1 :1%) at pH = 7.4	510/550	3.58×10^{-8}	0.2×10^{-5}	28	No	Cell imaging	**5.23g**

8.	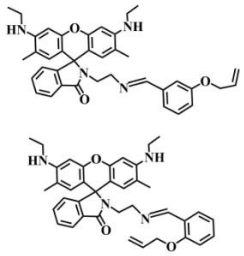	Al^{3+} Al^{3+}	10 mM HEPES buffer in H_2O/EtOH = 1:9 (v/v) (pH 7.4)	530/553	1.11×10^{-9} 1.05×10^{-9}	3.98×10^{4} 1.09×10^{4}	145 52	No	Cell imaging	**5.23 h**
9.	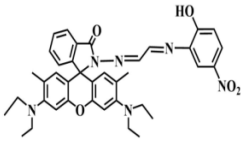	Fe^{3+} Al^{3+} Cr^{3+} and Hg^{2+}	EtOH/ H_2O (4/1, v/v HEPES, pH = 7.4)	559/582 559/582 559/582 and 555/578	10.20×10^{-9} 14.66×10^{-9} 58.78×10^{-9} and 73.33×10^{-9}	5.78×10^{5} 7.07×10^{5} 4.10×10^{5} 3.97×10^{5}	~15	No	Cell imaging	**5.23i**
10	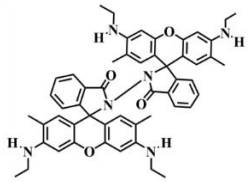	Al^{3+} Fe^{3+}	EtOH	530/560	0.76×10^{-9} 0.49×10^{-9}	---	>900	Yes	Cell imaging	**5.23j**
11	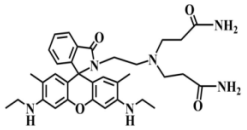	Fe^{3+}	H_2O (pH 7.2, 10 mM HEPES buffer)	510/551	4.184×10^{-6}	$(1.16\pm0.04)\times10^{4}$	14	No	Cell imaging	**5.23 k**
12	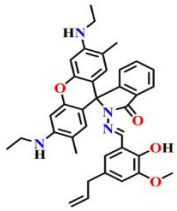	**Al^{3+}**	**HEPES buffer (9:1, MeOH: H_2O, v/v, pH 7.4)**	**500/552**	**2.82×10^{-6}**	**2.01×10^{5}**	**138**	**Yes**	**Cell imaging**	**This work**

5.2. Experimental section

5.2.1. Materials and physical measurements

Every chemical or reagent used is of analytical grade, and commercial sources were sourced for the solvents. These substances were employed without additional purification. An elemental analyzer (Perkin–Elmer 240C) was used to perform elemental analysis (C, H and N). A MICROMASS Q-TOF mass spectrometer and FTIR spectrophotometer using KBr pellets on a Nicolet Magna IR 750 series-II were used to record the electron spray ionisation mass (ESI-MS positive) and infrared spectra (400–4000 cm^{-1}), respectively. Using a quartz cell with a path length of one centimetre, the Cary 60 spectrophotometer (Agilent) was used to gather absorption spectra. Emission spectra were measured at room temperature (298 K) in HEPES buffer (9:1, MeOH: H_2O, v/v, pH 7.4) using a Fluromax-4 spectrofluorometer. To measure the fluorescence life-time, a time-resolved spectrofluorometer from IBH in the UK was used. NMR spectra of the ^{1}H and ^{13}C species were measured in d_6-DMSO solvent using a Bruker 400 spectrometer.

5.2.2. Synthesis

5.2.2.1. Synthesis of N-(rhodamine-6G) lactam-hydrazine

N-(rhodamine-6G)lactam-hydrazine was made using methods documented in literature [5.32].

5.2.2.2. Chemosensor H_3L5 [2-((5-allyl-2-hydroxy-3-methoxybenzylidene)amino)-3',6'-bis(ethylamino)-2',7'-dimethylspiro[isoindoline-1,9'-xanthen]-3-one] preparation

Methanolic solution of eugenol-5-aldehyde [5-allyl-2-hydroxy-3-methoxybenzaldehyde] (2.0 mmol, 0.384 g) was thoroughly mixed with N-(rhodamine-6G)lactam-hydrazine (2.0 mmol, 0.856g) in 20 mL methanol-chloroform (9:1,v/v). The solution mixture was then heated for around two hours while refluxing. Crystals of light pink colour were formed when the solvent

slowly evaporated. Subsequently, the crystal was utilized directly for complexation and characterization.

Yield: 1.094 g (80%). Anal. Calc. For $C_{37}H_{38}N_4O_4$: C 73.73%; H 6.36%; N 9.30%; Found: C73.70%; H6.35%; N 9.26%. IR (cm^{-1}, KBr): υ(O-H) 3401s; υ(C=O)1688s,υ(C=N) 1621s. ESI-MS (positive) in MeOH: *m/z*= 602.98 (base peak) $[\mathbf{H_3L5}+H]^+$. UV-Vis, λ_{max} (nm), (ε ($dm^3mol^{-1}cm^{-1}$)) in HEPES buffer (9:1, MeOH: H_2O, v/v, pH 7.4): 306 (106700), 355 (34700) and 500 (800).

^{1}H NMR (400 MHz, d_6-DMSO) δ ppm: 1.21 (-CH_3) (t, 6H, *J*=8Hz), 1.85 (Ar-CH_3) (s, 6H), 3.14 (-CH_2) (m, 4H), 3.23 (-CH_2) (d, 2H, *J*=8Hz), 3.71 (–OCH_3) (s, 3H), 5.01 (-NH) (d, 2H, *J*=8Hz), 5.08 (-CH_2) (m, 2H), 5.88 (=CH_2) (m,2H), 6.20 (Ar-H) (s, 2H), 6.32 (Ar-H) (s, 2H), 6.69 (Ar-H) (s, 1H), 6.78 (Ar-H) (s, 1H), 7.05 (Ar-H) (d, 1H, *J*=8Hz), 7.59 (Ar-H) (m, 2H), 7.92 (Ar-H) (d, 1H), 8.83 (-HC=N) (s, 1H), 10.18 (-OH) (s,1H).

^{13}C NMR (d_6-DMSO, 75 MHz) δ ppm: 14.62, 17.43, 37.95, 39.27, 56.23, 65.98, 79.65, 96.28, 104.72, 114.86, 116.13, 118.97, 120.63, 123.55, 124.24, 127.24, 128.80, 129.26, 130.88, 134.45, 138.15,145.82, 148.26, 148.38, 149.19, 151.46, 151.94, 164.04.

5.2.2.3. Complex 5.1, $Al(HL)(NO_3)_2$ preparation

In 20 mL methanol-chloroform (9:1, v/v) solution of **H_3L5 (**1mmol, 0.602 g), a 2 mL methanolic solution of aluminium nitrate nonahydrate (1 mmol, 0.375 g) was added drop wise. After around 4 hours of stirring, the resulting reaction mixture was refluxed for 1 hour. After the solvent evaporated slowly, a solid with a dark reddish pink colour was produced.

Yield: 0.406 g (86%). Anal. Calc. For $C_{37}H_{36}N_6O_{10}Al$: C 59.12%; H 4.83%; N11.18%. Found: C59.10%; H 4.80%; N11.13%. IR (cm^{-1}, KBr):($\upsilon_{C=O}$) 1605s; ($\upsilon_{C=N}$) 1530; υ(NO_3^-)1302s and 774s. ESI-MS (positive) in MeOH: The base peak was detected at *m/z*= 689.94 which

corresponds [Al(**HL5**) + NO_3]$^+$. UV-Vis, λ_{max} (nm), (ε ($dm^3mol^{-1}cm^{-1}$)) in HEPES buffer (9:1, MeOH: H_2O, v/v, pH 7.4): 299 (117500), 350 (54750) and 530 (189700).

^{1}H NMR (*d*$_6$-DMSO, 400 MHz) δ ppm: 1.21 (-CH_3) (t, 6H, J_1=8Hz, J_2=4Hz), 1.85 (-CH_3) (s, 6H), 3.13 (-CH) (d, 4H, *J*=4 Hz), 3.24 (-CH) (s, 2H), 3.71 (-OCH_3) (s, 3H), 5.02 (=CH_2, -NH) (t, 3H, *J*=8 Hz), 5.88 (=CH_2) (m, 1H), 6.19 (Ar-CH) (s, 2H), 6.32 (Ar-CH) (s, 2H), 6.68 (Ar-CH) (s, 1H), 6.77 (Ar-CH) (s, 1H), 7.04 (Ar-CH) (d, 1H, *J*=4 Hz), 7.59 (Ar-CH) (t, 2H, J_1= J_2=8 Hz), 7.92 (Ar-CH) (d, 1H, *J*=8Hz), 9.27 (-HC=N) (s, 1H).

^{13}C NMR (*d*$_6$-DMSO, 75 MHz) δ ppm: 14.56, 17.41, 38.10, 39.26, 56.24, 79.65, 96.57, 104.98, 114.87, 116.14, 118.98, 120.57, 123.56, 124.24, 127.29, 128.79, 129.30, 130.89, 134.47, 138.15, 138.41, 145.80, 148.25, 149.20, 151.42, 156.19, 157.25, 168.19.

5.2.3 Absorbance and fluorescence spectral analysis

Chemosensor (**H_3L5**) (1 × 10^{-3}M) and different analytes (1 × 10^{-3} M) were prepared in methanol solvent as stock solutions. Subsequently, the **H_3L5** solution was diluted to 1 × 10^{-5} M as needed. In HEPES buffer (9:1, MeOH:H_2O, v/v, pH 7.4), all spectroscopic investigations, including competitive testing of different cations and anions, were carried out. In order to maintain a concentration of 2 × 10^{-5} M, a quartz optical cell measuring 1.0 cm in optical path length was filled with 60 µL of **H_3L5** (1 × 10^{-3} M) solution and progressively mixed with the ion stock solutions. The test samples for competitive assay studies were made by combining the appropriate cations stock with 3 mL of **H_3L5** solution (2 × 10^{-5} M). The excitation wavelength for fluorescence measurements was set at 500 nm, while emission was measured between 505-700 nm.

5.2.4 Detection limit and association constant calculations

The limit of detection (LOD) was determined using the IUPAC approved formula:

$LOD = \frac{3\sigma}{\text{slope}}$ where σ signifiescurve's standard deviation.

The LOD was computed from the fluorescence titration data using equation (1). The chemosensor's (**H_3L5**) association constant (K) for Al^{3+} was computed using the following web resource: https://supramolecular.org [5.33].

5.2.5 X-ray crystallography

Single crystal X-ray data of chemosensor (**H_3L5**) was obtained using graphite mono-chromated Mo Kα radiation (λ = 0.71073 Å) using Bruker SMART APEX-II CCD diffractometer at room temperature. Using the Bruker Apex-II suite programme, data processing, structural solution, and refinement were investigated. All accessible reflections data in the $2\theta_{max}$ range were collected and corrected for polarization and Lorentz factors using Bruker SAINT plus [5.34]. Subsequently, SADABS was used to adjust reflections for absorption, inter-frame scaling, and various systematic flaws [5.35]. The structures were solved using direct methods and then refined using the SHELX-2017/1 software package and the full matrix least-square methodology based on F^2 [5.36]. Anisotropic thermal characteristics were used to refine every non-hydrogen atom. U_{iso}= 1/2U_{eq} was used to determine the geometrical positions at which C–H hydrogen atoms were bonded. **Table 5.1** contains the crystal data as well as information on the data collecting and refining process for the chemosensor (**H_3L5**).

5.2.6 Cell culture

Cells from the *MC3T3* cell line were cultured at a temperature of 37°C and 5% CO_2 incubator (Thermo Scientific™Heracell™ VIOS 160i) in alpha-MEM media (Gibco) infused with 10% fetal bovine serum (Gibco) and 1% Antibiotic-Antimycotic (100X) (Thermofisher

Scientific, USA) at 37°C and 5% CO_2. The cellular analyses were conducted after splitting the cell population by the enzymatic process using trypsin (Trypsin-EDTA (0.25%), phenol red), after reaching confluency.

5.2.7 Cell viability analysis

For determining the cell viability in the presence of various working concentrations of the solution of the ligand, **H_3L5**, an MTT assay was performed using cells from the ***MC3T3*** cell line. The cells were seeded in triplicates in 96 well plates, at a concentration of 1 x 10^4 per well, for an incubation period of 24 hours, at 37^{o}C and 5% CO_2, with solutions containing 0 µM, 20 µM, 40 µM, 60 µM, 80 µM and 100 µM concentrations of the **H_3L5**. After the process of incubation, the cells were washed with 1xPBS and were administered 50 µL of serum-free alpha-MEM media (Gibco) with 10 µl MTT solution (EZ count TM MTT cell Assay Kit, Hi Media, India) to incubate further for 4 hours, in the environment mentioned previously. After the stipulated period of incubation, 100 µL of Solubilisation Buffer was added to dissolve the formazan crystals. At 570 nm and 670 nm, the absorbance was measured using a UV-Vis spectrophotometer (Thermo Scientific Multiskan GO microplate spectrophotometer, Finland).

5.2.8 Cell imaging

For microscopic analysis, the cells belonging to the ***MC3T3*** cell line were seeded in the wells of a 48-well plate. They were incubated for 24 hours, in an environment having a temperature of 37^{o}C and 5% CO_2, with solutions having the five concentrations of **H_3L5** which included 0 µM, 20 µM, 40 µM, 60 µM, 80 µM and 100 µM and a solution of $Al(NO_3)_3$ (Loba Chemie, Pvt. Ltd., India), with a fixed concentration of 10^{-3} M as the source of the Al^{3+} ions. After 24 hours the cells in each well were washed with 1xPBS and observed under the microscope (Nikon eclipse Tí U, Japan) using a 10x objective lens in a bright field and

fluorescence at an excitation wavelength of 500 nm, which is suitable for the Al^{3+}. The fluorescent images were captured at an emission wavelength of 552 nm.

5.2.9 Fluorescent imaging for detecting intracellular Al^{3+} ions

Cells from the L929 cell line were cultured and seeded in a 48-well plate with the seeding density being maintained at 10^5 cells per well and were incubated for 24 hours in Thermo Scientific™ Heracell™ VIOS 160i having 37°C temperature and 5% CO_2. After incubation, solution (s) containing 100 µM, 80 µM, 60 µM, 40 µM, 20 µM and 0 µM of **H_3L5** were administered to the cells and were again incubated for 24 hours. For microscopic imaging, the cells were washed with 1x PBS, after incubation, and observed under a confocal microscope (Leica Stellaris 5) through a 40x lens in a bright field, and for fluorescent imaging, an excitation wavelength of 500 nm and an emission wavelength of 552 nm was used.

5. 3. Results and discussion

5.3.1. Synthesis and characterization

The chemosensor **H_3L5** has been prepared by Schiff base condensation reaction between rhodamine-6G based amine and 5-allyl-2-hydroxy-3-methoxybenzaldehyde in methanol-chloroform (9:1, v/v) in refluxing condition for *ca*. 2 h. Light pink colour crystal was obtained with good yield (**Scheme 5.1**) after slow evaporation of solvent. Then the crystal was directly used for further characterization and complexation. Various spectroscopic techniques (^{1}H NMR, ^{13}C NMR, UV-Vis and FT-IR) are used to fully characterize it. In the ESI-mass analysis, the base peak of the chemosensor was observed at *m/z* = 602.98, which corresponds to [**H_3L5**+H]$^+$ (**Fig. 5.1**). Again, the FT-IR spectrum of **H_3L5** revealed two distinct bands at 1688 and 1621 cm^{-1} as well as a broad band at around 3401 cm^{-1}. These bands indicate the existence of C=O, C=N and phenolic OH stretching frequencies, respectively (**Fig. 5.2**).

Stoichiometric (1:1) reaction between $Al(NO_3)_3.9H_2O$ with **H_3L5** in methanol medium resulted complex **5.1** {Al(**HL5**)$(NO_3)_2$} in good yield (Scheme 5.2). They were characterized by mass analysis and several spectroscopic techniques. The ESI-mass data of complex **5.1** was found *m/z* = 689.94 corresponding to [Al(**HL5**)NO_3]$^+$ (Fig. 5.3). The characteristics stretching frequency for υ(C=O) and υ(C=N) were seen at 1605 and 1530 cm^{-1} whereas at 1302 and 774 cm^{-1} two distinct peaks were found which signifies asymmetric stretching frequencies for NO_3^- group, respectively (Fig. 5.2).

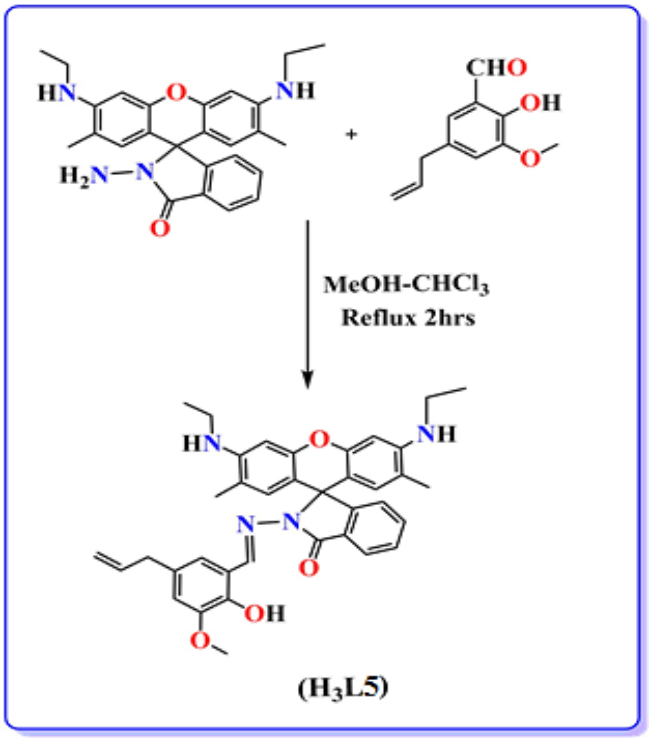

Scheme 5.1. Route to the synthesis of chemosensor (**H_3L5**).

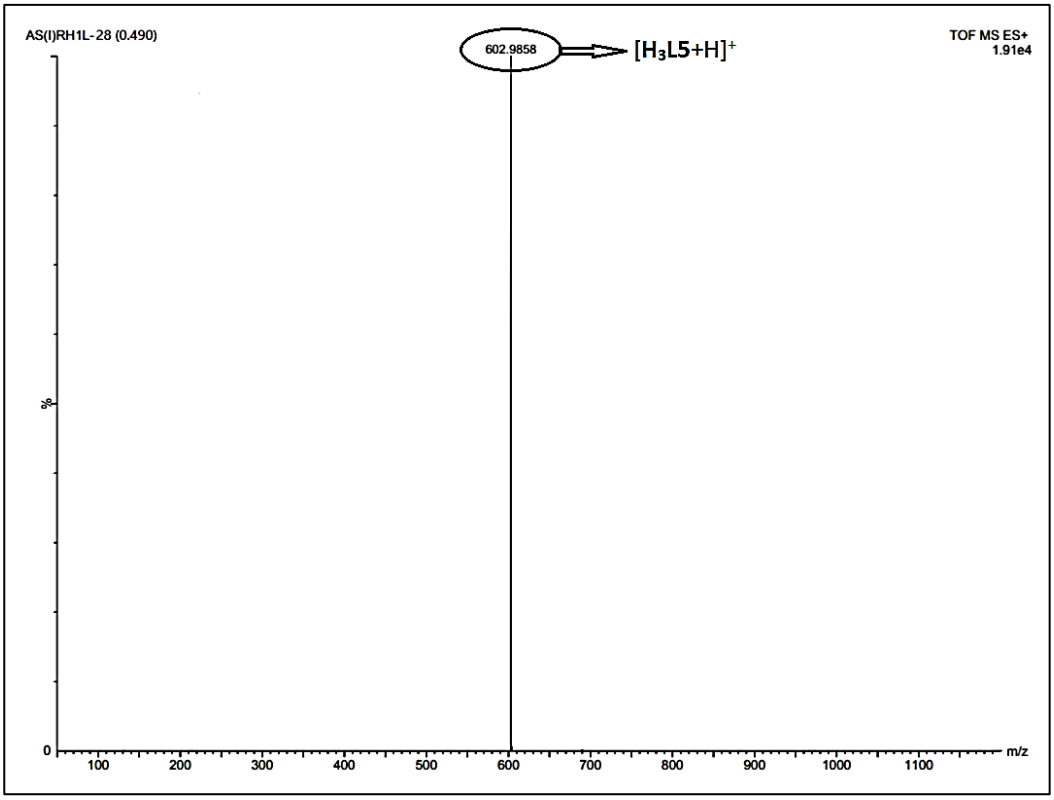

Fig. 5.1 ESI-MS$^+$ spectrum of [**H$_3$L5**+H]$^+$.

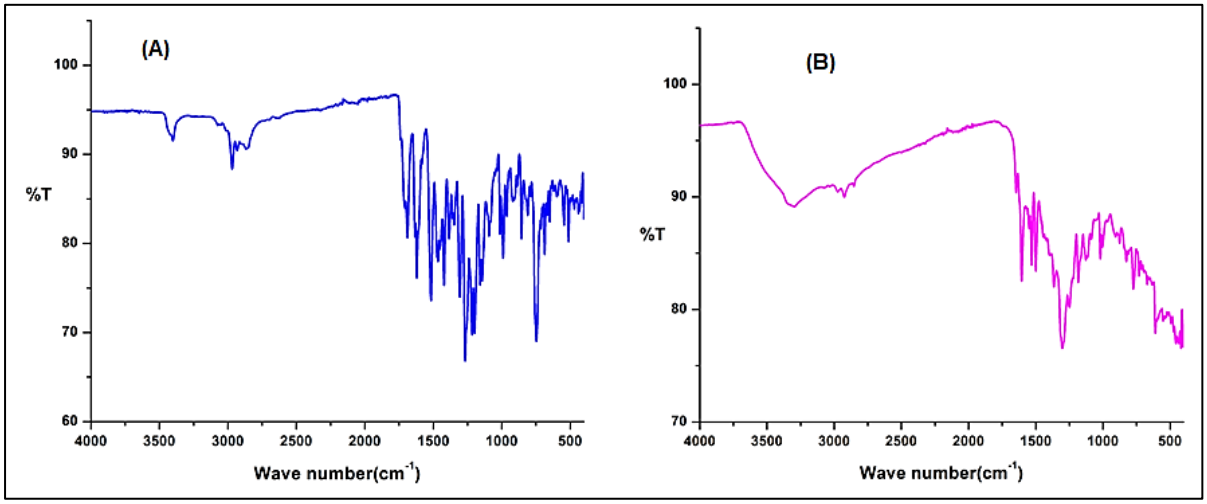

Fig. 5.2. FTIR spectra of (A) chemosensor **H$_3$L5** and (B) complex **5.1**, respectively.

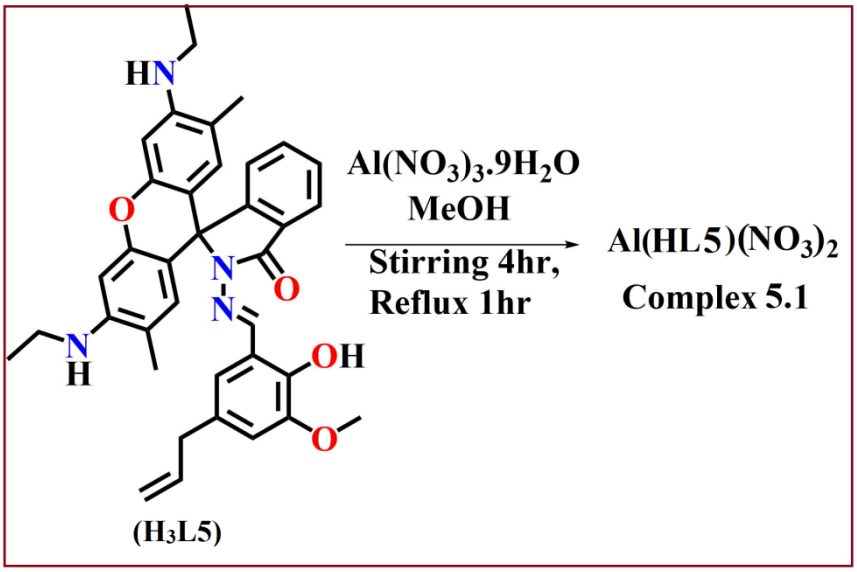

Scheme 5.2. Synthesis route of complex **5.1**.

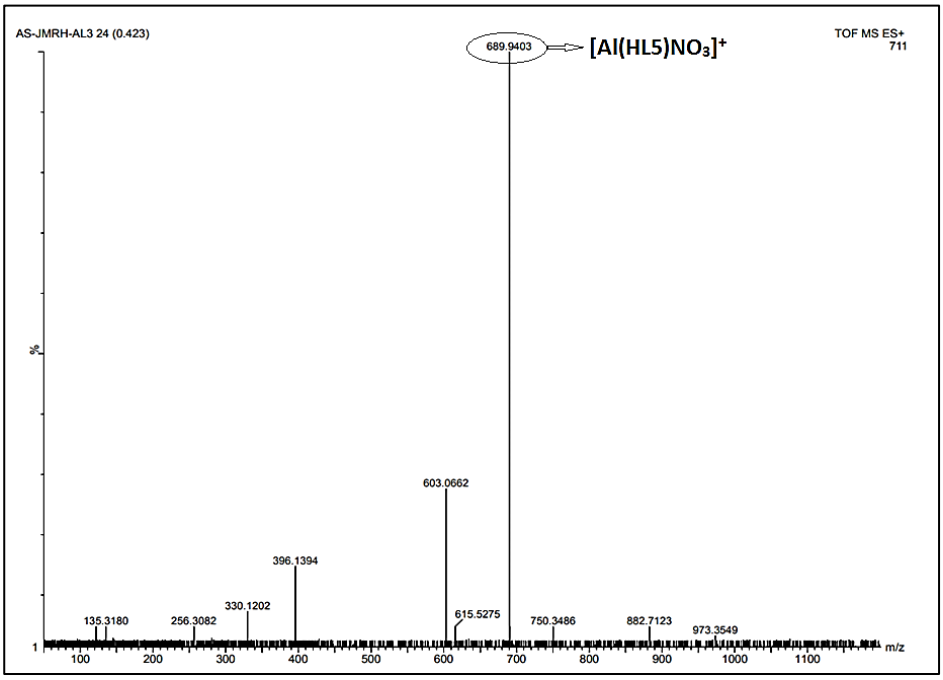

Fig. 5.3. ESI-MS$^+$ spectrum of complex **5.1 {**[Al(**HL5**)NO_3]$^+$}.

5.3.2 Elucidation of crystal structure of chemosensor (H_3L5)

Single crystal X-ray data of **H_3L5** shows that the molecule is present in the triclinic system with *P-1* space group (Table 5.1). Crystal structure of chemosensor **H_3L5** is depicted in Fig.5.4. The molecule is non-planer where closed spirolactam ring in the ligand framework supports its light pink coloration. Important bond distances and bond angles are tabulated in Table 5.2.

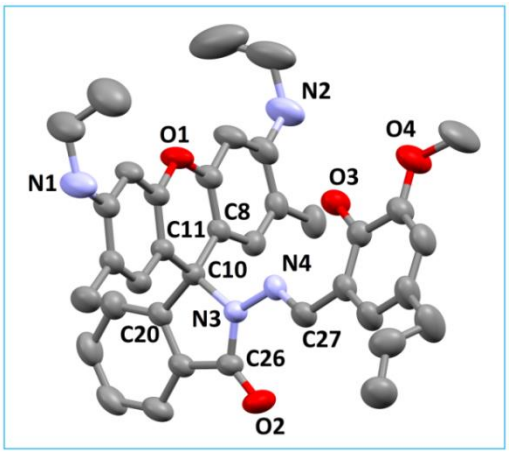

Fig. 5.4. Crystal structure of chemosensor **H_3L5**. Thermal ellipsoids are shown as 30% probability. H atoms are omitted for clarity.

Table 5.1. Crystal parameters and selected refinement details for chemosensor **H_3L5**.

Chemosensor H_3L5	
Empirical formula	$C_{37}H_{36}N_4O_4$
Formula weight	600.70
Temperature (K)	273(2)
Crystal system	Triclinic
Space group	*P-1*
a (Å)	9.3947(3)
b (Å)	12.3486(3)
c (Å)	14.4715(4)
α(°)	94.1270(10)
β(°)	103.7440(10)
γ(°)	94.6350(10)
Volume (Å^3)	1618.23(8)
Z	2
D_{calc} (g cm^{-3})	1.233
Absorption coefficient (mm^{-1})	0.081

F(000)	636
θ Range for data collection (°)	1.662-27.127
Reflections collected	52150
Independent reflection / R_{int}	5687/ 0.0419
Data / restraints / parameters	7140/0/406
Goodness-of-fit on F^2	1.042
Final *R* indices [I>2σ(I)]	R1 = 0.0726, wR2 = 0.2040
R indices (all data)	R1 = 0.0876 wR2 = 0.2181
Largest diff. peak / hole (e $Å^{-3}$)	0.531/ -0.420

Table 5.2. Selected bond lengths (Å) and bond angles (°) for chemosensor **H_3L5**.

Chemosensor H_3L5			
N3-C10	1.494(3)	C8-C10-C11	110.55(17)
N3-N4	1.376(2)	C11-C10-C20	112.47(17)
N3-C26	1.372(3)	N3-C10-C8	110.83(17)
C8-C10	1.515(3)	N3-C10-C11	109.50(16)
C11-C10	1.516(3)	N3-C10-C20	99.40(16)
C20-C10	1.518(3)	C26-N3-C10	115.33(17)
C26-O2	1.214(3)	C26-N3-N4	129.50(18)
		C27-N4-N3	121.37(19)
		O2-C26-N3	126.4(2)

5.3.3. Description of NMR studies

The DMSO-d_6 solvent is used to record all ^{1}H as well as ^{13}C NMR spectra. Both the phenolic -OH and -HC=N protons in the ^{1}H NMR spectrum of **H_3L5**, appear as sharp singlet at 10.18 and 8.83 ppm, respectively. Aromatic protons next to the spirolactam ring exhibit as doublet at 7.92 and 7.05 ppm and multiplet at 7.59 ppm. Also aromatic protons present in the aldehyde fragment of chemosensor give singlet at 6.78 and 6.69 ppm whereas in the xanthene part, they find as sharp singlet with two fold intensity at 6.32 and 6.20 ppm, respectively. Aliphatic amine (-NH) and aliphatic CH_2 protons are found as doublet and multiplet at 5.01 and 5.08 ppm, respectively. Aromatic -OCH_3 protons appear as singlet at 3.71 ppm. Aliphatic CH_2 protons in the xanthene part appear as multiplet at 3.14 ppm. At 3.23 ppm, the aldehyde part's aliphatic CH_2 protons show up as a doublet. At 1.85 ppm, aromatic CH_3 protons are seen as singlet, while aliphatic CH_3 protons are seen as triplet at 1.21 ppm (**Fig. 5.5**).

Complex **5.1** gives clean and similar type of ^{1}H NMR spectra in the DMSO-d_6 solvent. The phenolic -OH proton disappears in complex **5.1** when the metal coordinates with the chemosensor, while the imine proton's location (singlet, 9.27 ppm) shifts downfield. One aliphatic−NH proton vanishes during complexation, starting with the spirolactum ring opening. Interestingly, the aromatic and aliphatic protons remain same position after complexation (1.85 and 1.21 ppm, respectively) although slight broadening of the peaks is also noticed. (**Fig. 5.6**).

In ^{13}C NMR of **H_3L5**, spirolactam imine carbon gives peak at 164.04 and aromatic carbons at 151.94-104.72 ppm (**Fig. 5.7**). Complex **5.1** exhibits a downfield shift in the carbon positions of the imine, spirolactam amide and phenolic at 168.19, 157.25, and 156.19 ppm, respectively, due to metal coordination. The carbon atom that joins the spirolactam ring and the xanthene portion in the free chemosensor is sp^3 hybridised and manifests at 65.98 ppm. Al^{3+} coordination results in opening of spirolactam ring, therefore, the carbon atom links to the

xanthene part and spirolactam ring has switched from sp^3 to sp^2 hybridization and is visible at 138.41 ppm. Interestingly, the position of -OCH_3 carbon, aliphatic CH_2 and CH_3 carbon atoms remain almost same positions, both in free chemosensor (56.23, 17.43 and 14.62, respectively) and Al^{3+} bound form (appear at 56.24, 17.41 and 14.56 ppm, respectively) (**Fig. 5.8**).

Additionally, we have titrated ^{1}H NMR in DMSO-d_6 solvent. The phenolic-OH proton and the aliphatic ¸NH proton vanish when Al^{3+} (0-1equiv.) is gradually added to the chemosensor (**H_3L5**) solution, indicating that the spirolactam ring has opened and complexation has occurred through phenoxide oxygen, amide oxygen, and imine nitrogen atoms. During this titration procedure, broadening of the aromatic and aliphatic protons is also seen. (**Fig. 5.9**).

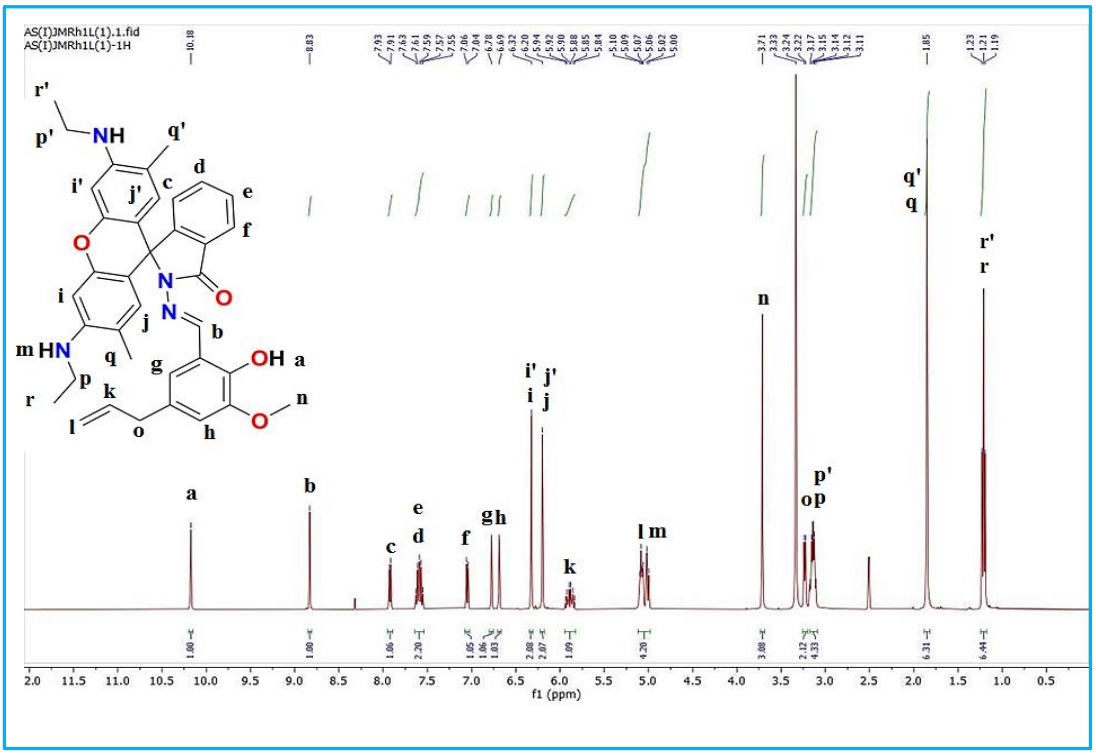

Fig. 5.5. ^{1}H NMR spectrum of **H_3L5** in DMSO-d_6 solvent.

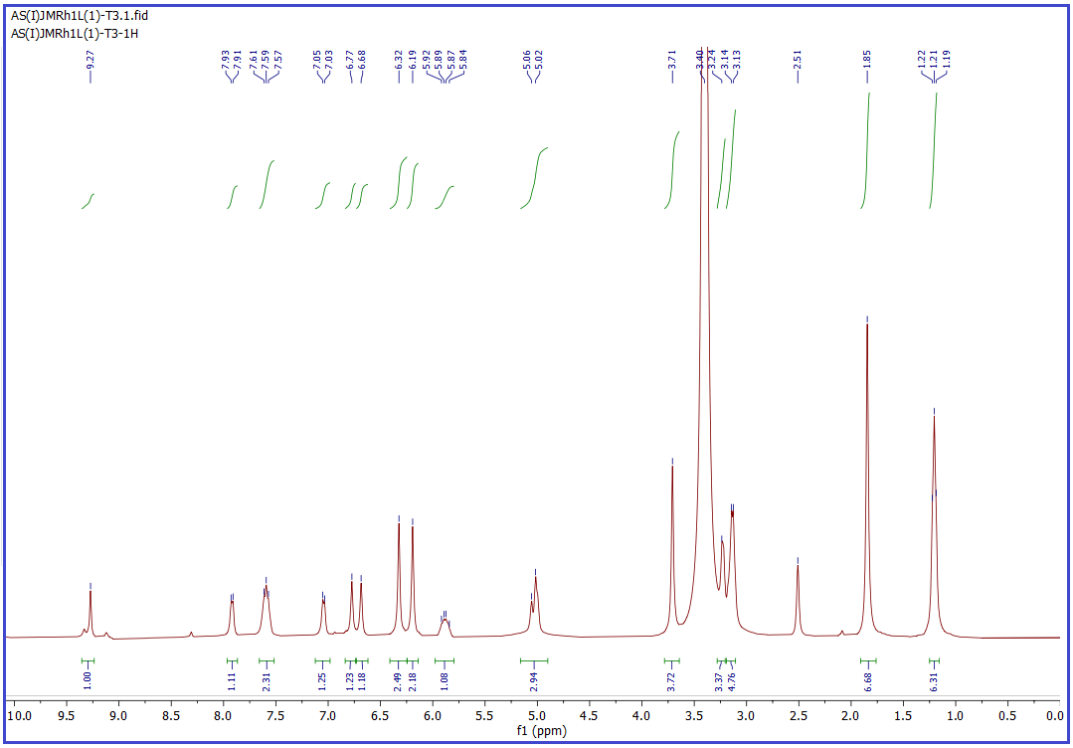

Fig. 5.6. ^{1}H NMR of complex **5.1** in DMSO-d_6 solvent.

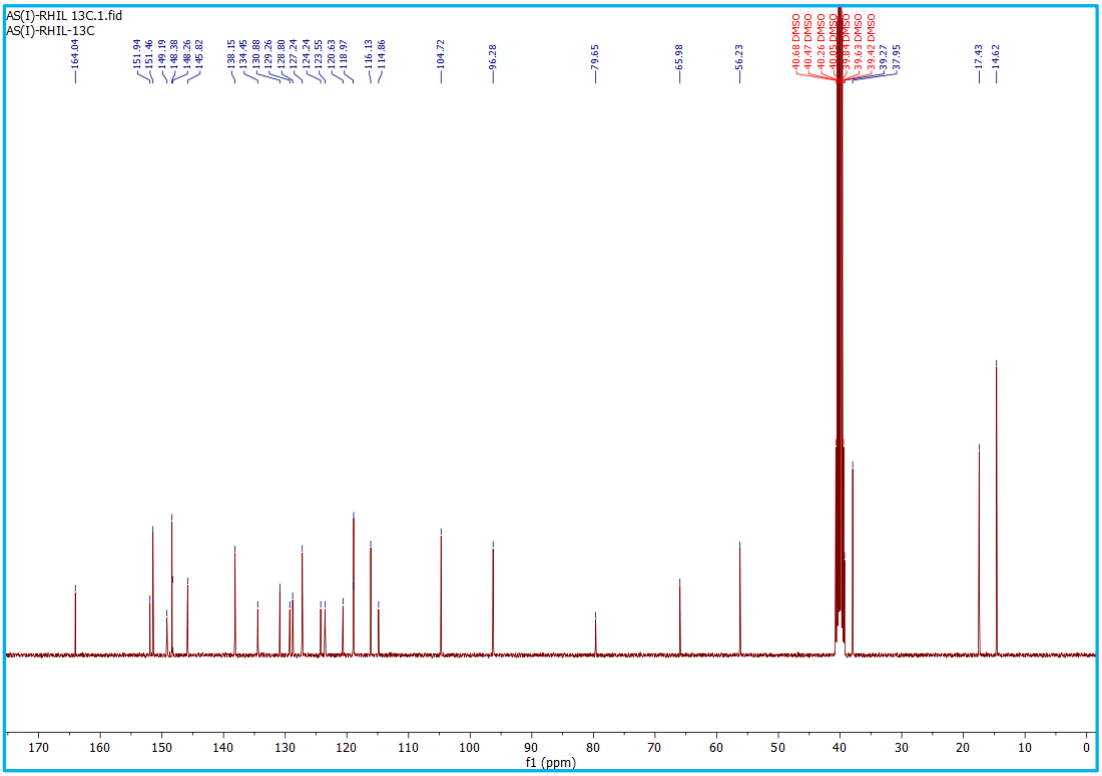

Fig. 5.7. ^{13}C NMR spectrum of chemosensor **H_3L5** in DMSO-d_6 solvent.

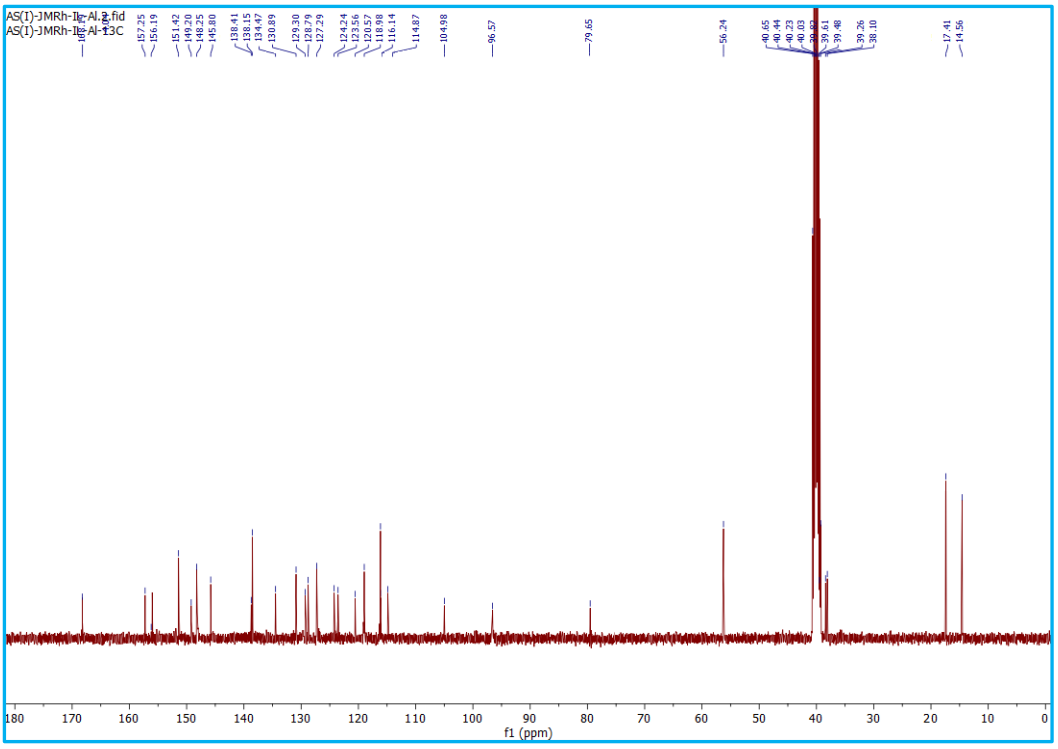

Fig. 5.8. ^{13}C NMR spectrum of complex **5.1** in DMSO-d_6 solvent.

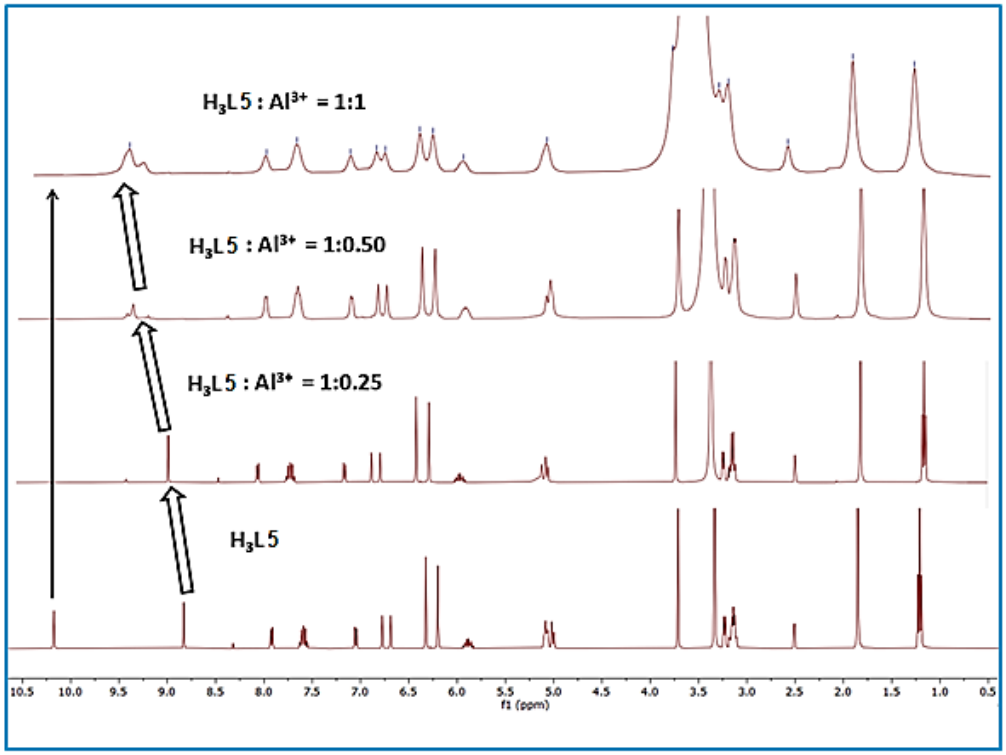

Fig. 5.9. ^{1}H NMR titration of the free ligand (**H_3L5)** and with the addition of 0.25, 0.50 and 1 equivalent of Al^{3+} in DMSO-d_6 solvent.

5.3.4. Absorption and fluorescence properties analysis

Absorption measurement for free chemosensor and with Al^{3+} ion was performed in HEPES buffer at pH 7.4 (MeOH:H_2O, 9:1, (v/v)). Well-defined bands at 306 and 355 nm were obtained from the free chemosensor (**H_3L5**), which were attributed to intramolecular π →π* or n →π* type transitions, respectively. A notable alteration in the chemosensor's spectra is noted when Al^{3+} ions are present. As seen in **Fig. 5.10**, there is a noticeable increase with simultaneous development of absorption peaks at 299, 350, and 530 nm upon the progressive addition of Al^{3+} (0-1.1 equiv.). It implies a robust interaction between Al^{3+} and **H_3L5**. However, other metal ions, such as Zn^{2+}, Cr^{3+}, Fe^{3+}, Cd^{2+}, Hg^{2+}, Pb^{2+}, Ag^{+}, Mn^{2+}, Ni^{2+}, Cu^{2+}, Na^{+}, K^{+}, Ca^{2+}, Mg^{2+} and Co^{2+} ions do not make significant changes to the absorption of probe **H_3L5**. The binding constant of the chemosensor towards Al^{3+} ion has been calculated involving absorbance titration data and the result is $2.01 \times 10^5 M^{-1}$ (**Fig. 5.11**) [5.33].

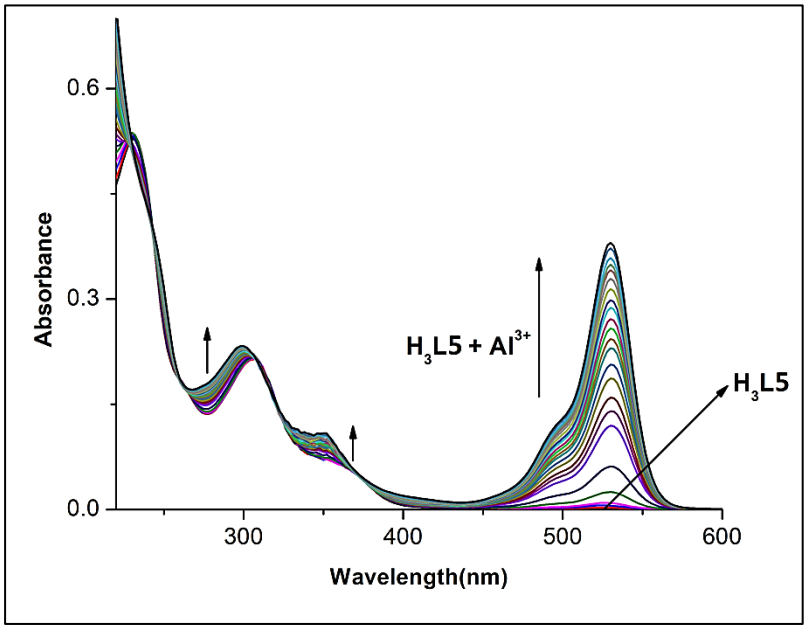

Fig. 5.10. Absorption titration spectra of **H_3L5** (20 µM) upon steady addition of Al^{3+} (0-22 µM) in HEPES buffer (9:1, MeOH:H_2O, v/v, pH 7.4).

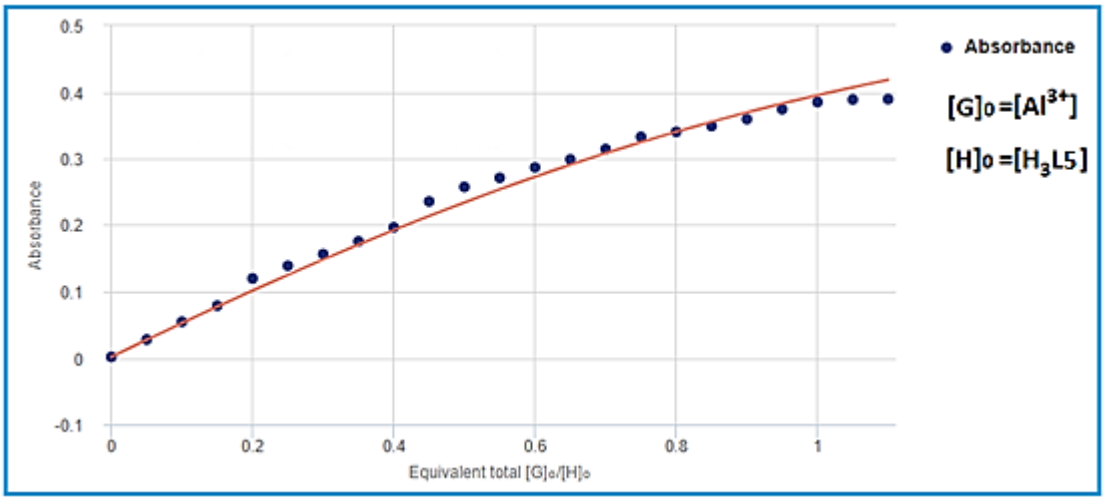

Fig. 5.11. Binding constant calculation for **H_3L5** with Al^{3+} ion in HEPES buffer at pH 7.4 (MeOH:H_2O, 9:1, (v/v)). [http://supramolecular.org]. Binding constant=$2.01 \times 10^5 M^{-1}$.

Free probe **H_3L5** was non-fluorescent. A significant increase in fluorescence at 552 nm is observed when the probe is exposed to trivalent metal ion (Al^{3+}, 0-22 μM, $\lambda_{ex.}$ at 500 nm) (**Fig. 5.12**). The fluorescence grows gradually until it reaches a maximum when approximately 1.1 equivalents of Al^{3+} metal ions are added. Because of the existence of a closed spirolactam ring, the free chemosensor is non-fluorescent. Fluorescence enhancement resulting from the opening of the spirolactam ring is initiated by metal coordination with imine N-atom, phenoxide O-atom, and O-atom of open spirolactam amide (CHEF on). In presence of Al^{3+} the emission enhancement is ~138 fold.

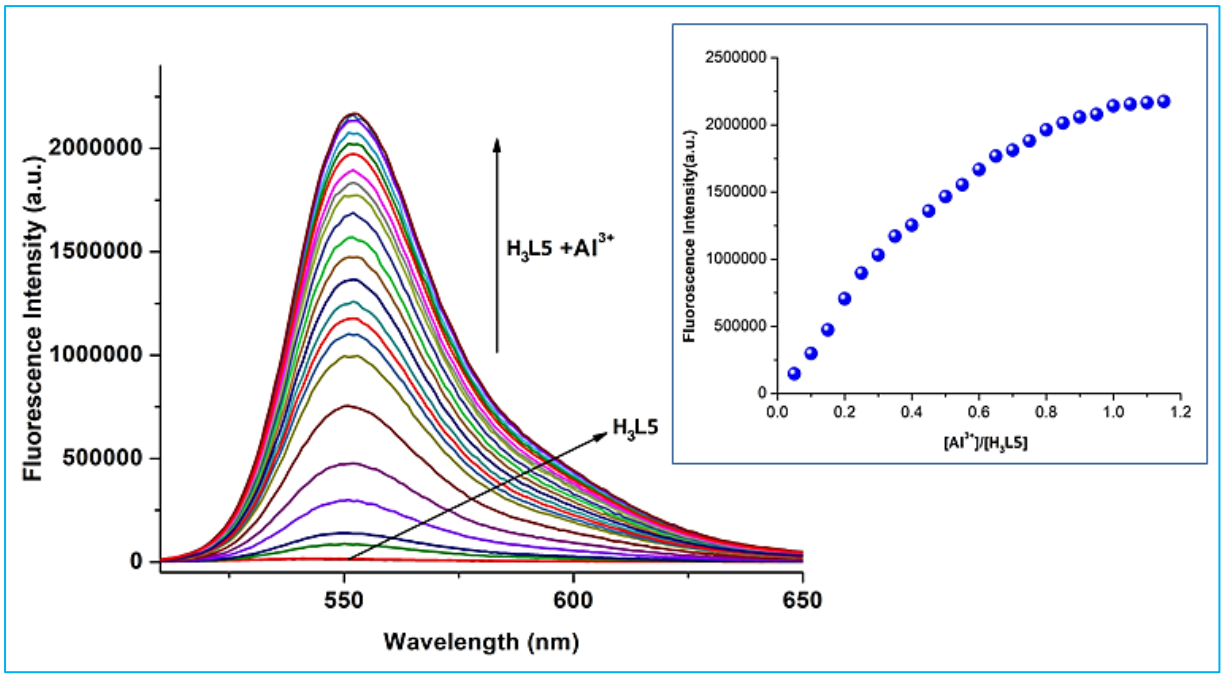

Fig. 5.12. Fluorescence titration spectra of **H_3L5** (20 µM) upon steady addition of Al^{3+} (0-22 µM) in HEPES buffer (9:1, MeOH:H_2O, v/v, pH 7.4) upon λ_{ex}= 500 nm (λ_{em}= 552 nm). Inset: non-linear graph of change in fluorescence intensity vs. [Al^{3+}]/[**H_3L5**].

A notable improvement of the quantum yield value of free **H_3L5** (0.014) to its metal-bound form (0.065 for **H_3L5** + Al^{3+}) was observed which also supports the above point (Table 5.3). Using the formula $\tau_f = a_1\tau_1 + a_2\tau_2$, where a_1 and a_2 are the relative amplitudes of the decay process, the average fluorescence lifetime experiment for the chemosensor (**H_3L5**) and Al^{3+} bound chemosensor was studied at 298 K in HEPES buffer at pH = 7.4 (MeOH:H_2O, 9:1, (v/v)). A significant enhancement of lifetime was observed in Al^{3+} bound chemosensor (1.29 nS, and 0.26 nS for free **H_3L5**) (Fig. 5.13, Table 5.3). Significantly, no discernible fluorescence responses were elicited by the presence of other metal ions. Fluorescence intensity against growing concentration of Al^{3+} in the presence of the probe was plotted which revealed a quick increase in fluorescence upto1 equivalent of Al^{3+} indicating a 1:1 binding between the chemosensor **H_3L5** and Al^{3+}. The 3σ approach is used to compute the limit of detection (LOD) of the probe for the Al^{3+} ion and the value is 2.82×10^{-6} M (Table 5.3).

Table 5.3. Apparent binding constant (K), LOD, lifetime (τ_f) and quantum yield (Φ) values of **H_3L5** and complex **5.1** from spectrofluorometric measurement.

	K (M^{-1})	LOD (M)	τ_f(nS) (average)	χ^2	Φ
H_3L5	-		0.26	0.990360	0.014
Complex **5.1**	2.01×10^5	2.82×10^{-6}	1.29	0.9031072	0.065

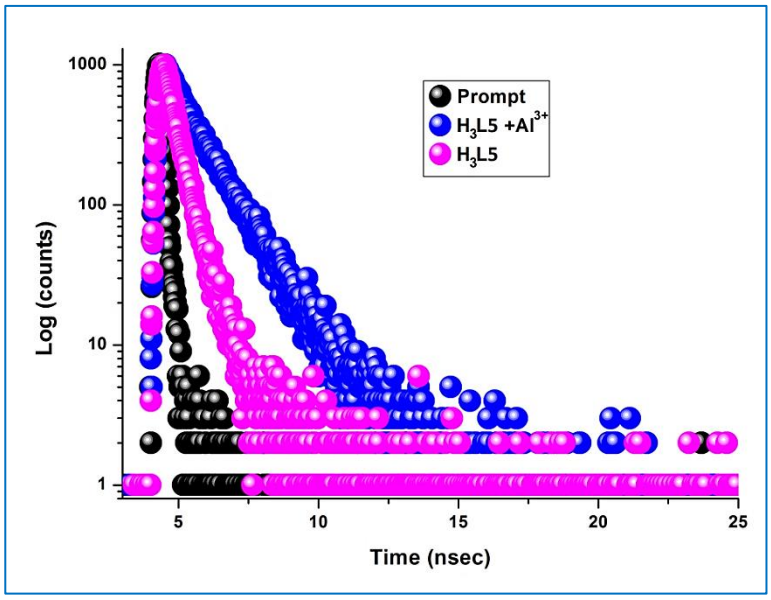

Fig. 5.13. Time-resolved fluorescence decay curves (logarithm of normalized intensity vs time in nS) of **H_3L5** in the absence ( ) and presence ( ) of Al^{3+} ion, ( ) indicates decay curve for the scattered.

Using a competition experiment, the probe's selectivity for the Al^{3+} ion was further investigated. Change in the intensity of the probe was not significant when additional common cations (Zn^{2+}, Fe^{3+}, Cd^{2+}, Hg^{2+}, Pb^{2+}, Ag^{+}, Mn^{2+}, Ni^{2+}, Cu^{2+}, Na^{+}, K^{+}, Ca^{2+}, Mg^{2+}, and Co^{2+} ions) were present (Fig. 5.14). Interestingly, the chemosensor, **H_3L5**, also act as a colorimetric probe with the selective recognition of Al^{3+} ion. The Al^{3+} ion exhibits fluorescent pinkish-yellow coloration in presence of the probe. As a result, the chemosensor will be a wise option for colorimetric Al^{3+} ion detection in biological and environmental applications (Fig. 5.15).

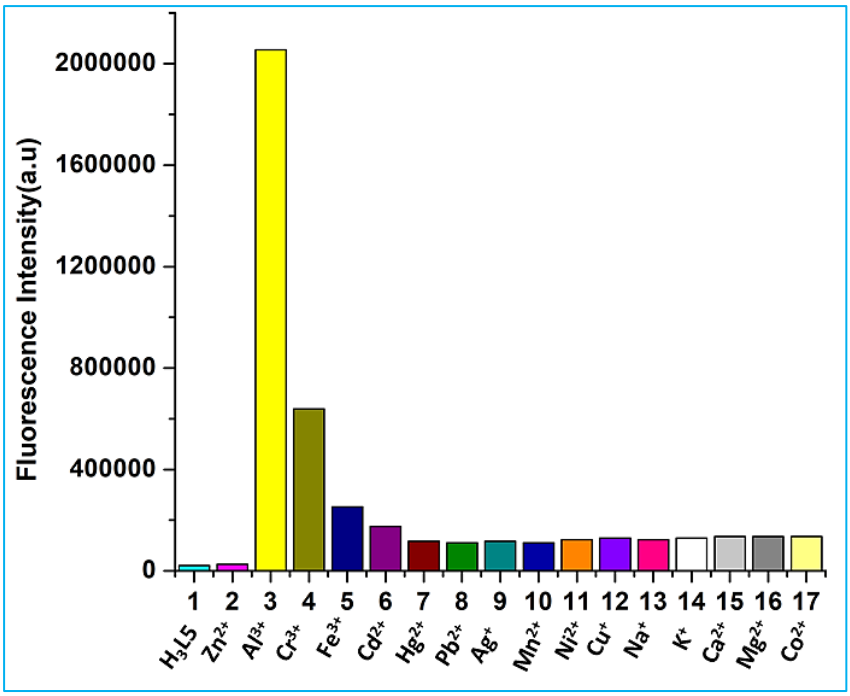

Fig. 5.14. Relative fluorescence intensity diagram of chemosensor (**H_3L5)** (20 µM) with different cations (20 µM) upon λ_{ex}= 500 nm in HEPES buffer (9:1, MeOH:H_2O, v/v, pH 7.4), where 2-Zn^{2+}, 3-Al^{3+}, 4-Cr^{3+}, 5-Fe^{3+}, 6-Cd^{2+}, 7-Hg^{2+}, 8-Pb^{2+}, 9-Ag^{+}, 10-Mn^{2+}, 11-Ni^{2+}, 12-Cu^{2+}, 13-Na^{+}, 14-K^{+}, 15-Ca^{2+}, 16-Mg^{2+} and 17-Co^{2+}, respectively.

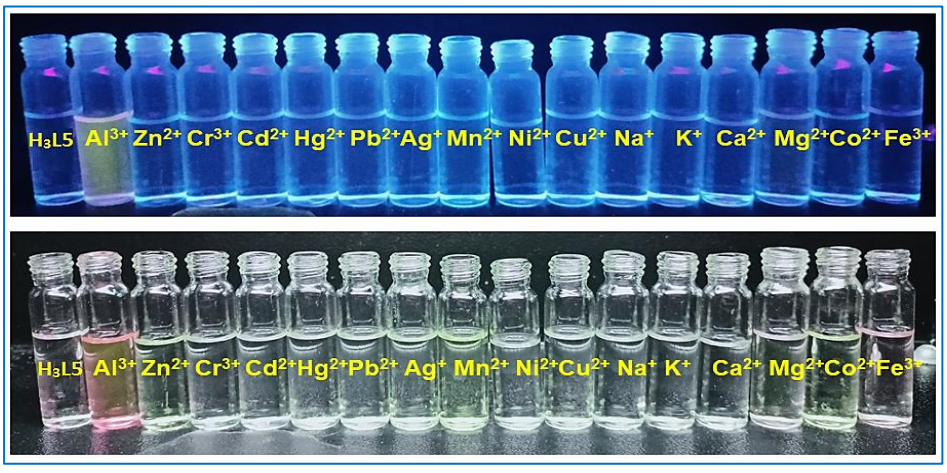

Fig. 5.15. Visual colour changes of chemosensor **H_3L5** (20µM) in presence of common metal ions (1 equivalent) in HEPES buffer (9:1, MeOH:H_2O, v/v, pH 7.4) under visible (below) and UV light (above).

Furthermore, **H_3L5** (1 equivalent) is mixed with an Al^{3+} ion while additional metal ions (5 equivalents) are present. The majority of the cations displayed constant fluorescence intensity (**Fig. 5.16**). This result suggests the selectivity of the chemosensor towards the Al^{3+} metal ion. Effect of various anions and biomolecules like AcO^-, OCN^-, F^-, Br^-, I^-, Cl^-, N_3^-, $S_2O_3^{2-}$, SO_3^{2-}, PF_6^-, $P_2O_7^{2-}$, NO_3^-, BF_4^-, ClO_4^-, $H_2PO_4^-$, HPO_4^{2-}, AsO_2^-, S^{2-}, SCN^-, PO_4^{2-}, L-Histidine, L-Cysteine, and ATP on **H_3L5** had been studied in the same buffer medium. No such significant fluorescence intensity enhancement or quenching was found (**Figs. 5.17** and **5.18**).

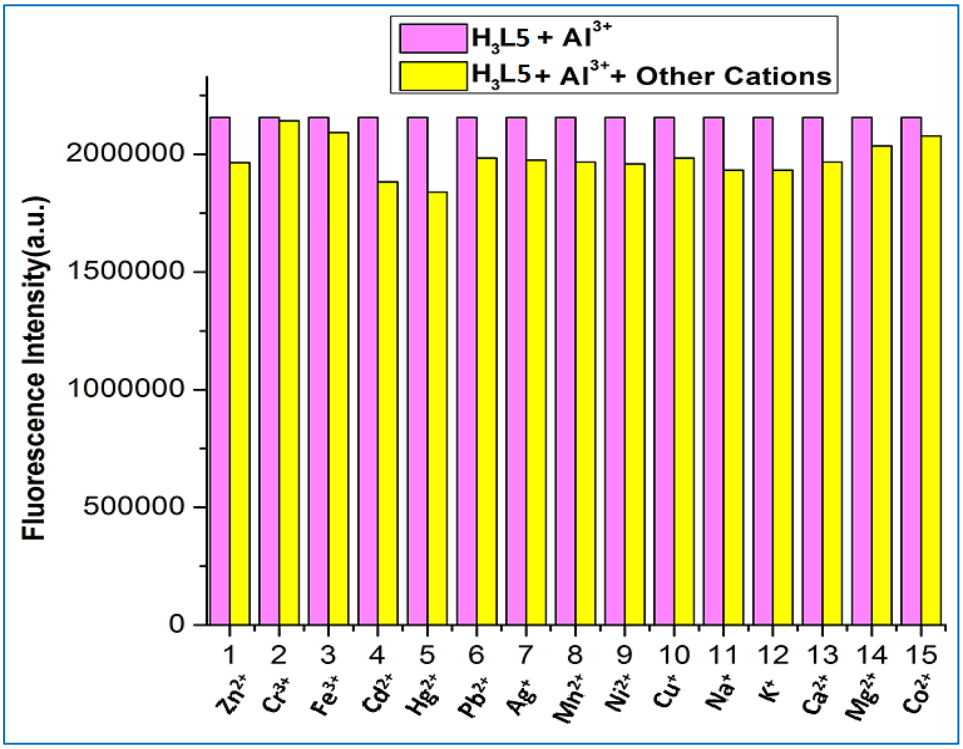

Fig. 5.16. Relative fluorescence intensity diagram of [**H_3L5**–Al^{3+}] with different cations upon λ_{ex}= 500 nm in HEPES buffer at pH 7.4 (MeOH:H_2O, 9:1, (v/v)) where **H_3L5** (20 µM) + Al^{3+} (20 µM) + M^{n+} (different cations) (100 µM), respectively.

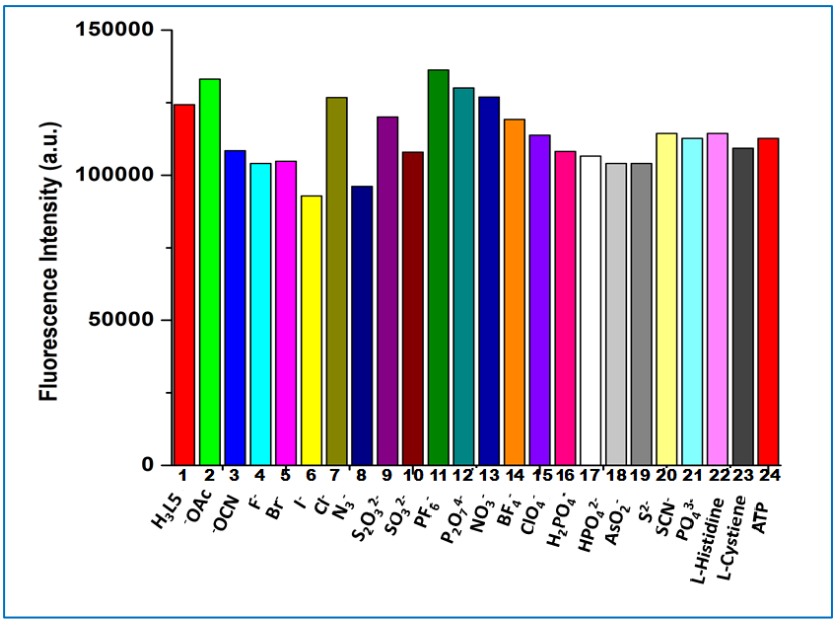

Fig. 5.17. Relative fluorescence intensity diagram of **H_3L5** with of different anions upon λ_{ex}= 500 nm in HEPES buffer at pH 7.4 (MeOH:H_2O, 9:1, (v/v)). 1=only **H_3L5** (20 µM); 2-24= **H_3L5** (20 µM) + M^{n-} (100 µM), where M^{n+}= 2-AcO^-, 3-OCN^-, 4-F^-, 5-Br^-, 6-I^-, 7-Cl^-, 8-N_3^-, 9-$S_2O_3^{2-}$, 10-SO_3^{2-}, 11-PF_6^-, 12-$P_2O_7^{2-}$, 13-NO_3^-, 14-BF_4^-, 15-ClO_4^-, 16-$H_2PO_4^-$, 17-HPO_4^{2-}, 18-AsO_2^-, 19-S^{2-}, 20-SCN^-, 21-PO_4^{3-}, 22-L-Histidine, 23-L-Cystiene and 24-ATP, respectively.

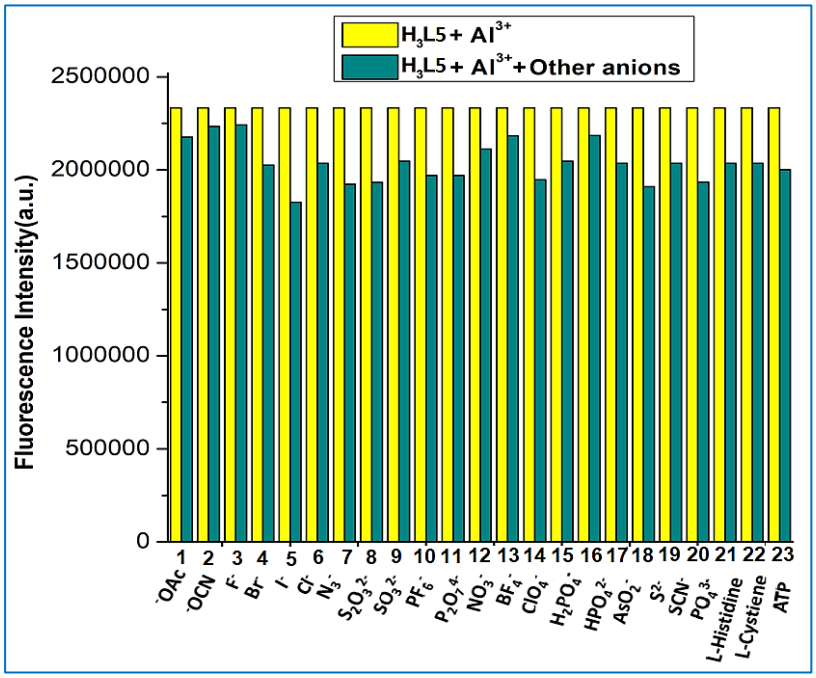

Fig. 5.18. Relative fluorescence intensity diagram of [**H_3L5**–Al^{3+}] with different anions upon λ_{ex}= 500 nm in HEPES buffer at pH 7.4 (MeOH:H_2O, 9:1, (v/v)) where **H_3L5** (20 µM) + Al^{3+} (20 µM) + M^{n-} (differenet anions) (100 µM), respectively.

Two essential components are the regeneration of free probe and the reversibility test to ensure its applicability in real sample analysis. A potent chelating ligand such as, 1 equiv. of Na_2EDTA (sodium salt of ethylenediaminetetraacetic acid) solution was used. First, a pinkish-yellow fluorescence is produced upon adding 1 equiv. of the Al^{3+} ion (**Fig. 5.19**). When Na_2EDTA was combined with **H_3L5** and one equivalent of Al^{3+} ion solution, the initial pinkish yellow fluorescence disappeared and a colourless solution was produced. Such events are caused by the development of a free probe and a metal-bound EDTA complex. Upon further addition of Al^{3+} ion initial pinkish yellow fluorescence returns.

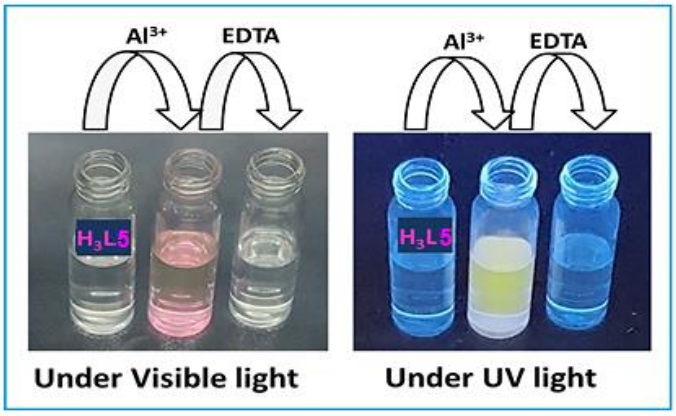

Fig. 5.19. Colour changes of chemosensor (**H_3L5**) (20μM) under UV and Visible light in HEPES buffer at pH 7.4 ($MeOH:H_2O$, 9:1, (v/v)).

We have used a paper strip experiment to support the probe's fluorescence detecting characteristic as part of its on-field usability. In this experiment, a paper strip is charged with Al^{3+} solution after being dipped in a free chemosensor. Under UV light, there was a noticeable colour shift in the strips from colourless to fluorescent blue (**Fig. 5.20**). Importantly, presence of various cations had no effect on the paper strip's colour intensity. The lower detection limit of this paper-based chemosensor **H_3L5** ($\sim 10^{-6}$ M) suggests that this simple process could be effectively used for fast and selective fluorescence detection of Al^{3+} for environmental sample analysis in remote areas where arrangement of analytical instrumentation is difficult.

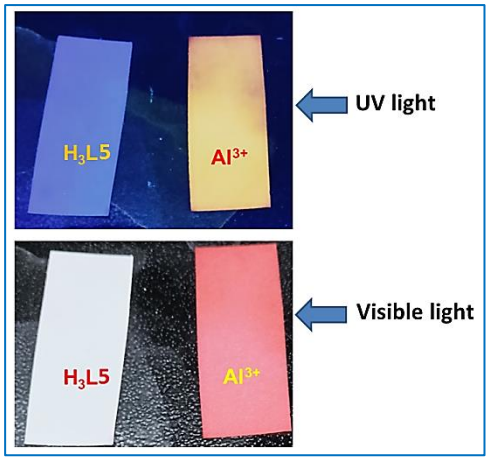

Fig. 5.20. Colour change of paper strips in presence of chemosensor **H_3L5** and **H_3L5** + Al^{3+}, respectively under visible light (below) and UV light (above).

The effect of pH on the chemosensor (**H_3L5**) both in the free condition and in the presence of Al^{3+} ion are studied fluorometrically. It is commonly known that spirolactam ring of the chemosensor opens in an acidic environment. An analogous observation is also noted when the Al^{3+} ion is present. As a result, at pH 2-4, both free chemosensor and chemosensor-Al^{3+} adduct show strong fluorescence. There is a noticeable drop in the fluorescence intensity of free chemosensor at pH 5. Its fluorescence intensity is relatively faint and stays constant between pH 5 to pH 11. This observation suggests reformation of the spirolactam ring in neutral and basic condition. The fluorescence intensity decreases slightly in the presence of Al^{3+} after pH 4 and then stays constant until pH 8.5. The fluorescence intensity of **H_3L5**-Al^{3+} adduct is seen to sharply fall at pH 9. Very mild fluorescence intensity is seen after pH 10 to pH 11. This is most likely caused by a free chemosensor and the production of metal hydroxide at a higher pH (**Fig. 5.21**). The pH experiment shows that the chemosensor can act as a selective fluorescent probe for investigation of Al^{3+} ion in presence of other metal ions in the biological system under physiological conditions.

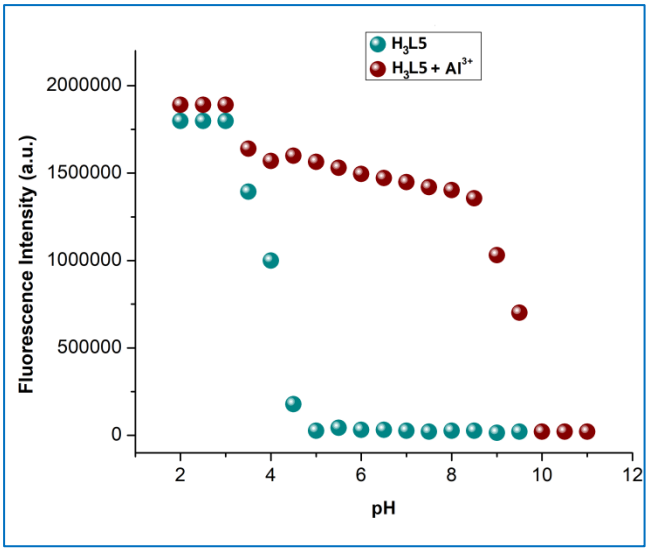

Fig. 5.21. Fluorescence intensity of **H_3L5** (20 µM) in the absence and presence of metal ions Al^{3+} (20µM) at different pH values in 10 mM HEPES buffer.

5.3.5. Mechanism of fluorescence intensity increment of probe (H_3L5) in presence of Al^{3+} ion

The free chemosensor is non-fluorescent due to presence of spirolactam ring. When Al^{3+} ion is present, the spirolactam ring of chemosensor opens due to coordination of metal ion with subsequent enhancement of fluorescence intensity by ~138 times. The mechanistic process is explained via ^{1}H, ^{13}C NMR and FT-IR spectroscopy, as well as X-ray crystallographic method. In ^{1}H NMR spectra of free chemosensor phenolic –OH peak, imine and aliphatic-NH protons appear around 10.18, 8.83 and 5.07 ppm. Presence of Al^{3+} ion causes opening of spirolactam ring followed by coordination of imine nitrogen, phenoxide oxygen and O-atom of open spirolactam amide with the metal centre. As a result phenolic -OH and aliphatic -NH protons vanish, imine and aromatic protons relocate downfield. In ^{13}C NMR spectra of free chemosensor (**H_3L5**) we have noticed sp^3 hybridized carbon atom connecting xanthene portion and spirolactam ring at 79.65 ppm. Remarkably, sp^3 hybridization changes into sp^2 hybridization when spirolactam ring opens upon metal coordination (**Figs. 5.7** and **5.8**) and a new peak emerges at 138.41 ppm. In the

FT-IR spectrum, free chemosensor displays stretching frequencies of the amide 'C=O' bond and imine (-HC=N) bond at~1688 and ~1621 cm^{-1}, respectively. For the metal-bound complex (Complex **5.1**), these values are substantially displaced to the lower value and appeared at ~1605 and ~1530 cm^{-1}, respectively. Such alterations in the FT-IR spectral pattern validate spirolactam ring opening and the coordination of the metal centre with the oxygen atoms of the amide, phenoxide and imine nitrogen. As a result, we can simply demonstrate coordination of the metal centre (Al^{3+}) with the chemosensor using the spectroscopic data above. Metal coordination also initiates increase of π electron delocalization inside the ligand framework, which causes significant colorimetric changes and enormous fluorescence enhancement.

5.3.6. Cell viability analysis

From the results of the MTT assay, it is evident that the cells show the highest viability in the presence of a 20 µM concentration of **H_3L5** followed by 40 µM. At concentrations of 60 µM and 80 µM, the viability of the cells plummet marginally, but are similar in value and the lowest viability is observed in the case of 100 µM (**Fig. 5.22**). It is suspected that the reduction observed in the cell viability at higher concentrations is observed due to cytotoxic effect of the higher concentration of methanol which is being used as the solvent for the ligand [5.37,5.38]. Hence, it is suggested that the methanol solution of **H_3L5** is diluted by using water to stave off the cytotoxic effect of the former for using the ligand for biological purposes.

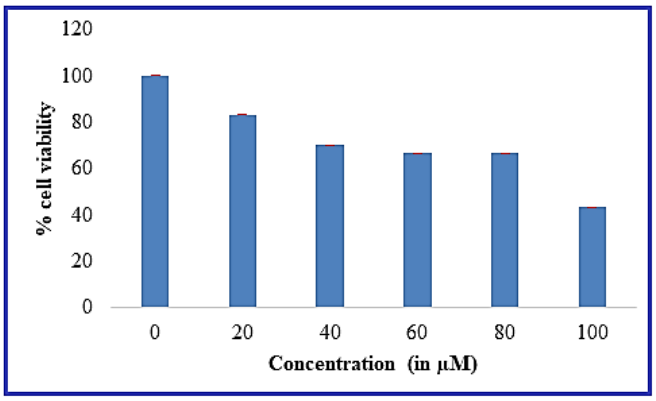

Fig. 5.22. Viability of ***MC3T3*** cells on exposure to the **H_3L5.**

5.3.7 Cell imaging

A fluorescence microscopic analysis conducted to determine the cellular uptake of the **H_3L5** and Al^{3+} ions at the mentioned concentrations, provides evidence that the cells readily internalize both in every case. A green fluorescent emission in the presence of Al^{3+} ion was generated by the cells administered with **H_3L5**, and was observed at 552 nm wavelength. The cells treated with the highest concentration of **H_3L5** (100 µM) show the most prominent fluorescence. In contrast, there is a reduction in the emission with the corresponding reduction in the concentration of the **H_3L5** administered to the cells (Fig. 5.23).

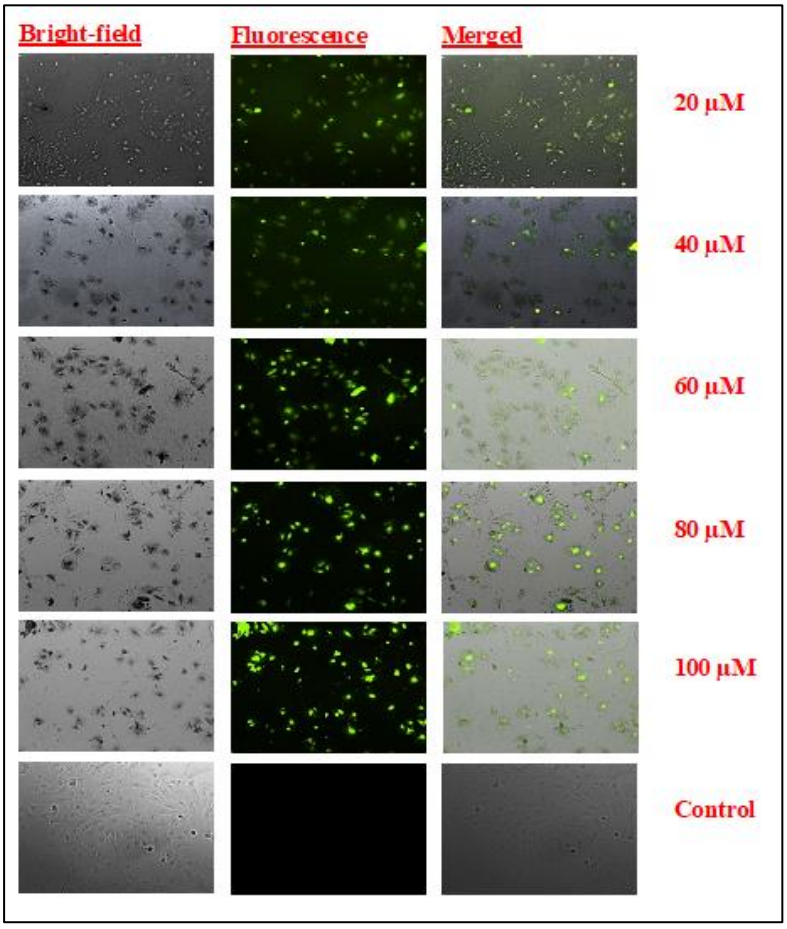

Fig. 5.23. Bright field, fluorescence, and merged microscopic images of treated ***MC3T3*** cells with **H_3L5** (20 µM, 40 µM, 60 µM, 80 µM and 100 µM), & untreated ***MC3T3*** cells (control)**.**

5.3.8 Detecting intracellular Al^{3+} ions

The fluorescent microscopy analysis showed that the presence of Al^{3+} ions was possible by utilizing **H_3L5** as a fluorescent probe. The cells treated with the highest concentration (100 µM) had successfully been able to detect Al^{3+} ions in the L929 cells with reductions observed in the fluorescence intensity as the corresponding concentrations of the fluorescent probe were also decreased as mentioned in Fig. 5.24. The fluorescence intensity was measured using LAS X Office software.

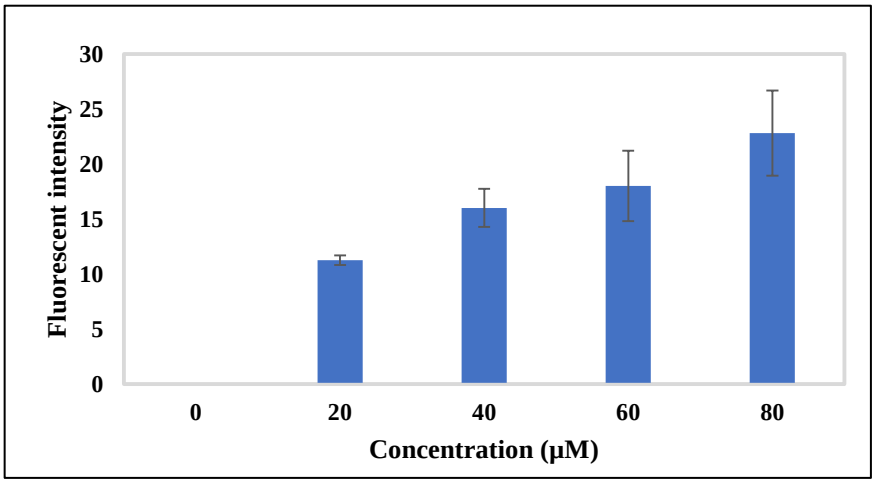

Fig. 5.24. Fluorescent intensity vs Concentration graph for cells treated with **H_3L5**.

5.4. Conclusion

Synthesis of chemosensors from natural products which have enormous use in our daily life especially in health care is a challenging task. Eugenol, popularly known as clove oil is one such compound with several health benefits. This work involves the development of a new fluorescent and colorimetric chemosensor (**H_3L5)** containing rhodamine 6G and eugenol-5-aldehyde units (5-allyl-2-hydroxy-3-methoxybenzaldehyde) which selectively detects trivalent metal ion Al^{3+} by colorimetric as well as fluorometric processes. The crystal structure of the chemosensor shows a closed spirolactam ring, which makes it non-fluorescent. **H_3L5** shows notable fluorescence increment towards Al^{3+} (~138-fold) ion in HEPES buffer at pH = 7.4

(MeOH:H_2O, 9:1, (v/v)). The main cause of the strong emission at 552 nm (λ_{ex}= 500 nm) is opening of spirolactam ring in presence of Al^{3+} ion followed by chelation-enhanced fluorescence (CHEF). Reversibility and regeneration of the chemosensor with chelating ligand Na_2EDTA are also investigated. **H_3L5** shows a low limit of detection (LOD) (2.82×10^{-6} M) and strong association constant (2.01×10^5 M^{-1}) towards the Al^{3+} ion, suggesting its potential utility in bio-imaging research. **H_3L5** was effectively utilized in the paper strip to identify the Al^{3+} ion. It is further used in biological samples (***MC3T3*** cell) for detection of Al^{3+} ion.

5.5. References

[5.1] J. P. Desvergne, A. W. Czarnik, Kluwer Academic Press, Netherlands (1997).

[5.2] A. P. de Silva, H. Q. N. Gunaratne, T. Gunnlaugsson,A. J. M. Huxley, C. P. McCoy, J. T. Rademacher, T. E. Rice, Chem. Rev. 97 (1997) 1515–1566.

[5.3] R. McRae, P. Bagchi, S. Sumalekshmy, C. J. Fahrni, Chem. Rev. 109 (2009) 4780–4827.

[5.4] S. B. Maity, S. Banerjee, K. Sunwoo, J. S. Kim, P. K. Bharadwaj, Inorg. Chem. 54 (2015) 3929–3936.

[5.5] J. Barcelo, C. Poschenrieder, Environ. Exp. Bot. 48 (2002) 75–92.

[5.6] Z. Krejpcio, R. W. P. Wojciak, Pol. J. Environ. Stud. 11 (2002) 251–254.

[5.7] P. Nayak, Environ. Res. 89 (2002) 101–115.

[5.8] N. Fimreite, O. O. Hansen, H. C. Pettersen, Bull. Environ. Contam. Toxicol. 58 (1997) 1–7.

[5.9] A. Salifoglou, Coord. Chem. Rev. 228 (2002) 297–317.

[5.10] M. E. Percy, T. P. A. Kruck, A. I. Pogue, W. J. Lukiw, J. Inorg. Biochem. 105 (2011) 1505–1512.

[5.11] G. D. Fasman, Coord. Chem. Rev. 149 (1996) 125–165.

[5.12] D. Krewski, R. A. Yokel, E. Nieboer, D. Borchelt, J. Cohen, J. Harry, S. Kacew, J. Lindsay, A. M. Mahfouz, V. Rondeau, J. Toxicol. Environ. Health, Part B 10 (2007) 1–269.

[5.13] E. Delhaize, P. Ryan, Plant Physiol. 107 (1995) 315–321.

[5.14] X. Li, J. Chen, E. Wang, Chin. J. Chem. 32 (2014) 429–433.

[5.15] S. Das, S. Goswami, K. Aich, K. Ghoshal, C. K. Quah, M. Bhattacharyya, H. K. Fun, New J. Chem. 39 (2015) 8582–8587.

[5.16] H. Sang, P. Liang, D. Du, J. Hazard. Mater. 154 (2008) 1127–1132.

[5.17] S. J. Djane, M. Gra, C. Korn, Spectrochim. Acta, Part B 55 (2000) 389–394.

[5.18] S. Abbasi, A. Farmany, Food Chem. 116 (2009) 1019–1023.

[5.19] V. K. Gupta, A. K. Jain, G. Maheshwari, Talanta 72 (2007) 1469–1473.

[5.20] (a) M. Khatun, P. Ghorai, J. Mandal, S. G. Chowdhury, P. Karmakar, A. Saha, J. Photochem. Photobiol., A: Chemistry 446 (2024) 115145; (b) M. Khatun, J. Mandal, V. W. Tamang, S. G. Chowdhury, P. Karmakar, A. Saha, J. Photochem. Photobiol., A: Chemistry 447 (2024) 115231: (c) M. Khatun, P. Ghorai, J. Mandal, S. G. Chowdhury, P. Karmakar, S. Blasco, E. García-España, A. Saha, ACS Omega 8 (2023) 7479−7491.

[5.21] P. Prakash, N. Gupta, Indian J. Physiol. Pharmacol. 49 (2005) 125–131.

[5.22] M. R. C. Raja, V. Srinivasan, S. Selvaraj, S. K. Mahapatra, Pharm. Anal. Acta, 2015, 6, 5, DOI: 10.4172/2153- 2435.1000367.

[5.23] (a) D. Das, R. Alam, Mahammad Ali, Analyst 147 (2022) 471; (b) J. Mandal, K. Pal, S. G. Chowdhury, P. Karmakar, A. Panja, S. Banerjee and A. Saha, Dalton Trans. 51 (2022) 15555; (c) A. Hazra, P. Roy, Anal. Chim. Acta 1193 (2022) 339378; (d) S. Gond, P. Yadav, A. Singh, S. Garai, A. Shekher, S. C. Guptab, V. P. Singh, Org. Biomol. Chem. 21 (2023) 4482; (e) S. Negi, P. Gahlyan, R. Bawa, B. Singh, M. Bhandari, R. Kakkar, B. Pani, R. Kumar, Anal. Methods 15 (2023) 4000; (f) S. S. Samanta, U. Mandal, B. Das, S. Mandal, P. Upadhyay, T. D. Singh and A. Misra, J. Photochem. Photobiol. A: Chemistry 442 (2023) 114806; (g) M. Prajapati, N. Pandey, S. Kalla, S. Bandaru and A. Sivaiah, Sens. Diagn. 3 (2024) 412; (h) S.

Ghosh, S. Mahato, T. Dutta, Z. Ahamed, P. Ghosh, P. Roy, Spectrochim. Acta Part A: Mol. Biomol. Spectrosc. 305 (2024) 123455; (i) K. Zhang, X. Tian, P. Xu, Y. Zhu, S. Guang, H. Xu, Spectrochim. Acta Part A: Mol. Biomol. Spectrosc. 318 (2024) 124484; (j) Y. Liu, M. Zhou, S. Wang, J. Feng, T. Chai, M. Zhang, X. Feng, L. Huang, C. Lu, G. Jin, J. Mol. Struct. 1312 (2024) 138552; (k) D. Das, R. Alam, M. Sasmal, A. Katarkar, A. Dutta, M. Ali, Inorg. Chim. Acta 563 (2024) 121902.

[5.24] H. Zheng, X. Q. Zhan, Q. N. Bian, X. J. Zhang, Chem. Commun. 49 (2013) 429–447.

[5.25] (a) H. N. Kim, M. H. Lee, H. J. Kim, J. S. Kim, J. Yoon, Chem. Soc. Rev. 37 (2008) 1465–1472; (b) X. Q. Chen, T. Pradhan, F. Wang, J. S. Kim and J. Yoon, Chem. Rev. 112 (2012) 1910–1956; (c) L. L. Huang, Y. X. Qiu, C. Y. Wu, Z. Y. Ma, Z. H. Shen, X. R. Jia, J. Mater. Chem. C 6 (2018) 10250–10255; (d) Z. Y. Ma, Y. J. Ji, Y. S. Lan, G. C. Kuang, X. R. Jia, J. Mater. Chem. C 6 (2018) 2270–2274; (e) L. N. Tan, S. Z. Mo, B. Fang, W. Y. Cheng, M. Z. Yin, J. Mater. Chem. C 6 (2018) 10270–10275.

[5.26] J. Mandal, P. Ghorai, K. Pal, T. Bhaumik, P. Karmakar, A. Saha, ACS Omega 5 (2020) 145−157.

[5.27] H. N. Kim, W. X. Ren, J. S. Kim, J. Yoon, Chem. Soc. Rev. 41 (2012) 3210–3244.

[5.28] X. Tang, Z. Zhu, Y. Wang, J. Han, L. Ni, L. Wang, H. Q. Zhang, J. Li, Y. Qiu, Sens. Actuators B 270 (2018) 35–44.

[5.29] Y. C. Chen, Y. Bai, Z. Han, W. J. He, Z. J. Guo, Chem. Soc. Rev. 44 (2015) 4517–4546.

[5.30] G. Singh, P. Raj, H. Singh, N. Singh, J. Mater. Chem. C 6 (2018) 12728–12738.

[5.31] A. Raman, G. Augustine, N. Ayyadurai, S. Easwaramoorthi, J. Mater. Chem. C 6 (2018) 10497–10501.

[5.32] X. Xie, M. Pan, L. Hong, K. Liu, J. Yang, S. Wang, S. Wang, J. Agric. Food Chem. 69 (2021) 7209-7217.

[5.33] D. B. Hibbert, P. Thordarson, Chem. Commun. 52 (2016) 12792–12805.

[5.34] G. M. Sheldrick, SAINT, Version 6.02, SADABS, Version 2.03, Bruker AXS Inc., Madison, Wisconsin (2002).

[5.35] G. M. Sheldrick, SADABS, University of Gottingen, Institute fur Anorganische Chemieder Universitat, Gottingen, Germany (1999-2003).

[5.36] G. M. Sheldrick, SHELXL. Acta Cryst. C71 (2015) 3–8.

[5.37] M. H. Wang, S. H. Jeong, H. Guo, J. B. Park, J. Oral Sci. 58 (2016) 125–131.

[5.38] A. KOC, A. Z. Karabay , T. Ozkan, Z. Buyukbingol, F. Aktan, J. Res. Pharm. 26 (2022) 494–501.

Chapter 6

An euganol-sulfonyl based fluorescent probe for recognition of Al^{3+} in biological sample

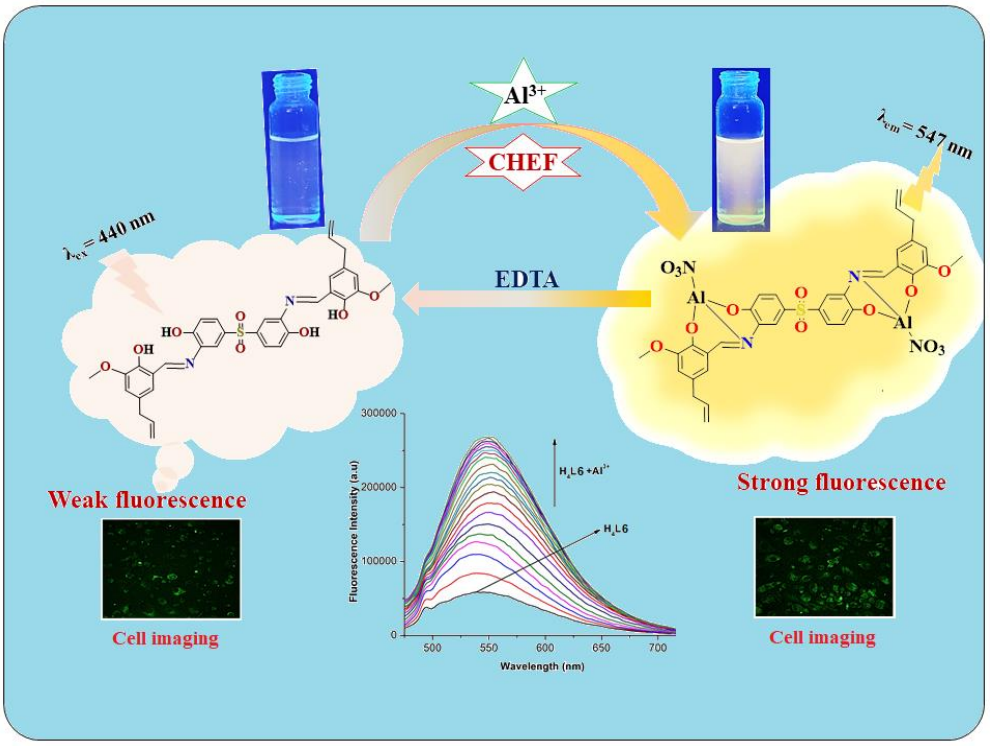

Abstract

The present work describes a eugenol-sulfonyl based fluorescence chemosensor, **H_4L6** [H4L=6,6'-((1E,1'E)-((sulfonylbis(6-hydroxy-3,1-phenylene))bis(azanylylidene))bis(methanylylidene))bis(4-allyl-2-methoxyphenol)], which shows maximum emission intensity towards Al^{3+} ion in presence of other competing metal ions. Upon excitation at 440 nm **H_4L6** exhibits a significant rise in fluorescence at 547 nm upon gradual addition of Al^{3+} ion in the HEPES buffer at pH = 7.4 (MeOH:H_2O, 4:1, (v/v)). The increasing value of fluorescence is mainly due to chelation enhanced fluorescence effect (CHEF). Complete characterization of the probe (**H_4L6**) and metal bound complex (**6.1**) have been determined using a range of methods, including UV-Vis absorption titration, fluorescence titration, NMR, ESI-mass, etc. Thus 1:2 binding stoichiometry between **H_4L6** and metal ion has been also proven. Another important aspect: regeneration and reversibility of **H_4L6** are investigated in presence of Na_2EDTA. **H_4L6** exhibits a detection limit (~10^{-6} M) and a significant binding constant (~10^6 M^{-1}) for the Al^{3+} ion, suggesting its potential use in bio-imaging studies. The probe was effectively used by the paper strip to locate the Al^{3+} ion.

6.1. Introduction

Metals are indispensible in human life. Some are present in the active site of different metallo-enzymes and play crucial roles like oxygen storage and transport (Fe), electron transport and red-ox reactions (Cu, Fe), hydrolysis of CO_2 (Zn) etc. Whereas, metal like aluminium which does not show any enzymatic activity, associated with our daily life in different ways. Aluminum (Al) is the third most common element found on the earth's crust after oxygen, silicon and the most abundant metal. Al has various uses in industries, aviation, construction, packaging, and cosmetics [6.1–6.3]. Thus continuous exposure of different Al containing materials increases conjunction of this metal within our body. WHO (The World Health Organization) recommended average dietary intake of Al^{3+} is within the range 3–10 mg in a day and its concentration in drinking water is upto 7.41 mmol L^{-1} [6.4]. In nature and living organisms Aluminium is usually present in its most common oxidation state, +3. Its (Al^{3+}) strong affinity to oxygen-carrying functional groups initiates entrance of Al^{3+} in the biosystems and influencing homeostasis of the host resulting Alzheimer's disease and tissue, organ failure [6.5–6.7]. Excessive accumulation of toxic metal like Al causes serious effects on the brain, liver, and reproductive system. Its toxic effect also responsible to damage fish and invertebrates present in aquatic ecosystems. In plants adverse effect of Al reduces crop yield by inhibiting root elongation and nutrient imbalance [6.8]. Inductively coupled plasma mass spectrometry (ICP-MS), surface-enhanced Raman scattering (SERS), and atomic absorption spectroscopy (AAS) are important methods which offer good accuracy for Al detection but high-cost and complicated operational techniques made these processes difficult to use [6.9, 6.10]. On the other hand fluorometric analysis becomes popular alternative of these traditional instrumental analytical methods due to their simplicity, sensitivity, selectivity, real-time nondestructive detection, and user friendly operational technique. Although, synthesis of chemosensor for selective

fluorometric detection of Al^{3+} is a difficult task since Al^{3+} undergoes hydrolysis easily, it has weak coordination ability and importantly due to similar electronic structures interference from trivalent ions, Fe^{3+} and Cr^{3+} occurs frequently during detection process [6.11]. Till now synthesis of chemosensor for detection of Al^{3+} in drinking water and biological samples is a challenging task since most of the physiological processes occur in aqueous medium at neutral pH. Some well-known fluorophoric units found in Al^{3+} based chemosensors are anthracene, BODIPY, fluorescein, rhodamine, resorufin, coumarin and cyanine based organic compounds [6.12, 6.13]. Although, searching of chemosensor which is easy to synthesize, detect Al^{3+} selectively with low LOD value (limit of detection) in biological samples is a continuous process. In this regard it is important to mention that chemosensors which accommodate more than one metal ion (here Al^{3+}) in their ligand framework, expected to have increase selectivity power.

In this work we have reported one eugenol-sulfonyl based chemosensor (**H_4L6**) which simultaneously binds two Al^{3+} ions. Sulfonyl-containg compounds have widespread applications in the field of pharmacology and material sciences [6.14, 6.15]. For instance, bicalutamide is used in the treatment of prostate cancer, [6.16] dapsone is used as antibiotic and present in the WHO Model List of essential medicines [6.17]. Polysulfones are high performance thermoplastics which display unique chemical and physical properties [6.18]. Eugenol, clove oil is used from ancient times mainly in pharmaceutical industries. It is a valuable therapeutic agent due to its several pharmacological characteristics, which include its anti-inflammatory, antioxidant, antibacterial, and anti-carcinogenic activities as well as its anaesthetic activity. It is a member of the Phenylpropanoids family. It was taken out of Eugenia caryophyllata, sometimes known as clove, leaves and buds. Eugenol has been classified as a GRAS (generally recognised as safe) chemical by the World Health Organisation [6.19, 6.20]. Importantly, sensing study and

coordination chemistry on eugenol platform is still unexplored. A literature survey of Al^{3+} sensors were done in **Chart 6.1** **[6.21a-u]**.

Here, we studied changes in emission intensity of the chemosensor **H_4L6** in presence of Al^{3+} ion among other competing metal ions. In the HEPES buffer at pH = 7.4 (MeOH:H_2O, 4:1, (v/v)), a sequential addition of Al^{3+} ion in **H_4L6** shows a notable increment in fluorescence at 547 nm upon λ_{ex} at 440 nm. The CHEF effect, or enhanced fluorescence brought on by chelation is the primary cause of this observation. Furthermore, the probe and metal bound complex (**6.1**) has been characterized through the use of several techniques such as fluorescence titration, NMR, ESI-mass, UV-Vis absorption titration, and others. The 1:2 binding stoichiometry between **H_4L6** and metal ions has been demonstrated by several spectroscopic data analysis. Also the regeneration and reversibility of the chemosensor in the presence of Na_2EDTA are examined. Again, **H_4L6** was useful in bio-imaging research due to its strong binding constant (~10^6 M^{-1}) and a detection limit (~10^{-6} M) for the Al^{3+} ion. The paper strip successfully located the Al^{3+} ion using the probe.

Chart 6.1. Literature survey of Al^{3+} sensors.

Sl. No.	Probe	Sensing mechanism	Detecting elements	Solvent used	Excitation/ Emission (nm)	Limit of detection (LOD) (M)	Binding constant (M^{-1})	Biological study	Refs.
1.	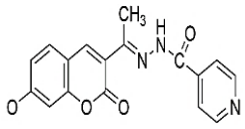	CHEF	Al^{3+}	Methanol (10 μM)	365/482	0.049×10^{-6}	3.680×10^{4}	None	6.21a
2.	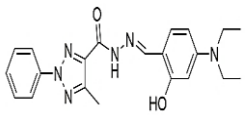	Fluorescent turn on	Al^{3+}	EtOH	390/475	5.84×10^{-9}	----	Cell imaging	6.21b

3.	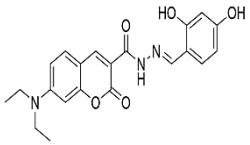	CHEF	Al^{3+}	DMSO: H_2O (7:3, v/v)	435/525	50×10^{-9}	2.14×10^{4}	None	6.21c
4.	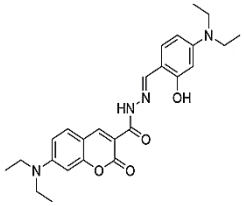	CHEF	Al^{3+}	DMSO-HEPES solution (4:1, v/v, pH = 7.4)	480/625	0.12×10^{-6}	---	Cell imaging	6.21d
5.	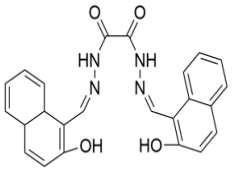	C=N isomerization and CHEF	Al^{3+}	DMSO-H_2O solution (1:1 v/v, HEPES = 50 mM, at pH = 7.4)	375/489	0.176×10^{-5}	6.6×10^{-2}	Cell imaging	6.21e
6.	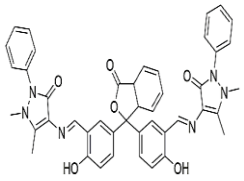	PET-off and C = N isomerisation	Al^{3+}	H_2O/CH_3CN (20/80, v/v)	365/468	51.5×10^{-9}	1.58×10^{7} M^{-2}	None	6.21f
7.	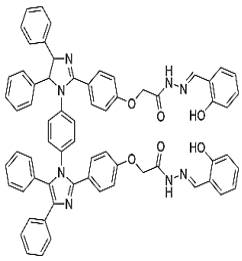	Fluorescent turn-on	Al^{3+}	DMF-H_2O	340/434	1.56×10^{-8}	8.6×10^{7}	None	6.21g
8.	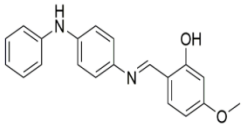	ESIPT	Al^{3+}	MeOH/ HEPES (6/4, v/v, pH = 7.4)	365/565	12.6×10^{-6}	9.08×10^{2}	None	6.21h

9.	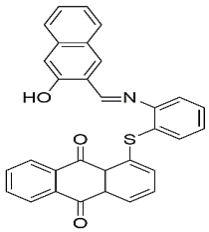	CHEF	Al^{3+}, pyrophosphate (PPi)	MeOH/ urotropine buffer medium (1:1, v/v, pH 4.5)	416/459	31.6×10^{-9} 56.8×10^{-9}	8.87×10^{4} M^{-2}	Cell imaging	6.21i
10	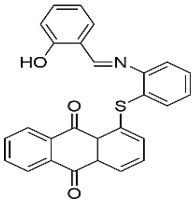	CHEF	Al^{3+}, pyrophosphate (PPi)	Methanol/water (v/v; 1:4)	385/498	47.6×10^{-9} 73.7×10^{-9}	4.53×10^{4} M^{-2}	Cell imaging	6.21j
11	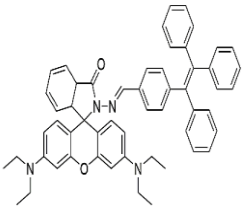	De-complexation	Al^{3+}	EtOH MeOH	557/597 557/600	0.0053 % (v/v) 0.0082 %(v/v)	8.004×10^{4}	None	6.21k
12	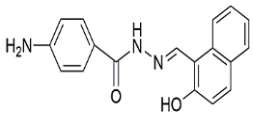	CHEF	Al^{3+}	HEPES buffer (10 mM, pH = 7.4)	395/475	6.7×10^{-9}	1.25×10^{5}	Cell imaging	6.21l
13	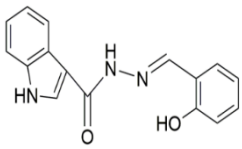	CHEF	Al^{3+}	ACN/H_2O (v: v = 1:9, pH = 7.4)	369/438	1.135×10^{-9}	7.1×10^{4}	Cell imaging	6.21 m
14	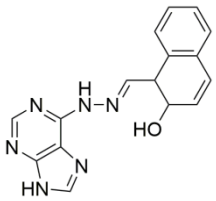	Fluorescent turn-on	Al^{3+}	CH_3OH /HEPES (1/9, v/v)	350/ 425-650	0.2×10^{-6}	2.11×10^{4}	Cell imaging	6.21n

15	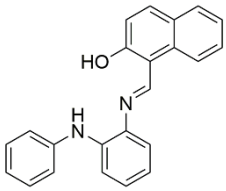	CHEF	Al^{3+}	DMSO-H_2O buffer	330/410	0.025×10^{-6}	6.19×10^{3}	None	6.21o
16	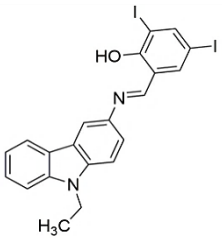	Fluorescent turn-on	Al^{3+}	90 % aqueous acetonitrile	385/540	0.403 mg/µL	5.44×10^{4}	None	6.21p
17	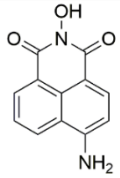	Fluorescent turn-on	Al^{3+}	water	438/538	0.28×10^{-15}	4.70×10^{4}	None	6.21q
18	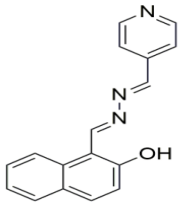	ICT	Al^{3+}	Different solvent	458/515	0.164×10^{-6}	5.81×10^{6}	Cell imaging	6.21r
19	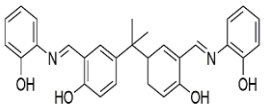	ICT-CHEF	Al^{3+}	10 mM HEPES buffer in H_2O/DMF = 4 : 1 (v/v) (pH 7.4)	430/519	4.6×10^{-7}	6.95×10^{8} M^{-2}	Cell imaging	6.21s
20	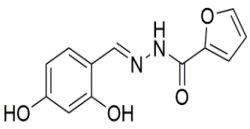	Fluorescent turn-on	Al^{3+}	Organic solvent/ H_2O	374/438	63×10^{-9}	3.32×10^{4}	None	6.21t

21	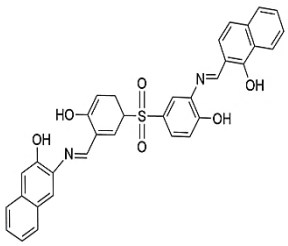	CHEF	Al^{3+}	DMF-HEPES buffer (1:4, v/v, pH 7.4)	482/532	6.18×10^{-6}	2.18×10^{4} M^{-2}	Cell imaging	6.21u
12	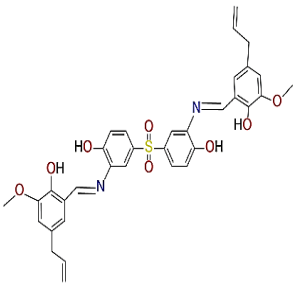	**CHEF**	**Al^{3+}**	**HEPES buffer at pH 7.4 (MeOH :H_2O, 4:1, (v/v))**	**440/547**	**2.18×10^{-6}**	**3.17×10^{6}**	**Cell imaging**	**This work**

6.2. Experimental section

6.2.1. Chemicals and instrumentations involved in this work

Eugenol-5-aldehyde (5-allyl-2-hydroxy-3-methoxybenzaldehyde) and 4,4'-sulfonylbis(2-aminophenol) were obtained from commercial supplier (TCI and Sigma-Aldrich, respectively). Additionally, all other required chemicals or reagents are of analytical quality, and the solvents were acquired from commercial supplier. These substances were employed without additional purification. A MICROMASS Q-TOF mass spectrometer and an FTIR spectrophotometer using KBr pellets on a Nicolet Magna IR 750 series-II were used to record the electron spray ionisation mass (ESI-MS positive) and infrared spectra (400–4000 cm^{-1}), respectively. Absorption spectra were obtained in the 200–800 nm wavelength range using a Shimadzu UV 1800 spectrophotometer equipped with a quartz cell with a 10-mm path length. Emission spectra were measured at room temperature (298 K) using a Fluromax-4 spectrofluorometer in HEPES buffer at pH 7.4 (MeOH:H_2O, 4:1, (v/v)). To measure the fluorescence lifetime, a time-resolved

spectrofluorometer from IBH in the UK was used. ^{1}H and ^{13}C NMR spectra were measured in d_6-DMSO solvent using a Bruker 400 spectrometer.

6.2.2. Synthesis

6.2.2.1. Synthesis process of chemosensor H_4L6 [H_4L6= 6,6'-((1E,1'E)-((sulfonylbis(6-hydroxy-3,1-phenylene))bis(azanylylidene))bis(methanylylidene))bis(4-allyl-2-methoxyphenol)]

First, 2 mmol (0.384g) of eugenol-5-aldehyde and 1 mmol (0.280g) of 4,4'-sulfonylbis(2-aminophenol) were carefully weighed and thoroughly mixed in 10 ml of MeOH. It was then left to stir continuously for around five hours at room temperature. The result was a precipitated dark orange solution. The mixture was then filtered and thoroughly dried in a desiccator. A solid product with a dark orange tint was produced, and it was described using several techniques.

Analytical data: Yield: 0.564 g (83%). IR (cm^{-1}, KBr): υ(O-H) 3639s and 2977; υ(C=N) 1632s; υ(S=O) 1354s. ESI-MS (positive): [$\mathbf{H_4L6}$+H_2O+CH_3OH+H]$^{+}$, m/z= 679.23. UV-Vis, λ_{max} (nm) (ε ($dm^3mol^{-1}cm^{-1}$)) in HEPES buffer at pH 7.4 (MeOH:H_2O, 4:1, (v/v)): 365 (8715) and 440 (6993), respectively.

^{1}H NMR (d_6-DMSO, 400 MHz) δ ppm: 3.34(-CH_2) (overlapped, 4H), 3.81(-OCH_3) (s, 6H), 5.09(-CH_2) (d, 4H, *J*=4Hz), 5.99(-CH) (m, 2H), 6.97(Ar-H) (d, 2H, *J*=4Hz), 7.09(Ar-H) (s, 2H), 7.11(Ar-H) (s, 2H), 7.72(Ar-H) (d, 2H, *J*=4 Hz), 7.95(Ar-H) (d, 2H, *J*=4 Hz), 9.01(-HC=N) (s, 2H), 10.88(-OH) (broad peak, 2H), 13.25(-OH) (s, 2H).

^{13}C NMR (d_6-DMSO, 100 MHz) δ ppm: 56.38, 56.57, 112.12, 114.07, 114.23, 116.31, 116.49, 116075, 117.34, 118.55, 119.00, 119.47, 122.66, 123.53,127.35, 124.70, 130.16, 130.19, 131.20, 132.58, 133.13, 133.29, 133.79, 136.03, 136.20, 137.93, 138.15, 148.42, 148.81, 149.66, 149.98, 155.34, 155.73, 164.07, 164.25.

6.2.2.2. Synthesis of complex 6.1, $Al_2(L6)(NO_3)_2$

Methanolic solution of 1.0 mmol (0.375g) of aluminium nitrate nonahydrate was added drop by drop, to the 0.5 mmol (0.314g) methanolic solution of **H_4L6**. For around four hours, the resulting reaction mixture was stirred. The orange colour of **H_4L6** remained unchanged after addition of Al^{3+}. Slow solvent evaporation resulted in the formation of the solid product (complex **6.1**).

Analytical data: Yield: 0.617 g (81%). IR (cm^{-1}, KBr): υ(C=N) 1622s, υ(NO_3^-) 1298, υ(S=O) 1145. ESI-MS (positive): [(**L6**)Al_2+2CH_3OH+Na-H]$^{2+}$, *m/z* = 383.08. UV-Vis, λ_{max} (nm), (ε ($dm^3mol^{-1}cm^{-1}$)) in HEPES buffer at pH 7.4 (MeOH:H_2O, 4:1, (v/v)): 375 (11655) and 435 (10340), respectively.

^{1}H NMR (d_6-DMSO, 400 MHz) δ ppm: 3.31(-CH_2) (d, 4H, *J*=4Hz), 3.83(-OCH_3) (s, 6H), 5.09(-CH_2) (d, 4H, *J*=16Hz), 5.98(-CH) (m, 2H), 6.91(Ar-H) (s, 2H), 7.05(Ar-H) (s, 2H), 7.09(Ar-H) (s, 2H), 7.55(Ar-H) (d, 2H, *J*=4Hz), 7.65(Ar-H) (d, 2H, *J*=12Hz), 9.12(-HC=N) (s, 2H).

^{13}C NMR (solvent used: d_6-DMSO, 100 MHz) δ ppm: 56.13, 56.56, 116.18, 116.50, 118.56, 119.28, 119.47, 122.64, 131.23, 132.43, 133.67, 137.92, 138.27, 148.81, 149.64, 151.24, 192.30.

6.2.3. Spectral study of absorbance and emissions

As stock solutions, nitrate salts of several metal ions were made in MeOH (1×10^{-3} M). Additionally, a stock solution of the chemosensor (**H_4L6**) at a concentration of 1×10^{-3} M was prepared in DMSO: MeOH (7:3, v/v). Next, methanol was added to dilute the **H_4L6** solution to a concentration of 1×10^{-5} M as needed. HEPES buffer at pH 7.4 (MeOH: H_2O, 4:1, (v/v)) was the used for all spectroscopic tests, including competitive testing of different cations and anions. In order to maintain a concentration of 2×10^{-5} M, a quartz optical cell measuring 1.0 cm in optical path length was filled with 60 µL of **H_4L6** (1×10^{-3} M) solution and progressively mixed with the ion stock solutions. The excitation wavelength for fluorescence measurements was set at 440

nm, while emission was measured between 455-750 nm. Using HEPES buffer, 1N HCl, and 1N NaOH solution in water, various pH solutions (pH=3–12) were created for pH metric titration.

6.2.4. LOD and binding constant calculations

The limit of detection (LOD) was determined using the IUPAC-approved formula: LOD=3σ/slope, where σ stands for the curve's standard deviation. The LOD was computed from the fluorescence titration data using equation (1). The web resource https://supramolecular.org was utilized to compute the binding constant (K) of the chemosensor (**H_4L6**) with respect to Al^{3+} [6.22].

6.2.5. Cell culture

Human lung cancer cell lines (A549) and human lung fibroblast cell lines (WI-38) were obtained from National Center for Cell Science (NCCS) Pune, India. The cells were grown in DMEM (Dulbecco's Modified Eagle Medium) with 10% FBS (Fetal Bovine Serum), penicillin/streptomycin (100units/ml) at 37ºC and 5% CO_2. All the treatments were conducted at 37ºC and at a cell density allowing exponential growth [6.23].

6.2.6. Cell imaging

The cells were grown in coverslips for 24 hrs. Then the cells were treated with 20 µM sample for 24 hrs at 37ºC. The cells were washed with 1X PBS (Phosphate-buffered saline) and then they were mounted on a glass slide and observed under fluorescence microscope (Leica) [6.23].

6.3. Results and discussion

6.3.1. Discussion on synthesis and characterization

Chemosensor **H_4L6** has been synthesized via an one step condensation reaction between eugenol-5-aldehyde and 4,4'-sulfonylbis(2-aminophenol) at 2:1 ratio in methanolic medium under 5h continuous stirring at room temperature. A dark orange colour solid product was obtained with good yield (**Scheme 6.1**). Complete characterization of **H_4L6** using various methods like FT-IR, ESI-mass spectrometry, ^{1}H NMR, ^{13}C NMR and UV-Vis spectral analysis were also done. In FT-IR spectrum of **H_4L6**, presence of a broad band and sharp bands at 3639 and 1632, 1354 cm^{-1} suggest stretching frequencies of aromatic OH, azomethine (–C=N) and sulfonyl (S=O) group, respectively (**Fig. 6.1**). ESI-mass spectrum of probe gave value of *m/z* =679.23, suggesting [**H_4L6**+H_2O+CH_3OH+H]$^+$ species (**Fig. 6.2**).

We have successfully prepared chemosensor bound complex, **6.1** upon reaction between **H_4L6** and $Al(NO_3)_3.9H_2O$ at 1:2 ratio (**Scheme 6.2**) under stirring condition at room temperature. The orange colored solid mass of complex **6.1** was isolated with high yield. Possible structure of **6.1** was also confirmed by different spectroscopic techniques. In mass spectrum, peaks at *m/z* = 383.08, corresponded to [(**L6**)Al_2+2CH_3OH+Na–H]$^{2+}$ (**Fig. 6.3**). Furthermore, a decrease value of stretching frequencies of azomethine (–C=N) and sulfonyl (S=O) groups (1622 and 1145 cm^{-1}, respectively) in **6.1** support the binding of the ligand to Al^{3+}. Additional a sharp peak at 1298 cm^{-1} represents stretching frequency for NO_3^- group in **6.1** (**Fig. 6.1**).

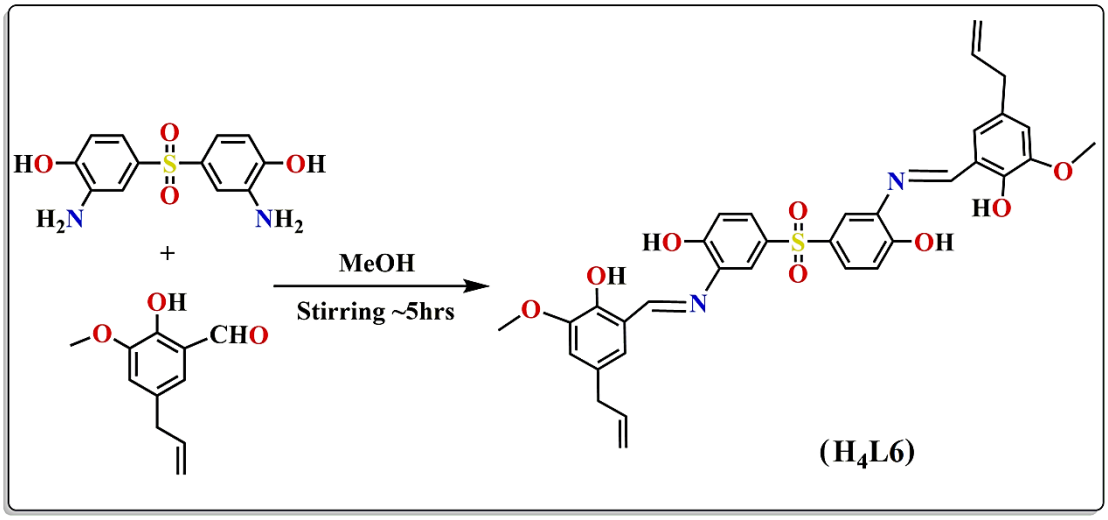

Scheme 6.1. Synthesis route of chemosensor (**H_4L6**).

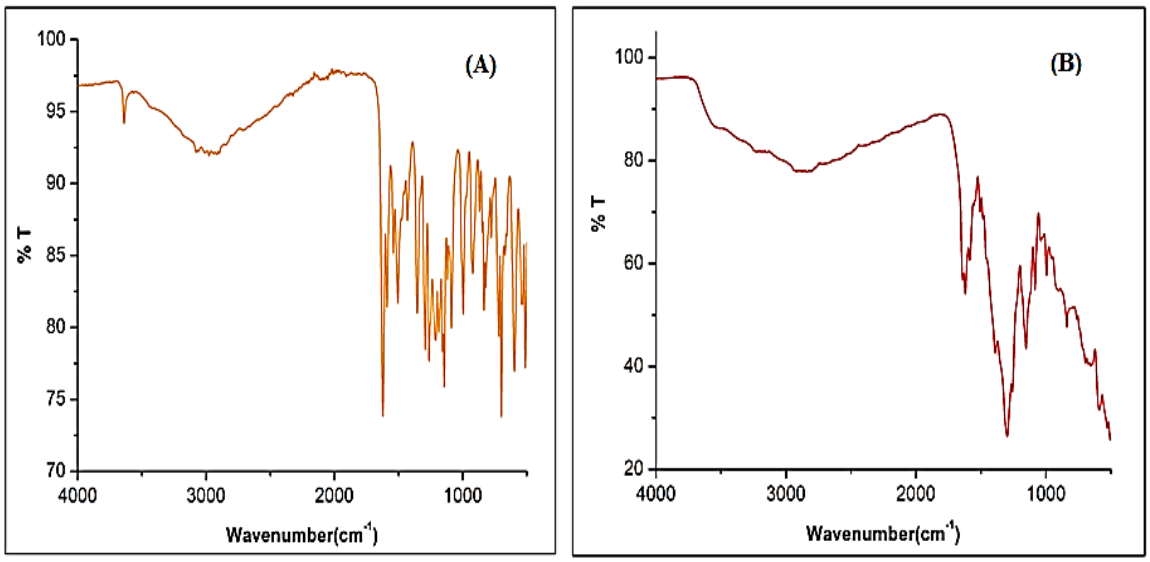

Fig. 6.1. FTIR spectra of (A) chemosensor **H_4L6** and (B) complex **6.1**, respectively.

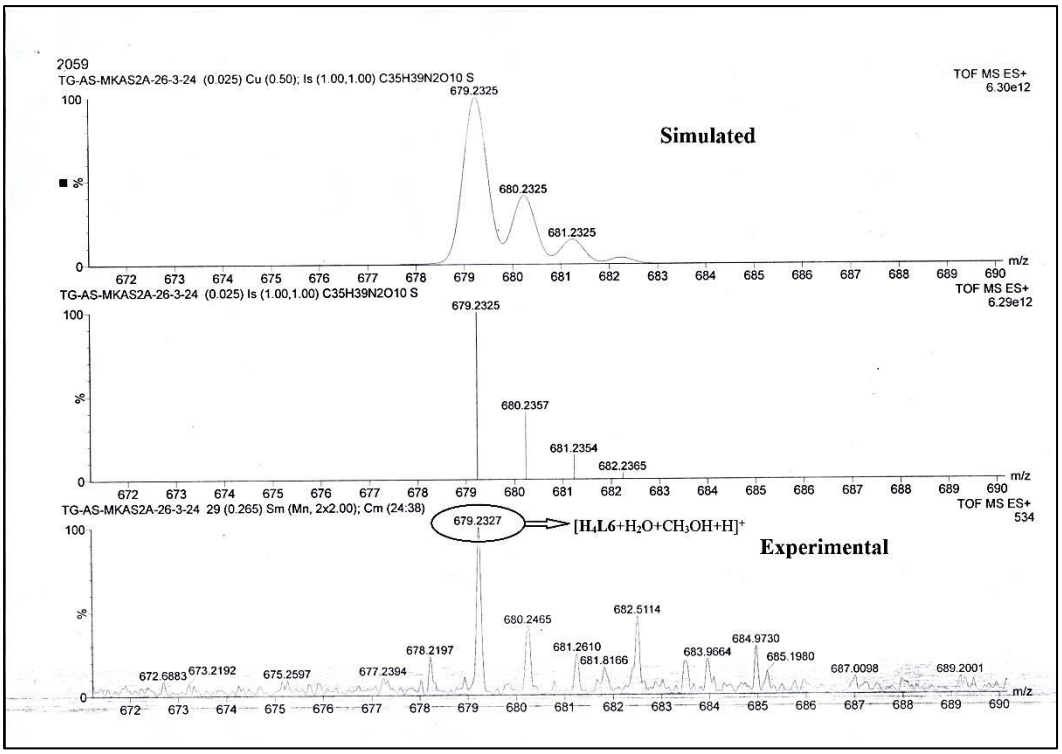

Fig. 6.2. ESI-MS$^+$ spectrum of [**H_4L6**+H_2O+CH_3OH+H]$^+$.

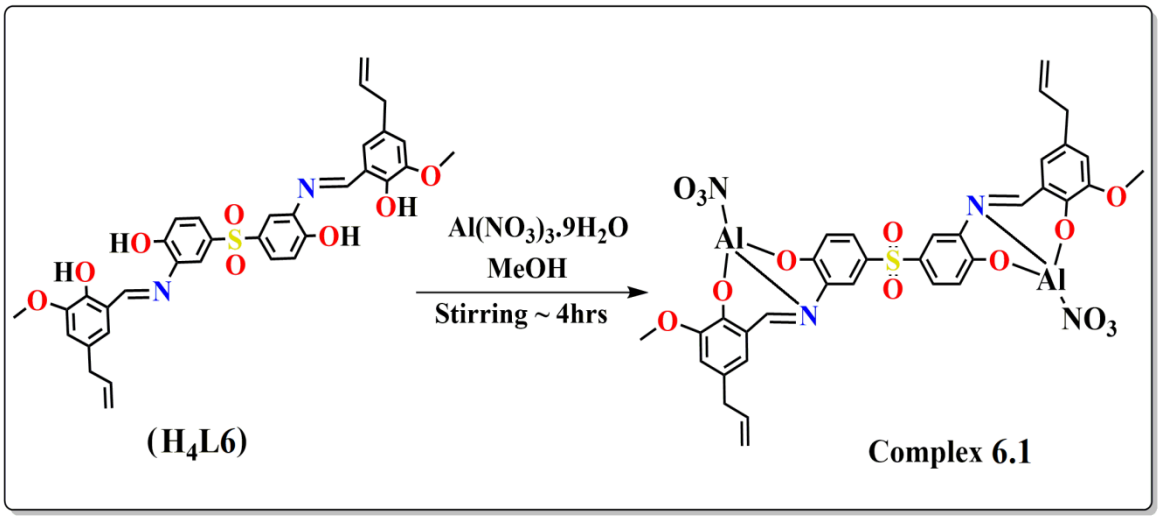

Scheme 6.2. Synthesis route of complex **6.1**.

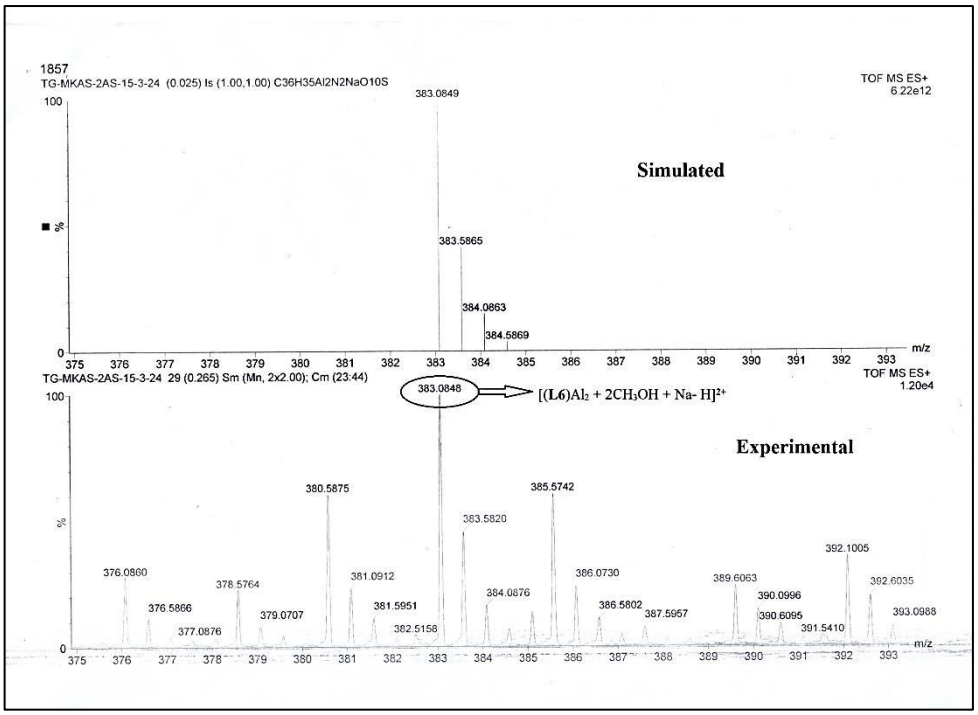

Fig. 6.3. ESI-MS^{+} spectrum of [(**L6**)Al_2+2CH_3OH+Na–H]$^{2+}$.

6.3.2. ^{1}H and ^{13}C NMR data analysis

In d_6-DMSO solvent, the ^{1}H and ^{13}C NMR spectra of the chemosensor (**H_4L6**) and metal-bound compound (**6.1**) were obtained. Interestingly both the molecules possess a *c2* symmetry. Two types of aromatic –OH protons: a sharp singlet at 13.25 ppm and a broad peak at 10.88 ppm found in the ^{1}H spectrum of the free chemosensor were coming from eugenol aldehyde part and sulfonyl amine part of **H_4L6**. Imine (H-C=N) protons were seen at 9.01 ppm, while aromatic protons were detected in the range 7.95–6.97 ppm (**Fig. 6.4**). In complex **6.1**, association of metal ions result disappearance of all four -OH protons, downfield shift of imine protons (9.12 ppm) (**Fig. 6.5**). This is a clear indication of coordination of Al^{3+} moiety with phenoxido oxygens and imine nitrogen of **H_4L6**. Furthermore, imine carbon atoms of **H_4L6** were detected at 164.25 and 164.07 ppm in ^{13}C NMR. These atoms moved to the downfield region at 192.30 ppm in **6.1** (**Figs. 6.6** and **6.7**). The metal-chemosensor binding mechanism was further established by ^{1}H NMR titration experiment using same solvent (d_6-DMSO). Incremental addition of Al^{3+} ions

(0.50 to 2 equivalents) to **H_4L6** consequence disappearance of aromatic -OH protons and downfield shift of imine protons was noticed (**Fig. 6.8**). Additionally, the 1:2, ligand to metal binding ratio was validated by this process.

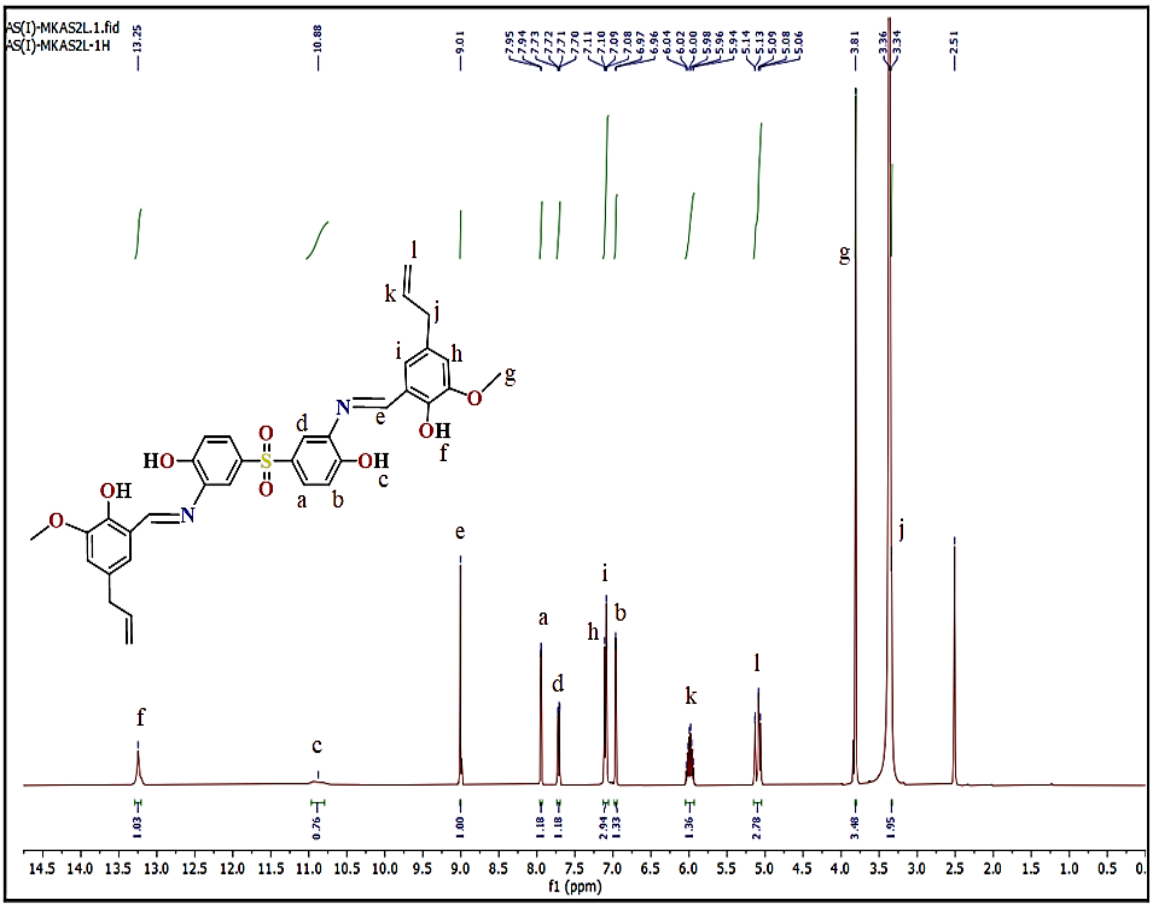

Fig. 6.4. ^{1}H NMR spectrum of **H_4L6** in DMSO-d_6 solvent.

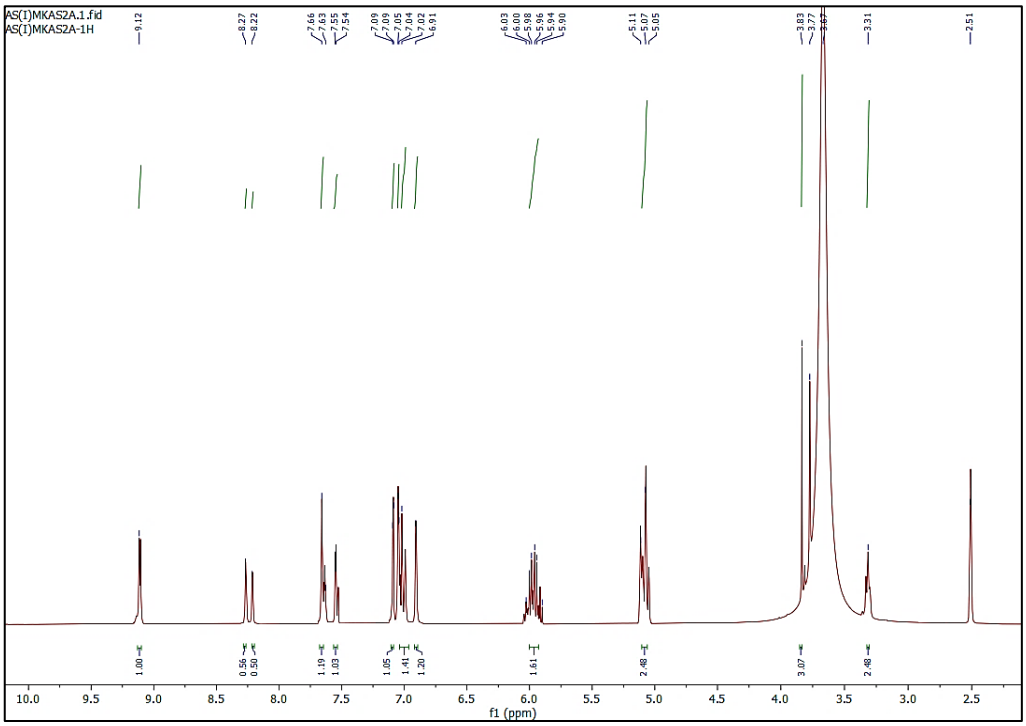

Fig. 6.5. ^{1}H-NMR of complex **6.1** in DMSO-d_6 solvent.

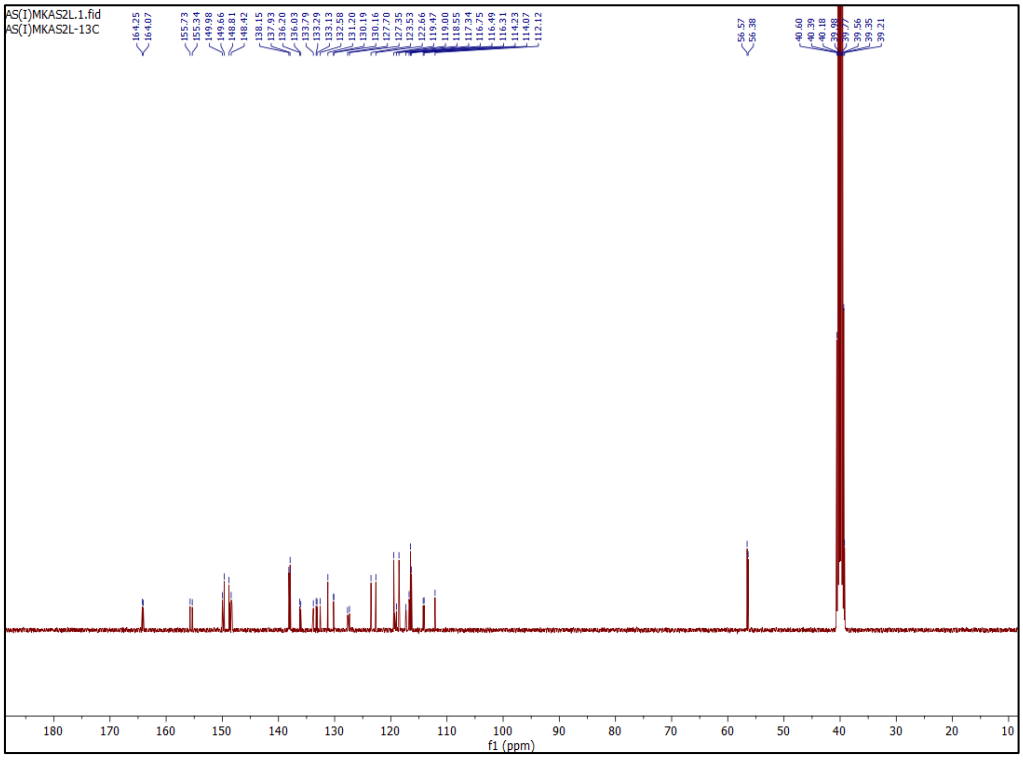

Fig. 5.6. ^{13}C NMR spectrum of **H_4L6** in DMSO-d_6 solvent.

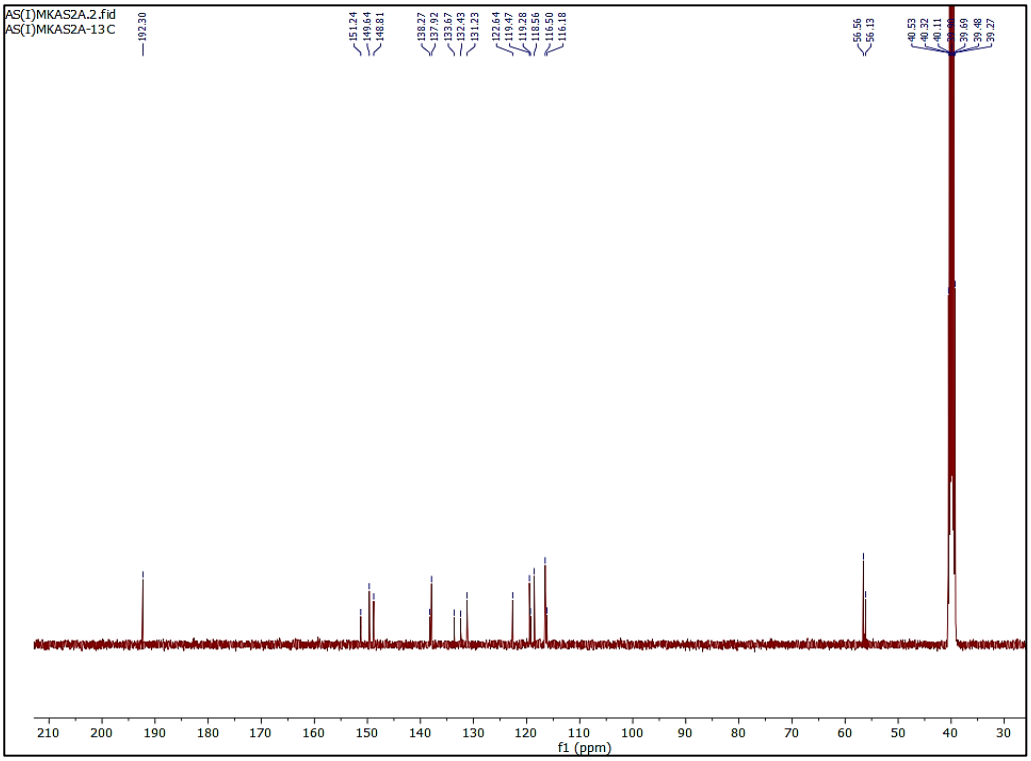

Fig. 6.7. ^{13}C NMR of complex **6.1** in DMSO-d_6 solvent.

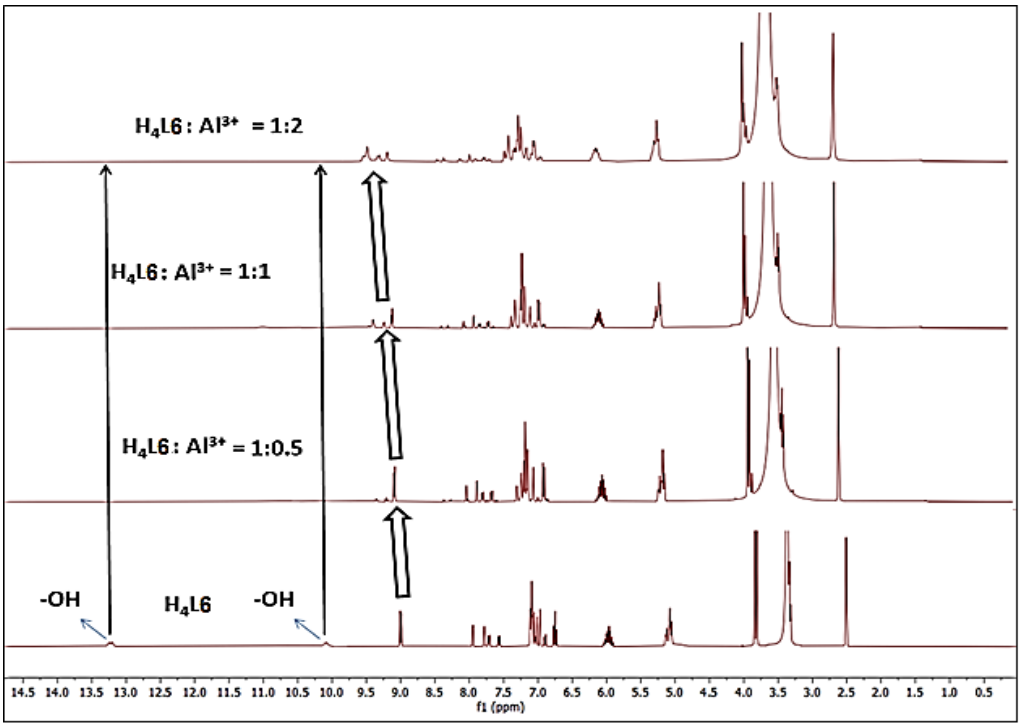

Fig. 6.8. ^{1}H-NMR titration of the free ligand (**H_4L6)** and with the addition of 0.50, 1 and 2 equivalent of Al^{3+} in DMSO-d_6 solvent.

6.3.3. Absorption spectral data

All the UV-Vis absorbance data were collected at pH 7.4 in HEPES buffer (MeOH:H_2O, 4:1, (v/v)). Two broad bands and a small hump at 365, 440 nm and 475 nm were seen in the spectra of free **H_4L6**. These spectral patterns could be attributed to the intramolecular π →π* and n →π* type of transitions. Gradual addition of Al^{3+} ion (0-40 μM) follows slight shifting in the probe's spectra. Peaks at 365 nm and 440 nm finally appeared at 375 and 435 nm, respectively (**Fig. 6.9**). This is a clear indication of metal-ligand complexation with 1:2 binding ratio. Absorbance titration data is further used to calculate the Al^{3+}-chemosensor binding constant value, and the result is 3.17×10^6 M^{-1}[6.22].

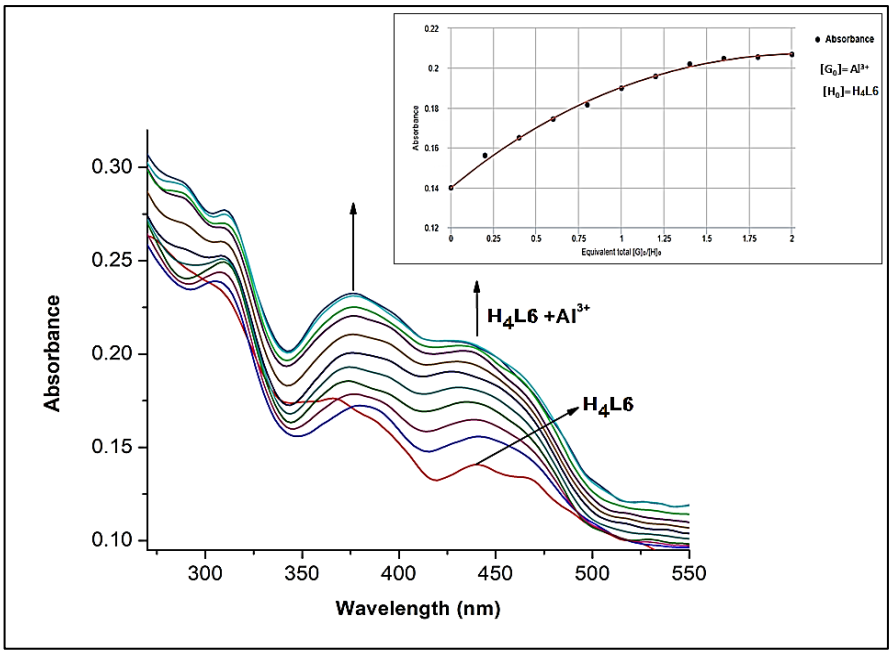

Fig. 6.9. Absorption titration of **H_4L6** (20 μM) in HEPES buffer at pH 7.4 (MeOH:H_2O, 4:1, (v/v)) with progressively addition of Al^{3+} (0–40 μM). Inset: Binding constant calculation for **H_4L6** with Al^{3+} ion. [http://supramolecular.org]. Binding constant = 3.17×10^6 M^{-1}.

Furthermore, absorption spectral experiment carried out with other mono, di and trivalent cations like Na^+, K^+, Ag^+, Cu^{2+}, Zn^{2+}, Ni^{2+}, Mn^{2+}, Pb^{2+}, Cd^{2+}, Co^{2+}, Ca^{2+}, Hg^{2+}, Mg^{2+}, Ga^{3+}, In^{3+}, Tl^{3+}, Cr^{3+} and Fe^{3+}. Absence of any considerable change proves its selectivity.

6.3.4. Fluorescence spectral analysis

Fluorescence intensity of the free probe **H_4L6** was very trivial. In its free state C=N isomerization and photo induced electron transfer (PET) originating from amide N-atoms were found. When the probe was exposed toward trivalent metal ion Al^{3+} (0-40 μM, λ_{ex}= 440 nm), there was a noticeable increase in fluorescence at 547 nm (**Fig. 6.10**). The fluorescence intensity increased progressively until about two equivalents of the Al^{3+} were added, at which point it reached its maximum value. In **H_4L6**, presence of hard donor centers, phenixido O atoms along with imine N atoms result strong coordination with hard Lewis acid, Al^{3+}. Restriction of C=N isomerization and PET processes and initiation of chelation enhanced fluorescence (CHEF) result a ~5 times increment of fluorescence intensity followed by change in quantum yield value from 0.011 to 0.026.

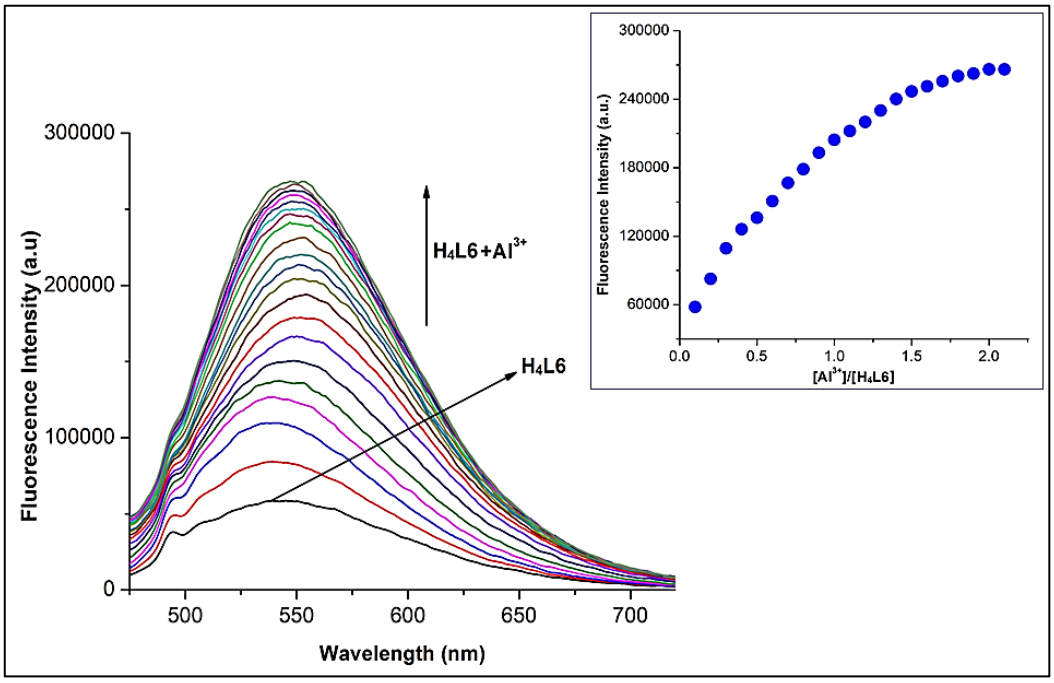

Fig. 6.10. Fluorescence spectra of **H_4L6** (20 μM) in HEPES buffer at pH 7.4 (MeOH:H_2O, 4:1, (v/v)) upon progressively addition of Al^{3+} (0–40 μM) (λ_{em}= 547 nm). Inset: non-linear graph of fluorescence spectra with respect to [Al^{3+}]/[**H_4L6**].

By comparing the fluorescence spectral data of a variety of metal ions in presence of **H_4L6** in the same buffer media, the selectivity of the probe towards Al^{3+} was verified. The inclusion of common cations (Ga^{3+}, In^{3+}, Tl^{3+}, Hg^{2+}, Cr^{3+}, Fe^{3+}, Cu^{2+}, Zn^{2+}, Ni^{2+}, Mn^{2+}, Pb^{2+}, Cd^{2+}, Co^{2+}, Na^{+}, K^{+}, Ca^{2+}, Ag^{+} and Mg^{2+} ions) did not significantly alter the probe's intensity (**Fig. 6.11**). However, a faint fluorescence band was observed at around 550 nm after Ga^{3+} and In^{3+} addition to the **H_4L6** solution. This finding suggests that the chemosensor **H_4L6** functions as an excellent fluorometric probe for identification of Al^{3+} ion among competing mono, di, or trivalent metal ions. In presence of Al^{3+} ion the probe displays brilliant yellow colour fluorescence. As a result, the chemosensor will be a wise option for fluorometric detection of Al^{3+} ion in biological and environmental samples (**Fig. 6.12**).

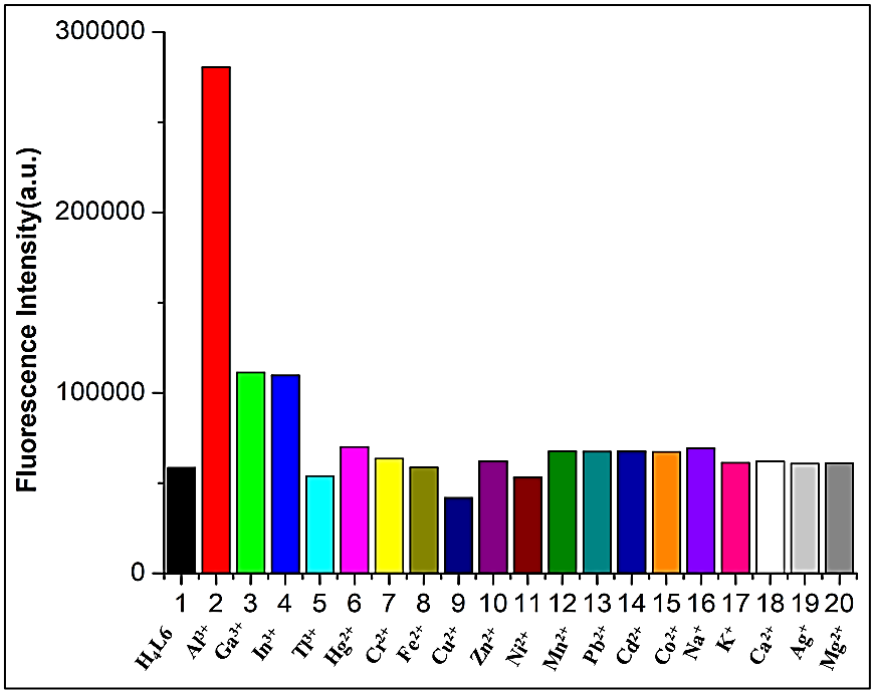

Fig.6.11. Fluorescence intensity profile of chemosensor **H_4L6** in the presence of different cations in HEPES buffer at pH 7.4 (MeOH:H_2O, 4:1, (v/v)) where **H_4L6** (20 µM) + M^{n+} (100 µM) and M^{n+}= 2-Al^{3+}, 3-Ga^{3+}, 4-In^{3+}, 5-Tl^{3+}, 6-Hg^{2+}, 7-Cr^{3+}, 8-Fe^{3+}, 9-Cu^{2+}, 10-Zn^{2+}, 11-Ni^{2+}, 12-Mn^{2+}, 13-Pb^{2+}, 14-Cd^{2+}, 15-Co^{2+}, 16-Na^{+}, 17-K^{+}, 18-Ca^{2+}, 19-Ag^{+} and 20-Mg^{2+} ions.

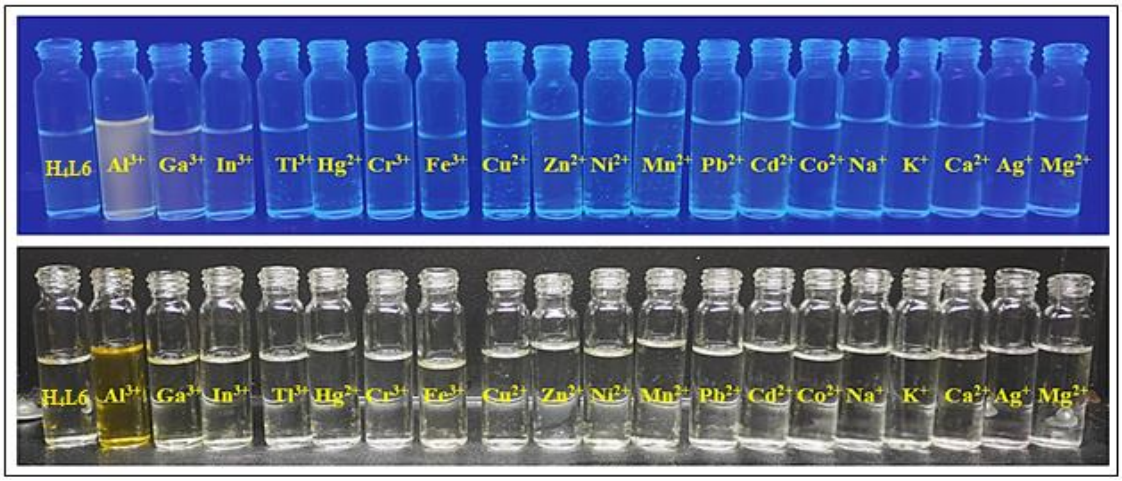

Fig. 6.12. Visual colour changes of chemosensor **H_4L6** (20μM) in presence of common metal ions (40μM) in HEPES buffer (4:1, MeOH:H_2O, v/v, pH 7.4) under visible (below) and UV light (above).

Effect of various anions and biomolecules like AcO^-, OCN^-, F^-, Br^-, I^-, Cl^-, N_3^-, $S_2O_3^{2-}$, SO_3^{2-}, PF_6^-, $P_2O_7^{2-}$, NO_3^-, BF_4^-, ClO_4^-, $H_2PO_4^-$, HPO_4^{2-}, AsO_2^-, S^{2-}, SCN^-, PO_4^{2-}, L-Histidine, L-Cysteine, and ATP on **H_4L6** has been studied in the same buffer medium. No such significant fluorescence intensity enhancement or quenching was found (**Fig. 6.13**). Furthermore, competition assay in presence of above mentioned cations, anions and biomolecules are performed. Here, **H_4L6** (1 equivalent) was mixed with an Al^{3+} (2 equiv.) while additional metal ions/ anions and biomolecules (5 equiv.) were added to this solution. Significant alteration in fluorescence intensity of [**H_4L6**-Al^{3+}] system was absent which confirm selectivity of **H_4L6** towards Al^{3+} ion (**Figs.6.14** and **6.15**).

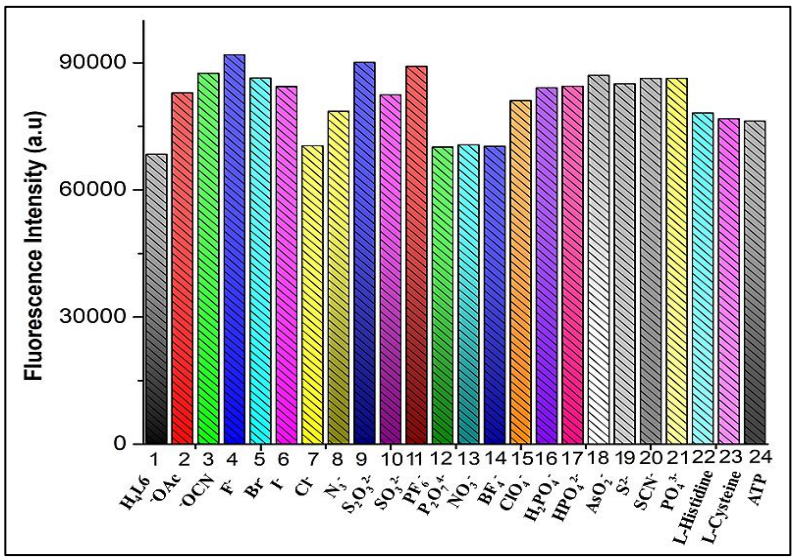

Fig. 6.13. Relative fluorescence intensity diagram of **H_4L6** with of different anions in HEPES buffer at pH 7.4 (MeOH:H_2O, 4:1, (v/v)) where 1=only **H_4L6** (20 µM) and 2-24= **H_4L6** (20 µM) + M^{n-} (different anions) (100 µM), respectively.

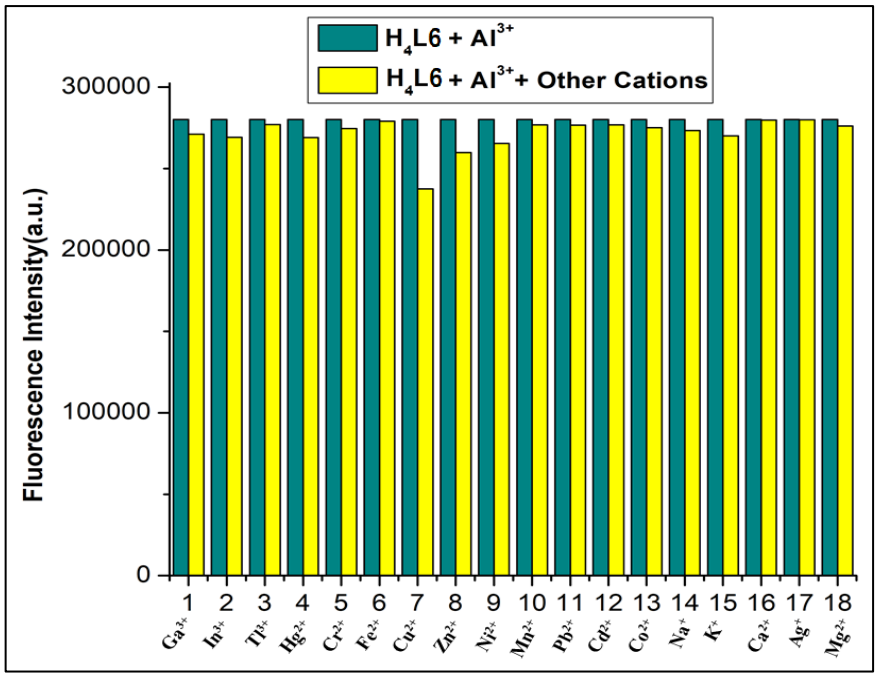

Fig. 6.14. Relative fluorescence intensity diagram of [**H_4L6**-Al^{3+}] system with different cations in in HEPES buffer at pH 7.4 (MeOH:H_2O, 4:1, (v/v)) where, 1-18= **H_4L6** (20 µM) + Al^{3+} (40 µM) + M^{n+} (different cations) (100 µM), respectively.

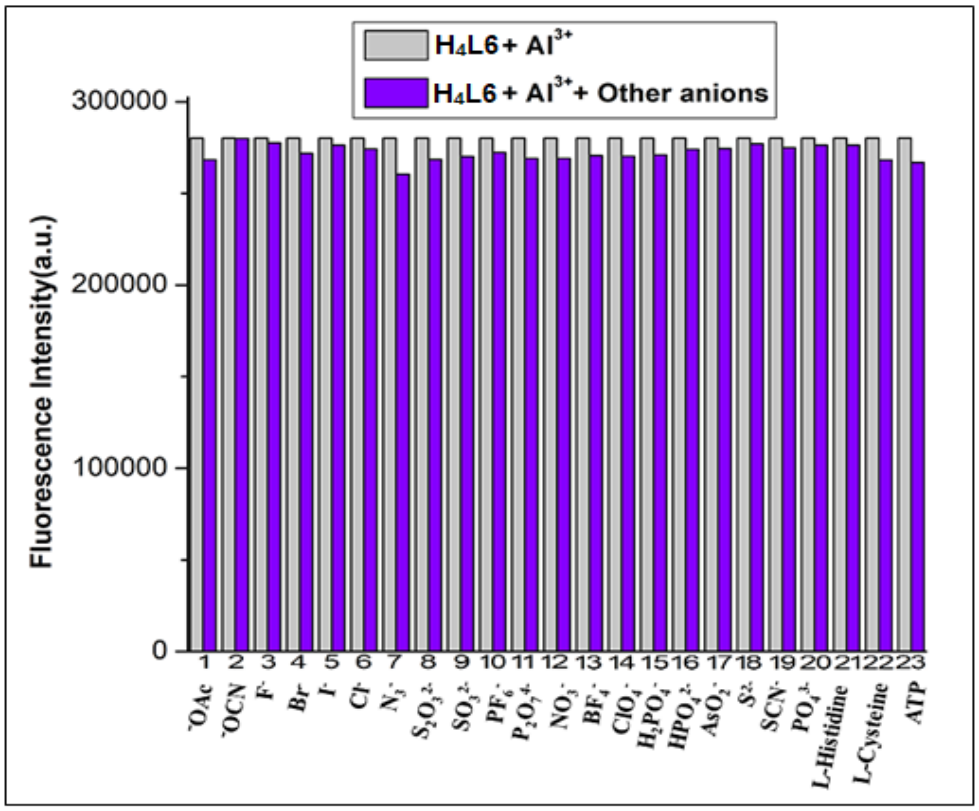

Fig. 6.15. Relative fluorescence intensity diagram of [**H_4L6**-Al^{3+}] system with different anions in HEPES buffer at pH 7.4 (MeOH:H_2O, 4:1, (v/v)) where, 1-23=**H_4L6** (20 µM) + Al^{3+}(40 µM) + M^{n-} (different anions) (100 µM), respectively.

6.3.5. Fluorescent lifetime and LOD measurements

Quantum yield and fluorescence lifetime of free **H_4L6** and metal bound **H_4L6** were examined to support selectivity of **H_4L6** towards Al^{3+}. In average fluorescence lifetime calculation we have used the formula $\tau_f = a_1\tau_1 + a_2\tau_2$, where a_1 and a_2 are the relative amplitudes of the decay process. The average fluorescence lifetime experiment was studied at 298 K in HEPES buffer at pH = 7.4 (MeOH:H_2O, 4:1, (v/v)). Al^{3+} bound chemosensor exhibits higher value from its free state (1.95 nS, and 1.49 nS) (**Fig. 6.16**, **Table 6.1**). Considerable enhancement of fluorescence of **H_4L6** in presence of Al^{3+} implies stability of adduct in the excited state. A high value of quantum yield of adduct compared to free **H_4L6** is found (0.026 and 0.011) (**Table**

6.1). The 3σ approach is used to compute the limit of detection (LOD) of the probe for the Al^{3+} ion and the value is 2.81×10^{-6}M (Table 6.1).

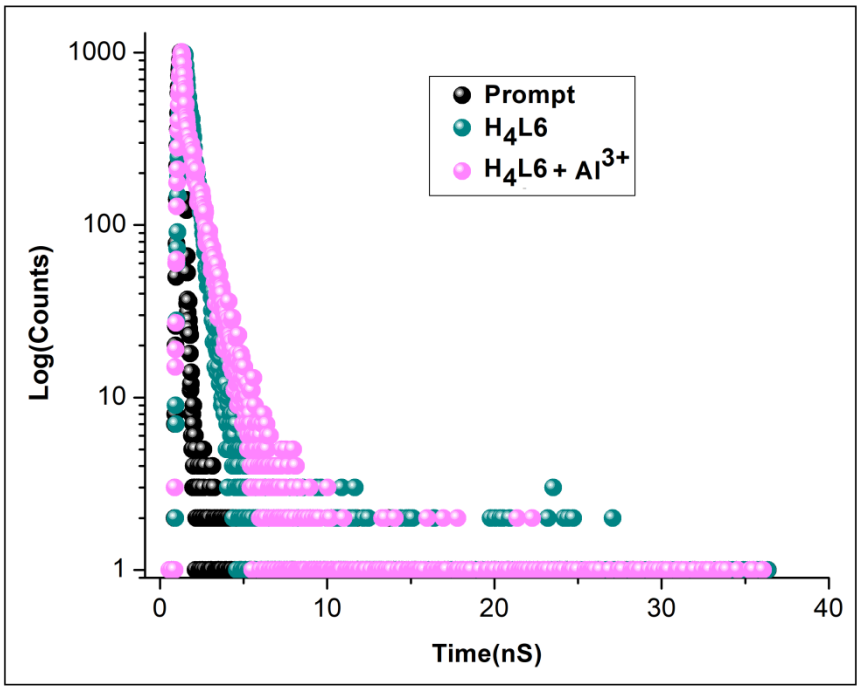

Fig. 6.16. The decay curves (●) for the scattered fluorescence of **H_4L6** in the absence (●) and presence (●) of Al^{3+} ions are represented by the time-resolved decay (logarithm of normalized intensity vs time in nS).

Table 6.1. Apparent binding constant (K), LOD, lifetime (τ_f) and quantum yield (Φ) values of **H_4L6** and complex **6.1** from spectrofluorometric measurement.

	K (M^{-1})	**LOD** (M)	τ_f (ns) (average)	χ^2	Φ
H_4L6	-		1.49	1.039131	0.011
Complex **6.1**	3.17×10^6	2.81×10^{-6}	1.95	1.04295	0.026

6.3.6. Reversibility test and paper strips test

Experiment to check reversibility and regeneration of the probe is vital for its real time application. A potent chelating ligand, Na_2EDTA (sodium salt of ethylenediaminetetraacetic acid) solution was used here. Initially, a solution of free probe **H_4L6** was taken which is colourless. Then upon addition of 2 equiv. of the Al^{3+} ion in the solution a yellow fluorescence is produced (**Fig. 6.17**). But when Na_2EDTA was mixed to this solution, the yellow fluorescence disappeared and a colourless solution was formed. Such event is due to regeneration of free probe and stable metal-EDTA complex. Upon further addition of Al^{3+} ion initial yellow fluorescence returns.

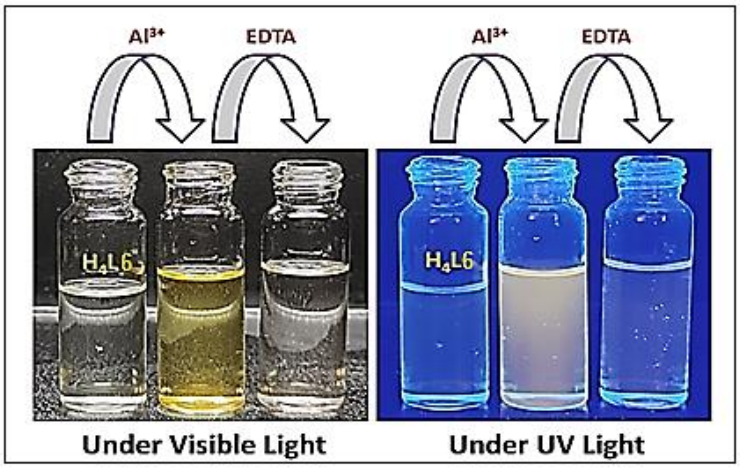

Fig. 6.17. Visual colour changes in reversibility experiment in HEPES buffer at pH 7.4 (MeOH:H_2O, 4:1, (v/v)). Here, **H_4L6** (20μM), **H_4L6** (20μM) + Al^{3+} (40μM), **H_4L6** (20μM) + Al^{3+} (40μM) + $EDTA^{2-}$ (40μM), respectively under visible light and UV lamp.

As a part of on-field usability of **H_4L6**, we have used paper strip experiment. In this experiment, a paper strip was charged with Al^{3+} solution after being dipped in free **H_4L6**. Under UV light, there was a noticeable colour shift in the strip from colourless to fluorescent yellow (**Fig. 6.18**). Importantly, presence of various cations had no effect on the paper strip's colour

intensity. With its LOD value (10^{-6} M), this paper-based chemosensor **H_4L6** will be a good choice for quick and accurate fluorescence detection of Al^{3+} in various environmental samples.

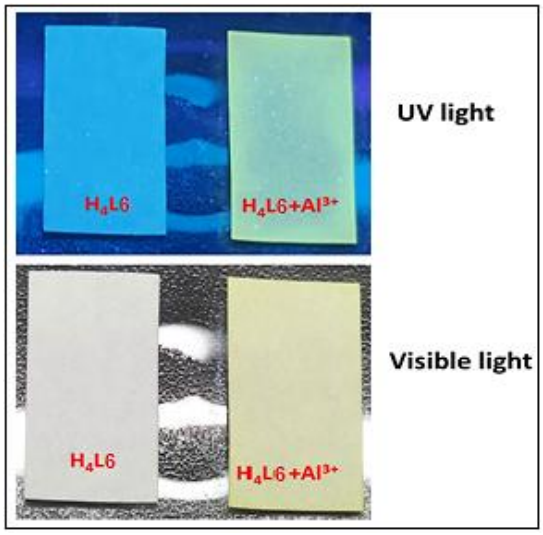

Fig. 6.18. Paper strips test under visible light (below) and UV light (above) in presence of chemosensor **H_4L6** and **H_4L6** + Al^{3+}, respectively.

6.3.6. Effect of pH

The impact of pH on the fluorescence intensity of the free chemosensor (**H_4L6**) and metal-bound form must be examined in order to investigate biological and environmental materials. It has been revealed that the free chemosensor's weak fluorescence intensity is independent of pH window, 3-11 (Fig. 6.19). In presence of Al^{3+}, very week fluorescence signal up to pH 6.5 (an acidic environment) indicate no complex formation between **H_4L6** and Al^{3+}ions. Fluorescence intensity sharply increased in the pH range of 6.5–7.5, indicating development of metal–chemosensor complex which remains unchanged until pH 9. Within this pH range, deprotonation of -OH protons of **H_4L6** occurs which further coordinate with metal centre resulting fluorescence amplification. This observation strongly supports applicability of **H_4L6** under physiological conditions. Beyond pH 9 a gradual decrease in fluorescence intensity suggests instability of metal-chemosensor adduct.

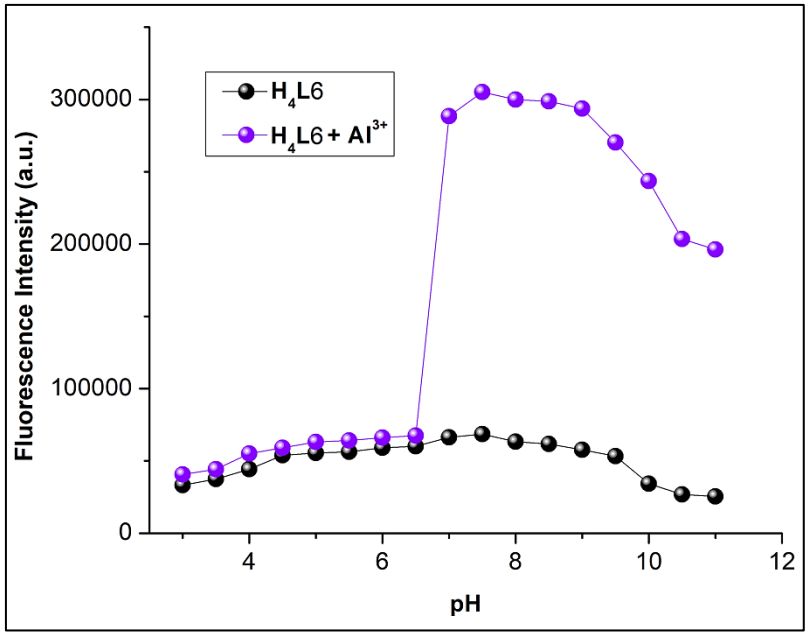

Fig. 6.19. Fluorescence intensity of **H_4L6** (20 µM) in the absence and presence of Al^{3+} ion (40 µM) at various pH values in HEPES buffer.

6.3.7. Cell Imaging and cell viability analysis

The fluorescence microscopy study is performed to ensure the cellular uptake of ligand (**H_4L6)** and Al^{3+} in A549 cells. A moderate green signal is found in the case of the cells treated with the ligand. But a strong fluorescent signal is observed when the cells were treated with **H_4L6** and respective metal salt under the microscope. Thus, we can conclude that the cells internalize the sample and producing fluorescence signal (**Fig. 6.20**). Initially, MTT assay was accomplished to evaluate the toxicity of probe **H_4L6** at different level of concentrations with WI-38 and A549 cell line, respectively. The probe **H_4L6** was amicable towards cells viability upto100 µM concentration (**Fig. 6.21**).

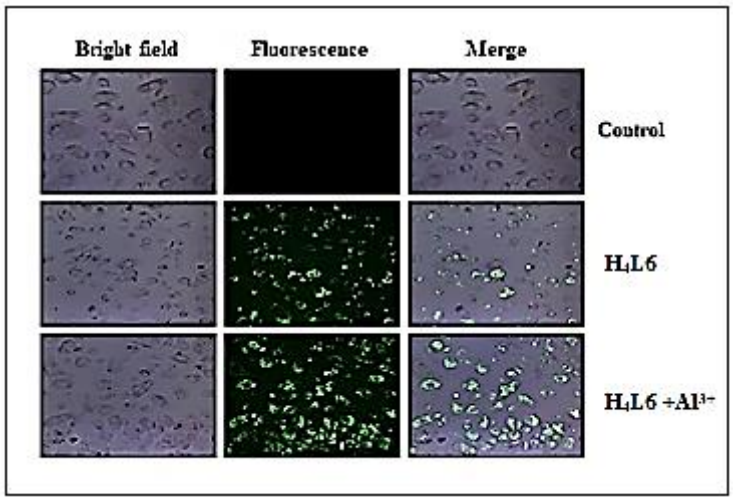

Fig. 6.20. Bright field, fluorescence and merged microscopic images of untreated A549 (Control), cells treated with **H_4L6** (20 µM), and **H_4L6** (20 µM) + Al^{3+} (20 µM), respectively.

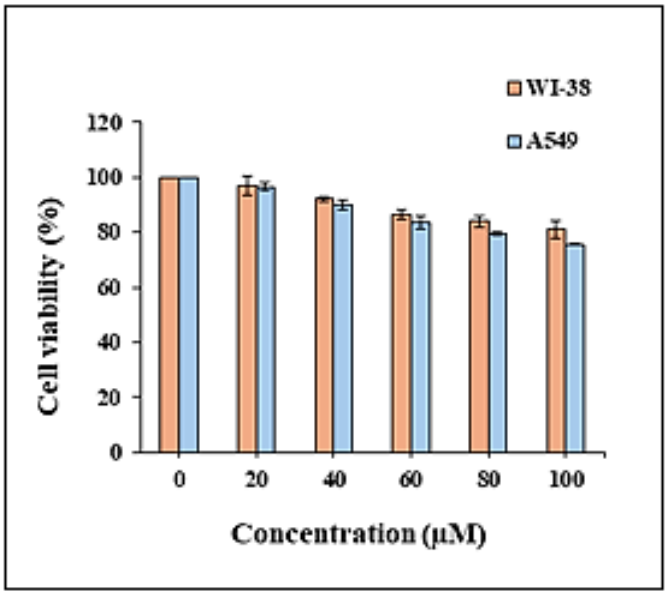

Fig. 6.21. Cell viability of WI-38 and A549 cell line on exposure to the **H_4L6**.

6.4. Conclusion

In this work, a chemosensor (**H_4L6**) on eugenol-sulfonyl scaffold was designed and utilized for fluorometric detection of Al^{3+} ion among other competing metal ions and different anions. In the presence of Al^{3+}ions, **H_4L6** (pH = 7.4, HEPES buffer (MeOH:H_2O, 4:1, (v/v)) shows a notable increase in fluorescence (5 times) at 547 nm upon excitation at λ_{ex} 440 nm. The probable mechanistic pathway is restriction of PET and C=N isomerization processes in free **H_4L6** followed by metal mediated CHEF on. The response mechanism of **H_4L6** with Al^{3+} has been investigated by UV-Vis absorbance, fluorescence, NMR, ESI-MS analysis. The detection limit (2.81×10^{-6}M) is found to be well below the WHO drinking water standard limit (upto 7.41 mmol L^{-1}). Studies are also conducted on the chemosensor's reversibility and regeneration when Na_2EDTA is present. The probe **H_4L6** featured low cytotoxicity towards biological cell assays and also successfully applied to fluorescence imaging of A549 cells. **H_4L6** could be used as a kit for rapid, simple and in-situ detecting method for Al^{3+} in real samples due to its excellent in-situ detection of Al^{3+} in test paper. Thus, development of a chemosensor with two opening cavities which successfully accommodate two Al^{3+} ions holds great prospect for developing new strategies and tools for further investigation in Al^{3+} detection and the analysis of associated diseases.

6.5. References

[6.1] J. Shen, X. Wen, Z. Fan, Sens. Actuators B 381 (2023) 133436.

[6.2] C. I. David, G. Prabakaran, R. Nandhakumar, Microchem. J. 169 (2021) 106590.

[6.3] P. Mohanty, R. Behura, V. Bhardwaj, P. P. Dash, S. K. Sahoo, B. R. Jali, Trends Environ. Anal. Chem. 34 (2022) e00166.

[6.4] WHO, Guidelines for Drinking-Water Quality: Fourth Edition Incorporating the First and Second Addenda (who.int), (2022).

[6.5] M. P. Nguyen, S. P. Kelly, J. B. Wydallis, C. S. Henry, Anal. Chim. Acta 1100 (2020) 156–162.

[6.6] P. Yadav, R. Kumar, S. Srikrishna, A. K. Pandey, L. H. Choudhury, C. Upadhyay, V. P. Singh, Spectrochim. Acta A: Mol. Biomol. Spectrosc. 267 (2022) 120552.

[6.7] N. Das, J. Raymick, S. Sarkar, Metab. Brain Dis. 36 (2021) 1627–1639.

[6.8] R. Shetty, C. S. N. Vidya, N. B. Prakash, A. Lux, M. Vaculik, Sci. Total Environ. 765 (2021) 142744.

[6.9] X. Wang, C. Shen, C. Zhou, Y. Bu, X. Yan, Chem. Eng. J. 417 (2021) 129125.

[6.10] S. Naqvi, Y. Zhang, S. Ahmed, M. I. Abdulraheem, J. Hu, M. N. Tahir, V. Raghavan, Talanta 236 (2022) 122823.

[6.11] Q. Wang, X. Wen, Z. Fan, J. Photochem. Photobiol. A: Chemistry 358 (2018) 92–99.

[6.12] M. K. Alici, J. Fluoresc. 30 (2020) 269–273.

[6.13] A. Gupta, N. Kumar, RSC Adv. 6 (2016) 106413–106434.

[6.14] (a) S. Patai, Z. Rappoport, The Chemistry of Sulphonic Acids, Esters, and their Derivatives, Wiley, Chichester (1991); (b) S. Patai, Z. Rappoport, C. Stirling, Sulphones and Sulphoxides, Wiley, Chichester (1988).

[6.15] (a) M. Feng, B. Tang, S. H. Liang, X. Jiang, Curr. Top. Med. Chem. 16 (2016) 1200–1216; (b) D. C. Meadows, J. Gervay-Hague, Med. Res. Rev. 26 (2006) 793–814.

[6.16] P. Iversen, C. J. Tyrrell, A. V. Kaisary, J. B. Anderson, H. van Poppel, T. L. J. Tammela, M. Chamberlain, K. Carrol, I. Melezinek, J. Urol. 164 (2000) 1579–1582.

[6.17] G. Wozel, C. Blasum, Arch. Dermatol. Res. 306 (2014) 103–124.

[6.18] J. K. Fink, High Performance Polymers, William Andrew, Norwich (2008).

[6.19] P. Prakash, N. Gupta, Indian J. Physiol. Pharmacol. 49 **(**2005) 125–131.

[6.20] M. R. C. Raja, V. Srinivasan, S. Selvaraj, S. K. Mahapatra, Pharm. Anal. Acta 6 (2015) 5, DOI: 10.4172/2153- 2435.1000367.

[6.21] (a) D. Ravichandran, M. Ranjani, G. P. Sankar, R. Shankar, M. Karthi, S. Selvakumar, R. Prabhakaran, J. Mol. Struct. 1273 (2023) 134329; (b) S. Wang, Y. H. Liao, H. J. Feng, L. Y. Wu, W. Y. He, J. Mol. Struct. 1296 (2024) 136730; (c) S. K. Ramasamy, A. Chinnathambi, S. A. Alharbi, G. Venkatesan, A. Pugazhendhi, G. Sathiyan, J. Mol. Struct. 1302 (2024) 137411; (d) G. Yang, P. Li, Y. Han, L. Tang, Y. Liu, H. Xin, K. N. Wang, S. Zhao, Z. Liu, D. Cao, Materials Chemistry and Physics 295 (2023) 127145; (e) S. Suguna, A. puthoor, D. Parimala devi, A. Abiram, R. Nandhakumar, J. Prabhu, J. Photochem. Photobiol. A: Chemistry 435 (2023) 114268; (f) D. Aydin, S. N. K. Elmas, F. N. Arslan, J. Photochem. Photobiol. A: Chemistry 446 (2024) 115139; (g) S. Huang, H. Yan, L. Lin, H. Guo, F. Yang, J. Photochem. Photobiol., A: Chemistry 447 (2024) 115212; (h) O. G. Yasar, S. N. K. Elmas, D. Aydin, F. N. Arslan, J. Photochem. Photobiol. A: Chemistry 447 (2024) 115238; (i) C. Zhao, H. Xu, X. Zhang, Y. Meng, S. Shuang,

C. Dong, J. Mol. Struct. 1308 (2024) 138022; (j) C. Zhao, M. Asif, W. Lu, S. Shuang, Y. Tang, C. Dong, J. Mol. Liquids 400 (2024) 124507; (k) L. Chen, H. Li, M. Guan, C. Fu, X. Yang, F. Wang, J. Photochem. Photobiol. A: Chemistry 447 (2024) 115274; (l) M. Liu, H. Zhu, Y. Fang, C. Liu, X. Li, X. Zhang, L. Ma, K. Wang, M. Yu, W. Sheng, B. Zhu, Spectrochim. Acta Part A: Mol. Biomol. Spectrosc. 307 (2024) 123578; (m) M. Li, N. Li, F. Shao, R. Wang, M. Chen, Y. J. Liu, Y. Zhao, R. Li, Spectrochim. Acta Part A: Mol. Biomol. Spectrosc. 308 (2024) 123676; (n) X. Y. Wang, L. D. Wang, Q. H. Liu, F. Sun, L. Yang, F. Ye, Spectrochim. Acta Part A: Mol. Biomol. Spectrosc. 308 (2024) 123706; (o) T. J. Dathees, S. P. M. Paul, A. Sanmugam, A. Abiram, S. Murugan, R. S. Kumar, A. I. Almansour, N. Arumugam, R. Nandhakumar, D. Vikraman, Spectrochim. Acta Part A: Mol. Biomol. Spectrosc. 308 (2024) 123732; (p) G. Suganthi, R. Ajitha, A. A. Babu, S. Kamalesu, R. Subramanian, T. Arun, A. Godlyn, K. Nagaraj, Inorg. Chem. Commun. 161 (2024) 112150; (q) B. Mohan, J. Kapoor, A. Shanmughan, M. K. Noushija, M. Sumithradevi, S. Shanmugaraju, Results in Chemistry 7 (2024) 101402; (r) B. Musikavanhu, Z. Huang, Q. Ma, Y. Liang, Z. Xue, L. Feng, L. Zhao, Spectrochim. Acta Part A: Mol. Biomol. Spectrosc. 301 (2023) 122961; (s) S. Bari, D. Mridha, S. Ghosh, P. Ghosh, T. Roychowdhury, P. Roy, New J. Chem. 47 (2023) 5056; (t) C. Yang, J. Zhao, RSC Adv. 14 (2024) 1464; (u) S. Bari, D. Maity, T. Dutta, K. Biswas, P. Roy, Spectrochim. Acta Part A: Mol. Biomol. Spectrosc. 301 (2023) 122981.

[6.22] D. B. Hibbert, P. Thordarson, Chem. Commun. 52 (2016) 12792–12805.

[6.23] (a) A. Pramanik, D. Laha, S. Chattopadhyay, S. K. Dash, S. Roy, P. Pramanik, P. Karmakar, Materials Science and Engineering C 65 (2016) 327–337; (b) D. Laha, A. Pramanik, S. Chattopadhyay, S. K. Dash, S. Roy, P. Pramanik, P. Karmakar, RSC Adv. 5 (2015) 68169–68178.

Appendix- I

List of Publications

&

Seminar attended

List of Publications

[1] **M. Khatun**, P. Ghorai, J. Mandal, S. G.Chowdhury, P. Karmakar, S. Blasco, E. G.España, A. Saha, Aza-phenol Based Macrocyclic Probes Design for "CHEF-on" Multi Analytes Sensor: Crystal Structure Elucidation and Application in Biological Cell Imaging, ACS Omega 8 (2023) 7479-7491 (**Chapter 2**).

[2] **M. Khatun**, P. Ghorai, J. Mandal, S. G. Chowdhury, P. Karmakar, A. Saha, Design and synthesis of a hydrazinopthalazine derived chemosensor to detect metal ions Zn^{2+}, Al^{3+} via CHEF effect with biological study and theoretical calculation, Journal of Photochemistry & Photobiology, A: Chemistry 446 (2024) 115145 (**Chapter 3**).

[3] **M. Khatun,** J. Mandal, V. W. Tamang, S. G. Chowdhury, P. Karmakar, A. Saha, A pyridoxal based bio-compatible fluorometric chemosensor for recognition of Zn^{2+} ions: Theoretical approaches and application in live cell imaging, Journal of Photochemistry & Photobiology, A: Chemistry 447 (2024) 115231 (**Chapter 4**).

[4] **M. Khatun**, J. Mandal, R. Ganguly, A. Barui, A. Saha, Derivative of clove oil used as chemosensor for colorimetric and fluorometric detection of Al^{3+}: crystal structure description and live cell imaging, (under revision in NJC, manuscript ID: NJ-ART-03-2024-001087) (**Chapter 5**).

[5] **M. Khatun**, A. Sanphui, S. Malik, S. G. Chowdhury, P. Karmakar, A. Saha, An euganol-sulfonyl based fluorescent probe for recognition of Al^{3+} in biological sample (under revision, manuscript ID: JPHOTOCHEM-D-24-01140) (**Chapter 6**).

[6] J. Mandal, A. Dey, S. Sarkar, **M. Khatun**, P. Ghorai, P. P. Ray, P. Mahata, A. Saha, Chromone-Based Cd (II) Fluorescent Coordination Polymer Fabricated to Study Optoelectronic and Explosive Sensing Properties, Inorg. Chem. 63 (2024) 4527−4544.

List of seminar attended and presented poster

[1] National seminar on **"Emerging Trends in Chemical Sciences"** under CAS II Program, organised by Department of Chemistry, Jadavpur University.

Held on January 07, 2020.

[2] National seminar on **"Recent Trends in Inorganic Chemistry"** under CAS II Program, organised by Inorganic Chemistry Section, Department of Chemistry, Jadavpur University.

Held on March 06, 2020.

[3] International conference on **"Aggregation-Induced Emission-From Fundamentals To Applications"** under ICAIEFA2022, organised by Department of Chemistry, BITS Pilani, K. K. Birla Goa campus.

Held on December16-18, 2022.

[4] National seminar on **"Recent Trends in Chemistry and Disciplines"** under CAS II Program, organised by Department of Chemistry, University of Burdwan.

Held on January 11, 2024.